Sołowski, Wojciech Tomasz

Material Point Method: the past and the future

Published in:
Proceedings of the 32nd Nordic Seminar on Computational Mechanics

Published: 01/01/2019

Please cite the original version:
Sołowski, W. T. (2019). Material Point Method: the past and the future. In A. H. Niemi, & H. Koivurova (Eds.), *Proceedings of the 32nd Nordic Seminar on Computational Mechanics* (pp. 25-28). (Raportti / Oulun yliopisto. Konetekniikka; No. 9). Oulun yliopisto.
https://www.oulu.fi/sites/default/files/content/NSCM32_Proceedings_not_archived_0.pdf

UNIVERSITY OF OULU

Mechanical Engineering

Oulu

Proceedings of NSCM 32: The 32nd Nordic Seminar on Computational Mechanics 24 – 25 October, 2019

Antti H. Niemi and Hannu Koivurova (editors)

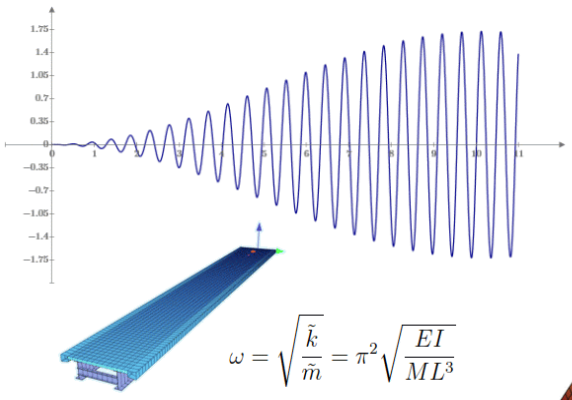

$$\omega = \sqrt{\frac{\tilde{k}}{\tilde{m}}} = \pi^2 \sqrt{\frac{EI}{ML^3}}$$

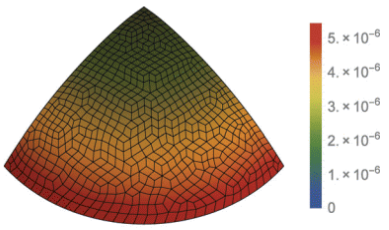

$$\mu = \frac{M_{\mathrm{Rd}}}{bd^2 f_{\mathrm{cd}}} = \frac{(1-0.6\omega) A_{\mathrm{p}} f_{\mathrm{pd}} d}{bd^2 f_{\mathrm{cd}}} = (1-0.6\omega)\omega$$

Report 9

Oulu 2019

University of Oulu
Mechanical Engineering series
Report 9

ISBN 978-952-62-2420-6 (pdf)
ISSN 2342-2599

Oulu 2019

Preface

The Nordic Association for Computational Mechanics (NoACM) was founded in October 1988 in Gothenburg, Sweden among the first organizations established in this field. Ever since the objective of NoACM has been to stimulate and promote research and practice in computational mechanics, to foster the interchange of ideas among the various fields contributing to computational mechanics, and to provide forums and meetings for dissemination of knowledge about computational mechanics. In particular, presentations by graduate students have always been welcomed. Thus, making a friendly and creative atmosphere for the participants is considered important.

This year's seminar is already the 32nd in the series. It is arranged for the first time in the municipality of Oulu located in the region of North Ostrobothnia in Finland. This is probably one of the northernmost locations in the world where a seminar on computational mechanics has ever been arranged. The seminar has attracted around 50 contributions distributed in two parallel sessions over two days.

The organizers would like to thank all authors for submitting their contributions, as well as their supporting organizations, to make NSCM32 in Oulu possible!

Linnanmaa, Oulu, 18 October, 2019

Antti H. Niemi
Hannu Koivurova

Table of content

Executive Committee of NoACM

Mats Larson (Chairman)	Sweden
Fredrik Larson (Secretary)	Sweden
Erik Lund	Denmark
Martin Otto	Denmark
Laver Hansen,	Denmark
Tanel Peets	Estonia (Baltic Countries)
Antti H. Niemi	Finland
Jarkko Niiranen	Finland
Jianying He	Norway
Trond Kvamsdal	Norway

Scientific advisory board

Tero Frondelius	Wärtsilä Finland Oy and University of Oulu
Reijo Kouhia	Tampere University
Jarkko Niiranen	Aalto University
Peter Råback	CSC - IT Center for Science Ltd.
Arja Saarenheimo	VTT Technical Research Centre of Finland Ltd
Rolf Stenberg	Aalto University

Local organizing committee

Antti H. Niemi (Chairman)
Filip Fedorik
Matti Kangaspuoskari
Hannu Koivurova
Hannu Lahtinen
Hannu Liedes
Jari Laukkanen
Jouko Lumijärvi

Structures and Construction Technology
University of Oulu
P.O. Box 4200
FI-90014 University of Oulu
FINLAND

Phone +358 294 482020
Fax +358 8 553 2026
http://www.oulu.fi/construction/

Downtown Oulu

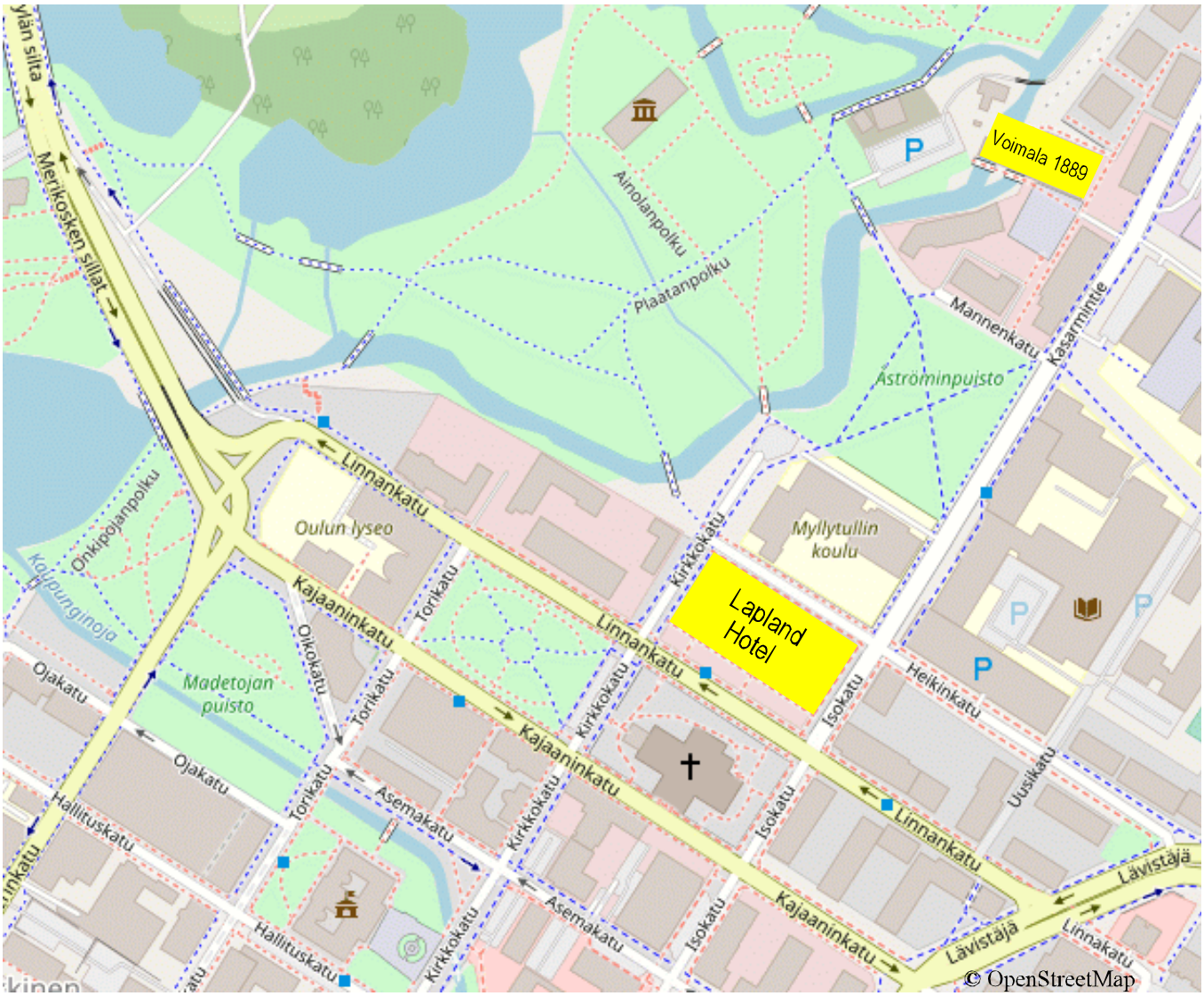

Program of the 32:nd Nordic Seminar in Computationl Mechanics

Venue: Lapland Hotels Oulu
Kirkkokatu 3, Oulu

Wednesday 23 October 2019 - Evening			
TIME	**Room**	**EVENT**	
19.00 - 21.00	Kuvernööri	**Registration and Get-together**	

Thursday 24 October 2019 - Morning			
TIME	**Room**	**EVENT**	**Page**
08.30 - 09.00	Saariselkä	**Registration**	
09.00 - 09.15	Saariselkä	**Opening: Dean Riitta Keiski, Faculty of Technology, University Oulu** **Chair Antti H. Niemi**	
09.15 - 10.45	Saariselkä	**Plenary lecture: Chair Antti H. Niemi** • **Marrying computational mechanics and materials science** **Lars-Erik Lindgren, Luleå University of Technology, Sweden** • **Higher Order Haar Wavelet Method. Application for Analysis of FGM and Nanostructures - Jüri Majak, Tallinn University of Technology, Estonia**	13 17
10.45 - 11.20		**Coffee break**	
11.20 - 13.00	Saariselkä	**Session I: Damage and Fracture, Chair Ralf Jänicke**	
11.20 - 11.40		On the regularisation property of the Kachanov-Rabotnov continuum damage model - a finite element study - Reijo Kouhia	43
11.40 - 12.00		Continuum damage modelling of quasi-brittle materials by using the material point method - Tuan H. A. Nguyen	160
12.00 - 12.20		Hard missile impact simulation with Abaqus - Alexis Fedoroff	51
12.20 - 12.40		Variationally consistent homogenization of phase field fracture model Ritukesh Bharali	47
12.40 - 13.00		Numerical modelling of concrete fracture: a mesoscopic approach based on embedded discontinuity FEM - Timo Saksala	146
11.20 - 13.00	Ylläs	**Session II: Optimization, Chair Keijo Ruotsalainen**	
11.20 - 11.40		Shape and topology optimization using CutFEM - Niels Aage,	33
11.40 - 12.00		JuliaFEM geometry optimization - Jouni Huopana	79
12.00 - 12.20		A new material contrast model for use in topology optimization of steady-state dynamic problems - Jakob S. Jensen	87
12.20 - 12.40		On optimal design of lug joints - N. L. Pedersen	131
12.40 - 13.00		Multiscale design optimization of structures with solid coating and periodic infill lattice - Eddie Wadbro	185
13.00 - 14.00		**Lunch**	

Thursday 24 October 2019 - Afternoon			
TIME	**Room**	**EVENT**	**Page**
14.00 - 14.45	Saariselkä	**Plenary lecture: Chair Trond Kvamsdal** **Hybrid Modeling as an enabler for Big data cybernetics** **Adil Rasheed, NTNU Trondheim, Norway**	21
14.50 - 16.10	Saariselkä	**Session III: Numerical methods, Chair Trond Kvamsdal**	
14.50 - 15.10		A posteriori Error Estimation for Isogeometric Analysis of the Advection-Diffusion equation - Abdullah Abdulhaque	37
15.10 - 15.30		On error-controlled numerical model reduction for computational homogenization of porous media - Fredrik Ekre	59
15.30 - 15.50		Least Squares Stabilized Nitsche in CutIGA - Mats G. Larson	110
15.50 - 16.10		How about version control? - Juha Jeronen	91
14.50 - 16.10	Ylläs	**Session IV: Material mechanics, modelling tehnique and applications**, **Chair Fredrik Larsson**	
14.50 - 15.10		A numerical framework for rate-independent for Fleck and Willis crystal plasticity Kim Lau Nielsen	119
15.10 - 15.30		Finite Element Simulation of the Performance of a Structural Electrolyte - Vinh Tu	162
15.30 - 15.50		Finite element modeling of Al6082 Plasma Electrolytic Oxidation coatings Sergei Khakalo	104
15.50 - 16.10		MFrontInterface.jl: MFront material models in JuliaFEM - Tero Frondelius	67
16.10 - 16.40	**Coffee break**		
16.40 - 17.40	Saariselkä	**Session V: Material mechanics, modelling tehnique and applications, Chair Lars-Erik Lindgren**	
16.40 - 17.00		Mathematical modelling of sustainable bioresidual concrete - Tero Tuovinen	166
17.00 - 17.20		FEM-DEM in Modeling Ice-structure Interaction Process - Arttu Polojärvi	133
17.20 - 17.40		Micropolar plate model for lattice core sandwich panels - Anssi Karttunen	102
17.40 - 18.00		Thurster Driveline Digital Twin – Bearing and Shaft Fatigue Life Prediction Taneli Leppänen	114
16.40 - 17.40	Ylläs	**Session VI: Dynamics, Chair Jüri Majak**	
16.40 - 17.00		A Modal System Reduction Procedure for a Flexible Structure with a Flexible Vibration Absorber - Jan Høgsberg	75
17.00 - 17.20		Numerical analysis of coupled nerve signal propagation - Tanel Peets	154
17.20 - 17.40		Crankshaft impact modelling - Antti-Jussi Vuotikka	177
17.40 - 18.00		Deep learning for future state estimation of the unsteady flows - Hamidreza Eivazi	55

19.00 -	**Conference dinner at Voimala 1889**

Friday 25 October 2019 - Morning			
TIME	**Room**	**EVENT**	**Page**
09.00 - 10.30	Saariselkä	**Plenary lecture: Chair Jarkko Niiranen** • **Material point method: the past and the futur** **Wojciech Solowski, Aalto University, Finland** • **A single-cell computation for dynamic turbulent cascade development - the 'Navier-Stokes Machine'** **Clara Marika Velte, Technical University of Denmark**	25 29
10.30 - 11.00	**Coffee break**		
11.00 - 12.40	Saariselkä	**Session V: Structural Mechanics, Chair Mats G. Larson**	
11.00 - 11.20		Goal Oriented Adaptive Isogeometric Methods applied to Structural Mechanics Trond Kvamsdal	108
11.20 - 11.40		Inelastic buckling of plates subjected to multi axial in-plane loads - Alireza Jahanpour	83
11.40 - 12.00		Parametric modelling of cellular beam and plate structures by orthotropic strain gradient thermo-elasticity - Jarkko Niiranen	124
12.00 - 12.20		On periodic boundary conditions in Variationally Consistent Homogenisation of beams and plates - Adam Sciegaj	150
12.20 - 12.40		Nonlinear bending of microarchitectural thin beams within strain gradient elasticity Loc V. Tran	158
11.00 - 12.40	Ylläs	**Session VI: Fatigue, Chair Tero Frondelius**	
11.00 - 11.20		On the integration of an evolution equation based high-cycle fatigue model Reijo Kouhia	95
11.20 - 11.40		Comparison 32CrMo12 QT steel fatigue testing with ultrasonic and servo-hydraulic testing machines - Taneli Rantakivi	136
11.40 - 12.00		Comparison of selected sequential design of experiment strategies for fatigue testing - Joona Vaara	170
12.00 - 12.20		Fatigue Testing - Informativity of the Experimental Data - Miikka Väntänen	180
12.40 - 13.40	**Lunch**		

Friday 25 October 2019 - Afternoon			
TIME	**Room**	**EVENT**	**Page**
13.40 - 15.00	Saariselkä	**Session VII: Material mechanics, modelling tehnique and applications, Chair Jarkko Niiranen**	
13.40 - 14.00		Achilles tendon modeling based on the absolute nodal coordinate formulation Leonid Obrezkov	127
14.00 - 14.20		Microstructural modelling of defect containing martensitic steels - Tom Andersson	39
14.20 - 14.40		Modeling of non-coulomb friction under fretting conditions part 2 - Jouko Hintikka	71
14.40 - 15.00		Modeling friction and wear in dynamically loaded clamped metal contacts A. Mäntylä	115
13.40 - 15.00	Ylläs	**Session VII: Structural Engineering, Chair Reijo Kouhia**	
13.40 - 14.00		Cost-optimized rise of tied-arch bridges - Esko Järvenpää	98
14.00 - 14.20		Comparison of hygrothermal simulation techniques in northern conditions Filip Fedorik	62
14.20 - 14.40		Waveguides that support trapped surface waves - Keijo Ruotsalainen	140
14.40 - 15.00		Reliability of Finnish steel trusses under snow load in light of the design standard EN 1990 - Antti H. Niemi	121
15.00 - 15.15	Saariselkä	**Closing - Organizers**	

Proceedings of the 32nd Nordic Seminar on Computational Mechanics
A.H. Niemi and H. Koivurova (Eds.)

Marrying Computational Mechanics and Materials Science

Lars-Erik Lindgren

(1)Luleå University of Technology 97187 Luleå, Sweden, lars-erik.lindgren@ltu,se

Summary. The advancement of computational resources and techniques enable the use of more accurate models both with respect to spatial and temporal resolution but also concerning the modeled physics. This is a benefit when simulating thermo-mechanical processes, as they often requires coupled microstructure and property models. Integration of these models combines the fields of mechanical and materials science.

Key words: manufacturing, microstructure, thermal properties, mechanical properties

Introduction

The response of metals and alloys for a given thermal and mechanical loading depends on its microstructure. The notation microstructure is used here to denote all scales from the lattice up to a collection of grains. The microstructure in turn, is a product of the previous thermo-mechanical history. It is therefore of interest to combine structure-property models according to the classic paradigm in material science, see figure 1. The microstructure models must be such that they do not require a resolution of the microstructure in order to be able to simulate manufacturing on the component scale. The talk will present some models for Ti-alloys, superalloys as well as steels that have been used in manufacturing simulations.

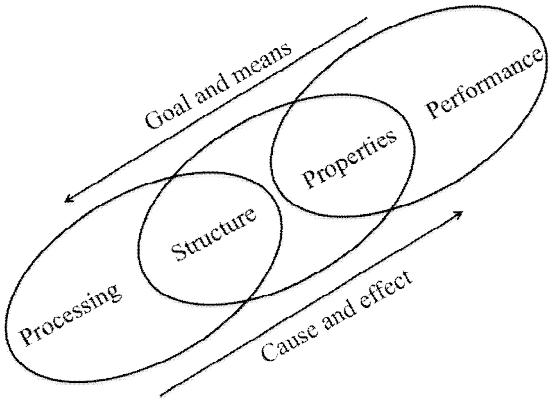

Figure 1. Process-Structure-Properties-Performance paradigm.

Ti-6Al-4V

A quite complete model for α-β phase changes in Ti-6Al-4V was developed by Charles-Murgau *et al*. [1]. It is built on various published sub-models and particularly on Kelly [2]. The model was combined with a dislocation density based plasticity model by Babu *et al*. [3]. It has been applied to additive manufacturing, see figure 2.

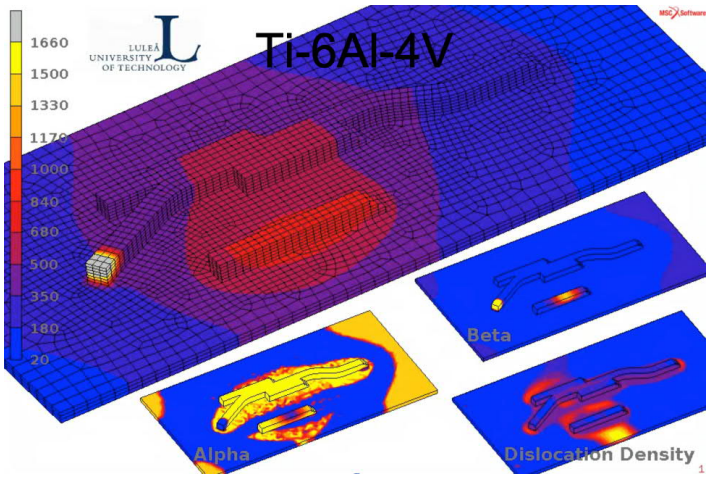

Figure 3. Metal deposition of Ti-6Al-4V. Temperature field shown in upper part whereas α-phase and β-phase fractions are shown below it. The dislocation density, used in the flow stress model, is shown in lower, right part.

Alloy 718

Alloy 718 is a precipitate hardened alloy where the γ'' phase gives the largest contribution to creep resistance. Simulation ageing and simultaneous stress relief requires a model that can predict the precipitate distribution as well as its effect on the plastic properties of the material. A model for this case has been developed and applied to repair welding and subsequent ageing [4-6], see figure 3.

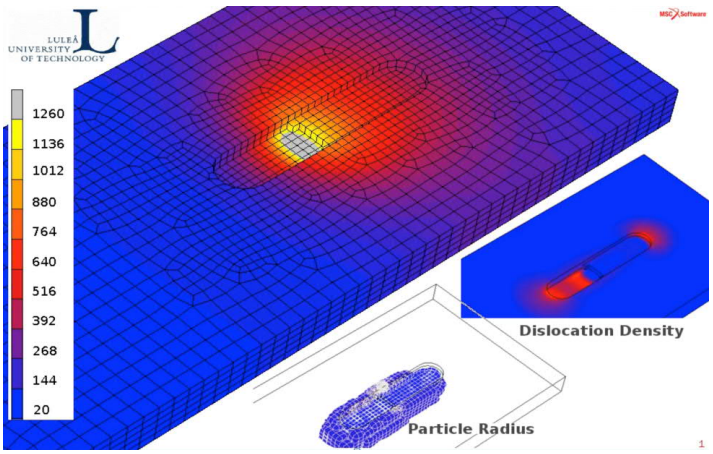

Figure 3. Repair welding of alloy 718.

Low alloy steels

A model for microstructure evolution of hypoeutectoid steels has been combined with property models [7-10]. The microstructure model is limited to computation of ferrite, austenite as well as pearlite, bainite and martensite. It can compute the thermal driven phase changes given chemical composition of the steel. The model can be improved if further information is available from time-temperature-transformation (TTT) or continuous-cooling-transformation (CCT) diagrams. This means that there is not additional split into, e.g. upper and lower bainite etc. The model can estimate thermal expansion, elastic and thermal properties also as a function of chemical composition and temperature. Two examples from the microstructure model are shown in figure 4 below. An example from the model for elastic properties is shown in figure 5. The relaxed modulus measurement has an anelastic effect, see [38].

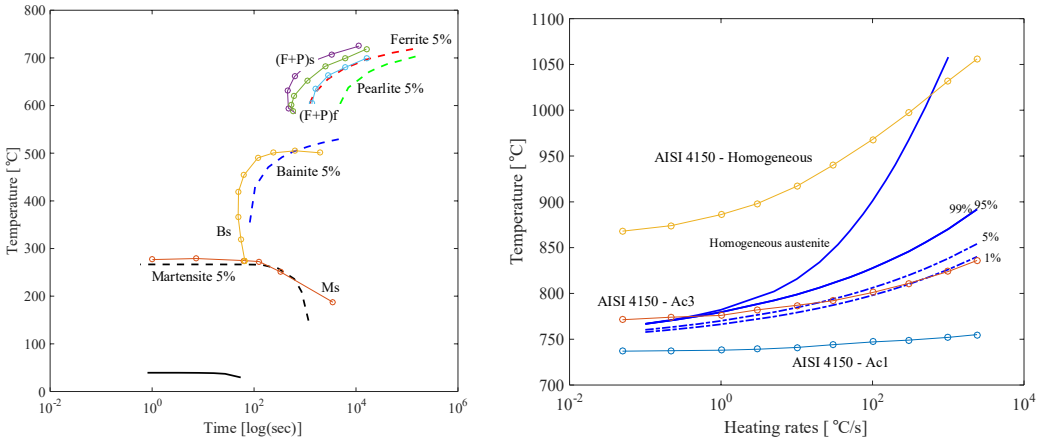

Figure 4. Left, computed CCT diagram for AISI 4150. Right, heating transformation diagram. Lines are from model and symbol from measurements.

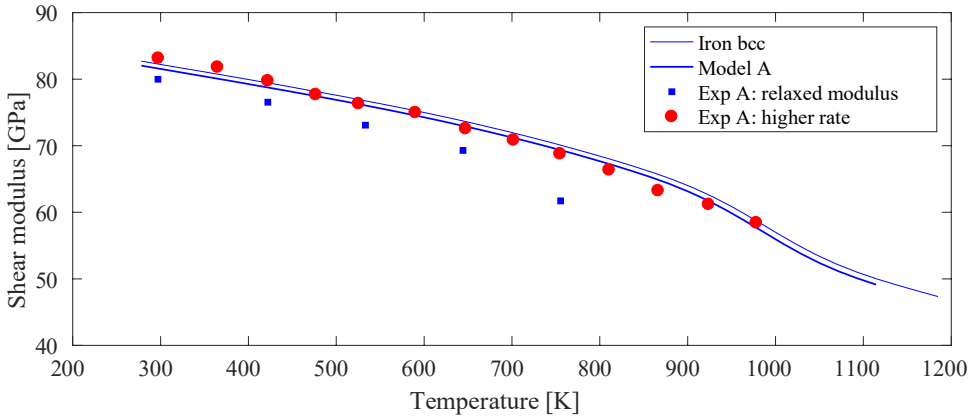

Figure 5. Model for shear modulus applied to a low alloy steel from [11].

Concluding remark

The combination of computational mechanics and materials science benefit both fields. The former get access to expertise and models from material science. The latter field profits by having a 'demanding customer'. The use of models in computational mechanics requires that they can be subjected to arbitrarily histories as well as must fulfill some invariance requirements.

References

[1] C. Charles Murgau, R. Pederson, and L.-E. Lindgren, A model for Ti-6Al-4V microstructure evolution for arbitrary temperature changes, *Modelling and Simulation in Materials Science and Engineering,* 20:055006, 2012.

[2] S. Kelly, Thermal and microstructure modeling of metal deposition processes with application to Ti-6Al-4V, Virginia Polytechnic Institute and State University, 2004, 2004.

[3] B. Babu, and L.-E. Lindgren, Dislocation density based model for plastic deformation and globularisation of Ti-6Al-4V, *International Journal of Plasticity,* 50:94-108, 2013.

[4] M. Fisk, and A. Lundbäck, Simulation and validation of repair welding and heat treatment of an alloy 718 plate, *Finite Elements in Analysis and Design,* 58:66-73, 2012.

[5] M. Fisk, J.C. Ion, and L.E. Lindgren, Flow stress model for IN718 accounting for evolution of strengthening precipitates during thermal treatment, *Computational Materials Science,* 82:531-539, 2014.

[6] M. Fisk, A. Lundbäck, J. Edberg, and J.M. Zhou, Simulation of microstructural evolution during repair welding of an IN718 plate, *Finite Elements in Analysis and Design,* 120:92-101, 2016.

[7] A.S. Oddy, J.M.J. McDill, and L. Karlsson, Microstructural predictions including arbitrary thermal histories, reaustenization and carbon segregation effects, *Canadian Metallurgical Quarterly,* 35:275-283, 1996.

[8] L.-E. Lindgren, and J.G. Back, Elastic properties of ferrite and austenite in low alloy steels versus temperature and alloying, *Materialia,* 5:100193, 2019.

[9] L.-E. Lindgren, J. Edberg, P. Åkerström, and Z. Zhang, Modeling of thermal stresses in low alloy steels, *Journal of Thermal Stresses,* 42:725-743, 2019.

[10] L.-E. Lindgren, A. Lundbäck, and A. Malmelöv, Thermal stresses and computational welding mechanics, *Journal of Thermal Stresses,* 42:107-121, 2019.

[11] F. Garofalo, P. Malenock, and G. Smith, 'The Influence of Temperature on the Elastic Constants of Some Commercial Steels', in ASTM *Symposium on Determination of Elastic Constants*, pp. 10-27, 1952.

Proceedings of the 32nd Nordic Seminar on Computational Mechanics
A.H. Niemi and H. Koivurova (Eds.)

Higher Order Haar Wavelet Method. Application for Analysis of FGM and Nanostructures

Jüri Majak[1], Maarjus Kirs[1], Mart Ratas[1]
[(1)]Tallinn University of Technology, Estonia, Juri.Majak@taltech.ee,
Maarjus.Kirs@taltech.ee, Mart.Ratas@taltech.ee

Summary. The wavelet methods provide new, interesting approach for solving differential, integro-differential and integral equations in comparison with traditional/classical methods. In the current paper is given an overview on higher order Haar wavelet method, introduced recently by workgroup, discussed first results obtained and future study in this area. The free vibration analysis of the functionally graded beam and nanobeam are considered as case studies.

Key words: Higher order Haar Wavelet method, functionally graded beam, nanobeam.

Introduction

The Haar wavelet method (HWM) has been introduced for solving differential equations by Chen and Hsiao in 1997, in particular for solving lumped and distributed parameter systems Ref. [1]. According to approach based by Chen & Hsiao, the higher order derivative included in differential equation is expanded into series of Haar wavelet fucntions. Later this approach was extended later for solving ordinary and partial differential Ref. [2,3], integro-differenial Ref. [4,5] and integral equations Ref. [6-7] covering wide range of applications like mathematical physics, evolution equations, nuclear reactor dynamics, unsteady-state free-surface ship models, mechanics of solids, two-point boundary value problems, etc. In Ref. [8-11] HWM is applied for analysis of composite structures. In Ref. [8] and Ref. [9] the free vibration analysis of the multilayer composite plate and delamination of the composite beam is studied, respectively. In Ref. [10-11] functionally graded structures are examined. An overview on HWM and its applications is given in monograph Ref. [12]. Most of papers, covering HWM and published during two decades are based Chen and Hsiao approach and strong formulation.

In these papers the implementation of the HWM is found simple. The HWM is characterized commonly with terms “simple” and “effective“. The estimates given for Chen and Hsiao approach based HWM rely on obtained results and are founded.

However, no comparison with advanced/powerful strong formulation based numerical methods with similar complexity (FDM, DQM, etc.) were performed. Recent study, based on comparison of the Chen and Hsiao approach based HWM with FDM and DQM, lead to a quite different results Ref. [13]. In general, the Chen and Hsiao approach based HWM was found in same range with FDM by accuracy, but it was outperformed by DQM.
The conclusion made was that the Chen and Hsiao approach based HWM need principal improvement in order to compete with advanced methods used in engineering design.

Higher Order Haar Wavelet Method

Recently, the higher order Haar wavelet method (HOHWM) for solving differential equations was introduced Ref. [14]. The proposed method is based on the following two subtasks:

- Higher order wavelet expansion(s) in general form.
- Concepts for determining integration constants included in higher order wavelet expansions.

$$f(x)=\frac{d^{n+2s}u(x)}{dx^{n+2s}}=\sum_{i=1}^{\infty}a_i h_i(x), \qquad s=1,2,... \tag{1}$$

In (1) n stands for the order of highest derivative included in differential equation. Thus, in the case of $s=1$ the derivative of order $n+2$ is expanded into Haar wavelets. It should be pointed out that, among higher order wavelet expansion (11), the accuracy of the solution depends substantially on conditions used for determining integration constants. The two approaches proposed for determining of integration constants are discussed in details in Ref. [14] and are omitted herein for conciseness sake.

Numerical results

In the following two sample problems are considered: the free vibration analysis of the simply supported FGM beam and nanobeam.

Free Vibration analysis of FGM beam

The pinned-pinned FGM beam with length $L=1m$, is considered. The cross-section of the beam is square, where the height and the width of the cross-section are equal to $b=0.01m$. Radial graduation functions applied for the bending stiffness $EI(x)$ and the distributed mass per unit length $\rho A(x)$ are given for the exponential law function as Ref. [15]:

$$EI(x)=EI(0)e^{2\beta x/L},\ \rho A(x)=\rho A(0)e^{2\beta x/L}. \tag{2}$$

Table 1. Fundamental frequency values Ω_1 of simpli supported FGM beam ($\beta=3$)

	HWM approach by Chen&Hsiao			**Proposed HOHWM (Majak et al.)**			
N	Fundamental frequency Ω_1	Absolute error	Converg. rate	Fundamental frequency Ω_1	Absolute error	Converg. rate	Error ratio
4	5.49612520	1.35E+00		7.81629606	9.73E-01		1.4
8	6.56237797	2.81E-01	2.2627	6.87693058	3.39E-02	4.8442	8.3
16	6.76542022	7.76E-02	1.8542	6.84538131	2.33E-03	3.8607	33.3
32	6.82322484	1.98E-02	1.9693	6.84319842	1.49E-04	3.9644	133.0
64	6.83806767	4.98E-03	1.9927	6.84305841	9.40E-06	3.9908	529.9
128	6.84180211	1.25E-03	1.9982	6.84304960	5.88E-07	3.9977	2120.6
256	6.84273719	3.12E-04	1.9995	6.84304905	3.68E-08	3.9995	8473.5
512	6.84297105	7.80E-05	1.9999	6.84304901	2.29E-09	4.0074	34044.6
Exact	**6.84304901**			**6.84304901**			

The values of the fundamental frequency, absolute errors and the rates of convergence corresponding to widely used Chen&Hsiao and current approaches are compared in Table 1, where the material grading index β is equal to three. It can be seen from Table 1, that the rate of convergence of the proposed higher order method is equal to four and the absolute error is several orders of magnitude less than that of Chen and Hsiao approach based HWM. The error ratio of the widely used and current approach is given in column 8 of the Table 1.

Free Vibration analysis of nanobeam

The Eringen nonlocal elasticity theory is utilized for free vibration analysis of the Euler-Bernoully nanobeam. The governing equations are given in Ref. [16]. The nonlocal parameter μ is taken equal to three. The values of the fundamental frequency, absolute errors and the rates of convergence corresponding to widely used Chen&Hsiao and current approaches are compared in Table 2.

Table 2. Fundamental frequency values Ω_1 of simpli supported nanobeam *(μ = 3)*

	HWM approach by Chen&Hsiao			**Proposed HOHWM (Majak et al.)**			
N	Fundamental frequency Ω_1	Absolute error	Converg. rate	Fundamental frequency Ω_1	Absolute error	Converg. rate	Error ratio
4	2.9631691775	1.88E-02		2.9454323919	1.07E-03		17.6
8	2.9490867632	4.72E-03	1.9930	2.9444268262	6.46E-05	4.0504	73.1
16	2.9455443778	1.18E-03	1.9988	2.9443662390	4.00E-06	4.0129	295.5
32	2.9446578302	2.96E-04	1.9997	2.9443624877	2.49E-07	4.0032	1184.8
64	2.9444361397	7.39E-05	1.9999	2.9443622538	1.56E-08	4.0008	4742.0
128	2.9443807138	1.85E-05	2.0000	2.9443622392	9.74E-10	4.0004	18973.2
256	2.9443668571	4.62E-06	2.0000	2.9443622383	6.28E-11	3.9559	73607.9
512	2.9443633929	1.15E-06	2.0000	2.9443622382	2.84E-12	4.4650	406411.2
Exact	**2.9443622382**			**2.9443622382**			

It can be observed from Table 2 that he numerical order of convergence is improved from two to four and the absolute error is substantially, depending on number of collocation points used. No remarkable increase of the numerical and implementation complexities has been observed in the case of posed simply supported nanobeam. However, in the case of vibrations analysis of the nanobeam, the complexity depend boundary conditions used.

Conclusions

In the case of problems considered the higher order Haar wavelet method (HOHWM) outperform HWM. The accuracy has been improved principally. However, the problems solved are rather simple and the results obtained can be considered as introduction to further study in this area. The work on extension of the HOHWM to partial differential equations and also fractional differential equations is in progress. The first results obtained are promising, but expected.

References

[1] CF. Chen, CH. Hsiao, Haar wavelet method for solving lumped and distributed-parameter systems, *IEE Proc. Contr. Theor. Appl.* 144(1) :87–94,1997.

[2] Ü. Lepik Solving PDEs with the aid of two dimensional Haar wavelets. Computers & Mathematics with Applications. 61 (2011) 1873-1879.

[3] X. Xie, G. Jin, T. Ye, Z. Liu, Free vibration analysis of functionally graded conical shells and annular plates using the Haar wavelet method. *Applied Acoustics*. 85:130-142, 2014.

[4] Ü. Lepik, Haar wavelet method for nonlinear integro-differential equations. *Applied Mathematics and Computation*.176:324-333, 2006.

[5] SU. Islam, I. Aziz, AS. Al-Fhaid, An improved method based on Haar wavelets for numerical solution of nonlinear integral and integro-differential equations of first and higher orders. *Journal of Computational and Applied Mathematics*. 260: 449–469, 2014.

[6] I. Aziz, SU. Islam, F. Khana, A new method based on Haar wavelet for the numerical solution of two-dimensional nonlinear integral equations, *J. Comput. Appl. Math.* 272:70–80, 2014.

[7] I. Aziz, SU. Islam, New algorithms for the numerical solution of nonlinear Fredholm and Volterra integral equations using Haar wavelets, *J. Comput. Appl. Math.* 239(1):333–345, 2013.

[8] J. Majak, M. Pohlak, M. Eerme, Application of the Haar Wavelet-based discretization technique to problems of orthotropic plates and shells. *Mechanics of Composite Materials*, 45(6):631-642, 2009.

[9] H. Hein L., Feklistova Computationally efficient delamination detection in composite beams using Haar wavelets. *Mechanical Systems and Signal Processing* 25(6): 2257-2270, 2011.

[10] X. Xie, G. Jin, Y. Yan SX. Shi, Z. Liu. Free vibration analysis of composite laminated cylindrical shells using the Haar wavelet method, *Composite Structures* 109:169-177, 2014.

[11] G. Jin, X. Xie, Z. Liu. The Haar wavelet method for free vibration analysis of functionally graded cylindrical shells based on the shear deformation theory, *Composite Structures* 108:435–448, 2014.

[12] Ü. Lepik, Hein H. *Haar wavelets: with applications*. Springer, 2014.

[13] M. Kirs, *Evaluation of Haar wavelet method for analysis of functionally graded and nanostructures*, Doctoral Theses, 2018.

[14] J. Majak, M. Pohlak, K. Karjust, M. Eerme, J. Kurnitski, BS. Shvartsman, New higher order Haar wavelet method: Application to FGM structures. *Composite Structures*, 201:72-78, 2018.

[15] Z.R. Lu, X.X. Lin, Y. M. Chen, M. Huang. Hybrid sensitivity matrix for damage identification in axially functionally graded beams. *Applied Mathematical Modelling*, 41:604–617, 2017.

[16] M. Kirs, M. Mikola, A. Haavajõe, E. Õunapuu, B. Shvartsman, J. Majak. Haar wavelet method for vibration analysis of nanobeams. Waves, Wavelets and Fractals Advanced Analysis, 2:20−28, 2016.

Proceedings of the 32nd Nordic Seminar on Computational Mechanics
A.H. Niemi and H. Koivurova (Eds.)

Hybrid Analysis and Modeling as an enabler for Big Data Cybernetics

Adil Rasheed[1,5], Omer San[2], Haakon Robinson[3] and Trond Kvamsdal[4,5]

(1) Department of Engineering Cybernetics, NTNU adil.rasheed@ntnu.no
(2) Mechanical and Aerospace Engineering, Oklahoma State University, osan@okstate.edu
(3) Department of Engineering Cybernetics, NTNU, haakon.robinson@ntnu.no
(4) Department of Mathematical Sciences, NTNU, trond.kvamsdal@ntnu.no
(5) Department of Mathematics and Cybernetics, SINTEF Digital

Summary. In this work we introduce Hybrid Analysis and Modeling (HAM) as an enabler for Big Data Cybernetics. HAM approach combines the interpretability, robust foundation and understanding of physics-based models with the accuracy, efficiency, and automatic pattern-identification capabilities of advanced machine learning (ML) and artificial intelligence (AI) algorithms for real-time steering of any physical asset towards a set point using big data. At a time when blackbox ML and AI algorithms are struggling to find large scale acceptability in safety critical engineering applications, it is argued that HAM will be an attractive alternative.

Key words: Big Data Cybernetics, Hybrid Analysis and Modeling

Background

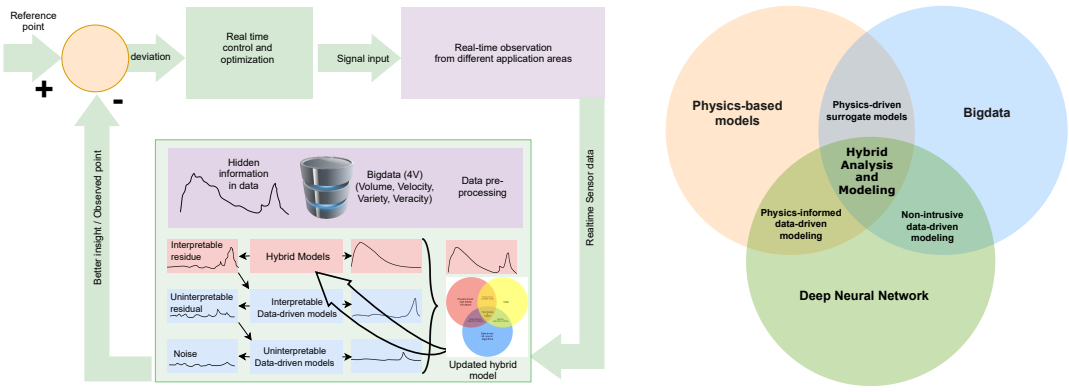

(a) Big Data Cybernetics (b) Hybrid Analysis and Modeling

Figure 1. HAM in the context of Big Data Cybernetics

In the context of upcoming technologies like Digital Twin [1] the role of cybernetics is to steer the system / asset towards an optimal set point. In order to do so, the output of the system is continuously monitored and compared against a reference. The difference, called the error signal is applied as feedback to the controller which generates a system input to bring the output set-point closer to the reference. With the availability of more and more sensors and communication technologies, increasingly larger volumes of data (in fact big data) is getting available in real-time. The challenge is then to develop a better understanding of the big data

before it can be used for control purposes. The newly established field of Big Data Cybernetics (an adaptation of the concept first conceived in [2] at the Norwegian University of Science and Technology) offers to address this challenge in a real-time control context. At the first step, the big data is interpreted using well understood mechanistic models based on known physics. The rest is termed as interpretable residual which in a second step is modeled using interpretable data-driven approach. After the second step, an uninterpretable residual remains which is modeled using more complex and blackbox models like Deep Neural Networks (DNN). The remaining residual is generally noise which can be discarded. The three steps result in a better understanding of the data and hence improved models provided new approaches can be developed to combine existing physics based modeling, interpretable and non-interpretable data-driven modeling with big data. The steps are continuously looped with the availability of new data (i.e., see Figure 1(a)) resulting in ever adapting and improving models. In the following section we present different approaches to conducting HAM.

Different approaches to HAM

Complete replacement of the equations with DNN

This approach can be used when there is a need to replace computationally demanding numerical solvers with trained DNN that can make predictions in ll time. The approach will be very specific to the problem in hand and will not generalize well. In [3] we demonstrated various DNN frameworks predicting the evolution of dynamical systems by learning from using discrete state of the system.

Modeling the unknown using DNN and imposing sanity check using equations based on known physics

This approach involves modeling the known physics using equations but employing trained DNN for modeling the unknown physics. In the context of turbulent flow modeling using coarse grid, the overall mass and momentum conservation principles can be well represented using the Navier Stokes Equations however, the subgrid scales require modeling. In [4, 5] we demonstrated that the subgrid scale phenomena can be learned using a DNN and any unexpected behavior of the network can be detected using the mass and momentum conservation principles. We call this physics-informed detection of misbehaviour as in-built sanity check mechanism in the context of HAM. This particular approach can be represented by the intersection of the DNN and physics-based modeling in Figure 1(b).

Memory embedded reduced order modeling of turbulent flows

Intrusive reduced order modeling (ROM) involves conducting high fidelity numerical simulations to construct snapshots on which Proper Orthogonal Decomposition (POD) is performed to extract dominant reduced bases. The original equations are then projected on these reduced bases to give a system of ordinary differential equations which can be solved in real-time to get an evolution of the model coefficients which can be used to reconstruct the full field. There are two major issues with this particular approach in relation to the modeling of turbulent flows: firstly one requires the form of the underlying equations (that generated the data) which is not always possible and secondly the mode truncation introduces numerical error and instability in the ROM model. To alleviate these problems, in [7], we demonstrated a fully non-intrusive ROM approach where we employ long-short-term memory (LSTM) network to learn and predict the evolution of the modal coefficients.

Physics / knowledge / regulations informed machine learning

This particular approach involves programming physics, domain knowledge or regulations directly into the DNN. In DNN, the cost function that is minimized is generally the mean squared

error which includes little direct information about the underlying physics. One way to inform the DNN of the underlying physics (or knowledge and regulation) is to regularize the cost function with the residual of the governing equations based on physics. Alternatively, the cost function (or rewards function in the context of Deep Reinforcement Learning) can be penalized or rewarded in the hope of learning new knowledge. Work in this direction pertains to path following and collision avoidance of autonomous ships.

Dissecting DNN

Numerous HAM approaches mentioned above exploit the universal approximation properties of DNN and therefore, for a risk free adoption of the approaches in safety critical application it is imperative to make the neural networks more interpretable. A first step to interpreting these networks is to develop alternative representations that allow for further analysis. It has been shown that neural networks with piecewise affine activation functions are themselves piecewise affine, with their domains consisting of a vast number of linear regions. So far, the research on this topic has focused on counting the number of linear regions, rather than obtaining explicit piecewise affine representations. Our recent work [8] presents a novel algorithm that can compute the piecewise affine form of any fully connected neural network with rectified linear unit activation.

Conclusions

In this paper we presented a new paradigm in modeling called the HAM that combines the best of both the worlds: physics based modeling and data driven modeling. We followed this up by proposing five distinct approaches to doing HAM. It is foreseen that a combination of these different approaches will lead us to the center of the Venn diagram presented in Figure 1(b). Operating at that point one will be able to exploit the full potential of the novel concept of Big Data Cybernetics.

Acknowledgement

We would like to thank all our colleagues and students who have contributed significantly to the development and demonstration of the approaches mentioned and cited in this paper.

References

[1] Rasheed, A., San, O., Kvamsdal, T., Digital Twin: Values, Challenges and Enablers, https://arxiv.org/abs/1910.01719

[2] H. Martens. Bigdatacybernetics. [Online]. Available: http://folk.ntnu.no/martens/?BigDataCybernetics

[3] Pawar, S., Rahman, S. M., Vaddireddy, H. , San, O., Rasheed, A. and Vedula, P., A deep learning enabler for non-intrusive reduced order modeling of fluid flows, Physics of Fluids, 31, 085101, 2019.

[4] Romit, M., San, O., Rasheed, A. and Vedula, P., Sub-grid modelling for two-dimensional turbulence using neural networks, Journal of Fluid Mechanics, 858, 122-144, 2019.

[5] Romit, M., San, O., Rasheed, A. and Vedula, P., Data-driven deconvolution for large eddy simulations of Kraichnan turbulence, Physics of Fluids, 30, 125109, 2018.

[6] Fonn, E., Brummelen, H. Kvamsdal, T., Rasheed, A., Fast divergence-conforming reduced basis methods for steady Navier–Stokes flow, Computer Methods in Applied Mechanics and Engineering, 346, 486-512, 2019

[7] Rahman, Sk.M., Pawar, S., San, O., Rasheed A., Iliescu T., A non-intrusive reduced order modeling framework for quasi-geostrophic turbulence, https://arxiv.org/abs/1906.11617

[8] Robinson, H., Rasheed, A. and San, O., Dissecting Deep Neural Network, Submitted to IEEE Transactions on Neural Network and Learning

Proceedings of the 32nd Nordic Seminar on Computational Mechanics
A.H. Niemi and H. Koivurova (Eds.)

Material Point Method: the past and the future

Wojciech Sołowski[1]

[(1)]Aalto University, Civil Engineering Department, wojciech.solowski@aalto.fi

Summary. This article presents the overview of the Material Point Method, a numerical method for simulation of large deformation problems described by continuum mechanics. The paper gives general idea and assumption of the method, describes the improvements in the algorithm over time, as well as identifies some remaining challenges. In conclusion, it suggests that Material Point Method is maturing quickly and reaching the point where numerical simulations of engineering problems can be done accurately and robustly.

Key words: Material Point Method, Generalized Interpolation Material Point Method, Convected Particle Least Square Material Point Method, numerical simulations

The idea

The Material Point Method has been first proposed by Sulsky *et al.* (1994). The method was a modification of a FLIP method, adjusted to use for solids instead of fluids. This original formulation of MPM bases on the continuum mechanics and was fully dynamic. The discretized equations are the same as those used for derivation of the Finite Element Method. The difference is in the discretization – in the Material Point Method the data is associated with the material points, which freely move over computational grid. However, similarly as in the Finite Element Method, the calculations use quantities integrated at the computational nodes of the grid. That means the material point data must be transmitted to the grid nodes and back in each time step. However, the benefit of the formulation include avoidance of grid distortion and the ability to simulate dynamic problems with very large displacements and strains. Therefore, as all the material models are the same as in the Finite Element Method, the Material Point Method quickly becomes a preferred method for those problems, and much effort has been spent on reducing its original shortcomings.

The Improvements

The original formulation of the Material Point Method has significant shortcomings. In particular, the method is only convergent when the material points cross the cell boundaries simultaneously, as otherwise the computation scheme leads to results distorted by a finite error being result of the point moving from one cell to another. Also,

as the material points do not have any physical domain associated with them, at large strains the neighbouring points may stop contributing to the same nodes. That leads to a material separation, which resembles material cracking, but is controlled by the grid and material point discretisation, not by physical properties of the material. Such occurrence of the material separation also breaks down the assumptions of continuum and therefore makes any formal proof of the method convergence impossible.
The development of the Generalized Interpolation Material Point Method (GIMP) by Bardenhagen and Kober (2004) was a major step forward and still today GIMP is quite widely used. In GIMP, material points gained computational domains. That improvement greatly reduces the errors related to the grid cell crossing, and improves the continuity, especially in the version of the method which track and updates the material point domains size. However, the material separation may still occur in problems with large shear strains since the material point domains remain rectangular and ignore shear deformations. Nonetheless, GIMP allows for rather successful simulations that capture qualitatively the material behaviour. Yet, as separation is still possible, in certain problems convergence of the method to the accurate solution is not guaranteed and a mathematical proof of GIMP correctness is not achievable.
In 2013 Sadeghirad *et al.* further developed the Material Point Method, introducing Convected Particle Domain Interpolation (CPDI) Material Point Method. The new interpolation allows for the material point domain to become a quadrilateral and thus allow for shearing. Additionally, in the CPDI, the material points are connected with the shape functions, so they do not separate even in problems with very large strains and deformations. However, more recent research show that despite those favourable characteristics, the CPDI still does not guarantee second order convergence in large deformation problems.

Challenges for the Future

To become a valuable method to solve engineering problems, the Material Point Method needs to be a method which gives accurate solutions in reasonable time, even for large problems. Many of the current theoretical developments concentrate on guaranteeing the convergence and accuracy of the method, as well as reduce the time of calculations. For example, the Convected Particle Least Square Material Point Method (CPLS) by Tran *et al.* (2019, under review) seems to exhibit second order convergence rate in large deformation regime. Nonetheless, a Material Point Method with higher order convergence than two is not yet convincingly established for large deformation regime. Ideally, an arbitrarily high order Material Point Method formulation is sought after, with users being able to define the order of convergence, similarly as a user of Finite Element Method may choose the order of element used in the simulation.
Theoretically, the order of the method depends on how smoothly the method is able to approximate the fields and compute the relevant integrals. In the Material Point Method we generally have more material points than nodes. Therefore, we can rather easily achieve a high order of field smoothness when we map the data from the material points to the nodes. However, we only use linear functions to map the updated data from the nodes to the material points. That is likely the reason why currently we have the order of the method limited to two. Additionally, as we often have more material points than the

grid nodes, the mapping from the nodes to points is creating a null-space. The presence of the null-space affects the results and leads to errors. However, recently, among others, Tran & Sołowski (2019) have shown how to filter out the null-space errors, leading to a significant improvement in the method accuracy.
The reduction of the numerical errors is especially important in simulations which are sensitive to changes in strain field. That is the case in porous materials with pores fully saturated with water, such as fully saturated soils. As water is almost incompressible, small numerical fluctuations of the strain values in the water phase affect the solution very significantly. Thus, simulations requiring hydro-mechanical coupling and thermo-hydro-mechanical coupling are currently still require special treatment, usually connected to some selective damping and dissipation of energy.
Furthermore, the materials at very large displacements and strains also tend to reach the limits of their strength and crack. As the Material Point Method aim is to be the method for simulation of problems characterised by large deformations, another challenge, only partially solved up to date (e.g. Bardenhagen *et al.* 2011, Sadeghirad *et al.* 2013), is to introduce discontinuities in the material in a controllable fashion and allow for crack creation, growth and closure.

Conclusions

The Material Point Method is one of the most dynamically improving methods for simulations of materials described by continuum mechanics. There are still numerous challenges remaining, but those are acknowledged by the community and significant improvements are reported yearly. Also, already currently, the Material Point Method can give accurately simulate many large displacement problems and converge reliably.
The Material Point Method also have reached several important milestones. Those include demonstration of a consistent convergence rate, increases in accuracy allowing for robust calculations and applications in engineering problems, including large scale simulations, and developments in coupled analysis and coupling with the Finite Element Method and the Computational Fluid Dynamics methods.
To conclude, for large deformation problems difficult to tackle with the Finite Element Method, where the use of continuum mechanics constitutive models is important, the Material Point Method gradually becomes the method of choice for engineering simulations. Such simulations, unfortunately, still require significant expertise, but in time the software will develop further, allowing for more routine calculations with the Material Point Method, with the method becoming likely a natural extension to Finite Element Method simulations when large deformations are encountered.

References

Bardenhagen, S. G., & Kober, E. M. (2004). 'The generalized interpolation material point method.' CMES - Computer Modeling in Engineering and Sciences. 5(6): 477-495.

Bardenhagen, S. G., Nairn, J. A. and Lu, H. (2011) 'Simulation of dynamic fracture with the Material Point Method using a mixed J-integral and cohesive law approach', *International Journal of Fracture*. doi: 10.1007/s10704-011-9602-1.

Sadeghirad, A., Brannon, R. M. and Burghardt, J. (2011) ‘A convected particle domain interpolation technique to extend applicability of the material point method for problems involving massive deformations’, *International Journal for Numerical Methods in Engineering*. doi: 10.1002/nme.3110.

Sadeghirad, A., Brannon, R. M. and Guilkey, J. E. (2013) ‘Second-order convected particle domain interpolation (CPDI2) with enrichment for weak discontinuities at material interfaces’, *International Journal for Numerical Methods in Engineering*. doi: 10.1002/nme.4526.

Sulsky, D., Chen, Z., & Schreyer, H. L. (1994). ‘A particle method for history-dependent materials.’ Computer Methods in Applied Mechanics and Engineering. 118 (1-2): 179-196 https://doi.org/10.1016/0045-7825(94)90112-0

Tran, Q. A., Berzins, M. & Sołowski, W. (2019) ‘An improved moving least squares method for the Material Point Method’, 2nd International Conference on the Material Point Method for Modelling Soil-Water-Structure Interaction. mpm2019.06

Tran, Q. A., Berzins, M. & Sołowski, W. (under review) ‘A Convected Particle Least Square Interpolation Material Point Method (CPLS)’, International Journal for Numerical Methods in Engineering.

Tran, Q. A. and Sołowski, W. (2019) ‘Temporal and null-space filter for the material point method’, International Journal for Numerical Methods in Engineering. doi: 10.1002/nme.6138.

Proceedings of the 32nd Nordic Seminar on Computational Mechanics
A.H. Niemi and H. Koivurova (Eds.)

A single-cell computation for dynamic turbulent cascade development - the 'Navier-Stokes Machine'

Clara M. Velte[1] and Preben Buchhave[2]

[(1)]Technical University of Denmark, Department of Mechanical Engineering, Nils Koppels Allé b. 403, 2800 Kgs. Lyngby, Denmark, cmve@dtu.dk
[(2)]Intarsia Optics, Sønderskovvej 3, 3460 Birkerød, Denmark, buchhavepreben@gmail.com

Summary. We present a method that allows us to follow an arbitrary input velocity record as it develops in time by following it through a large number of infinitesimal passes through a 1D projection of the force terms in the Navier-Stokes equation onto the flow direction. This method, if applied with sufficiently small steps, will build up the nonlinear effects, in principle without approximation. As a result, we can study the so-called triad interactions between Fourier components of the spectral representation of the flow field and follow the evolution of turbulence through both space and time.

Key words: Turbulence, triad interactions, velocity power spectrum

Introduction

It is generally accepted that the Navier-Stokes equation is the key to understanding how a turbulent flow develops after being exposed to various forms of momentum injection/extraction. Momentum can be altered in a flow by many processes: boundary layers, pump action, objects in the flow, pressure differences etc. The immediate effect is to create an imbalance between the large energy containing velocity structures ('eddies') and the smaller high frequency velocity structures. The imbalance will eventually develop into a flow with equilibrium between the eddies, where energy has been transferred from large to small eddies until they become so small that the energy is converted to heat due to viscous actions.

This process is often assumed to follow the so-called Richardson-Kolmogorov cascade, where eddies of similar size predominatingly exchange energy with a net flux from large to small scales. This picture is nowadays being subject to increasing scrutiny, not least due to our increasing technological capabilities, see e.g. Figure 1. In fact, the exact process from non-equilibrium to equilibrium turbulence is one of the least understood features of turbulence today. It is also one of the most important to understand, both from a theoretical point of view and from a practical one, since it is of crucial importance in the development of engineering models.

We present herein a combination of theory, computer simulations and laboratory experiments with the objective to explore the action of the Navier-Stokes equation to expose the

true energy flux across scales in developing turbulence. The novel single-cell simulations are based on a 1D projection of the Navier-Stokes equation onto the instantaneous velocity direction (the so-called 'convection record' [1]). The 1D projection prevents us from obtaining certain features of the 3D flow field, but it does allow computation of the kinetic energy, the velocity power spectra in both the spatial and temporal domain as well as calculation of the 2nd and 3rd order structure functions.

The non-linear (triad) interactions inherent in the Navier-Stokes equation and their dynamics may be said to form the basic "machinery" of fluid flow evolution, and a detailed understanding of their function is important for both theory and modelling of turbulence.

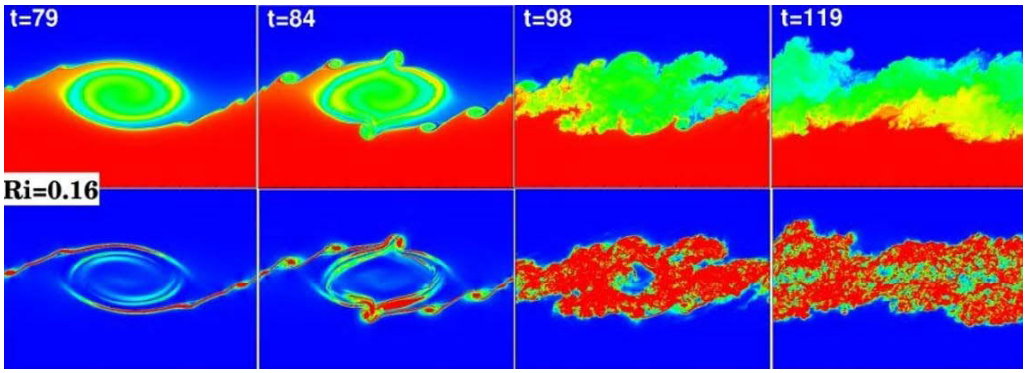

Figure 1. Interactions between widely different scales in a stratified shear layer simulation. (Upper) Density (Lower) Rate of dissipation of kinetic energy. Used with permission from Dr. Ali Mashayek from [2].

The 1D single-cell Navier-Stokes simulation

We will in the present talk explain the underlying ideas behind the Navier-Stokes simulator computer program. The program can run based solely on variables in physical space (velocity, velocity spatial gradients, pressure gradients etc. within the single computational cell). However, since the structure of the interactions between various spatial velocity scales (eddies) is more clearly revealed in Fourier space (or "k-space"), we have developed a version of the program operating on the Fourier components of the velocity. We can then directly see which Fourier components are interacting with what other Fourier components.

Since the nonlinear term in Navier-Stokes equation is of the second order, the interactions of Fourier components will always happen between three components, two Fourier components corresponding to two incident k-vectors, say $\boldsymbol{k_1}$ and $\boldsymbol{k_2}$, and a resulting Fourier component of the spatial frequency $\boldsymbol{k} = \boldsymbol{k_1} + \boldsymbol{k_2}$, the so-called triad interactions.

We then provide some examples of the N-S-simulator operating on different samples of velocity records including measured velocity traces from an experiment with a single velocity eddy (Fourier component) generated by vortex shedding in a low turbulence intensity round jet in air. We then discuss what we have learned from the computer experiments and to which extent these results can apply to predictions in fully three-dimensional turbulence.

In one example we generate an incident velocity time record with a relatively low frequency von Kármán-type spectrum. The subfigure to the upper left in Figure 2 shows a single 0.5 s time record and the lower left subfigure shows the corresponding velocity power spectrum at initial point in time. The right column shows, respectively, the time trace and spectrum after 10,000

iterations where the flow has had time to develop towards a more (statistically) stable state. In the latter state, the spectrum has developed the expected characteristics and the time trace of the velocity signal displays sharp jumps as expected from measurements. Leaving out the pressure term (which in this context acts as a noise term) brings out in a clearer way some of the effects of the nonlinear convection term. As the velocity record and the corresponding power spectrum are allowed to develop fully, the influence of the initial conditions decreases and eventually disappears completely. Both the velocity record and the spectrum attain a form that does not change with further exposure to the Navier-Stokes equation; one may speak of a "soliton-like" behaviour. The only effect of further iterations is a slow reduction of the energy of the spectrum brought about by the dissipation term. The shape of the spectrum does not change.

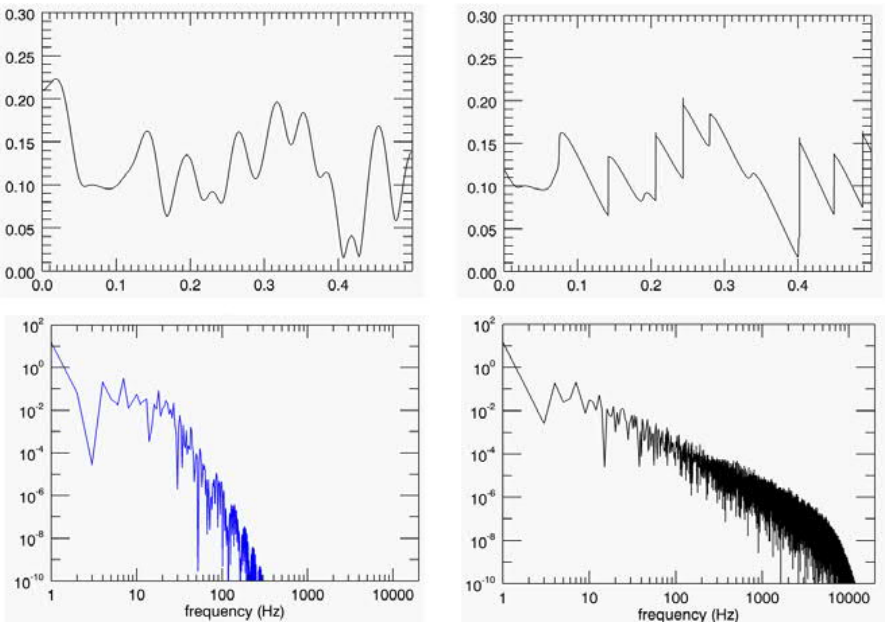

Figure 2. Development of incident von Kármán time trace (upper left) and spectrum (lower left) into a converged soliton-like time-trace with sharp shocks/jumps (upper right) and corresponding spectrum (lower right).

Single Fourier mode injection

Validation of the computational method is performed through comparison with experimental data. In the essentially laminar core of a round jet (100 mm exit diameter), a single Fourier component could be injected using a rod of rectangular cross-section, see Figure 3. The downstream development of the initial single frequency in the laminar flow could be traced by hot-wire measurements in several points along the downstream direction.

The most upstream measurement velocity record (with only the single initial frequency) was used as input signal to the Navier-Stokes machine simulation and the corresponding flow development was in this manner simulated. Computations showed good agreement between measurements and computer simulation, see Figure 4. The differences observed are predominatingly due to the filter settings of the spectral representation in the acquisition hardware, creating a slowly declining background variation of energy across frequency in the measured record.

Figure 3. Round jet with an extended laminar core. A rod with a rectangular cross-section with sharp edges was used to generate a sharp single frequency in the initial flow development.

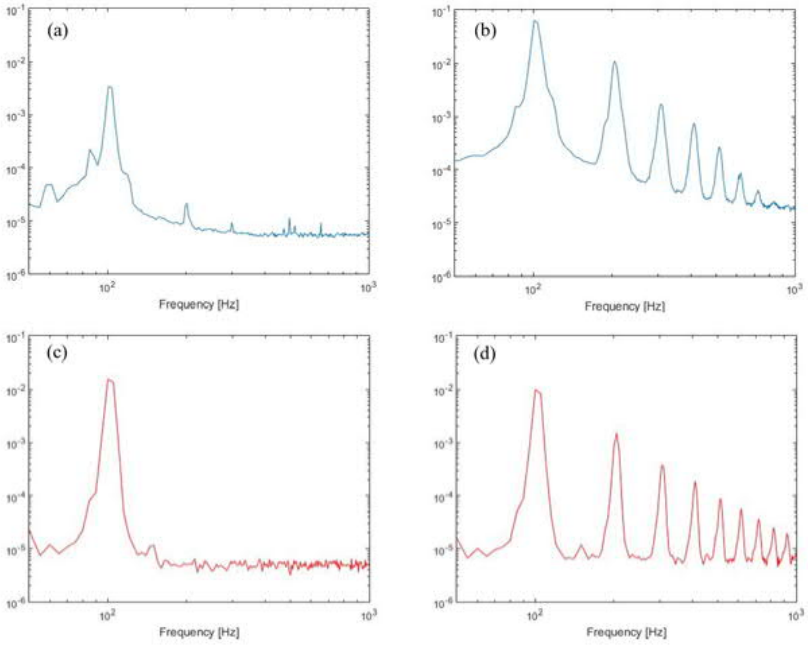

Figure 4. Blue/upper: Measurements. Red/lower: Numerical simulations. (Left) Initial peak (Right) Downstream development.

References

[1] Buchhave, P., Velte, C. M. (2017) *Measurement of turbulent spatial structure and kinetic energy spectrum by exact temporal-to-spatial mapping*, Physics of Fluids 29, 085109, https://doi.org/10.1063/1.4999102

[2] Mashayek, A., Caulfield, C. P. and Peltier, W. R. (2013) "Time-dependent, non-monotonic mixing in stratified turbulent shear flows: implications for oceanographic estimates of buoyancy flux," Journal of Fluid Mechanics. Cambridge University Press, 736, pp. 570–593. doi: 10.1017/jfm.2013.551.

Proceedings of the 32nd Nordic Seminar on Computational Mechanics
A.H. Niemi and H. Koivurova (Eds.)

Shape and topology optimization using CutFEM

Niels Aage[1], Reinier Giele[2], Sümer Dilgen[1], Cetin Dilgen[1] and Casper Schousbo Andreasen[1]

(1)Technical University of Denmark, Mechanical Engineering, naage@mek.dtu.dk, sudil@mek.dtu.dk, cedil@mek.dtu.dk, csan@mek.dtu.dk
(2)Technical University of Delft, reiniergiele@gmail.com

Summary. This work presents a CutFEM shape and topology optimization methodology based on well-known techniques from density based topology optimization. That is, the design field representation, the use of projection filters, the sensitivity analysis as well as the design update scheme is identical to those used in standard density based methods. The only noticeable differences are the finite element analysis, which here employs a CutFEM approach to achieve crisp and well-defined material interfaces, as well as the localization of sensitivity information due to the lack of intermediate densities (ersatz material) in the design domain. The numerical examples includes both 2D and 3D solid mechanics as well as multiphysics problems from vibro-acoustics.

Key words: Topology optimization, Shape optimization, CutFEM, Solid mechanics, Vibroacoustics

Introduction

In structural optimization, density methods are often the weapon of choice due to their simplicity when compared to level set methods i.e. generalized shape optimization [1]. That is, density methods are easy to implement, regularization techniques are well established and robust, and due to the ersatz material model, the sensitivity information is global to the design domain [2]. This is in contrast to generalized shape optimization in which the sensitivity is confined to the material interface and regularization schemes, namely length scale control, still poses an unsolved problem in general. However, the family of shape optimization methods that operate with crisp interface representations, e.g. XFEM and CutFEM, have an extremely attractive quality in that they are capable of resolving and imposing complex interface conditions, which is not the case for density methods in general. Hence, it is reasonable to combine the best from both optimization disciplines in order to develop new and more flexible design tools in engineering.

Methods

The main contribution of the presented work is the combination of a density design representation with a crisp interface immersed boundary finite element method. That is, the design field is

introduced as a scalar nodal field which is filtered, projected and mapped to a convenient range using the classical robust formulation, i.e.

$$x_{phys} = M(H(F(x))) \tag{1}$$

Here x is the design variables, $F(x)$ refers to a convolution filter, $H(x)$ is a smooth Heaviside filter and $M(x)$ is a linear mapping of the 0-1 design field onto a mesh size dependent interval. The latter is included to make the usual 0-1 scaling of the design field robust to mesh refinement. The lhs x_{phys} is constructed using several projection parameters, exactly as done for density methods in [2], and for the minimum compliance problem we use the so-called poor mans approach such that only a single finite element analysis is needed.

The employed immersed boundary method is best described as a simplified CutFEM method with the main difference of omitting ghost penalties [3], since all our numerical experiments showed that these were not needed. Therefore the method consists of cutting the physical design field x_{phys} at a specified level using marching squares (2D) or marching cubes (3D). The cut elements are then triangulated or tetrahedralized and the sub element Gauss points are mapped back into the parent quadrilateral or hexahedral element in which the integration is performed. Similar to density methods, the void regions are given an artificial material parameter to ensure that the system can be solved on the full domain without any renumbering of the dofs.

Thus, the resulting finite element systems are very alike those encountered in standard density methods, i.e. heterogeneous with high contrast, and we are therefore able to use the same type of preconditioners as presented in [4]. The optimization problem is solved using gradient based methods and the sensitivities are obtained using discrete adjoint analysis. The only difference between density based sensitivity calculations and those used here, is the computation of the system matrix differentiated with respect to the physical design variable. To simplify the implementation the term is obtained by a simple finite difference, i.e.

$$\frac{\partial K_e}{\partial x} \approx \frac{K_e^{pert} - K_e}{h} \tag{2}$$

The proposed design method is implemented in Matlab for 2D problems and using the TopOpt in PETSc [3] framework for 3D problems.

Numerical example

The developed design method is demonstrated on examples from solid mechanics, through a number of minimum compliance and mechanism design problems in both 2D and 3D. One such result for a stiffness optimized 3D cantilever beam is seen in Figure (1), which shows the initial guess (top left) and the final optimized design (bottom right). The design domain is discretized into 525.000 elements and a solid block of material using 75% volume is chosen as the starting guess. The evolution of the design in Figure(1) shows how the volume constraint is first made feasible and afterwards that holes appear, although no hole insertion strategy is used, i.e. holes are growing in from the sides. It should be noted that although the appearance of new holes is common in 3D, it is hardly ever seen in 2D, and thus we apply the topological derivative for 2D problems. However, the main problem here is that it generally is hard to provide feasible *and* meaningful starting guesses for generalized shape optimization problems. Therefore a noticeable amount of computational effort is devoted to making the problem feasible, and special care must be taken with the initial scaling such the constraints and objective are reasonably balanced. For

the design problem shown in Figure (1), the extra computation effort amounted to 42 design cycles. The easiest way to alleviate this problem is to only use the proposed design method as a post processing tool for standard density methods. This is easily done since both methods uses the exact same design representation and is therefore a good choice for problems that can easily be solved by density methods. But, this does not apply to problems for which density methods have problems. This is often the case for problems that involves complicated interface conditions and/or problems with multiple physics.

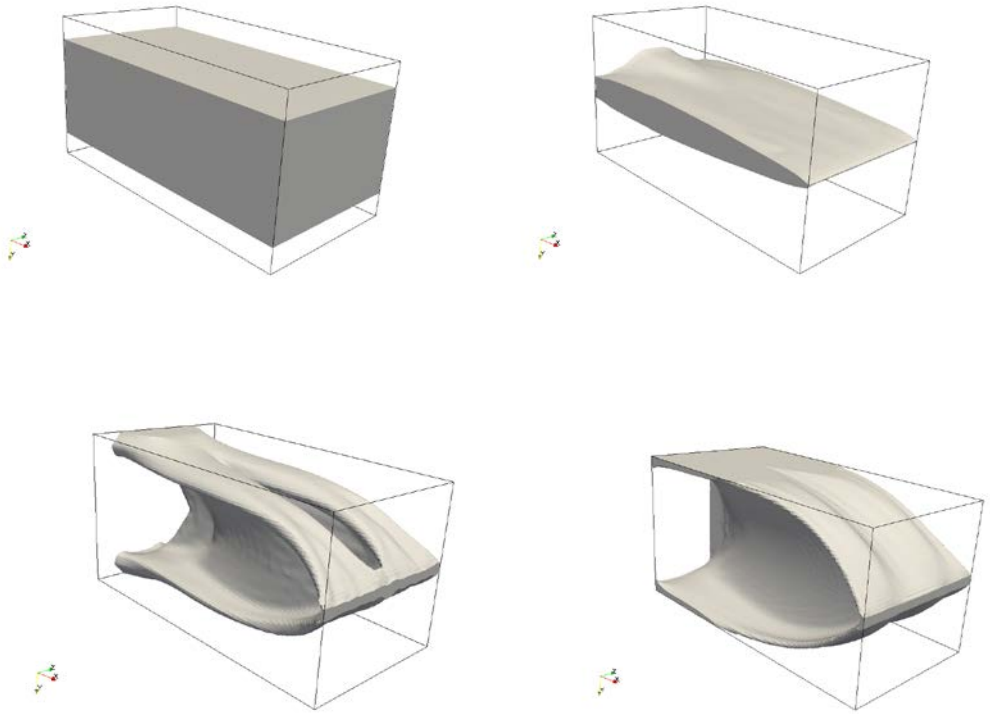

Figure 1. Minimum compliance result and selected design history (iteration 0, 42, 96 and 400, respectively) for a 3D cantilever design problem using 12% volume.

Therefore, to utilize the true strength of the presented CutFEM optimization approach, examples in which interface conditions are paramount will be presented. Focus will be on vibroacoustics, in which the acoustic pressure exerts a pressure load on the structure and the structure provides an acceleration to the fluid. We note that these coupling conditions are particularly easy to incorporate into the CutFEM solver since both couplings arise through Neumann conditions. The method is then applied to design problems using both frequency domain and time dependent problems formulations, and the results are compared to designs obtained using a density method based on the mixed formulation [5]. The study shows that the CutFEM optimized design generally are of a higher quality than the density designs.

References

[1] Sigmund, O., & Maute, K. (2013). Topology optimization approaches. *Structural and Multidisciplinary Optimization*, *48*(6), 1031–1055.

[2] Wang, F., Lazarov, B. S., & Sigmund, O. (2011). On projection methods, convergence and robust formulations in topology optimization. *Structural and Multidisciplinary Optimization*, *43*, 767–784.

[3] Burman, E., Claus, S., Hansbo, P., Larson, M. G., & Massing, A. (2014). CutFEM: Discretizing geometry and partial differential equations. *International Journal for Numerical Methods in Engineering*, 472–501.

[4] Aage, N., Andreassen, E., & Stefanov Lazarov, B. (2015). Topology optimization using PETSc: An easy-to-use, fully parallel, open source topology optimization framework. *Structural and Multidisciplinary Optimization*, *51*, 565–572.

[5] Yoon, G. H., Jensen, J. S., & Sigmund, O. (2007). Topology optimization of acoustic–structure interaction problems using a mixed finite element formulation. *International Journal for Numerical Methods in Engineering*, *70*(9), 1049–1075.

Proceedings of the 32nd Nordic Seminar on Computational Mechanics
A.H. Niemi and H. Koivurova (Eds.)

A posteriori Error Estimation for Isogeometric Analysis of the Advection-Diffusion equation

Abdullah Abdulhaque [1], Trond Kvamsdal [1], Mukesh Kumar [2] and Arne Morten Kvarving [3]

[1] Department of Mathematical Sciences
Norwegian University of Science and Technology, Trondheim, Norway e-mail:
abdullah.abdulhaque@ntnu.no, trond.kvamsdal@ntnu.no

[2] Department of Mathematics College of Charleston, South Carolina, USA e-mail:
kumarm@cofc.edu

[3] Department of Applied Mathematics and Cybernetics SINTEF ICT, Norway
e-mail: arne.morten.kvarving@sintef.no

Summary. In this article, we will develop and present suitable error estimators for adaptive mixed isogeometric methods for solving the Advection-Diffusion-Reaction equation. We will compare the use of residual-based error estimators with superconvergent patch recovery methods [2]. The adaptive refinement will be based on LR B-splines [3], using the general theory of isogeometric finite element modelling [1]. The different estimators will be thoroughly tested on problems with (manufactured) analytical solutions.

Key words: Asogeometric Analysis, Adaptive finite element method, residual estimation, superconvergent patch recovery

Isogeometric Finite Element Modelling

The Advection-Diffusion-Reaction equation is the canonical form of elliptic partial equations, and it has a wide range of applications. Solving it with the Finite Element Method has been known for decades, but most of the of the approaches were done either with the classical Finite Element Method or the Spectral Element Method. We will examine a new method called Isogeometric Analysis, where the equation is discretized by splines. This approach has several advantages like exact meshing of the domain, isoparametric elements for any degree and continuity, low error due to high continuity, and better interoperability between Finite Element Analysis (FEA) and Computer-Assisted Design (CAD) [1].

Adaptive Error Estimation

The Adaptive Finite Element Method will be the main focus of our research. The procedure is solving a PDE on a domain, looping through every element, and estimating their local errors. Those elements with highest error are subdivided into smaller elements, and then we repeat the same process again until the global estimated error becomes low enough [4].
This approach has been tested on the Advection-Diffusion-Reaction equation for a long time, and it seems to work well. But combining adaptive error estimation together with Isogeometric Analysis is relatively new and still in development [2]. We will test this approach on the equation by using a certain type of splines called LR B-splines, which enables us to perform local refinement [3]. The process is based on residual estimation and superconvergent patch recovery.

References

[1] T. J. R. Hughes, J. A. Cottrell and Y. Bazilevs. Isogeometric analysis: CAD, finite elements, NURBS, exact geometry and mesh refinement. Comput. Methods Appl. Mech. Engrg. (2005) 194:4135–4195.

[2] Kumar, M., Kvamsdal, T. and Johannessen, K. A. Superconvergent patch recovery and a posteriori error estimation technique in adaptive isogeometric analysis. Computer Methods in Applied Mechanics and Engineering, 316, pp. 1086-1156, 2017.

[3] K. A. Johannessen, T. Kvamsdal, and T. Dokken. Isogeometric analysis using LR B-splines. Computer Methods in Applied Mechanics and Engineering, 269:471–514, 2014.

[4] R. Verfürth. A Posteriori Error Estimation Techniques for Finite Element Methods. UK: Oxford University Press, 2013.

Proceedings of the 32nd Nordic Seminar on Computational Mechanics
A.H. Niemi and H. Koivurova (Eds.)

Microstructural modelling of defect containing martensitic steels

Tom Andersson[(1)], Anssi Laukkanen[(1)], Matti Lindroos[(1)], Sami Majaniemi[(1)], Tomi Suhonen[(1)], Tero Frondelius[(2,3)], Joona Vaara[(2)], Antti Mäntylä[(2)]

[(1)] VTT, tom.andersson@vtt.fi, [(2)] R&D and Engineering, Wärtsilä , [(3)] University of Oulu

Key words: Heterogeneous material, Microstructural-modeling, Micromechanics

Material microstructure informed multiscale modeling is found to be useful for estimating how different microstructural features affect the behaviour and lifetime of a material. Detailed and accurate microstructural information is needed for the model to be useful. Micromechanical characterisation methods like the Scanning Electron Microscope (SEM) equipped with an Electron Backscatter Diffraction (EBSD) and Energy Dispersive Spectroscopy (EDS) detectors and Focused Ion Beam Milling (FIB), X-ray tomography (XCT) and Transmission Electron Microscopy (TEM) have enabled much more reliable and detailed modelling of material microstructures. The SEM and TEM typically create 2D images of material surfaces at small size scales. FIB enables machining into the sample and taking 2D images from several depths of the sample thus enabling the compilation of 3D image of the microstructure structure. With the EBSD it is possible to obtain accurate crystallographic information of different materials. With X-ray tomography it is possible to take 3D images of material microstructures at relevant size scales without destroying the sample but this is often limited to soft (i.e. less dense) materials and relatively thin sections. [1, 2]

With different image analysis tools one can process and segment the image separating each individual phase of the microstructure, for examples in steels the actual steel with crystallographic orientation and inclusions (and even inclusion's separate phases) or other defects/secondary phases see Figure 1. These regions with differing properties can be treated as separate objects or regions with differing material properties and varying adhesion to be used in a Finite Element (FE) model, see Figure 2.

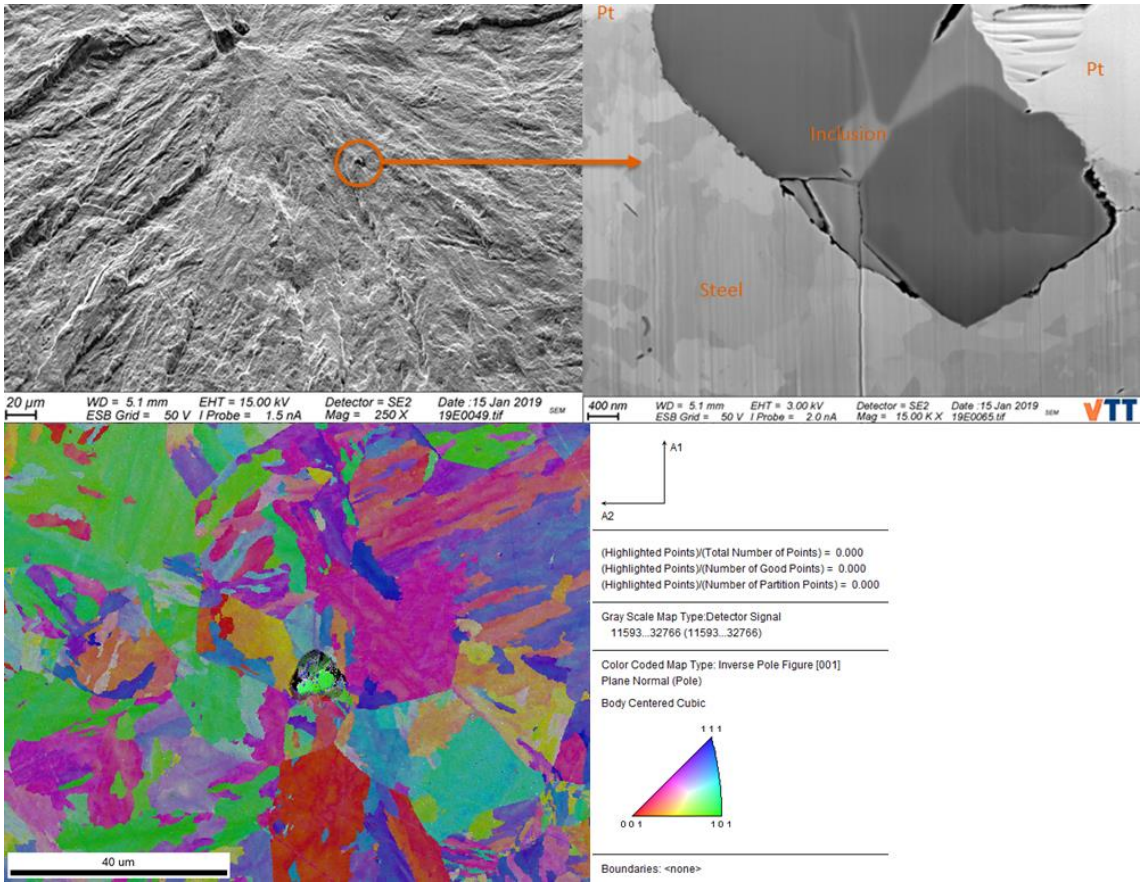

Figure 1. Upper row Fracture surface and FIB slice of inclusion. Lower row EBSD map of the steel microstructure.

Some of the challenges in image based modelling are related to image quality and segmentation. The segmentation algorithms are mostly tackling the 2D slices of the image instead of 'seeing in 3D'. Besides this the image resolution and quality are not always perfect, and the greyscale difference (in XCT) between material phases can be small thus the interface between phases can be imprecise. This problem does not typically apply to SEM-images although other sample preparation related problems might cause concern. The size of the modelled volume, often called a Representative Volume Element (RVE) is also crucial. Too small area of a non-periodic material microstructure can be misleading.

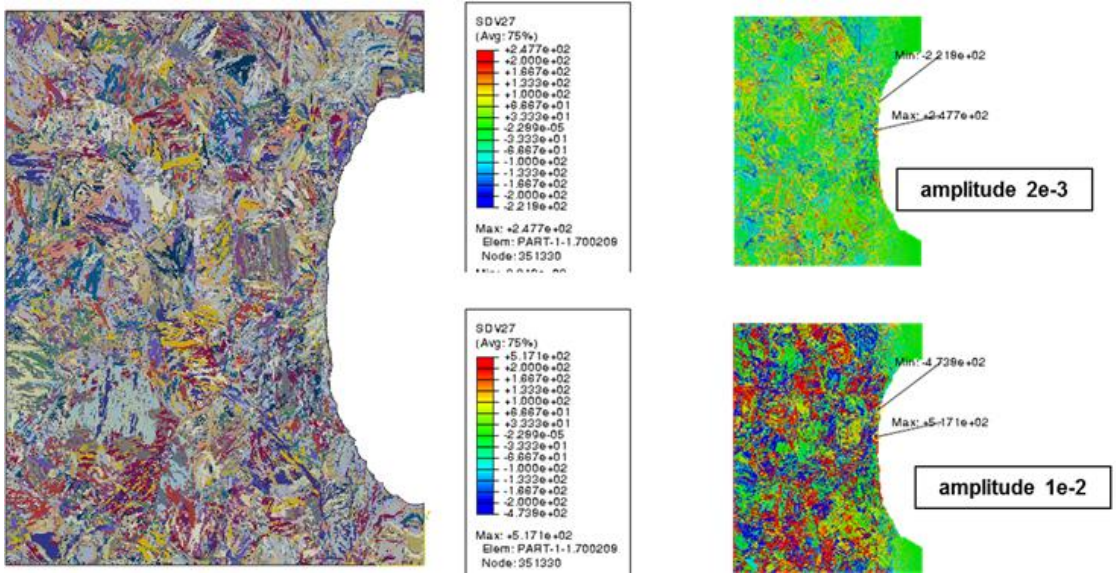

Figure 2. Orientation plot of FE model martensitic steel microstructure containing free surface with notch and computation of 20 cycles in strain control with R=-1, different amplitudes: Maximum shear stress (of all slip systems)

Intrinsic property of image based FE modelling is that it is not easily modifiable for examples by changing the volume fractions of the material phases, textures or grain sizes. The material values can be changed easily, though. The synthetic tessellation based models are more suitable for predicting changes in volume fraction, particle size etc. A basic 3D tessellation routine uses a cloud of points in a volume of space, and divides the volume into sub-volumes by creating boundaries that are at equal distance from each of the closest points. By modifying the routine, it is possible to add more complicated features to the model to obtain for examples a microstructure resembling and statistically near-equivalent to that of a steel. A combination of these two methods is the semi-synthetic models, in which representative objects from an image based model are added one after another into a synthetic model in order to obtain statistically near-equivalent model.

Typically the resulting FE models are very large, they may contain tens of millions of elements or more. If the material model is also complicated, for examples a viscoelastic or viscoplastic model thus utilizing high-performance computing clusters are essential. After solving the model the results are analysed by studying distributions and cumulative distributions of stresses and strains. These distributions and the contour plots together have revealed that the highest stresses in such a model often occur in very small areas and a lot higher than the bulk stress and strain. There are several ways the results of these models are utilized. One is to give insight to the deformation fracture/damage mechanisms. These models enables the prediction of material behaviour (e.g. stiffness and strength) and mechanisms of failure (fracture, creep) of heterogeneous materials with less experiments than what would be necessary without modelling. In addition, the most suitable material microstructures can even be estimated for certain application based on the understanding and phenomena in the microscale. The results of these models are also used in prediction of friction and wear of materials under severe loadings and environmental conditions, for example wear resistant steels exhibiting Twinning Induced Plasticity (TWIP) during operation in a jaw crusher crushing rocks. [2]

One interesting application area is predicting fatigue in metals. For this special Crystal Plasticity Finite Element (CPFE) models are used. In such a model the microstructure and crystal

orientations are taken from EBSD images. The CPFE models assume that plastic deformation in crystalline material occurs along predetermined orientations along the slip systems typical for these crystals. A typical result in such a study is the distribution of the cumulative slip, which can be corporated with damage models to predict material behavior as realistically as possible and to investigate the effect of different features to the overall deformation behavior. [3, 4]

An important development is linking the microstructures and strength of the material under combined loadings, linking material behavior at laboratory and actual operational conditions. This calls for a parallel experimental and modelling study - of the typical structural steels for example - in which the bulk loadings in tensile, compressive and shear tests and the probability levels of stresses and strains in the microstructure are linked together. The gain is be huge: The results enables tailoring of materials to the applications and loadings, as the design engineer would have tools for taking into account the microstructure in designing the structural component of a machine or a building.

References

[1] Frondelius, Tero; Mäntyä, Antti; Vaara, Joona; Könnö, Juho; Andersson, Tom; Lindroos, Matti; Verho, Tuukka; Laukkanen, Anssi (2018) Micromechanical modeling of the role of Inclusions in high cycle fatigue damage Initiation and short crack growth. In: CAASE18: The Conference on Advancing Analysis & Simulation in Engineering. June 5-7, 2018, Cleveland, Ohio, USA, pp. 1-5.
[2] Laukkanen, A., Pinomaa, T., Holmberg, K. and Andersson, T., 2016. Effective interface model for design and tailoring of WC-Co microstructures. Powder Metallurgy, 59, pp. 20-30.
[3] Lindroos, M., Laukkanen, A. and Kuokkala, V-T., 2017. A crystal plasticity approach for shear banding in hot rolled high-strength steels. Metallurgical and Materials Transactions A, 48, pp. 5608-5615.
[4] Lindroos, M., Laukkanen, A., Andersson, T., Vaara, J., Mäntylä, A., Frondelius, T., Micromechanical modeling of short crack nucleation and growth in high cycle fatigue of martensitic microstructures. Computational Materials Science, 170, pp. 109185.

Proceedings of the 32nd Nordic Seminar on Computational Mechanics
A.H. Niemi and H. Koivurova (Eds.)

On the regularisation property of the Kachanov-Rabotnov continuum damage model - a finite element study

Harm Askes[1], Juha Hartikainen[2], Kari Kolari[3], Reijo Kouhia[2],Timo Saksala[2] and Jani Vilppo[2]

[(1)]The University of Sheffield, h.askes@sheffield.ac.uk
[(2)]Tampere University, juha.hartikainen@tuni.fi, reijo.kouhia@tuni.fi, timo.saksala@tuni.fi, jani.vilppo@tuni.fi
[(3)]VTT Technical Research Centre of Finland Ltd, kari.kolari@vtt.fi

Summary. In this paper the regularising properties of the Kachanov-Rabotnov type continuum damage constitutive model are studied using a simple one-dimensional dynamic problem. It is found that the width of the localisation zone is independent of the mesh size if the loading rate is below a certain threshold value.

Key words: continuum damage mechanics, Kachanov-Rabotnov model, strain softening, localisation, dynamic problem, finite element analysis

Introduction

A well known model to describe continuous degradation of a material is the Kachanov-Rabotnov model, which was first introduced in 1958 [3, 7]. Since then, continuum damage mechanics has developed into an important and active field of continuum mechanics, see e.g. [2, 4, 5, 6, 8].

As it is shown in [1], two different formulations either based on stiffness or flexibility approaches can be considered to be identical when certain relations are fullfilled between the model parameters. The stiffness formulation of an elastic-damaging material model can be described by the equations

$$\boldsymbol{\sigma} = (1-D)\,\boldsymbol{C}_\mathrm{e} : \boldsymbol{\varepsilon}, \tag{1}$$

$$\dot{D} = \frac{1}{t_\mathrm{d}(1-D)^p}\left(\frac{Y}{Y_\mathrm{r}}\right)^r, \tag{2}$$

where $\boldsymbol{C}_\mathrm{e}$ is the elasticity tensor, $\boldsymbol{\sigma}, \boldsymbol{\varepsilon}$ stress and strain tensors and : denotes the double dot-product. For the flexibility formulation the corresponding constitutive equations are

$$\boldsymbol{\varepsilon} = (1+\alpha)\,\boldsymbol{C}_\mathrm{e}^{-1} : \boldsymbol{\sigma}, \tag{3}$$

$$\dot{\alpha} = \frac{(1+\alpha)^m}{t_\mathrm{d}^\mathrm{c}}\left(\frac{Z}{Z_\mathrm{r}}\right)^n. \tag{4}$$

Expressions for the thermodynamic forces Y and Z can be written as

$$Y = \frac{1}{2}\boldsymbol{\varepsilon} : \boldsymbol{C}_\mathrm{e} : \boldsymbol{\varepsilon} = \frac{1}{2(1-D)^2}\boldsymbol{\sigma} : \boldsymbol{C}_\mathrm{e}^{-1} : \boldsymbol{\sigma}, \tag{5}$$

$$Z = \frac{1}{2}\boldsymbol{\sigma} : \boldsymbol{C}_\mathrm{e}^{-1} : \boldsymbol{\sigma} = \frac{1}{2(1+\alpha)^2}\boldsymbol{\varepsilon} : \boldsymbol{C} :_\mathrm{e} \boldsymbol{\varepsilon}. \tag{6}$$

A reasonable choice for the reference values Y_r and Z_r is

$$Y_\mathrm{r} = Z_\mathrm{r} = \frac{\sigma_\mathrm{r}^2}{2E} = \frac{1}{2} E \varepsilon_\mathrm{r}^2, \tag{7}$$

where $\sigma_\mathrm{r} = E\varepsilon_\mathrm{r}$ is a reference stress, and ε_r is a corresponding reference strain.

Physically the damage variable D can be interpreted as a ratio of the differential damaged area element to the original area element. However, interpretation of the damage parameter α is not so straightforward.

It is shown in [1] that the two models yield identical stress-strain responses if

$$n = r, \quad m = p + 2n + 2 \quad \text{and} \quad t_\mathrm{d}^\mathrm{c} = t_\mathrm{d}. \tag{8}$$

However, it should be noticed that the damage variables are not identical: $D \neq \alpha$.

Strain and damage localisation

As in viscoplasticity, the damage evolution equations (2) and (4) contain a material parameter which has the unit of time, i.e. t_d or t_d^c. It is therefore assumed that the apparent viscosity could regularise the governing equilibrium equations or the equations of motion in dynamic analysis.

For strain-softening in inviscid solids localisation takes place in a plane of zero thickness. Viscosity added to either plasticity or damage models may bring in the desired non-zero material length-scale. To investigate the regularising behaviour of the Kachanov-Rabotnov continuum damage model, a one-dimensional finite element analysis is carried out. A semi-infinite bar subjected to a linearly increasing displacement boundary condition $u(0,t) = \eta\epsilon_\mathrm{r} L t/t_\mathrm{d}$ has been analysed with different uniform mesh sizes. The computational domain is chosen to be large enough that reflections from the other boundary do not occur. The length L is chosen as $L = c_\mathrm{e} t_\mathrm{d}$, where c_e is the elastic wave speed $c_\mathrm{e} = \sqrt{E/\rho}$. A standard central difference scheme is used to integrate the equations of motion with a constant time-step equal to the critical time step of the elastic bar.

From the numerical computations presented in [1], it can be concluded that the width of the localisation zone l_loc is constant if

$$(\dot{\varepsilon} t_\mathrm{d})^{2r} = \text{constant}, \tag{9}$$

however, the situation is more subtle and here a more detailed investigation of the regularising properties of the Kachanov-Rabotnov model is carried out.

A localisation study is performed with varying prescribed rate η and the damage localisation width is defined as the measure of the domain where

$$D^* \leq x \leq 1, \tag{10}$$

where D^* is the damage value at fracture stress for quasi-static constant strain-rate loading

$$D^* = 1 - \left(\frac{2r-1}{2r+p+2} \right)^{1/(p+1)}, \tag{11}$$

and it is independent of the aplied strain-rate.

The width of the localisation zone is shown as a function of the loading rate η in figure 1 for three different mesh sizes $h = L/100, L/1000$ and $L/10000$ for the cases $r = 2, p = 1$, and $r = 4, p = 1$. As it can be seen, the width of the damage localisation zone is mesh-size independent if the loading rate satisfies $\eta < 0.75$.

In figure 2 the damage profiles for the case $p = 1, r = 2, \eta = 0.5$ at times $t_\mathrm{d}, 2t_\mathrm{d}, 3t_\mathrm{d}$ and at the fracture $t = 3.76 t_\mathrm{d}$ are shown for a mesh with $h = L/1000$.

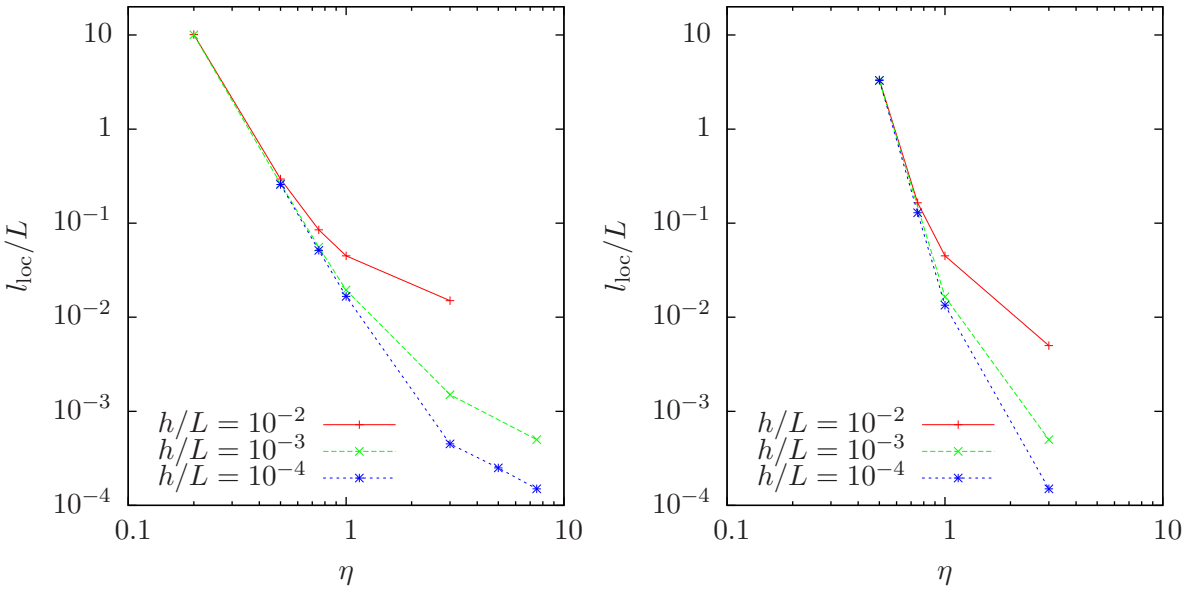

Figure 1. Damage localisation width as a function of the prescribed loading rate, $r = 2$ (lhs), $r = 4$ (rhs). In both cases $p = 1$.

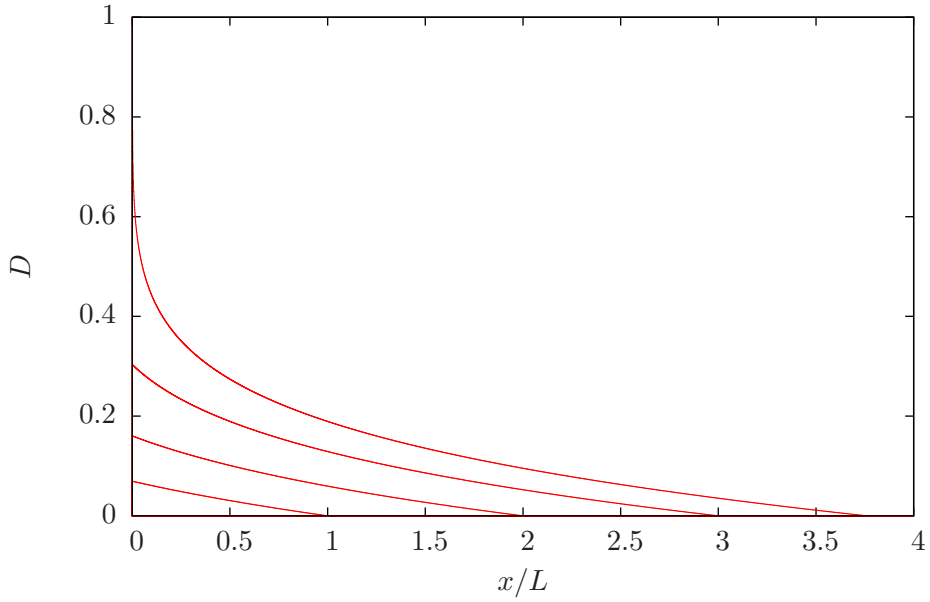

Figure 2. Damage profiles for the case $r = 2, p = 1$ and $\eta = 0.5$ at times $t_{\rm d}, 2t_{\rm d}, 3t_{\rm d}$ and at the fracture $t = 3.76t_{\rm d}$. Mesh size is $h = L/1000$.

Concluding remarks

A preliminary finite element study on the lcalisation behaviour of the Kachanov-Rabotnov type continuum damage model is performed. It is found that the width of the damage localisation zone is independent of the mesh size if the loading rate is below a certain treshold depending on the material parameters of the model.

References

[1] H. Askes, J. Hartikainen, K. Kolari, R. Kouhia, T. Saksala, and J. Vilppo. On the Kachanov-Rabotnov continuum damage model. Manuscript submitted to *Rakenteiden Mekaniikka*, May 2019.

[2] J. Betten. *Creep Mechanics*. Springer-Verlag, Berlin, 2005.

[3] L.M. Kachanov. On the creep fracture time. *Izv. Akad. Nauk SSSR. Otd. Tekhn. Nauk*, (8): 26–31, 1958. (in Russian).

[4] D. Krajcinovic. *Damage Mechanics*, volume 41 of *North-Holland series in Applied Mathematics and Mechanics*. Elsevier Science B.V., Amsterdam, 1996.

[5] J. Lemaitre. *A Course on Damage Mechanics*. Springer-Verlag, Berlin, 1992.

[6] S. Murakami. *Continuum Damage Mechanics*, volume 185 of *Solid Mechanics and Its Applications*. Springer Netherlands, 2012.

[7] Y.N. Rabotnov. A mechanism of the long term fracture. *Voprosy prochnosti materialov i konstruktsii AN SSSR*, pages 5–7, 1959. (In Russian).

[8] W. Zhang and Y. Cai. *Continuum Damage Mechanics and Numerical Applications*. Springer, 2010.

Proceedings of the 32nd Nordic Seminar on Computational Mechanics
A.H. Niemi and H. Koivurova (Eds.)

Variationally consistent homogenization of phase field fracture model

Ritukesh Bharali[1], Ralf Jänicke[2], and Fredrik Larsson[3]

[(1,2,3)]Chalmers University of Technology, [(1)]ritukesh.bharali@chalmers.se,
[(2)]ralf.janicke@chalmers.se, [(3)]fredrik.larsson@chalmers.se

Summary. A two-scale phase field model for fracture is developed from a fully resolved phase field model using the variationally consistent homogenization technique.

Key words: Damage upscaling, Variationally Consistent Homogenization, Phase Field Model

Introduction

The phase field model (PFM) emerged as an alternative to discrete techniques for fracture mechanics, and has much gained popularity over the recent years. Apart from not requiring a priori crack path, the PFM (by construction) handles topologically complex fractures (branching, merging and curvillinear cracks) both in two and three dimensions. Discrete techniques, like the eXtended Finite Element Method (X-FEM) on the other hand requires an explicit tracking of the discontinuity surface such that the corresponding nodal displacements can be enriched. Incorporating such intricacies for problems with complex fractures could be an arduous task. Putting forward a simple remark, the phase field variable is akin to the damage variable in continuum damage mechanics in physical interpretation as well as in mathematical bounds - zero denoting the virgin (undamaged) state and one corresponding to fully damage state.

In [1], a thermodynamically consistent framework for the PFM for fracture in elastic solids and its corresponding multi-field finite element approach was proposed. Since, the PFM is an active field of research, for more literature on the topic, the reader is referred to [1–3] and references therein.

The Variationally Consistent Homogenization (VCH) technique [4] provides an elegant procedure to derive pertinent scales for a hierarchical multiscale problem, from the fully resolved fine scale problem. The critical ingredient in the method lies in the conjunction of the Variational MultiScale method [5] and the separation of scales adopted in classical (first) order homogenization techniques. The Hill-Mandel macrohomogeneity conditions are fulfilled through equivalent variationally consistent macrohomogeneity conditions. The advantages of such a technique lies in its applicability in homogenization for a general class of problems and subsequent scale-bridging strategies.

In this paper, the advantages of the PFM and the VCH are exploited together in order to develop a two-scale phase field fracture model.

Phase field model for fracture

The PFM for fracture involves solving for a continuous phase (damage)-field $\omega(\mathbf{x}, t)$ in addition to the displacement field $\mathbf{u}(\mathbf{x}, t)$ in the computational domain Ω. For a detailed treatment of

the underlying energy functional and the derivation of the strong form, the reader is referred to [1]. The strongly coupled Euler-Lagrange set of equations (strong form) in the absence of body forces, assumes the generic from:

$$\boldsymbol{\sigma} \cdot \nabla = 0, \quad \text{in} \quad \Omega, , \tag{1}$$

$$\frac{G_c}{l}[\omega - l^2 \Delta\omega] - [(1-\omega)\boldsymbol{\epsilon}[\mathbf{u}] \colon \mathbb{E} \colon \boldsymbol{\epsilon}[\mathbf{u}]] + \eta\langle\dot{\omega}\rangle_- = 0 \quad \text{in} \quad \Omega, \tag{2}$$

where $\boldsymbol{\sigma}$ is the Cauchy stress tensor, G_c is Griffith's fracture toughness, $\mathbb{E}$ is the fourth-order elastic stiffness tensor and l is a length scale parameter as found in the PFM literature. The term $\eta\langle\dot{\omega}\rangle_-$ is a penalty term ensuring crack irreversibility. Here, $\langle\cdot\rangle_-$ indicates a negative Macaulay bracket. The coupled field equations (1) and (2) are supplemented with Dirichlet boundary conditions,

$$\begin{cases} \mathbf{u} = \mathbf{u}^{\mathrm{p}} & \text{on} \quad \Gamma_{\mathrm{D}}^{(u)} \\ \omega = \omega^{\mathrm{p}} & \text{on} \quad \Gamma_{\mathrm{D}}^{(\omega)} \end{cases} \quad \text{for existing cracks,} \tag{3}$$

and Neumann boundary conditions,

$$\begin{cases} (1-\omega)^2 \boldsymbol{\sigma} \cdot \mathbf{n} = \mathbf{t}^{\mathrm{p}} & \text{on} \quad \Gamma_{\mathrm{N}}^{(u)} \\ G_c l \mathbf{n} \cdot \boldsymbol{\nabla}\omega = q^{\mathrm{p}} & \text{on} \quad \Gamma_{\mathrm{N}}^{(\omega)} \end{cases} \tag{4}$$

for a unique solution.

Variationally consistent homogenization of phase field fracture

The variationally consistent homogenization (VCH) approach is adopted to derive a two-scale (FE^2) PFM model for fracture. This involves the introduction of (i) running averages[1] in the weak format and (ii) scale separation via first order homogenization. The detailed mathematical procedure which is avoided here for conciseness, could be followed from [4].

The macroscale problem assumes the form

$$\int_\Omega \overline{\boldsymbol{\sigma}} \colon \boldsymbol{\epsilon}[\delta\overline{\mathbf{u}}] \mathrm{d}\Omega = \int_{\Gamma_N^{(u)}} \bar{\mathbf{t}}^{\mathrm{p}} \delta\overline{\mathbf{u}} \mathrm{d}\Gamma \tag{5}$$

$$- \int_\Omega \overline{\boldsymbol{\gamma}} \cdot \mathbf{h}[\delta\overline{\omega}] \mathrm{d}\Omega + \int_\Omega \overline{\Phi} \delta\overline{\omega} \mathrm{d}\Omega \tag{6}$$

$$+ \int_\Omega \overline{\mathbf{Q}} \cdot \mathbf{h}[\delta\overline{\omega}] \mathrm{d}\Omega - \int_\Omega \overline{D} \delta\overline{\omega} \mathrm{d}\Omega - \int_\Omega \overline{\mathbf{D}}^{(2)} \cdot \mathbf{h}[\delta\overline{\omega}] \mathrm{d}\Omega = - \int_{\Gamma_N^{(\omega)}} \bar{\gamma}^{\mathrm{p}} \cdot \delta\overline{\omega} \mathrm{d}\Omega$$

where the following definitions are introduced

$$\begin{array}{ll} \overline{\boldsymbol{\sigma}} := \langle\boldsymbol{\sigma}\rangle_\square = \langle(1-\omega)^2 \mathbb{E} \colon \boldsymbol{\epsilon}[\mathbf{u}]\rangle_\square, & \overline{\boldsymbol{\gamma}} := \langle\boldsymbol{\gamma}\rangle_\square = -\langle G_c l \boldsymbol{\nabla}\omega\rangle_\square, \\ \overline{\Phi} := \langle\Phi\rangle_\square = \langle \frac{G_c}{l}\omega - (1-d)\boldsymbol{\epsilon}[\mathbf{u}] \colon \mathbb{E} \colon \boldsymbol{\epsilon}[\mathbf{u}]\rangle_\square, & \overline{\mathbf{Q}} := \langle\Phi(x-\bar{x})\rangle_\square, \\ \overline{D} := \langle D\rangle_\square = \langle\eta\langle\dot{\omega}\rangle_-\rangle_\square, & \overline{\mathbf{D}}^{(2)} := \langle D(x-\bar{x})\rangle_\square, \end{array} \tag{7}$$

with relevant Dirichlet and Neumann conditions at macro-level, cf. (3), (4). The microscale problem obtained through the standard VCH procedure is

$$a_\square^{(u)}(\mathbf{u}, \omega; \delta\mathbf{u}) - d_\square^{(u)}(\boldsymbol{\lambda}^{(u)}, \delta\mathbf{u}) = 0, \tag{8}$$

[1] $\langle\cdot\rangle_\square$ and $\langle\langle\cdot\rangle\rangle_\square$ indicate volume and surface averaging respectively.

$$a_{\square}^{(\omega)}(\omega;\delta\omega) + m_{\square}(\omega;\delta\omega) + b_{\square}(\omega,\mathbf{u};\delta\omega) - c_{\square}(\dot{\omega};\delta\omega) + d_{\square}^{(\omega)}(\lambda^{(\omega)},\delta\omega) + \langle\langle\bar{\lambda}^{(\omega)}\delta\bar{\omega}\rangle\rangle = 0, \quad (9)$$

$$-d_{\square}^{(u)}(\delta\boldsymbol{\lambda}^{(u)};\mathbf{u}) + d_{\square}^{(u)}(\delta\boldsymbol{\lambda}^{(u)};\bar{\boldsymbol{\epsilon}}\cdot\mathbf{x}) = 0, \quad (10)$$

$$-d_{\square}^{(\omega)}(\delta\lambda^{(\omega)};\omega) + d_{\square}^{(\omega)}(\delta\lambda^{(\omega)};\mathbf{h}[\bar{\omega}]\cdot\mathbf{x}) = 0, \quad (11)$$

$$\delta\bar{\lambda}^{(\omega)}\langle\langle\omega\rangle\rangle - \delta\bar{\lambda}^{(\omega)}\langle\langle\bar{\omega}\rangle\rangle = 0. \quad (12)$$

which holds for suitable test functions, $\delta\mathbf{u}$, $\delta\omega$, $\delta\boldsymbol{\lambda}^{(u)}$ and $\delta\lambda^{(\omega)}$, and where the following notations are incorporated

$$\begin{array}{ll} a_{\square}^{(u)}(\mathbf{u},\omega;\mathbf{v}) := \langle(1-\omega)^2\boldsymbol{\epsilon}[\mathbf{u}]\colon\mathbb{E}\colon\boldsymbol{\epsilon}[\mathbf{v}]\rangle_{\square}, & a_{\square}^{(\omega)}(\omega;p) := \langle G_c l\boldsymbol{\nabla}\omega\cdot\boldsymbol{\nabla}p\rangle_{\square}, \\ b_{\square}(\omega,\mathbf{u};p) := -\langle(1-\omega)\boldsymbol{\epsilon}[\mathbf{u}]\colon\mathbb{E}\colon\boldsymbol{\epsilon}[\mathbf{u}]p\rangle_{\square}, & m_{\square}(\omega;p) := \langle\omega\frac{G_c}{l}p\rangle_{\square}, \\ m_{\square}(\omega;p) := \langle\omega\frac{G_c}{l}p\rangle_{\square}, & c_{\square}(\dot{\omega};p) := \langle\eta\langle\dot{\omega}\rangle_{-}p\rangle_{\square}, \\ d_{\square}^{(u)}(\mathbf{s};\mathbf{t}) := \langle\langle\mathbf{s}\cdot\mathbf{t}\rangle\rangle_{\square}, & d_{\square}^{(\omega)}(s;t) := \langle\langle st\rangle\rangle_{\square}. \end{array} \quad (13)$$

Equations (10)-(12) are the prolongation rules/constraints imposed at the micro-level on the representative volume element (RVE). The unknowns $\mathbf{u}$ and ω are split into macro-level and micro-level contributions through an additive split (first order homogenization),

$$\mathbf{u} := \mathbf{u}^{\mathrm{M}}[\bar{\mathbf{u}}] + \mathbf{u}^{\mathrm{s}} \quad \text{where,} \quad \mathbf{u}^{\mathrm{M}}[\bar{\mathbf{u}}] = \boldsymbol{\epsilon}[\bar{\mathbf{u}}]\cdot(\mathbf{x}-\bar{\mathbf{x}}), \quad (14)$$

$$\omega := \omega^{\mathrm{M}}[\bar{\omega}] + \omega^{\mathrm{s}} \quad \text{where,} \quad \omega^{\mathrm{M}}[\bar{\mathbf{u}}] = \bar{\omega} + \mathbf{h}[\bar{\omega}]\cdot(\mathbf{x}-\bar{\mathbf{x}}). \quad (15)$$

Although, the phase field (damage) variable as represented in (15) consists of macro and micro contributions, it is reasonable to make further simplifications. One such approach would be to set either the macro contribution or the micro contribution to zero ($\omega^{\mathrm{M}}[\bar{\omega}]$ or $\omega^{\mathrm{s}} = 0$). These choices allow the construction of a family of two-scale PFMs, based on the explicit or implicit treatment/upscaling of the phase field variable. Thereby, data abstraction pertinent to the phase field variable can be exercised in the material law.

Numerical Study

A 2D unit square (in mm) with a fully damaged slit (0.1 mm length) is considered for an RVE study, cf. Figure 1a & Table 1. A strain-controlled analysis is carried out (Dirichlet [dbc] and Strongly periodic boundary conditions [spbc]) in the direction perpendicular to the slit axis. As seen from the average stress-strain response, cf. Figure 1b[2], the spbc leads to a softer response, whereas an artificial stiffening is observed in the case of dbc. Furthermore, the assumption $\omega^{M}[\bar{\omega}] = 0$ was made in this study. Therefore the damage lives only in the micro-level whereas its effect can be implicitly incorporated in the macro-level Gauss point stress-strain relation, cf. Fig.1b.

Conclusion

In this work, a two-scale phase field model for fracture was developed using the variationally consistent homogenization procedure. This method demonstrated data abstraction capabilities pertaining to the damage parameter. Based on the relevance of the macro- or micro-scale damage in the RVE, a family of multi-scaled damage models is established.

[2] ω : *nbc* indicates a no flux condition on the phase field.

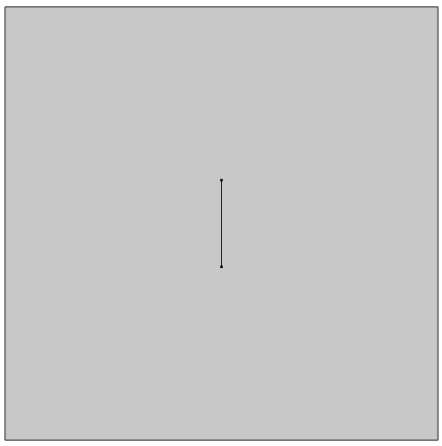

(a) RVE problem

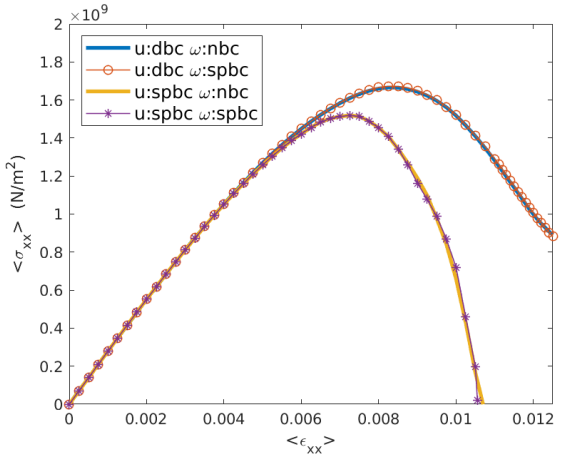

(b) Avg. stress-strain plot

Figure 1. RVE problem and results from strain-controlled analysis.

Table 1. Parameters for the RVE study

Property	Value
RVE	1 mm × 1 mm, Plane strain
λ, μ	131.154 GPa, 80.769 GPa
G_c, l	2700 N/m, 1.5e-2 mm
Max. element size	$l/2$

References

[1] Miehe, C. , Welschinger, F. and Hofacker, M. (2010), Thermodynamically consistent phase-field models of fracture: Variational principles and multi-field FE implementations. *Int. J. Numer. Meth. Engng.*, 83, 1273-1311. doi:10.1002/nme.2861

[2] Heister, T., Wheeler, M. F., Wick, T. (2015), A primal-dual active set method and predictor-corrector mesh adaptivity for computing fracture propagation using a phase-field approach. *Computer Methods in Applied Mechanics and Engineering.*, 290, 466-495, doi.org/10.1016/j.cma.2015.03.009

[3] Gerasimov, T., De Lorenzis, L. (2016), A line search assisted monolithic approach for phase-field computing of brittle fracture. *Computer Methods in Applied Mechanics and Engineering*, 312, 276–303. doi.org/10.1016/j.cma.2015.12.017

[4] Larsson, F. , Runesson, K. and Su, F. (2010), Variationally consistent computational homogenization of transient heat flow. *Int. J. Numer. Meth. Engng.*, 81, 1659-1686. doi:10.1002/nme.2747

[5] Hughes, T.J.R., Feijóo, G.R., Mazzei, L., Quincy, J-B. (1998), The variational multiscale method—a paradigm for computational mechanics, *Computer Methods in Applied Mechanics and Engineering*, 166, 3-24. doi.org/10.1016/S0045-7825(98)00079-6.

Proceedings of the 32nd Nordic Seminar on Computational Mechanics
A.H. Niemi and H. Koivurova (Eds.)

Calibration of Abaqus CDP model parameters

Kim Calonius[1], Alexis Fedoroff[1], Kari Kolari[1], Reijo Kouhia[2] and Jani Vilppo[2]

(1)VTT Technical Research Centre of Finland, Ltd., firstname.lastname@vtt.fi
(2)Tampere University, firstname.lastname@tuni.fi

Summary. This article proposes a relaxed strategy for the calibration of the Abaqus Concrete Damaged Plasticity (CDP) model in order to avoid the use of computationally expensive optimization techniques.

Key words: Concrete Damaged Plasticity (CDP), model calibration, Abaqus

Introduction

The Concrete Damaged Plasticity (CDP) built-in material model available in the Abaqus commercial finite element software, [1], is widely used for beyond design criteria analyses of reinforced concrete structures within the Abaqus users community. In particular, the CDP model has proven to be versatile enough to be used in beyond design basis earthquake analyses, [2, 3, 4], as well as in benchmark impact test analyses, [5, 6, 7], and full scale airplane crash simulations, [8].

Originally developed on top of the "Barcelona" yield surface, [9], and later on the isotropic hardening laws proposed by Lee and Fenves, [10, 11], that separate the internal plastic variables into a tensile and a compressive part, the CDP model in Abaqus enables also field variable dependent customized approaches. For example, a user enhanced Abaqus CDP model with confinement stress dependent compressive hardening evolution and strain rate dependent tensile softening evolution was proposed in [12]. Such custom material models are, indeed, necessary in special applications, in case of the previous example, in hard missile impact simulations.

Material model calibration as an optimization problem

Formally, the material model calibration is an optimization problem: "For a given material defined by its physical properties, X_{exp}, find material model input data, X_{sim}, such that the distance between the experimental test output data, $Y_{\text{exp}} = \mathcal{T}(X_{\text{exp}})$, and the simulated test output data, $Y_{\text{sim}} = \mathcal{S}(X_{\text{sim}})$, is minimum." Figure 1 shows the mapping diagram relative to material model calibration. One can, therefore, consider the formal (constrained) minimization problem of with the following objective function: $F(X_{\text{sim}}) = \text{dist}\big(\mathcal{T}(X_{\text{exp}})\,,\,\mathcal{S}(X_{\text{sim}})\big)$.

The fundamental difficulty which arises in the context of concrete modeling, is that the physical properties of a given material, such as cement chemical composition and aggregate size distribution, are totally unrelated to the material model input data. In case of the Abaqus CDP model the material input data is a collection of elasto-damage-plasticity parameters that define the elastic properties, the initial shape of the yield surface and its evolution with the increase of the internal hardening variables. On the other hand, the mechanical properties of concrete defined in the Eurocode and the FIB model code, [13, 14], are values that depend on the experimental setup such as sample size, boundary conditions and loading speed. Typically, the concrete material experiment set includes uniaxial monotonic or cyclic compression tests to

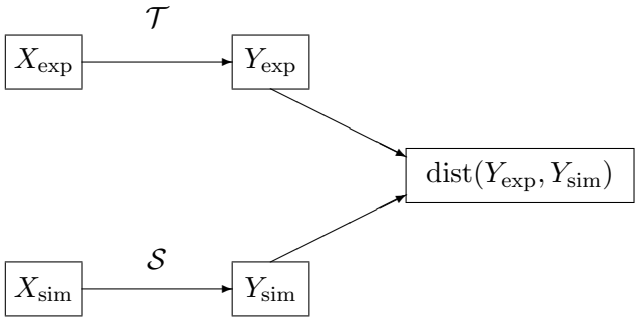

Figure 1. The basic structure of material model calibration.

determine elastic and compressive behavior and three point bending tests on notched specimen as well as split tensile tests to determine tensile behavior. In addition, the experiment set may include triaxial and/or biaxial tests to determine the failure surface shape and confinement dependency, as well as tensile and compressive split Hopkinson pressure bar tests to determine loading rate sensitivity.

Table 1. Mechanical material parameters for concrete defined in Eurocode

Denomination	Symbol	Unit
Compressive peak strength	f_{cm}	(MPa)
Total strain at compressive peak strength	ϵ_{c1}	(%)
Tensile peak strength	f_{ctm}	(MPa)
Fracture energy	G_{f}	(N/m)
Secant modulus of elasticity	E_{cm}	(MPa)
Poisson ratio	ν_{cm}	(-)
Confinement increase factor for compressive stress	CIF	(-)
Dynamic increase factor for tensile stress	DIF_{f}	(-)
Dynamic increase factor for tensile fracture energy	DIF_{g}	(-)
equibiaxial to uniaxial initial yield ratio	$\sigma_{\text{b}_0}/\sigma_{\text{c}_0}$	(-)
tensile to compressive meridians slope ratio	K_{c}	(-)

Therefore, it would be a mistake to consider the Eurocode mechanical concrete properties as intrinsic material parameters that can be mapped one-to-one to the material model parameters. Nevertheless, by comparing the contents of Table 2 and Table 1, one can conclude that at least some of the Eurocode mechanical concrete properties can be used as an initial guess, $X_{\text{sim}}^{(0)}$ for the minimization problem defined by the objective function F. On the other hand, it is clear that carrying out all the experiments cited above is a tough requirement. Therefore, one has to figure out a relaxed strategy to calibrate the material model with fewer experimental results.

Relaxed strategy for material model calibration

The proposed relaxed strategy for the CDP material model calibration relies on the assumption that not all of the material model parameters mentioned in Table 2 are equally important. To define the most important material parameters, the sensitivity of the model to the material parameters was studied first. Based on observations of the model behavior, an iteration order for material test simulations is proposed as shown Table 3. For each simulation, model parameters to be determined by iteration as well as fixed parameters are prescribed. The value for a given

Table 2. CDP model input parameters

Denomination	Symbol		Expression
Elastic stiffness modulus	E	$\approx$	E_{cm}
Elastic Poisson ratio	ν	$\approx$	ν_{cm}
Yield surface shape parameter	α	$=$	$\big(\sigma_{\mathrm{b0}}/\sigma_{\mathrm{c0}} - 1\big)/\big(2\,\sigma_{\mathrm{b0}}/\sigma_{\mathrm{c0}} - 1\big)$
Yield surface shape parameter	γ	$=$	$\big(3(1 - K_{\mathrm{c}})\big)/\big(2\,K_{\mathrm{c}} - 1\big)$
Uniaxial compressive hardening function	$\sigma_{\mathrm{c}}(\epsilon_{\mathrm{c}}^{\mathrm{p}})$	$=$	$\sigma_{\mathrm{c0}}\big((1 + a_{\mathrm{c}})\,e^{-b_{\mathrm{c}}\,\epsilon_{\mathrm{c}}^{\mathrm{p}}} - a_{\mathrm{c}}\,e^{-(1+k)b_{\mathrm{c}}\,\epsilon_{\mathrm{c}}^{\mathrm{p}}}\big)$
Uniaxial tensile hardening function	$\sigma_{\mathrm{t}}(\epsilon_{\mathrm{t}}^{\mathrm{p}})$	$=$	$\sigma_{\mathrm{t0}}\,e^{-b_{\mathrm{t}}\,\epsilon_{\mathrm{t}}^{\mathrm{p}}}$
Uniaxial initial compressive yield stress	σ_{c0}	$\approx$	$0.4\,\mathrm{CIF}\,f_{\mathrm{cm}}$
Uniaxial initial tensile yield stress	σ_{t0}	$\approx$	$\mathrm{DIF_f}\,f_{\mathrm{ctm}}$
Characteristic length	l_{ch}	$\approx$	average element dimension
Characteristic fracture energy	g_{F}	$=$	$\mathrm{DIF_g}\,G_{\mathrm{F}}/l_{\mathrm{ch}}$
Ratio	μ	$=$	$\max\sigma_{\mathrm{c}}(\epsilon_{\mathrm{c}}^{\mathrm{p}})/\sigma_{\mathrm{c0}}$
Compressive hardening parameter	a_{c}	s.t.	$k^k\,(1 + a_{\mathrm{c}})^{1+k} - (1 + k)^{1+k}\,\mu^k\,a_{\mathrm{c}} = 0$
Compressive hardening parameter	b_{c}	$=$	$-\big(k\,\mathrm{argmax}\,\sigma_{\mathrm{c}}(\epsilon_{\mathrm{c}}^{\mathrm{p}})\big)^{-1}\,\ln\frac{1+a_{\mathrm{c}}}{(1+k)a_{\mathrm{c}}}$
Compressive hardening parameter	k	$\in$	$\{1, 2, 3, \ldots\}$
Tensile hardening parameter	b_{t}	$=$	$\sigma_{\mathrm{t0}}/\big(g_{\mathrm{F}} + \frac{1}{2}\,(\sigma_{\mathrm{t0}})^2/E\big)$
Dilation angle	ϕ		
Eccentricity of Drucker-Prager hyperboloid	e		

fixed parameter is obtained from an appropriate simulation result on the previous iteration round. If there is no appropriate simulation result available, then an Eurocode value is applied as suggested by Table 2.

Table 3. Material test simulation iteration order

Order	Simulation	Parameter to be iterated	Fixed parameters
1.	Uniaxial compression	$E, \nu, \sigma_{\mathrm{c}}(\epsilon_{\mathrm{c}}^{\mathrm{p}})$	$\sigma_{\mathrm{t}}(\epsilon_{\mathrm{t}}^{\mathrm{p}}), \gamma, \alpha, \phi, e$
2.	Triaxial compression	$\gamma, \alpha, \mathrm{CIF}$	$\sigma_{\mathrm{t}}(\epsilon_{\mathrm{t}}^{\mathrm{p}}), \phi, e, E, \nu, \sigma_{\mathrm{c}}(\epsilon_{\mathrm{c}}^{\mathrm{p}})$
3.	Notched 3 point bending	$\sigma_{\mathrm{t}}(\epsilon_{\mathrm{t}}^{\mathrm{p}})$	$\sigma_{\mathrm{c}}(\epsilon_{\mathrm{c}}^{\mathrm{p}}), \gamma, \alpha, \phi, e, E, \nu$
4.	Direct shear	ϕ, e	$\sigma_{\mathrm{c}}(\epsilon_{\mathrm{c}}^{\mathrm{p}}), \sigma_{\mathrm{t}}(\epsilon_{\mathrm{t}}^{\mathrm{p}}), \gamma, \alpha, E, \nu$
5.	Split tensile	$\max\,\sigma_{\mathrm{t}}$	$\sigma_{\mathrm{c}}(\epsilon_{\mathrm{c}}^{\mathrm{p}}), \gamma, \alpha, \phi, e, E, \nu$

Further studies

In order to understand the wider context of this specific study, it is necessary to consider the experimental reinforced concrete slab impact testing, [15, 16] and concrete material model development, calibration and validation work, [12, 7] that has been going on in the Technical Research Centre of Finland (VTT). The primary objective of this research work is to provide a scientifically validated computational analysis tool that enables large scale airplane crash on concrete buildings to be performed. The calibration of the concrete material model parameters is therefore done as suggested in this study using concrete material test results from the VTT experimental impact testing program. The validation of the simulation model is then carried out against selected benchmark impact experiments from the same experimental program.

References

[1] Simulia. *Abaqus Manual*. Dassault Simulia, 2016.

[2] V. Jussila and L. Fülöp. Damping estimates based on the level of non-linear response in stiff concrete buildings. *VTT report: VTT-R-05636-14*, 2014.

[3] V. Jussila, Y. Li, and L. Fülöp. Statistical analysis of the variation of floor vibrations in nuclear power plants subject to seismic loads. *Nuclear Engineering and Design, 84-96.*, 2016.

[4] A. Fedoroff and L. Fülöp. Study of the seismic response of a nuclear powerplant building. *VTT report: VTT-R-02604-18*, 2018.

[5] J Rodriguez, F. Martinez, and J. Marti. Concrete constitutive model, calibration and applications. *2013 SIMULIA Community Conference*, 2013.

[6] A. Fedoroff, J. Kuutti, and A. Saarenheimo. A physically motivated element deletion criterion for the concrete damage plasticity model. In *SMiRT-24 transactions*. International Association for Structural Mechanics in Reactor Technology, 2017.

[7] A. Fedoroff and K. Calonius. Using the abaqus cdp model in impact simulations. *Rakenteiden Mekaniikka (Journal of Structural Mechanics), accepted for publication*, 2019.

[8] A. Fedoroff. Parametric study of aircraft impact simulation on nuclear power plant. *VTT report: VTT-R-05152-17*, 2017.

[9] J Lubliner, J. Oliver, S Oller, and E. Oñate. A plastic-damage model for concrete. *Int.J. of Solids and Structure*, 25(3):299–326, 1989.

[10] J.H. Lee. *Theory and implementation of plastic-damage model for concrete structures under cyclic and dynamic loading*. PhD dissertation, University of Berkley, California, 1996.

[11] J.H. Lee and G. Fenves. Plastic-damage model for cyclic loading of concrete structures. *Journal of Engineering mechanics*, 124(8):892–900, 1998.

[12] A. Fedoroff, K. Calonius, and J. Kuutti. Behavior of the abaqus cdp model in simple stress states. *Rakenteiden Mekaniikka (Journal of Structural Mechanics), 52(2), 87-113.*, 2019.

[13] FIB. *Fib Model Code 2010*. International Federation for Structural Concrete, Lausanne, 2010.

[14] CEN European Committee for Standardization. *Eurocode - Basis of structural design*. Finnish Standards Association SFS, 1990.

[15] A. Vepsä, A. Saarenheimo, F. Tarallo, J.-M. Rambach, and N. Orbovic. Impact tests for iris 2010 benchmark exercise. *Journal of Disaster Research, 7(5), 619-628*, 7(5):619–628, 2012.

[16] A. Vepsä, K. Calonius, A. Fedoroff, L. Fülöp, V. Jussila, A. Saarenheimo, P. Varis, B. Fälth, B. Lund, and M. Tuomala. Experimental and numerical methods for external event assessment improving safety (ernest). In *SAFIR2018 The Finnish Research Programme on Nuclear Power Plant Safety 2015-2018: interim report*. VTT, Technical Research Centre of Finland, 2016.

Proceedings of the 32nd Nordic Seminar on Computational Mechanics
A.H. Niemi and H. Koivurova (Eds.)

Deep learning for future state estimation of the unsteady flows

Hamidreza Eivazi[1], Mehran Masdari[2], and Ramak Soleymani[3]

(1)Faculty of New Sciences and Technologies, University of Tehran, Tehran, Iran, hamid.eivazi@ut.ac.ir
(2)Faculty of New Sciences and Technologies, University of Tehran, Tehran, Iran
(3)Department of Information Technology, Uppsala University, Uppsala, Sweden

Summary. In fluid dynamics, reduced-order modeling of the unsteady flows is significant in terms of future state estimation, feature extraction, and control. The primary goal is to decompose Unsteady fluid flows, which are nonlinear high-dimensional dynamical systems, to a set of features most important for future state prediction and control, typically using a dimensionality reduction technique. In this work, a deep learning based data-driven technique, developed by authors, is used for reduced-order modeling of the unsteady flow over a pitch oscillating airfoil and a cylinder. A deep autoencoder network is used for nonlinear dimension reduction and feature extraction as an alternative for Singular Value Decomposition (SVD), and furthermore, the extracted features are used as an input for Long Short-Term Memory network (LSTM) to predict the velocity field at future time instances. Training and Testing data are acquired from numerical simulation. For the airfoil, the data on the dynamic mesh is first interpolated on a constant mesh using K-Nearest Neighbors (KNN) machine learning algorithm. In the second test case, cylinder, Reynolds number is reduced with the time to asses the performance of the proposed method in modeling of a multi-frequency problem. The autoencoder-LSTM method is compared with Dynamic Mode Decomposition (DMD) as the data-driven base method. Results show that the autoencoder-LSTM method is considerably capable of predicting the fluid flow evolution, where higher values for the coefficient of determination R^2 are obtained using autoencoder-LSTM comparing to DMD.

Key words: deep learning, Unsteady Flows, Autoencoder, LSTM, ROM

Introduction

Unsteady fluid flows are nonlinear high dimensional dynamical systems that can experience complex nonlinearities with a wide range of special and temporal features. It is of interest in the analysis of unsteady fluid flows to extract dominant features and introduce a reduced model of the complex system based on physically important features. During the last three decades, several theoretical and methodological advancements made it possible to develop general ideas in reduced-order modeling of the unsteady flows [1, 2, 3]. Deep learning is a subset of machine learning methods based on artificial neural networks, which is capable of extracting hidden information with multiple levels of representation from nonlinear and complex dynamical systems [4].

Numerical Analysis

Two-dimensional Navier-Stokes equations are solved using Finite Volume Method (FVM). First, the flow around a pitch oscillating NACA0012 airfoil is simulated at Reynolds number $Re = U_\infty C/\nu$ of 1.35×10^5, where C is the airfoil chord. Airfoil oscillates sinusoidally ($\alpha = \alpha_{mean} + \alpha_{amp} \times \sin(\Omega t)$) about its $\frac{1}{4}$ chord with the reduced frequency $k = \Omega C/2U_\infty$ of 0.1. Figure 1 presented the lift coefficient versus angle of attack obtained from present simulation against experimental and numerical data [5, 6].

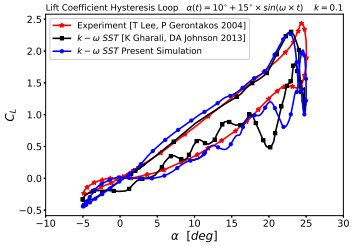

Figure 1. Lift coefficient versus angle of attack for the pitch oscillating airfoil; comparison of the present simulation and experimental [5] and numerical [6] data

At the second test case, free-stream velocity U_∞ is decreased relative to the time from its value corresponding to $Re = 3900$ as $U_\infty = U_{\infty,Re=3900}/t$, where t is the time. Variation of lift coefficient besides training and testing data sets are shown in Figure 2. The gradual decrease of the free-stream velocity weakens the vortex shedding and leads to the change in its frequency.

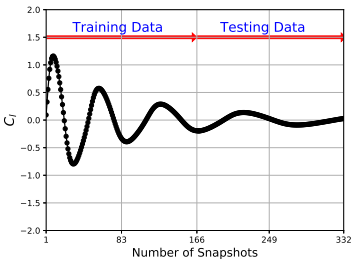

Figure 2. Variation of Lift coefficient with time for the second test case

Methodology

For the first test case, the snapshots are constructed from the velocity domain were $-1c < x < 7c$ and $-4c < y < 4c$. This leads to a snapshot containing 99473 nodes. In this regard, the input and output layers of the autoencoder have 99473 nodes. Mapping and demapping layers consist of 500 nodes, and the bottleneck layer contains 50 nodes. Figure 3a shows a general architecture of an autoencoder network; it consists of an encoder part that converts a given velocity domain to a code layer, and then decode it back to reproduce the input.

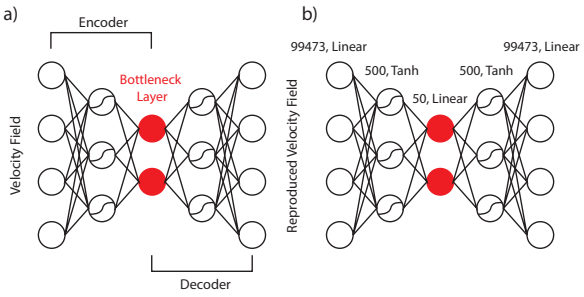

Figure 3. The architecture of autoencoder network

Sequences of features, which are the reduced values, are used as inputs of the LSTM network. It brings the ability to have a perspective about the future of a dynamical system just from past measurements, and it can be used to design a proper actuator to control the system's unsteadiness.

Results and Discussion

For each test case, autoencoder and LSTM networks are trained through 200 epochs. R^2 and MSE obtained from the autoencoder network and the autoencoder-LSTM method in prediction of the training and testing data are reported in Table 1 together with the results acquired from the DMD.

Table 1. Coefficient of determination R^2 and MSE for the autoencoder Network, autoencoder-LSTM method, and DMD

	Test 1 (Train)		Test 1 (Test)	
	R^2	MSE	R^2	MSE
Autoencoder Network	0.9873	5.04×10^{-3}	0.9872	5.14×10^{-3}
Autoencoder-LSTM	0.9986	5.42×10^{-4}	0.9983	7.13×10^{-4}
DMD	0.9198	3.70×10^{-2}	0.8981	4.64×10^{-2}
	Test 2 (Train)		Test 2 (Test)	
	R^2	MSE	R^2	MSE
Autoencoder Network	0.9994	8.21×10^{-8}	0.8967	2.61×10^{-6}
Autoencoder-LSTM	0.9996	5.74×10^{-8}	0.8577	4.05×10^{-6}
DMD	0.9937	4.58×10^{-7}	0.0826	2.00×10^{-5}

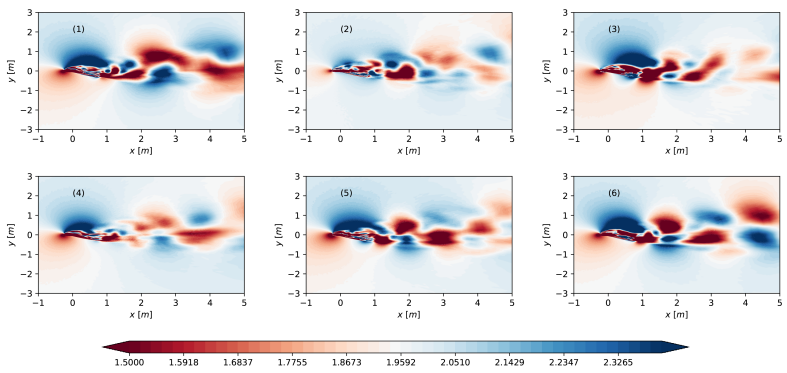

Figure 4. First 6 features of the unsteady flow over the pitch oscillating airfoil extracted by the autoencoder network

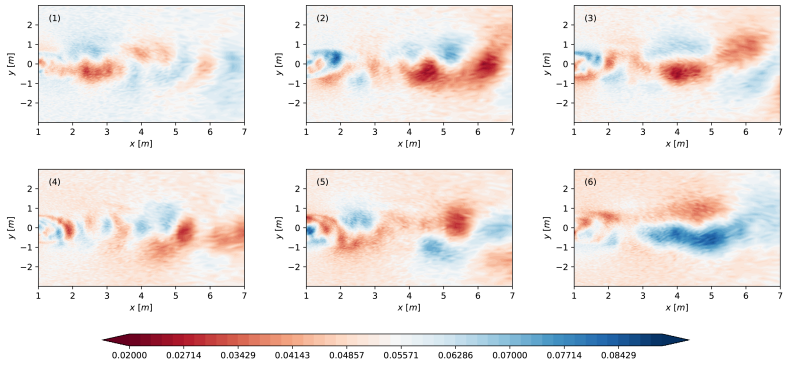

Figure 5. First 6 features of the flow for the second test case extracted by the autoencoder network

Figures 4 and 5 illustrate the first 6 features extracted by the autoencoder network from the velocity field for the two test cases, respectively. For both cases, autoencoder network is able to extract features feasible for the reconstruction of the data where the R^2 values for the testing data of the first and second test cases are equal to 0.9872 and 0.8967, respectively (Table 1).

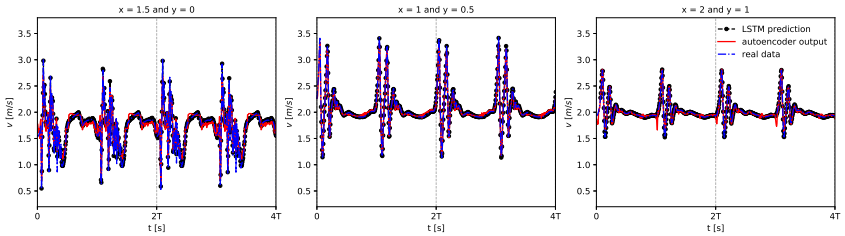

Figure 6. LSTM prediction and autoencoder output against real data at 3 different points in the wake of the oscillating airfoil

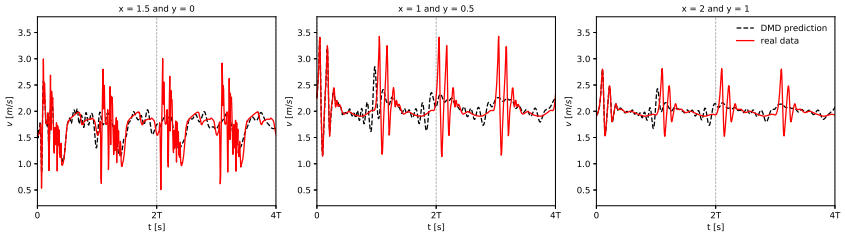

Figure 7. DMD prediction with SVD rank truncation of 50 against real data for 3 different points in the wake of the oscillating airfoil

To depict the performance of the LSTM network in the prediction of the velocity evolution through the time from the reduced data of the autoencoder network, variations of velocity at three different points in the wake of the oscillating airfoil. Figures 6 and 7 represent the performance of the autoencoder-LSTM method and the DMD with rank truncation of 50 in prediction of the velocity variations at aforementioned points for the first test case.

Conclusion

In this paper, a new data-driven reduced-order method based on deep learning is used for future estate estimation of the complex unsteady fluid flows. Results are compared with the results of the well-known DMD method. The performance of each method is assessed with the use of the coefficient of determination R^2 and MSE. For both cases, the autoencoder-LSTM network obtains more accurate results in the prediction of the velocity field in future time instances.

References

[1] Lumley J L 1967 *Atmospheric Turbulence and Radio Wave Propogation* pages 166–78

[2] Schmid P J 2010 *Journal of Fluid Mechanics* **656** 5–28 ISSN 14697645

[3] Rowley C W, Mezi I, Bagheri S, Schlatter P and Henningson D S 2009 *Journal of Fluid Mechanics* **641** 115–127 ISSN 00221120

[4] LeCun Y, Bengio Y and Hinton G 2015 *Nature* **521** 436 URL `https://doi.org/10.1038/nature14539 http://10.0.4.14/nature14539`

[5] LEE T and GERONTAKOS P 2004 *Journal of Fluid Mechanics* **512** 313–341

[6] Gharali K and Johnson D A 2013 *Journal of Fluids and Structures* **42** 228–244 ISSN 0889-9746

Proceedings of the 32nd Nordic Seminar on Computational Mechanics
A.H. Niemi and H. Koivurova (Eds.)

On error-controlled numerical model reduction for computational homogenization of porous media

Fredrik Ekre[1], Fredrik Larsson[1], Kenneth Runesson[1], and Ralf Jänicke[1]

(1) Department of Industrial and Materials Science, Chalmers University of Technology, fredrik.ekre@chalmers.se, fredrik.larsson@chalmers.se, kenneth.runesson@chalmers.se, ralf.janicke@chalmers.se

Summary. In this contribution, we present an explicit estimator for the error induced by using numerical model reduction for finite element analysis of porous media in the context of computational homogenization. The linear quasi static problem is considered, whereby it is possible to derive guaranteed bounds of the error in the solution. Two approaches for numerical model reduction are implemented and compared: a reduced basis derived from snapshots of training simulations using Proper Orthogonal Decomposition, and a reduced basis solved based on spectral decomposition for an auxiliary decoupled problem.

Key words: numerical model reduction, computational homogenization, a posteriori error estimation

Introduction

In order to model the effective mechanical behavior of fluid saturated porous rock, computational homogenization can be adopted whereby the the coupled porous media problem is studied on the microscale. The resulting macroscopic behavior can under certain assumptions be derived as apparently visco-elastic. Hence, the dissipative mechanism on the macroscale can be related to the seepage of pore fluid on underlying microscale. If the length scales are sufficiently separated, the effective viscoelastic properties can be derived from quasi-static consolidation on Representative Volume Elements (RVEs) on the resolved microscale.

Jänicke et al. [1] derived the effective viscoelastic model numerically by using numerical model reduction for the poro-elasticity problem on the RVE. Replacing the finite element problem on the RVE by its reduced counterpart showed to be very efficient. However, the relation between the reduced basis and the applied loading is crucial, and it is hard to a priori ascertain a sought level of accuracy.

In this contribution, we extend the work in [1] by presenting an a posteriori error estimate for the error introduced by adopting a reduced basis as compared to the full-fledged finite element problem.

The RVE problem

Inside the RVE $\Omega_\square$ we consider the linear consolidation problem in terms of solving for a displacement field $\boldsymbol{u}$ and the pore pressure p from

$$-\boldsymbol{\sigma} \cdot \boldsymbol{\nabla} = 0 \quad \text{in } \Omega_\square, \tag{1}$$

$$\mathrm{d}_t \Phi + \boldsymbol{w} \cdot \boldsymbol{\nabla} = 0 \quad \text{in } \Omega_\square, \tag{2}$$

where $\boldsymbol{\sigma}$ is the (total) Cauchy stress tensor, Φ is the stored fluid per reference volume of mixture and $\boldsymbol{w}$ is the seepage of migrating fluid.

We introduce computational homogenization by imposing linear boundary conditions on the displacement field and homogeneous pressure boundary conditions,

$$\boldsymbol{u} = \bar{\boldsymbol{\epsilon}} \cdot [\boldsymbol{x} - \bar{\boldsymbol{x}}] \quad \text{on } \partial\Omega_\square, \tag{3}$$

$$p = 0 \quad \text{on } \partial\Omega_\square, \tag{4}$$

where $\bar{\boldsymbol{x}}$ is the centroid of the RVE and $\bar{\boldsymbol{\epsilon}}$ is the imposed macroscopic strain that acts as data for the space-time problem. Finally, the implicit history-dependent macroscopic stress is evaluated as

$$\bar{\boldsymbol{\sigma}} = \bar{\boldsymbol{\sigma}}\{\bar{\boldsymbol{\epsilon}}\} := \frac{1}{|\Omega_\square|} \int_{\Omega_\square} \boldsymbol{\sigma} \mathrm{d}V. \tag{5}$$

Numerical Model Reduction

Following [1], we first make use of the linearity and time-invariance of the balance of momentum equation (1). This allows for (formal) elimination of the displacement field from the problem. Secondly, we introduce a reduced approximation for the pressure field on the form

$$p(\boldsymbol{x}, t) \approx p_{\mathrm{R}}(\boldsymbol{x}, t) = \sum_{a=1}^{N_{\mathrm{R}}} p_a(\boldsymbol{x}) \xi_a(t), \tag{6}$$

where $\{p_a\}_{a=1}^{N_{\mathrm{R}}}$ is a reduced basis of pressure modes, to be discussed in more detail below, and $\{\xi_a\}_{a=1}^{N_{\mathrm{R}}}$ are the pertinent time-depending coefficients. The elimination of the displacement field discussed above allows for a priori computation of displacement modes, such that

$$\boldsymbol{u}(\boldsymbol{x}, t) \approx \boldsymbol{u}_{\mathrm{R}}(\boldsymbol{x}, t) = \sum_{i,j} \hat{\boldsymbol{u}}^{(ij)}(\boldsymbol{x}) \bar{\epsilon}_{ij}(t) + \sum_{a=1}^{N_{\mathrm{R}}} \boldsymbol{u}_a(\boldsymbol{x}) \xi_a(t), \tag{7}$$

where $\hat{\boldsymbol{u}}^{(ij)}$ are the sensitivities w.r.t. macroscopic strain component $\bar{\epsilon}_{ij}$, and each $\boldsymbol{u}_a$ is the sensitivity w.r.t. its pertinent pressure mode p_a.

Finally, based on the a priori computed fields, a numerically derived macroscopic model is obtained, that can be used in macroscale analyses.

A posteriori Error Estimation

We follow along the lines of Ekre et al. [2], and derive guaranteed upper and lower bounds for the approximations introduced in (6) and (7). More specifically, the space-time weak format of the problem is utilized to construct a suitable "energy" norm of the solution. As an extension, the procedure of goal-oriented error estimation are elaborated to derive guaranteed bounds on arbitrary linear output functionals. In particular, we are interested in assessing the accuracy in the macroscopic stress $\bar{\boldsymbol{\sigma}}$ defined in (5).

The derived estimator is guaranteed independently of the origin of the pressure basis. However, using spectral decomposition (cf. below) allows for tightening of the error bounds.

Different strategies to extract the reduced basis

We shall now elaborate on the different possibilities of constructing a suitable basis for the pore pressure approximation. First, we follow the original implementation in [1], which was based on Proper Orthogonal Decomposition (POD) of snapshots from training simulation. The procedure is known to be very efficient in terms of generating small errors already for a low number of modes. This is indeed observed, and acknowledged by the computed estimator. However, we

see that the effectivity index, i.e. the ratio between estimated and true error, deteriorates when adding pressure modes.

As a second alternative, we consider basis functions from spectral decomposition of the decoupled pressure equation, omitting the coupling to the displacement field. Since these basis are not directly related to the problem at hand, we see that convergence of the error w.r.t. number of included number of pressure modes is much worse than for the POD basis. However, selecting the modes with the lowest eigenvalues allow for sharper estimates of the error.

The two different strategies are investigated for a few numerical example RVEs in three spatial dimensions for heterogeneous poro-elastic properties, illustrating the findings above.

References

[1] R. Jänicke, F. Larsson, H. Steeb and K. Runesson. Numerical identification of a viscoelastic substitute model for heterogeneous poroelastic media by a reduced order homogenization approach. *Comper Methods in Applied Mechanics and Engineering*, 298, 108–120, 2016.

[2] F. Ekre, F. Larsson, and K. Runesson. On error controlled numerical model reduction in FE^2-analysis of transient heat flow. *International Journal for Numerical Methods in Engineering*, 119, 38-73, 2019.

Proceedings of the 32nd Nordic Seminar on Computational Mechanics
A.H. Niemi and H. Koivurova (Eds.)

Comparision of hygrothermal simulation techniques in northern conditions

Filip Fedorik, Hannu Lahtinen, Hannu Koivurova and Antti H. Niemi

Structures and Construction Technology Research Unit
Faculty of Technology
University of Oulu, Finland
filip.fedorik@oulu.fi, hannu.lahtinen@oulu.fi, hannu.koivurova@oulu.fi and antti.niemi@oulu.fi

Summary. We analyze and verify different approaches towards hygrothermal design of a building envelope.

Key words: heat and moisture transfer, structural health, arctic engineering

Introduction

Requirements towards energy efficiency oblige designs to create envelopes of high thickness, especially in Nordic countries and northern parts of Russia. These structures have larger water vapour resistance and may lead to structural fault performance. The presented study identifies different approaches towards hygrothermal design of building envelope. The current market offers number of numerical tools allowing multidisciplinary simulations in engineering. Structural design must meet many requirements determined by international and national norms. The aim of reducing energy consumption brings multiple challenges in terms of structural durability, sustainability and health indoor environment. Health indoor environment and structural durability significantly depend on overall hygrothermal performance of the building. The hygrothermal conditions have major impact on material properties in short as well as long terms. The building physics approach towards building design consists in controlling an extensive moisture and amount of interstitial condensate water. Steady-state manual calculation of condensed and/or evaporated water is usually performed by Glaser method. Besides the traditional approach an advanced analyses can be used. The structure subjected to the presented study is represented by a log-house envelope. The envelope structure consists of a double-log layer filled with mineral wool insulation.

Boundary conditions

The outdoor boundary conditions within the presented study are represented by a typical test year from the Finnish Meteorological institute (https://ilmatieteenlaitos.fi). The indoor relative humidity is formed according to Finnish national code RIL 107-2012 [1] from outdoor conditions considering the service use of the structure. The indoor temperature is defined constant at 21^0C. The numerical approach was created in 2-dimensional environment, however representing 1-dimensional hygrothermal problem (Figure 1).

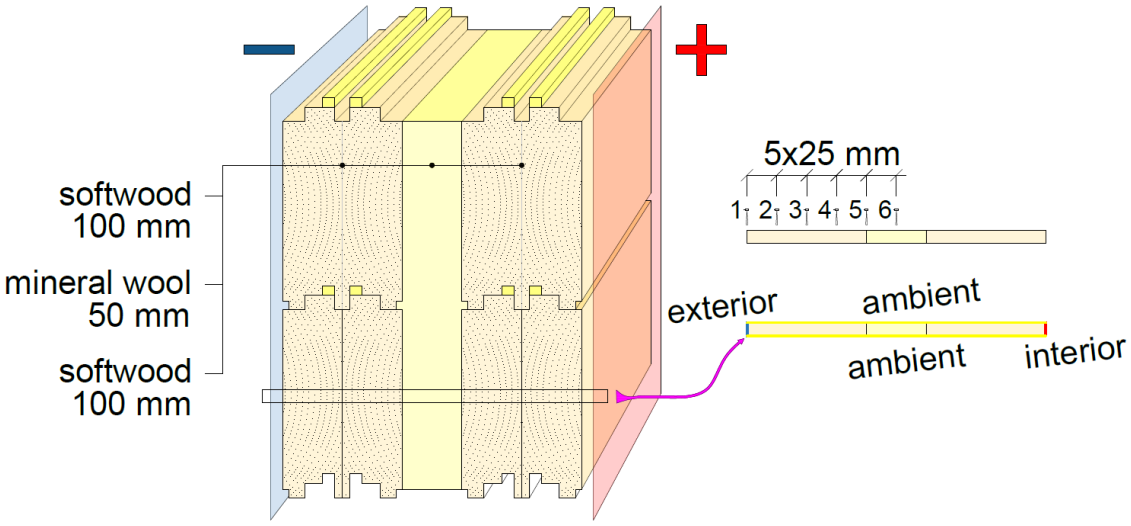

Figure 1. Studied structure, numerical model and location of monitored points in dynamic simulation.

Manual approach

The Glaser method was used for calculating the water phase transition to provide interstitial hygrothermal conditions and to identify rate of condensation and evaporation. The calculation was performed for each month using average temperatures and relative humidity. Material properties needed are thermal conductivity λ and water vapour diffusion resistance μ (Table 1). The process consists of 6 steps; 1) defining characteristic temperatures on surfaces and interfaces, 2) evaluation of water vapour pressure at saturation, 3) determining internal and external water vapour pressures, 4) plot the water vapour pressure at saturation against equivalent thicknesses, 5) plot water vapour pressure at the internal and external surfaces and connecting them with a straight line and 6) if condensation or evaporation appears, the rate of condensation or evaporation is calculated.

Table 1. Material properties

	steady state			dynamic		
material	$\mu[-]$	$\lambda[W/mK]$	$\rho[kg/m^3]$	C_p [J/kgK]	$DW_{80}[m^2/s]$	W_{80} [kg/m^3]
softwood	200	0.12	400	1400	0	60.00
mineral wool	1.3	0.04	60	850	0	1.79

Steady-state numerical approach

The structure was also subjected to numerical steady state simulation by using multidisciplinary Finite Element Method numerical tool Comsol. This approach is analogous to the manual calculation, except the simulation allows more detail water vapour diffusion profile at any location of analysed structure. The relative humidity profiles for every month is illustrated in the Figure 2. It can be seen, the humidity significantly exceeds 80% inside the external log layer from October to March. Although, no significant condensed water is found, high humidity may lead to a biological growth and cause damage and/or further deterioration of building material.

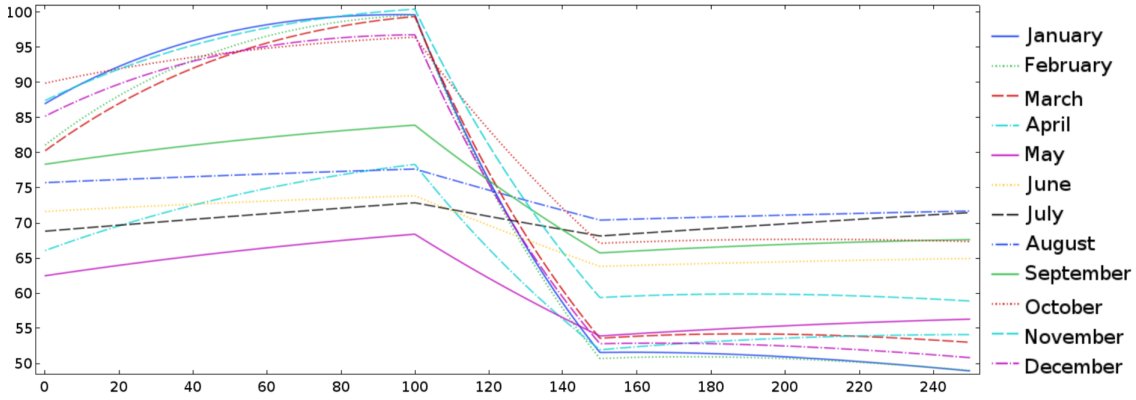

Figure 2. Steady relative humidity each month.

Table 2. Mould index M_{index} obtained at observed points

	analysed points					
	1	2	3	4	5	6
M_{index}	0.73	0.01	0.78	2.12	4.43	0.00

Dynamic simulation approach

Time-dependent simulation was performed using Wufi 2D. It represents numerical tool for hygrothermal simulation in building components in one and two dimensional environment [2].

The material properties needed for the dynamic simulation are thermal conductivity λ, water vapour diffusion resistance μ, density ρ, heat capacity C_p, liquid transport coefficient DW and moisture storage function W (Table 1.). The simulation was performed for a period of 1 year with 1 h time-step. Therefore, 8760 time-steps were performed. The hygrothermal conditions were monitored at 6 points and the boundaries were defined as illustrated in the Figure 1.

Interpretation of results

The presented approaches require different results' interpretations. The manual calculation focuses on identifying interstitial condensation and evaporation based on water vapour pressure profile. The benefit of applying numerical approach consists in ability to define location of critical conditions anywhere over the structural profile. However, the indoor comfort highly depends on temperature, humidity and air flow. Specific combinations of temperature and humidity promote mould growth which may lead to allergic reactions and other health issues for inhabitants, as well as influence the behavioural properties of structural elements [3]. A mathematical model allowing identification of biological growth is represented by M_{index} value in the Finnish Mould Growth Model [4]. The input data for mould growth risk are temperature, relative humidity, material sensitivity and exposure time. Therefore, the dynamic simulation is required to identify the hygrothermal conditions in time. The model defines favourable conditions for mould growth that are represented by temperature between 0^0C and 50^0C and relative humidity is limited by 80 % or 85 % depending on material sensitivity. The maximum M_{index} values obtained at each monitored point are summarized in the Table 2. The Figure 3 represents graphical illustration of hygrothermal conditions and M_{index} development during the analysed year.

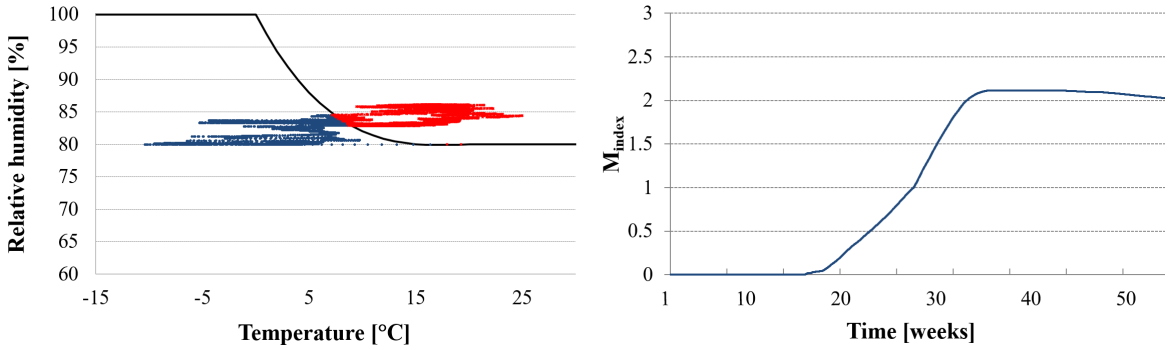

Figure 3. Graphical illustration of hygrothermal conditions (red dots indicate period of 1 hour when structure is exposed to favourable conditions for mould growth initiation and blue dots denote conditions unfavourable for mould growth) and M_{index} development at point 4.

Conclusion

The presented study analyses three different approaches towards hygrothermal performance of log-house envelope. The manual approach shows small amount of condensed water within one month. The remaining periods achieve water vapour diffusion without any interstitial condensation. Therefore, it is assumed, that the structure allows the condensed water to dry out. The numerical steady-state analyses determines higher relative humidity inside the outdoor log layer. Hence, the hygrothermal conditions were monitored via the time-dependent analyses and the results were subjected to the Finnish Mould Growth Model. The humidity inside the outdoor log increases during the analysed period and exceeds 80 % for most of the analysed year.

Acknowledgements

This research has been supported by the Kolartic-CBC project KO1089 Green Arctic Building. This support is gratefully acknowledged.

References

[1] RIL 107-2012 (2012) *Rakennusten veden- ja kostudeneristysohjeet*, Suomen Rakennusinsinöörien Liitto RIL r.y., language: Finnish

[2] Künzel, H.M. (1995). *Simultaneous heat and moisture transport in building components.* PhD-thesis report. Fraunhofer Institute of Building Physics, ISBN: 3-8167-4103-7.

[3] Krus, M., Seidler, M., Sedlbauer, K. (2010). *Comparative Evaluation of the Predictions of Two Established Mold Growth Models*, Buildings XI, Thermal Performance of the Exterior Envelopes of Whole Buildings XI, Buildings Conference, December 5-9, 2010, ISBN: 978-1-933742-89-2, 2010

[4] Ojanen, T., Peuhkuri, R., Viitanen, H., Lähdesmäki, K., Vinha, J., Salminen, K., (2011, May). *Classification of Material Sensitivity - New Approach for Mould Growth Modeling.* In: Proceeding of the 9th Nordic Symposium on Building Physics - NSB 2011, Tampere, Finland, May 2011, pp. 867-874

Proceedings of the 32nd Nordic Seminar on Computational Mechanics
A.H. Niemi and H. Koivurova (Eds.)

MFrontInterface.jl: MFront material models in JuliaFEM

Tero Frondelius[1,3], Thomas Helfer[4], Ivan Yashchuk[2], Joona Vaara[3], and Anssi Laukkanen[2]

(1)University of Oulu, firstname.lastname@oulu.fi
(2)VTT Technical Research Centre of Finland, firstname.lastname@vtt.fi
(3)Wärtsilä Research & Development and Engineering, firstname.lastname@wartsila.com
(4)CEA, DEN, DEC, Cadarache F-13108 Saint-Paul-Lez-Durance, France, thomas.helfer@cea.fr

Summary. This article describes the `MFrontInterface.jl` package which aims at allowing mechanical behaviours generated by the `MFront` code generator to be used in `JuliaFEM`. `MFrontInterface.jl` is build on top of the `MFrontGenericInterfaceSupport` library.

Introduction

This article describes the `MFrontInterface.jl` package which aims at allowing mechanical behaviours generated by the `MFront` code generator to be used in `JuliaFEM`. `MFrontInterface.jl` is build on top of the `MFrontGenericInterfaceSupport` library. See Figure 1 for calrification.

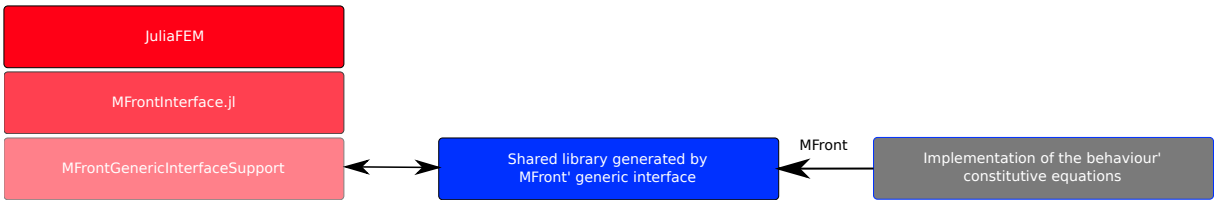

Figure 1: Sofware layers involved

A short introduction to `MFront` and `MGIS`

Overview of the `MFront` code generator

The behaviour of solid materials is modelled using so-called constitutive equations which describe how the internal state of the material evolves. Those state variables can describe many microstructural aspects of the material (i.e. grain size, dislocation density, hardening state) or be considered as purely phenomenological.

More precisely, after discretization in time of the problem, the solver provides an estimate of the local change of loading of the material (for example the strain increment for small strain behaviours) to the constitutive equations which allow:

- The computation of the values of the internal state variables at the end of a time step knowing their values at the beginning of the time step.

- The local thermodynamic forces (for example the stress for small strain behaviours) which affects the material equilibrium at the structural scale.

This step is called behaviour integration. In the following, the term behaviour becomes a synonym for constitutive equations. `MFront` is an open-source and cross-platform code generator dedicated to various material knowledge, such as material properties, behaviours and simple physical models, see [1, 2] for details. `MFront` is developed in the framework of the `PLEIADES` project which is co-developed by CEA, EDF and Framatome.

`MFront` provides a set of domain-specific languages on top of `C++` which allows the code of the constitutive equations to be fairly close to the mathematical expressions. Concerning mechanical behaviours, which is the most exciting aspect of `MFront` regarding this paper, `MFront` allows the user to implement, small and finite strain behaviours, as well as cohesive zone models. Isotropic and orthotropic behaviours are supported.

Thanks to the notion of `interfaces`, code specific to various mechanical solvers can be generated. As of version 3.2, `MFront` provides interfaces for e.g. `Cast3M`, `code_aster`, `Europlexus`, `Cyrano`, `CalculiX`, `Abaqus/Standard` and `Abaqus/Explcit`, `AMITEX_FFTP`, `Ansys`. The generated code is then compiled a shared library which can be plugged in the targeted solver.

An interface named `generic` has been introduced in version 3.2. Behaviours generated with the `generic` interface are meant to be used through the `MFrontGenericInterfaceSupport` library, which is described hereafter. `MFront` has been carefully designed to meet the high-quality standards of the nuclear industry. In particular, an extensive set of unit tests has been set up to guarantee its reliability.

Overview of the `MGIS` *library*

This `MFrontGenericInterfaceSupport` library (`MGIS`) aims at proving tools (functions, classes, bindings, etc...) to handle behaviours written using `MFront` generic interface, see [3–5] for details. Those tools are meant to be used by (`FEM`, `FFT`, etc.) solver developers. Permissive licences have been chosen to allow integration in open-source and proprietary codes. In particular, the `MGIS` library provides:

- functions to load behaviour from a shared library. Along with a pointer to the function implementing the behaviour, various metadata are also retrieved, such as the number of state variables, their nature (scalar, tensorial), their name. Those metadata can be used to properly allocate the storage of the internal state variable, check that the user input file is consistent (i.e. does not try to initialize a non-existing variable), provides additional information on which variable can be post-processed.
- data structures to store the material states at the beginning of the time and at the end of the time step for one integration points or a set of integration points. Views data structure are available to use externally allocated memory.
- functions to perform behaviour integration over one time step. If a set of integration points is handled, parallelization of the behaviour, integration can be handled by the `MGIS` library.

`MGIS` is written in `C++` and provides bindings for `C`, `Fortran 2003`, `python` and `Julia` [6] thanks the `CxxWrap.jl` library. The `Julia` bindings are written in pure `C++` and are barely usable per se.

The `MFrontInterface.jl` package

The `MFrontInterface.jl` package wraps `MGIS`' `Julia` bindings to make its usage much more convenient and consistent with the `Julia` language, in other words make `MFront` material models

available in `JuliaFEM` [7–12]. `BinaryBuilder.jl` package is used for binary dependencies, which makes the package installation easy and convenient, like shown below:

```
(v1.2) pkg> add MFrontInterface

julia> using MFrontInterface
```

After adding and using, the following example shows how to load a behaviour in a shared library and how to retrieve some of the metadata:

```
julia> b = load("data/libBehaviour.so","Norton", mbv.Tridimensional)
behaviour Norton in shared library data/libBehaviour.so for modelling hypothesis
Tridimensional generated from Norton.mfront using TFEL version: 3.3.0-dev.

julia> get_parameters(b)
11-element StringsVector
 epsilon
 YoungModulus
 PoissonRatio
 ....
julia> get_external_state_variables(b)
1-element VariablesVector
 Temperature
```

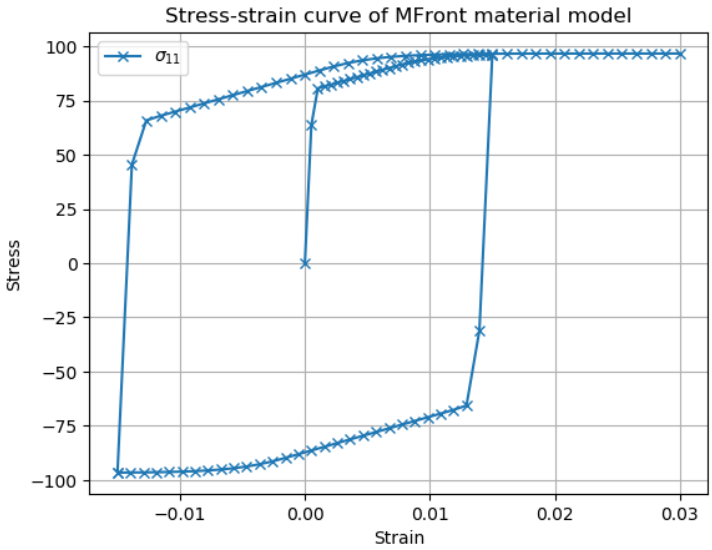

Figure 2: Stress-strain curve of MFront material model calculated with `MFrontInterface.jl`

The `MFrontInterface.jl` package already allows calling the behaviour on one time step. This has been used to build the stress-strain curve depicted in Figure 2 for a simple plastic behaviour following a kinematic hardening rule introduced by Chaboche et al. [13].

Conclusions

This short extended abstract shows the potential of `MFrontInterface.jl` package. Development has started but like all open source projects we would appreciate any kind of contributions gracefully. Next step is to get all modified and created packages registered. This will guarantee a nice user experience.

Acknowledgements

The authors would like to acknowledge the financial support of Business Finland for both ISA Wärtsilä Dnro 7734/31/2018, and ISA VTT Dnro 7980/31/2018 projects. In addition, this research was supported financially by the CEA in the framework of the 'PLEIADES' project.

References

[1] CEA and EDF. MFront Web Site, 2019.

[2] Thomas Helfer, Bruno Michel, Jean-Michel Proix, Maxime Salvo, Jérôme Sercombe, and Michel Casella. Introducing the open-source mfront code generator: Application to mechanical behaviours and material knowledge management within the PLEIADES fuel element modelling platform. *Computers & Mathematics with Applications*, 2015.

[3] Thomas Helfer. The MFrontGenericInterfaceSupport project.

[4] Thomas Helfer. MGIS. original-date: 2018-06-20T12:41:49Z.

[5] Thomas Helfer. A brief introduction to the MGIS C++ library for mechanical behaviours.

[6] Jeff Bezanson, Alan Edelman, Stefan Karpinski, and Viral B Shah. Julia: A fresh approach to numerical computing. *SIAM review*, 59(1):65–98, 2017.

[7] Tero Frondelius and Jukka Aho. JuliaFEM —open source solver for both industrial and academia usage. *Rakenteiden Mekaniikka*, 50(3):229–233, 2017. open access.

[8] Marja Rapo, Jukka Aho, and Tero Frondelius. Natural frequency calculations with JuliaFEM. *Rakenteiden Mekaniikka*, 50(3):300–303, 2017. open access.

[9] Marja Rapo, Jukka Aho, Hannu Koivurova, and Tero Frondelius. Implementing model reduction to the JuliaFEM platform. *Rakenteiden Mekaniikka*, 51(1):36–54, 2018. open access.

[10] Marja Rapo, Joona Vaara, Jukka Aho, Teemu Kuivaniemi, Niclas Liljenfeldt, Antti Vuohijoki, and Tero Frondelius. Pipe route optimization to avoid undesired vibration by using juliaFEM. *Rakenteiden Mekaniikka*, 52(3):177–191, 2019. open access.

[11] Jukka Aho, Ville Jämsä, Teemu Kuivaniemi, Niclas Liljenfeldt, and Tero Frondelius. JuliaFEM beam element implementation. *Rakenteiden Mekaniikka*, 52(3):160–176, 2019. open access.

[12] Jukka Aho, Antti-Jussi Vuotikka, and Tero Frondelius. Introduction to JuliaFEM an open-source fem solver. *Rakenteiden Mekaniikka*, 52(3):148–159, 2019. open access.

[13] J. L. Chaboche, P. Kanouté, and F. Azzouz. Cyclic inelastic constitutive equations and their impact on the fatigue life predictions. *International Journal of Plasticity*, 35:44–66, 2012.

Proceedings of the 32nd Nordic Seminar on Computational Mechanics
A.H. Niemi and H. Koivurova (Eds.)

Modeling of non-coulomb friction under fretting conditions part 2

Jouko Hintikka[1], Antti Mäntylä[1], Tero Frondelius[1]

(1)RD and Engineering, Wärtsilä, P.O.Box 244, 65101 Vaasa, Finland, jouko.hintikka@wartsila.com, antti.mantyla@wartsila.com, tero.frondelius@wartsila.com

Summary. In non-Coulomb friction, tangential force increases when fretting motion approaches its extreme position. Core principle and experimental background of the model was presented in NSCM-29. Here the work was developed further so that the non-Coulomb friction model was upgraded to consists of dissipating and non-dissipating parts. Once the model was ready, it was used to analyse experimental fretting conditions of bolted join fretting apparatus. Model successfully captures the non-Coulomb friction phenomenon; however initial results show that constant Coulomb model produces already good enough results considering resulting slip amplitude and highest tangential tractions.

Key words: Fretting, friction, modeling

Introduction

Fretting has been described as the action of reciprocating surface sliding. It causes fretting fatigue and fretting wear. Friction is typically high in fretting conditions producing high tangential traction and high cyclic surface stresses, which can cause fatigue damage. Surface degradation caused by fretting wear may also accelerate fretting fatigue damage. [1, 2, 3]

Certain materials such as quenched and tempered steel exhibit so called non-Coulomb friction, where the tangential force increases when fretting motion approaches its extreme positions. In fretting experiments the non-Coulomb friction produces 'hook'-shaped fretting loops. In ideal Coulomb friction, tangential force remains at a constant during gross-sliding [4]. Furthermore, the non-Coulomb increase in friction can be substantial, because about 50 % of total tangential force may originate from non-Coulomb friction [5, 6]. Non-Coulomb friction can originate from tangential fretting scar interactions leading to inclined sliding within the fretting interface [5, 6]. Schematic illustration of this is shown in Fig. 1.

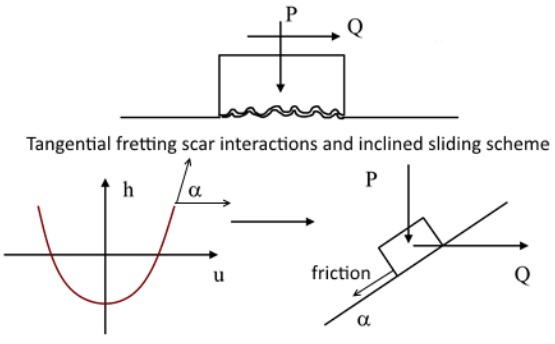

Figure 1. Tangential fretting scar interaction and inclined sliding scheme

Ideal Coulomb friction models are used commonly in analysis of frictional interfaces, both in industrial and academic cases. However, this may lead to inaccuracy if non-Coulomb friction prevails. This study is continuation of the work that was first presented in NSCM-29, where the non-Coulomb friction model was implemented in Abaqus using its FRIC-subroutine [7]. Here the non-Coulomb friction model and the subroutine is updated and used to analyse contact conditions of fretting bolted join test setup presented by Juoksukangas et al [8]. The FE-model of the bolted join cantilever beam fretting conditions was modeled by Mäntylä et al [9] utilizing different kind of subroutine; however the same mesh and loads are re-used in this study.

FRIC-subroutine

The modeling of non-Coulomb friction was done using Abaqus and its FRIC-subroutine, based on penalty friction formulation. FRIC-replaces Abaqus native tangential traction calculation. FRIC enables to formulate friction as a function of contact parameters such as slip amplitude, which may be unknown beforehand. Friction (also COF) is assumed to compose of two parts, dissipating part (COF_d) and non-dissipating part (COF_{nd}). Experiments have shown that the non-Coulomb component of friction increases approximately exponentially as a function of slip per slip amplitude [6, 7]. Because non-Coulomb friction originates from inclined sliding under ideal friction at asperity scale [6], it is assumed here that the angle of inclined sliding (α) varies exponentially as a function of slip (u) and slip amplitude (u_a) according to Eq. 1.

$$\alpha(u, u_a) = \alpha_0 * (u/u_a)^2 \tag{1}$$

In inclined sliding the total resistance against sliding was presented in [6], from which resistance against "up hill" and "down hill" sliding can be derived (Eqs. 2-3):

$$COF_p = (COF_0 * \cos(\alpha) + \sin(\alpha))/(\cos(\alpha) - COF_0 * \sin(\alpha)) \tag{2}$$

$$COF_m = -(COF_0 * \cos(\alpha) - \sin(\alpha))/(\cos(\alpha) + COF_0 * \sin(\alpha)) \tag{3}$$

From Eqs 2-3, dissipating and non-dissipating components of friction can be derived as follows (Eqs. 4-5):

$$COF_d = abs(COF_p - (COF_p + COF_m)/2) \tag{4}$$

$$COF_{nd} = (COF_p + COF_m)/2 \tag{5}$$

All of the frictional dissipation is caused by COF_d, while COF_{nd} is more like elastic spring. In the subroutine COF_0 was given as ideal friction value of 0.3. Angle α_0 was taken from measurements [6] representing quite high angle that is necessary to produce the observed non-Coulomb effect. Used COF_0 and α_0 yield COF_{nd} of about 0.4 in maximum. COF_d was modeled as normal penalty friction being linearly dependent on the value of elastic slip (1 μm), based on standard Abaqus formulation, while COF_{nd} was solely dependent on the u/u_a-ratio. Schematic illustration of these COF components is shown in Fig. 2.

Furthermore, the slip history is recorded in the subroutine so that slip amplitude can be calculated. Basically, the subroutine tracks when slipping reverses. Once a new slip reversal is found, tracking of subsequent slip reversals commences using the recently obtained slip reversal as new origin. Slip is determined to reverse when the slippage starts to reduce. By doing so, a fresh value for slip amplitude is obtained every half cycle. Because slip amplitude can develop during each load cycle and in each nodes, it follows that multiple load cycles needs to be simulated before solution stabilizes.

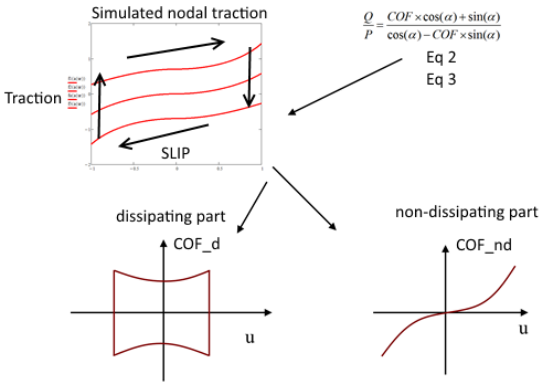

Figure 2. Dissipating and non-dissipating friction components

FE-model and results

The idea of FE-model is shown in Fig. 3, where two beams are bolted together and clamped from the left side. The right end of the beam assembly is reciprocated up and down resulting in fretting in the close proximity of the bolt join. Total of 20 fretting cycles were simulated in each FE-run. Slippage results are also shown in Fig. 3 for used non-Coulomb implementation and constant COF of 0.3 and 0.7 conditions.

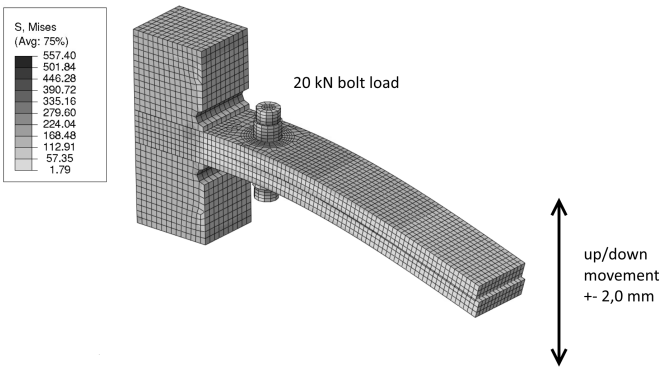

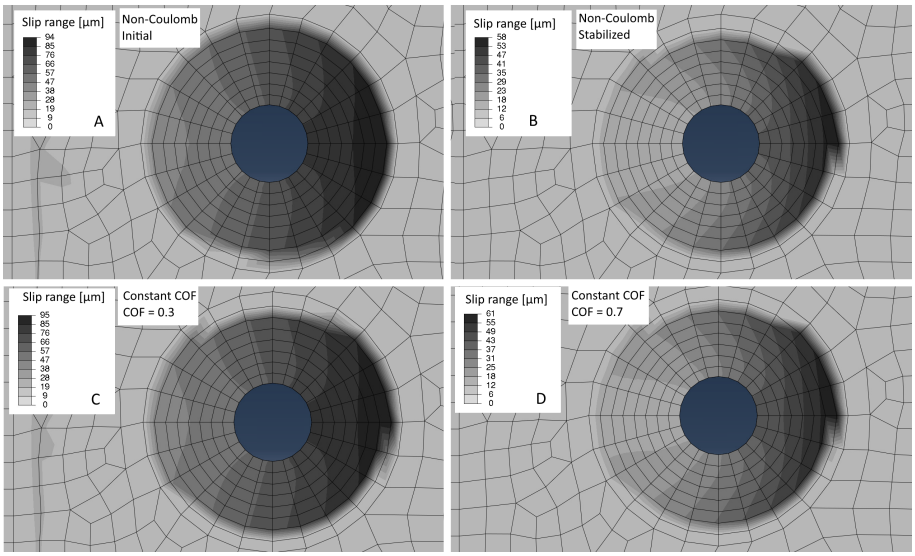

Figure 3. FE-model and slippage results from non-Coulomb (A,B) and ideal friction simulations (C,D)

During the non-Coulomb friction simulation the slippage reduces gradually as shown in Figs. 3A&B. Solution is largely stabilized already after 10 load cycles. Results show that contact slippage in non-Coulomb conditions match closely to constant friction conditions in the beginning of analysis Figs. 3A&C, when non-Coulomb model has not activated yet, and in the end of analysis when non-Coulomb model has fully stabilized 3B&D. In stabilized non-Coulomb conditions, the tangential traction will be identical to constant COF conditions at end of loading steps when the stresses are at maximum because all points exhibit slippage and equivalent COF is nearly the same in both cases. Although stress history may be somewhat different, it is expected that resulting fatigue loads will be very similar between ideal Coulomb and non-Coulomb conditions. Hence it appears to be so that ideal Coulomb model reproduces slippage and stresses of non-Coulomb friction assuming that ideal COF corresponds to maximum of $COF_d + COF_{nd}$ of the non-Coulomb model. This is convenient considering engineering applications because it seems that standard ideal Coulomb assumption is good enough; however, more simulations is required to validate this fully. Results may also depend on used geometry and contact type, and used parameter values.

Acknowledgements

The authors would like to acknowledge the financial support of Business Finland in the form of a research project ISA Wärtsilä Dnro 7734/31/2018.

References

[1] RB Waterhouse. *Fretting corrosion*. Pergamon press, Oxford, ISBN 0 08 16902 3, 1972.

[2] D.A. Hills. *Mechanics of fretting fatigue*. Kluwer Academic Publishers, ISBN 0-7923-2866-3, 1994.

[3] Janne Juoksukangas, Verner Nurmi, Jouko Hintikka, Minnamari Vippola, Arto Lehtovaara, Antti Mäntylä, Joona Vaara, and Tero Frondelius. Characterization of cracks formed in large flat-on-flat fretting contact. *International Journal of Fatigue*, 124:361–370, 2019.

[4] KL Johnson. *Contact Mechanics*. Cambridge University Press, Cambridge, 1985.

[5] D.M. Mulvihill, M.E. Kartal, A.V. Olver, D. Nowell, and D.A. Hills. Investigation of non-coulomb friction behaviour in reciprocating sliding. *Wear*, 271(5):802 – 816, 2011.

[6] Jouko Hintikka, Arto Lehtovaara, and Antti Mäntylä. Normal displacements in non-coulomb friction conditions during fretting. *Tribology International*, 94:633 – 639, 2016.

[7] Jouko Hintikka, Arto Lehtovaara, and Antti Mäntylä. Modeling of non-coulomb friction under fretting conditions. *NSCM29-Conference proceedings (https://research.chalmers.se/publication/244480)*, 2016.

[8] Janne Juoksukangas, Arto Lehtovaara, and Antti Mäntylä. Experimental and numerical investigation of fretting fatigue behavior in bolted joints. *Tribology International*, 103:440 – 448, 2016.

[9] Antti Mäntylä, Jouko Hintikka, Tero Frondelius, Janne Juoksukangas, and Arto Lehtovaara. Prediction of contact condition and surface damage by simulating variable friction coefficient and wear. *ISFF9-Book of abstracts (https://isff9.org/)*, pages 109–110, 2019.

Proceedings of the 32nd Nordic Seminar on Computational Mechanics
A.H. Niemi and H. Koivurova (Eds.)

A Modal System Reduction Procedure for a Flexible Structure with a Flexible Vibration Absorber

Jan Høgsberg

Department of Mechanical Engineering, Technical University of Denmark
DK-2800 Kongens Lyngby, Denmark, jhg@mek.dtu.dk

Summary. Vibration absorbers are common assumed non-flexible with a single vibratory mass directly connected to the structure by a spring-dashpot element [1]. In practical applications the absorber may possess inherent dynamics and with a non-trivial absorber-to-structure connection. A general system reduction procedure is proposed, in which the absorber motion is described relative to the structure displacement for the absorber damper mechanism fully locked. For this transformation of the absorber equations, the corresponding structural eigenvalue problem used for modal expansion corresponds to the system for which the absorber structure is connected to the host structure by rigid damper links. The coupled modal equations are derived and supplemental coupling coefficients are identified, which may be calibrated to take into account the interaction with residual structure and absorber modes. The presentation will illustrate the calibration procedure and its accuracy by numerical examples.

Key words: Structural dynamics, modal analysis, tuned mass dampers, vibration absorbers

Structural equation

Consider a full flexible structure with a tuned vibration absorber attached. The discretized (FE) equations of motion for the combined system can then be written as

$$\mathbf{M}\ddot{\mathbf{q}} + \mathbf{C}\dot{\mathbf{q}} + \mathbf{K}\mathbf{q} = \mathbf{f} \tag{1}$$

in which the displacement vector

$$\mathbf{q} = \begin{bmatrix} \mathbf{u}_s \\ \mathbf{u}_a \end{bmatrix} \tag{2}$$

is conveniently separated into the structural degrees-of-freedom (dofs) in $\mathbf{u}_s$ and the absorber dofs in $\mathbf{u}_a$, whereby the system matrices are separated as

$$\mathbf{M} = \begin{bmatrix} \mathbf{M}_{ss} & \mathbf{M}_{sa} \\ \mathbf{M}_{sa}^T & \mathbf{M}_{aa} \end{bmatrix} \quad , \quad \mathbf{K} = \begin{bmatrix} \mathbf{K}_{ss} & \mathbf{K}_{sa} \\ \mathbf{K}_{sa}^T & \mathbf{K}_{aa} \end{bmatrix} \quad , \quad \mathbf{C} = \begin{bmatrix} \mathbf{C}_{ss} & \mathbf{C}_{sa} \\ \mathbf{C}_{sa}^T & \mathbf{C}_{aa} \end{bmatrix} \tag{3}$$

with symmetric ss and aa block diagonals and the coupling array sa. The external force is assumed to only act only on the structure: $\mathbf{f} = [\mathbf{f}_s^T, \mathbf{0}^T]^T$. The mode shapes used for design and calibration of the vibration absorber are often simply based on the ss-system as

$$\Big(-\omega_{sj}^2 \mathbf{M}_{ss} + \mathbf{K}_{ss} \Big) \mathbf{u}_{sj} = \mathbf{0} \tag{4}$$

for a particular structural vibration mode j with natural frequency ω_{sj} and mode shape vector $\mathbf{u}_{sj}$. However, this straight forward approach might activate other non-resonant modes, when the absorber damper is applied differently than the absorber stiffness. Furthermore, the problem in (4) without absorber is not consistent, as it is not recovered in either of the undamped limits with vanishing or infinite absorber damping.

Relative absorber displacement

To recover an appropriate generalized eigenvalue problem without damping, the absorber damping must be either vanishing or infinite. For vanishing absorber damping, the absorber mass will typically vibrate because of the absorber stiffness. For the infinite absorber damping, the associated rigid damper links will connect the absorber to the structure at the damper locations, for which the absorber might still have residual motion for a flexible absorber with local damper mechanisms. Thus, it is important to redefine the structure as the actual structure plus the residual absorber part that is free to vibrate when the damper connection is fully rigid.

As the absorber displacement is conveniently expressed by its displacement relative to the structural motion for fully locked damper links, the absorber motion will consequently vanish when the absorber damping approaches infinity. This condition implies that the relative absorber displacement is given as

$$\mathbf{v}_a = \mathbf{u}_a + \mathbf{C}_{aa}^{-1}\mathbf{C}_{sa}^T\mathbf{u}_s = \mathbf{u}_a + \mathbf{B}_{sa}^T\mathbf{u}_s \tag{5}$$

introducing the correction array

$$\mathbf{B}_{sa} = \mathbf{C}_{sa}\mathbf{C}_{aa}^{-1} \tag{6}$$

which is independent of the damper magnitude and thus refers to a connectivity or participation array that represents the absorber's damper attachment on the structure.

When eliminating the absolute absorber displacement $\mathbf{u}_a$ by (5), the equation of motion (1) can be written in terms of the relative displacement $\mathbf{v}_a$ as

$$\begin{aligned} \mathbf{m}_{ss}\ddot{\mathbf{u}}_s + \mathbf{c}_{ss}\dot{\mathbf{u}}_s + \mathbf{k}_{ss}\mathbf{u}_s + \mathbf{m}_{sa}\ddot{\mathbf{v}}_a + \mathbf{k}_{sa}\mathbf{v}_a &= \mathbf{f}_s & (7)\\ \mathbf{m}_{aa}\ddot{\mathbf{v}}_a + \mathbf{c}_{aa}\dot{\mathbf{v}}_a + \mathbf{k}_{aa}\mathbf{v}_a + \mathbf{m}_{sa}^T\ddot{\mathbf{u}}_s + \mathbf{k}_{sa}^T\mathbf{u}_s &= \mathbf{0} & (8) \end{aligned}$$

The corrected structural matrices and arrays in (7) and (8) follow from the variable transformation as

$$\begin{aligned} \mathbf{m}_{ss} &= \mathbf{M}_{ss} - \Big(\mathbf{M}_{sa}\mathbf{B}_{sa}^T + \mathbf{B}_{sa}\mathbf{M}_{sa}^T\Big) + \mathbf{B}_{sa}\mathbf{M}_{aa}\mathbf{B}_{sa}^T \\ \mathbf{k}_{ss} &= \mathbf{K}_{ss} - \Big(\mathbf{K}_{sa}\mathbf{B}_{sa}^T + \mathbf{B}_{sa}\mathbf{K}_{sa}^T\Big) + \mathbf{B}_{sa}\mathbf{K}_{aa}\mathbf{B}_{sa}^T \\ \mathbf{c}_{ss} &= \mathbf{C}_{ss} - \Big(\mathbf{C}_{sa}\mathbf{B}_{sa}^T + \mathbf{B}_{sa}\mathbf{C}_{sa}^T\Big) + \mathbf{B}_{sa}\mathbf{C}_{aa}\mathbf{B}_{sa}^T = \mathbf{C}_{ss} - \mathbf{C}_{sa}\mathbf{C}_{aa}^{-1}\mathbf{C}_{sa}^T \end{aligned} \tag{9}$$

while the absorber matrices remain unchanged,

$$\mathbf{m}_{aa} = \mathbf{M}_{aa} \quad , \quad \mathbf{c}_{aa} = \mathbf{C}_{aa} \quad , \quad \mathbf{k}_{aa} = \mathbf{K}_{aa} \tag{10}$$

The two coupling arrays in (7)-(8) are corrected by the absorber matrices

$$\begin{aligned} \mathbf{m}_{sa} &= \mathbf{M}_{sa} - \mathbf{B}_{sa}\mathbf{M}_{aa} \\ \mathbf{k}_{sa} &= \mathbf{K}_{sa} - \mathbf{B}_{sa}\mathbf{K}_{aa} \end{aligned} \tag{11}$$

while the damping coupling array $\mathbf{c}_{sa} = \mathbf{0}$ vanishes because $\mathbf{v}_a$ in (5) is specifically introduced as the relative absorber motion with respect to the absorber damping attachment.

The correction $\mathbf{C}_{sa}\mathbf{C}_{aa}^{-1}\mathbf{C}_{sa}^T$ in the expression for $\mathbf{c}_{ss}$ in (9) implies that for most calibration purposes, the structural damping matrix $\mathbf{c}_{ss} \simeq \mathbf{0}$, only leaving absorber damping via the matrix $\mathbf{c}_{aa}$ in (8). This simplifies the subsequent absorber tuning.

Modal representation and equations

As explained previously a consistent modal expansion assumes infinite absorber damping, which corresponds to $\mathbf{v}_a \to 0$ in (7)-(8). This recovers the two eigenvalue problems

$$\big(\mathbf{k}_{ss} - \omega_s^2\mathbf{m}_{ss}\big)\bar{\mathbf{u}}_s = \mathbf{0} \quad , \quad \big(\mathbf{k}_{aa} - \omega_a^2\mathbf{m}_{aa}\big)\bar{\mathbf{v}}_a = \mathbf{0} \tag{12}$$

for the structure and absorber, respectively. Thus, the motion of the structure and absorber are expressed by the modal representations in terms of the mode shape vectors in (12),

$$\mathbf{u}_s = \sum_{s=1}^{n_s} \bar{\mathbf{u}}_s p_s \qquad , \qquad \mathbf{v}_a = \sum_{a=1}^{n_a} \bar{\mathbf{v}}_a r_a \tag{13}$$

in which p_s and r_a are the modal coordinates for the structure and absorber modes, respectively.

The modal expansions are substituted into the equations of motion (7) and (8). When the structure equation is pre-multiplied with $\bar{\mathbf{u}}_s^T$ and the corresponding absorber equation by $\bar{\mathbf{v}}_a^T$, the modal equations can upon use of the orthogonality relations from (12) be expressed as

$$m_{jj}^{ss}\ddot{p}_j + \sum_{s=1}^{N_s} c_{js}^{ss}\dot{p}_s + k_{jj}^{ss}p_j + \sum_{k=1}^{N_a} m_{jk}^{sa}\ddot{r}_k + \sum_{k=1}^{N_a} k_{jk}^{sa}r_k \;=\; f_j \tag{14}$$

$$m_{kk}^{aa}\ddot{r}_k + \sum_{a=1}^{N_a} c_{ka}^{aa}\dot{r}_a + k_{kk}^{aa}r_k + \sum_{j=1}^{N_s} m_{kj}^{sa}\ddot{p}_j + \sum_{j=1}^{N_s} k_{kj}^{sa}p_j \;=\; 0 \tag{15}$$

with index $j = 1, 2, \ldots, N_s \leq n_s$ and $k = 1, 2, \ldots, N_a \leq n_a$ representing the number of modes included. The modal mass and stiffness are given as

$$m_{jj}^{ss} = \bar{\mathbf{u}}_j^T \mathbf{m}_{ss} \bar{\mathbf{u}}_j \quad , \quad k_{jj}^{ss} = \bar{\mathbf{u}}_j^T \mathbf{k}_{ss} \bar{\mathbf{u}}_j \quad , \quad m_{kk}^{aa} = \bar{\mathbf{v}}_k^T \mathbf{m}_{aa} \bar{\mathbf{v}}_k \quad , \quad m_{kk}^{aa} = \bar{\mathbf{v}}_k^T \mathbf{k}_{aa} \bar{\mathbf{v}}_k \tag{16}$$

while the corresponding damping coefficients are

$$c_{js}^{ss} = \bar{\mathbf{u}}_j^T \mathbf{c}_{ss} \bar{\mathbf{u}}_s \quad , \quad c_{ka}^{aa} = \bar{\mathbf{v}}_k^T \mathbf{c}_{aa} \bar{\mathbf{v}}_a \tag{17}$$

The coupling coefficients are finally determined by similar expressions,

$$m_{ja}^{sa} = \bar{\mathbf{u}}_j^T \mathbf{m}_{sa} \bar{\mathbf{v}}_a \quad , \quad k_{ja}^{sa} = \bar{\mathbf{u}}_j^T \mathbf{k}_{sa} \bar{\mathbf{v}}_a \quad , \quad m_{ks}^{sa} = \bar{\mathbf{v}}_k^T \mathbf{m}_{sa}^T \bar{\mathbf{u}}_s \quad , \quad k_{ks}^{sa} = \bar{\mathbf{v}}_k^T \mathbf{k}_{sa}^T \bar{\mathbf{u}}_s \tag{18}$$

Absorber calibration

In the present case only a single absorber mode $N_a = 1$ is assumed, thus neglecting any damping coupling with other absorber modes. The structural motion is furthermore omitted, whereby $c_{js}^{ss} = 0$. In the frequency domain, the modal equations then reduce to

$$(-\omega^2 m_{jj}^{ss} + k_{jj}^{ss})p_j + (-\omega^2 m_{j1}^{sa} + k_{j1}^{sa})r_1 \;=\; f_j \tag{19}$$

$$(-\omega^2 m_{11}^{aa} + i\omega c_{11}^{aa} + k_{11}^{aa})r_1 + (-\omega^2 m_{1r}^{sa} + k_{1r}^{sa})p_r \;=\; 0 \tag{20}$$

in which the coupling with other structure modes has been neglected as well. This leaves the modal equations in (19)-(20) for damping of vibration mode $j = r$. The equations are conveniently normalized by the modal structure stiffness k_{rr}^{ss}, which gives

$$(-\xi^2 + 1)p + (-\xi^2\mu_* + \kappa_*)r \;=\; f \tag{21}$$

$$(-\xi^2\mu + i\xi\beta + \kappa)r + (-\xi^2\mu_* + \kappa_*)p \;=\; 0 \tag{22}$$

in which $p = p_r$ and $r = r_1$ to simplify the notation. The non-dimensional frequency is defined as

$$\xi = \omega\sqrt{\frac{m_{11}^{ss}}{k_{rr}^{ss}}} \tag{23}$$

while the absorber mass, stiffness and damper ratios are introduced as

$$\mu = \frac{m_{11}^{aa}}{m_{rr}^{ss}} \qquad , \qquad \kappa = \frac{k_{11}^{aa}}{k_{rr}^{ss}} \qquad , \qquad \beta = \frac{c_{11}^{aa}}{\sqrt{m_{rr}^{ss}k_{rr}^{ss}}} \tag{24}$$

with the two coupling ratios given similarly as

$$\mu_* = \frac{m_{r1}^{sa}}{m_{rr}^{ss}} \qquad , \qquad \kappa_* = \frac{k_{r1}^{sa}}{k_{rr}^{ss}} \tag{25}$$

Hereby the modal system of equations contain five absorber parameters, two more than for the classic absorber format [2]. These supplemental coupling ratios μ_* and κ_* may be chosen to represent the modal interaction with other structure and absorber modes, [3]. The characteristic equation can be written as

$$(\mu - \mu_*^2)\xi^4 - \xi^2(\kappa + \mu - 2\mu_*\kappa_*) + \kappa - \kappa_* + i\xi\beta(-\xi^2 + 1) = 0 \tag{26}$$

which recovers the classic equation for the tuned mass absorber when $\mu_* = \mu$ and $\kappa_* = 0$. It may be verified that for an infinite damper ratio $\beta \to \infty$, the characteristic equation recovers the correct solution $\xi = 1$. The equal modal calibration from [2, 4] then leads to the following optimality conditions

$$\kappa = \mu - \mu_*^2 + \kappa_* \qquad , \qquad \beta = \sqrt{2(\mu_*^2 + \kappa_*(1 - 2\mu_*))(\mu - \mu_*^2)} \tag{27}$$

which depends on the coupling ratios μ_* and κ_*.

Results

The presentation will demonstrate the calibration procedure for the present absorber format. Initially the two coupling ratios μ_* and κ_* are tuned so that the characteristic equation (26) matches the correct two natural frequency ratios ξ_A and ξ_B associated with $\beta = 0$, obtained by solving the full flexible FE problem. Subsequently the actual absorber stiffness ratio κ and damper ratio β are calibrated from (27) for a given mass ratio μ. Because the coupling coefficients are properly adjusted with respect to the flexible vibration absorber placed on a flexible structure, the accuracy of the present procedure is illustrated by a numerical example.

References

[1] J.P. Den Hartog, *Mechanical Vibrations* (4th edn). McGraw-Hill, New York (Reprint by Dover, New York, 1985), 1956. ISBN 10: 0486647854.

[2] S. Krenk, "Frequency analysis of the tuned mass damper," *Journal of Applied Mechanics*, vol. 72, pp. 936-942, 2005. DOI: 10.1115/1.2062867.

[3] S. Krenk and J. Høgsberg, "Tuned resonant mass or inerter-based absorbers: unified calibration with quasi-dynamic flexibility and inertia correction," *Proceedings of the Royal Society A - Mathematical, Physical and Engineering Sciences*, vol. 472, paper no. 20150718 (23pp), 2016. DOI: 10.1098/rspa.2015.0718.

[4] S. Krenk and J. Høgsberg, "Equal modal damping design for a family of resonant vibration control formats," *Journal of Vibration and Control*, vol. 19, pp. 1294-1315, 2013. DOI: 10.1177/1077546312446796.

Proceedings of the 32nd Nordic Seminar on Computational Mechanics
A.H. Niemi and H. Koivurova (Eds.)

JuliaFEM geometry optimization

Jouni Huopana[1], Taneli Rantakivi[1], Miikka Väntänen[1], Antti-Jussi Vuotikka[1], Antti Tanskanen[2], Joona Vaara[3], Siiri Sikkilä[4] and Tero Frondelius[3,4]

(1) Global Boiler Works Oy, Lumijoentie 8, 90400, Oulu, Finland
jouni.huopana@gbw.fi, taneli.rantakivi@gbw.fi, miikka.vantanen@gbw.fi, antti-jussi.vuotikka@gbw.fi
(2) VTT Technical Research Centre of Finland Ltd, Kaitoväylä 1, 90571 Oulu, Finland, antti.tanskanen@vtt.fi
(3) Wärtsilä, Järvikatu 2-4, 65100 Vaasa, Finland, joona.vaara@wartsila.com, tero.frondelius@wartsila.com
(4) University of Oulu, Pentti Kaiteran katu 1, 90570, Finland, siiri.sikkila@oulu.fi, tero.frondelius@oulu.fi

Summary. This article presents a geometrical optimization with JuliaFEM and Gmsh. The structure of the optimization loop and chosen methods and approaches are described and discussed. An eigenfrequency optimization example case with two different geometrical bars is shown. Results demonstrate that JuliaFEM and Gmsh provide a useful and fast platform for geometrical optimization.

Keywords: JuliaFEM, Gmsh, optimization, eigenfrequency analysis

Introduction

JuliaFEM is a free, open-source finite element solver that enables users to efficiently simulate mechanical systems with speed and accuracy [1]. When using JuliaFEM with tools like Gmsh, it is possible to create parametric geometries and mesh through Julia. Gmsh is a free tool for 3D finite element mesh generation. It can be used to generate a CAD geometry and includes some post-processing possibilities. Gmsh is designed for efficient and parametric geometry creation. Gmsh itself has also solver, but in this case, JuliaFEM is used instead. Gmsh also has a graphical user interface and script files, but it can also be used efficiently through C++, C, Python, and Julia API. [2]

Used together, JuliaFEM and Gmsh, enables the user to create, iterate, and optimize geometrical forms fast. Created geometry, based upon input parameters, is generated and simulated inside the optimization loop. Depending on the design, input parameters are set and limited to a range which creates a realistic shape. The maximum number of parameters is not clearly defined, but keeping the number relatively small helps to observe more apparent changes in the goal parameters. In this text, a model is created to optimize two simple geometrical bars,

shown in Figure 1, to match their eigenfrequencies to a specific range. JuliaFEM has been previously shown to be a reliable solver for eigenfrequency problems [3].

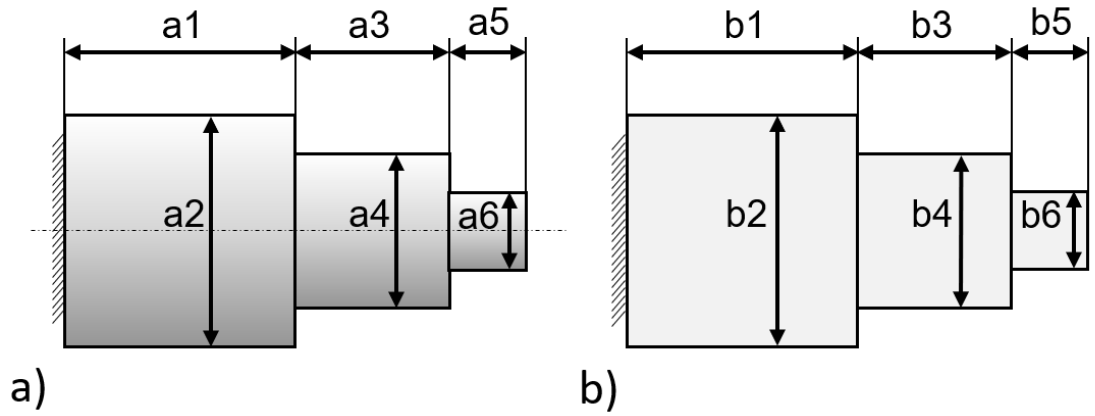

Figure 1. Bar geometry with a) circular and with b) square cross-section.

Material and Methods

In a geometrical shape optimization case, it is essential to set appropriate boundary conditions for the input parameters. Input parameters should always produce a valid geometry. In simple terms, this means that for example, you should limit the hole diameter inside the bar to be smaller than the bar diameter. It is also possible to chain these parameters together to have more robust geometrical input. After the input data is defined the geometry itself is formed. In this case, this is was done with Gmsh. Gmsh has its parametric geometry generation tools that use simple parametric inputs to generate different geometrical options. These include basic shapes, features, and operations, such as solids, fillets, and Boolean operations. Gmsh has its visualization option, which is useful when first creating a valid geometry. With the boundary conditions applied, it is possible to generate an input geometry and a good quality mesh quickly.

Mesh is saved as an external file to ensure documentation, but it is also conceivable to use the created mesh directly in JuliaFEM, without the need for external files. However, this was not implemented in this test but could be considered as a possible further development.

Julia optimization toolbox contains a wide variety of optimization algorithms. They are roughly divided into two categories based on the requirement of function derivative. Most conventional algorithms are based on the known change of the optimized function. In this case, the result of the optimization is obtained through simulation. It is not feasible to estimate the derivative of the object in question but to consider the problem as derivative-free. Julia's JuMP package includes many optimization solvers and problem classes [4]. In this case, a derivate free optimization is used, namely COBYLA, (Constrained optimization by linear approximation). COBYLA is a numerical optimization method for constrained problems where the derivative of the objective function is not known, invented by Michael J. D. Powell. The algorithm iteratively approximates the actual problem with linear models. An approximate linear programming problem is solved during the iteration, and the possible optimal solution is achieved. This solution is evaluated using the original objective and constraint functions. This creates a new point in the optimization space. Based on this solution, the new iteration is made, and progress on the solution is checked. If the solution converges to a specific value or when the number of

maximum iterations is reached, the final solution is given [5] The structure of the optimization loop is shown in Table 1.

Table 1. Steps in optimization loop.

Step	Action
1	Generate input parameters for optimisation algorithm.
2	Create geometry based on inputs.
3	Mesh geometry (and export).
4	Read mesh into JuliaFEM.
5	Create JuliaFEM model.
6	Solve JuliaFEM Model.
7	Return result to the optimization algorithm.

Results and discussion

The result of the optimization shows that it is possible to quickly iterate through several possible parameters sets and find optimized results. Example result shown in Figure 2. A single iteration step takes only a few minutes. In this case, the created model had multiple local minima. The effect of this was observed by the sensitivity for the starting parameters. By selecting suitable parameters, it was possible to obtain an optimized solution.

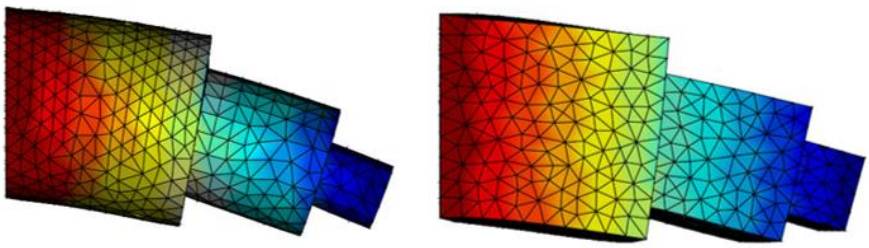

Figure 2. Examples of both bars first eigenmode.

Acknowledgements

This work was supported by Business Finland trough the ISA (Intelligent Steel Applications) Project, ISA GBW 7752/31/18, ISA VTT 7980/31/18, ISA Wärtsilä 7734/31/18, ISA University of Oulu 7537/31/18.

References

[1] T. Frondelius and J. Aho, *JuliaFEM — open source solver for both industrial and academia usage,* Rakenteiden Mekaniikka, Vol. 50, pp. 229-233, 2017.

[2] C. Geuzaine and J.-F. Remacle, *Gmsh: a three-dimensional finite element mesh generator with built-in pre- and post-processing facilities*, International Journal for Numerical Methods in Engineering 79(11), pp. 1309-1331, 2009.

[3] M. Rapo, J. Aho and T. Frondelius, *Natural frequency calculations with JuliaFEM,* Rakenteiden Mekaniikka, Vol. 50, pp. 300-303, 2017.

[4] I. Dunning, J. Huchette, M. Lubin, *JuMP: A modeling language for mathematical optimization,* SIAM Review, Vol. 59, pp. 295-320, SIAM, 2017.

[5] M. J. D. Powell, *A view of algorithms for optimization without derivatives,* Cambridge University Technical Report, DAMTP, 2007.

Proceedings of the 32nd Nordic Seminar on Computational Mechanics
A.H. Niemi and H. Koivurova (Eds.)

Inelastic buckling of plates subjected to multi axial in-plane loads

Alireza Jahanpour[1, 2] and Reijo Kouhia[1]

(1) Tampere University, alireza.jahanpour@tuni.fi, reijo.kouhia@tuni.fi
(2) Malayer University, a.jahanpour@malayeru.ac.ir

Summary. During inelastic buckling and according to the deformation theory of plasticity, Poisson's ratio varies in the elastoplastic region of stress-strain curve as well as the other parameters such as secant modulus and strains. In this study, the inelastic buckling equation of plate are perfectly developed due to variation of Poisson's ratio when the plate is subjected to multi axial loads. Using generalized integral transform, this equation is solved for simply supported plate and the results is compared with those in which Poisson's ratio is ½ (the incompressible value for isotropic materials). The results show that the inelastic buckling loads is generally decrease and for thicker plate, the differences significantly decrease.

Key words: inelastic buckling, deformation theory, Poisson's ratio, Ramberg-Osgood curve

Introduction

Deformation theory of plasticity and Incremental theory of plasticity are two main theories to describe inelastic buckling of plates. In deformation theory of plasticity, the total strain is related to the total stress by the secant modulus [1] and variations of strains and stresses during buckling are used to develop inelastic buckling equation of plate. In the previous studies, it is supposed that in the nonlinear (elastoplastic) region of stress-strain curve, the material is incompressible and then, Poisson's ratio is always ½ (for isotropic materials). As a result, the variation was being only applied on the strains and secant modulus in the stress-strain relations (Hook's low) [2]. For a nonlinear stress-strain curve such as the Ramberg-Osgood representation [3], Poisson's ratio changes from the elastic value to the incompressible value of ½ as the stress is increased above the yield stress [4]:

$$\nu = \frac{1}{2} - \frac{E_{sec}}{E}\left(\frac{1}{2} - \nu_e\right) \tag{1}$$

where E is the Young's modulus, E_{sec} is the secant modulus and ν_e is the elastic value of Poisson's ratio. Then, it is necessary to apply variation to Poisson's ratio as well as the other parameters. Recently, variation of Poisson's ratio has been applied and some imperfect equations have been developed for inelastic buckling of plates [1].

In this paper, using J_2 deformation theory of plasticity [1] and applying variation to all mechanical properties, the perfect equation for inelastic buckling of plates under multi axial

stresses is developed. Using generalized integral transform method [5], the equation is solved for simply supported plate and effect of variation of Poisson's ratio on the inelastic buckling load is compared with those of previous studies.

The inelastic buckling of plate

Figure 1 shows a rectangular plate with $a \times b \times t$ dimensions under biaxial and shear stresses. Using the stress-strain relations, with general nonlinear materials properties, E_{sec} and ν (Eq. 2) and applying variations on them, Eq. (3) will be obtained which shows the moment-curvature relations.

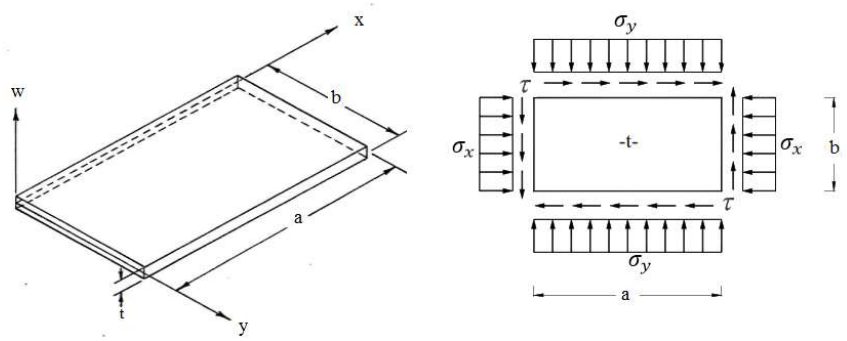

Figure 1. A simply supported plate subjected to multi axial stresses.

$$\begin{aligned} \sigma_x &= \frac{E_{sec}}{1-\nu^2}(\varepsilon_x + \nu\varepsilon_y) \\ \sigma_y &= \frac{E_{sec}}{1-\nu^2}(\varepsilon_y + \nu\varepsilon_x) \\ \tau &= \frac{E_{sec}}{2(1+\nu)}\gamma \end{aligned} \tag{2}$$

$$\begin{bmatrix} \delta M_x \\ \delta M_y \\ \delta M_{xy} \end{bmatrix} = \frac{E_{sec}t^3}{12(1-\nu^2)} \begin{bmatrix} D_{11} & D_{12} & D_{13} \\ D_{12} & D_{22} & D_{23} \\ D_{13} & D_{23} & D_{33} \end{bmatrix} \begin{bmatrix} \delta\varepsilon_x \\ \delta\varepsilon_y \\ \delta\gamma \end{bmatrix} \tag{3}$$

where $\delta\varepsilon_x = \frac{\partial^2(\delta w)}{\partial x^2}$, $\delta\varepsilon_y = \frac{\partial^2(\delta w)}{\partial y^2}$, $\delta\gamma = 2\frac{\partial^2(\delta w)}{\partial x \partial y}$ (δw is variation of plate deflection in z direction) and

$$\begin{aligned} D_{11} &= 1 - \frac{K}{4(1-\nu^2)}\left[(2-\nu)\sigma_x - (1-2\nu)\sigma_y\right]^2 \\ D_{12} &= \nu - \frac{K}{4(1-\nu^2)}\left[(2-\nu)\sigma_x - (1-2\nu)\sigma_y\right]\left[(2-\nu)\sigma_y - (1-2\nu)\sigma_x\right] \\ D_{13} &= -\frac{3K\tau}{4(1+\nu)}\left[(2-\nu)\sigma_x - (1-2\nu)\sigma_y\right] \end{aligned} \tag{4}$$

$$D_{22} = 1 - \frac{K}{4(1-\nu^2)}\left[(2-\nu)\sigma_y - (1-2\nu)\sigma_x\right]^2$$

$$D_{23} = -\frac{3K\tau}{4(1+\nu)}\left[(2-\nu)\sigma_y - (1-2\nu)\sigma_x\right]$$

$$D_{33} = \frac{1-\nu}{2}\left[1 - \frac{9K\tau^2}{2(1+\nu)}\right]$$

In Eqs. (4), $K = \frac{1}{\sigma_i^2 H}\left(1 - \frac{E_{tan}}{E_{sec}}\right)$ where $\sigma_i = \sqrt{\sigma_x^2 - \sigma_x\sigma_y + \sigma_y^2 + 3\tau^2}$,

$$H = 1 - \frac{E_{sec}}{E}\frac{1-2\nu_e}{2(1-\nu^2)}\left(1 - \frac{E_{tan}}{E_{sec}}\right)\left\{2\nu - \frac{1}{2\sigma_i^2}\left[(1+2\nu)\left(\sigma_x^2+\sigma_y^2\right) - 2(2+\nu)\sigma_x\sigma_y + 6(1+\nu)\tau^2\right]\right\} \quad (5)$$

and E_{tan} is the tangent modulus. Eqs. (4) show that as expected, the bending stiffness matrix (Eq. 3) is symmetric.

Substituting Eqs. (3) in the plate equation of equilibrium [6], the inelastic buckling equation of plates will be obtained:

$$D_{11}\frac{\partial^4(\delta w)}{\partial x^4} + 4D_{13}\frac{\partial^4(\delta w)}{\partial x^3\partial y} + 2(D_{12}+2D_{33})\frac{\partial^4(\delta w)}{\partial x^2\partial y^2} + 4D_{23}\frac{\partial^4(\delta w)}{\partial x\partial y^3} + D_{22}\frac{\partial^4(\delta w)}{\partial y^4} + \frac{12(1-\nu^2)}{E_{sec}t^2}\left[\sigma_x\frac{\partial^2(\delta w)}{\partial x^2} + 2\tau\frac{\partial^2(\delta w)}{\partial x\partial y} + \sigma_y\frac{\partial^2(\delta w)}{\partial y^2}\right] = 0 \quad (6)$$

The results and discussion

The generalized integral transform method can be used to solve Eq. (6) and obtain the buckling stresses in the different modes [5]. Table 1 shows the buckling stresses of plates that have been already considered in Ref. [7]. In these examples, a=b=20 in. and the Ramberg-Osgood curve model are used with $E = 10^7$psi, $\sigma_{0.7} = 10^5$ psi and n=10. In Ref. [7], Poisson's ratio is always supposed to be ½ and a finite element method has been used to find the buckling load. In Eq. (6), $\nu_e = 0.3$ and ν is obtained from Eq. (1). Table 1 shows three load cases: uniaxial, biaxial and shear loadings. To validate the analytical method with those of finite element method [7], the buckling stresses are obtained again when $\nu = 0.5$ as shown in Table 1.

The results show that due to variation of Poisson's ratio, in both uniaxial and shear loadings the inelastic buckling loads decrease, although increasing the plate thickness, decreasing the differences. However, for biaxial loading and thicker plates, the inelastic buckling load is overestimated, while the differences is not significant similar to the previous load cases.

Table 1. Buckling stress of simply supported plate under three load cases

Thickness (in.)	Critical Stress (psi)			Diff. (%)	Thickness (in.)	Critical Stress (psi)			Diff. (%)
	Present		[7]			Present		[7]	
	$\nu < 0.5$	$\nu = 0.5$				$\nu < 0.5$	$\nu = 0.5$		
$\sigma_x \neq 0, \sigma_y = \tau = 0$					$\sigma_y = \sigma_x, \tau = 0$				
0.77867	54610	65000	65000	16	1.12500	56482	65000	65000	13.1
0.85800	65405	75000	75000	12.8	1.29980	70218	75000	75000	6.4
0.96449	78124	85000	85000	8	1.60231	83657	85000	85000	1.6
1.12019	90991	95000	95000	4.2	2.08258	95162	95000	95000	0.17
1.36678	102903	105000	105000	2	2.77755	105550	105000	105000	0.52
1.76752	113907	115000	115000	0.95	3.78569	115462	115000	115000	0.4
2.39053	124413	125000	125000	0.47	5.26002	125298	125000	125000	0.24
$\sigma_x = \sigma_y = 0, \tau \neq 0$									
0.4	33288	39336	39414	15.5	0.6	52635	56565	56604	7
0.5	45275	50251	50313	10	0.7	57910	60760	60792	4.7

Conclusion

Applying variation to Poisson's ratio, an analytical method is developed to obtain inelastic buckling load of simply supported plate subjected to multi axial loads. The results show that the buckling load usually decreases if the variation of Poisson's ratio is considered, although increasing the plate thickness, decreasing the differences for all loading cases.

References

[1] R.M. Jones, *Deformation Theory of Plasticity*, Bull Ridge Publishing, 2009.

[2] E.Z. Stowell, A unified theory of plastic buckling of columns and plates, NACA, TN 1556, 1948.

[3] W. Ramberg & W. R. Osgood, Description of stress-strain curves by three parameters, NACA, TN 902, 1943.

[4] G. Gerard & S. Wildhorn, A study of Poisson's ratio in the yield region, NACA, TN 2561, 1952.

[5] S. Ullah, Y. Zhong & J. Zhang, Analytical buckling solutions of rectangular thin plates by straightforward generalized integral transform method, *International Journal of Mechanical Sciences*, 152:535-544, 2019.

[6] S.P. Timoshenko & J.M. Gere, *Theory of Elastic Stability*, McGraw-Hill, Second Edition, 1963.

[7] A. Pifko & G. Isakson, A finite-element method for the plastic buckling analysis of plates, *AIAA Journal*, 7:1950-1957, 1969.

Proceedings of the 32nd Nordic Seminar on Computational Mechanics
A.H. Niemi and H. Koivurova (Eds.)

A new material contrast model for use in topology optimization of steady-state dynamic problems

Jakob S. Jensen

Department of Mechanical Engineering, Technical University of Denmark, jsj@mek.dtu.dk

Summary. Gradient- and density-based topology optimization algorithms for steady-state dynamic problems in acoustics or structural vibrations involve the definition of artificial material parameters in hard scattering or void regions. In this paper, a new model is proposed that remedies some observed problems with existing models.

Key words: Fictitious domain, topology optimization, diffusion equation

Introduction

Gradient- and density-based topology optimization inherently involve the definition of one or more artificial material parameters in hard scattering or void regions (fictitious domains). For static structural problems an artificial low stiffness is assigned to void regions in order to avoid a singular stiffness matrix. Generally, the choice of this minimum value is trivial and results regarding the accuracy of the corresponding solution has been provided [1].

Dynamic problems such as in acoustics, elastic wave propagation and steady-state structural vibrations involve a second material parameter (eg. mass density). The effect of the choice of the corresponding value in the fictitious domain is non-trivial and less studied, eg. [2] discusses the occurrence of low frequency structural resonances in the void region for structural vibration problems and [3] discuss similar issues for acoustic wave propagation problems.

Here, we present a new model based on the transition from the wave equation to the diffusion equation in the fictitious domain. The model is developed using a 1D simplified model and will be extended for topology optimization problem is forthcoming works.

A 1D model

We consider a 1D model for wave propagation as illustrated in Fig. 1. with wave propagation modelled by the general one-dimensional wave equation:

$$(Au')' + \omega^2 Bu = 0, \tag{1}$$

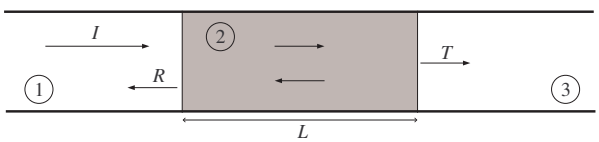

Figure 1. A 1D wave propagation example. I is an incoming (plane) wave, R is the wave reflected at the interface to the inclusion and T is the wave transmitted through the inclusion.

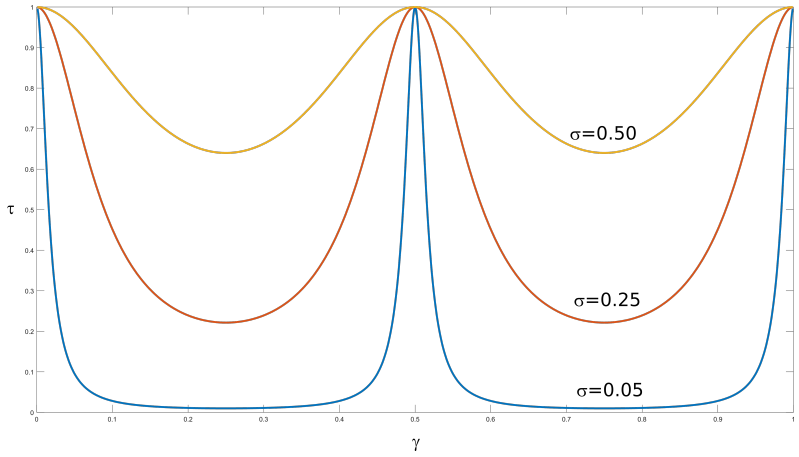

Figure 2. Wave transmission coefficient $\tau = |t|^2$ shown vs. wavenumber parameter $\gamma = \omega L/(2\pi c_{\text{inc}})$ for different values of the impedance contrast parameter $\sigma = \sqrt{A_{\text{inc}}B_{\text{inc}}/(AB)}$.

in which ω is the wave frequency and A and B are generalized material parameters. We consider the reflection and transmission of an incident wave (I) by an inclusion (shaded gray) of length L. Both ends of the domain are considered open. In domain 1 the wave motion is specified by:

$$u_1(x) = e^{-i\frac{\omega}{c}x} + re^{i\frac{\omega}{c}x}, \tag{2}$$

in which $c = \sqrt{A/B}$ is the wave speed. The first part represents the incoming wave (of unit magnitude) and the second part represents the reflected wave with (complex) reflection factor r. In domain 3 we have the transmitted wave:

$$u_3(x) = te^{-i\frac{\omega}{c}x}, \tag{3}$$

where t is the (complex) transmission factor.

The standard inclusion model

In standard models the two material parameter inside the inclusion domain, denoted A_{inc} and B_{inc}, are chosen as sufficiently large parameters. In Fig. 2 we show the resulting transmission coefficient $\tau = |t|^2$ plotted versus the non-dimensional wavenumber parameter $\gamma = \omega L/(2\pi c_{\text{inc}})$ for different values of the impedance contrast parameter $\sigma = \sqrt{A_{\text{inc}}B_{\text{inc}}/(AB)}$. The resonance effect discussed extensively in [3] is noted from the figure for $\gamma = 1/2$ (and multiples hereof). As also suggested in [3] this problem can be effectively avoided by tailoring the value of γ by modifying the ratio between A_{inc} and B_{inc} (thus changing the wave speed within the inclusion $c_{\text{inc}} = \sqrt{A_{\text{inc}}/B_{\text{inc}}}$).

Here, the main focus is on another problematic issue with the existing model which is illustrated in Fig. 3. Here, we plot the wave field within the 1D domain with the inclusion spanning the x-axis from 0.2 to 0.8. Left column shows results for a low frequency wave and right column plots are for a wave of higher frequency. The top row is for $\gamma = 0.05$ and bottom row for $\gamma = 0.25$. Additionally, all plots include results for two different values of the impedance contrast.

Noteworthy is that regardless of the value of the contrast parameter, frequency and γ parameter chosen there will always exist a finite wave field inside the inclusion. The wave amplitude decays, at most, linearly as seen in the top row figures for the high value of σ. Thus, with the traditional model we have little flexibility to control of the field level present in the inclusion.

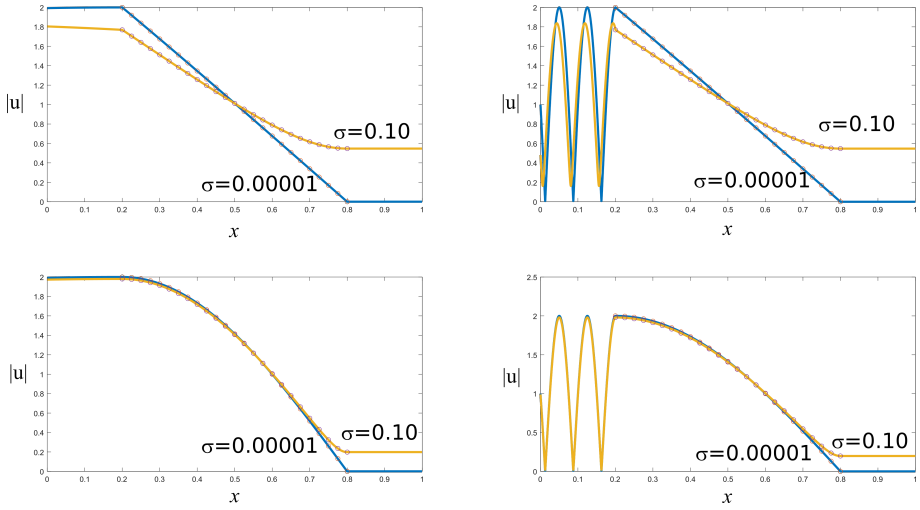

Figure 3. Wave amplitude vs. position in the domain with the inclusion spanning the x-axis from 0.2 to 0.8. Left column: low frequency wave, right column: high frequency wave. Top row: $\gamma = 0.05$, bottom row: $\gamma = 0.25$.

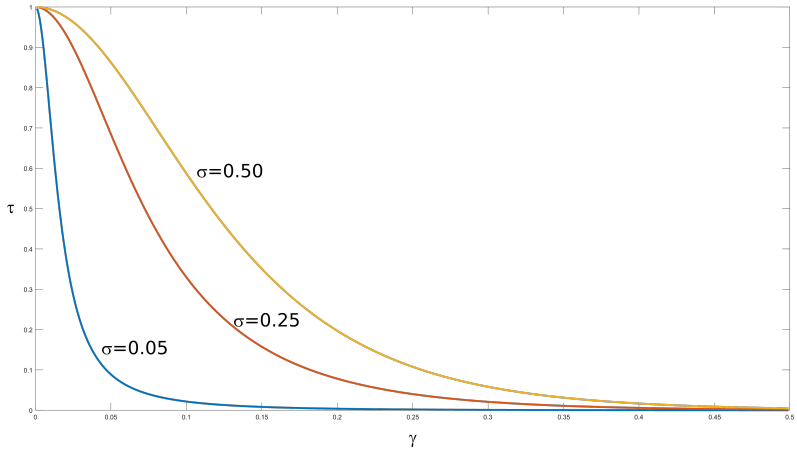

Figure 4. Wave transmission coefficient $\tau = |t|^2$ shown vs. wavenumber $\gamma = \omega L/(2\pi c_{\text{inc}})$ for different values of the material contrast parameter $\sigma = \sqrt{A_{\text{inc}} B_{\text{inc}}/(AB)}$.

The proposed model

In order to avoid the limitations of the existing model, we propose to model the inclusion domain using the diffusion equation rather that the wave equation:

$$(A_{\text{inc}} u')' - \omega^2 B_{\text{inc}} u = 0, \tag{4}$$

which provides a solution of the form

$$u_2(x) = a e^{-\frac{\omega}{c_{\text{inc}}} x} + b e^{\frac{\omega}{c_{\text{inc}}} x}, \tag{5}$$

ie. in the form of an exponential decaying and growing term.

In Fig. 4 we see the corresponding plot of the transmission coefficient τ. We note that the new model effectively eliminates the resonance problem. The transmission decays smoothly when increasing the wavenumber parameter γ and also when increasing the impedance contrast parameter σ.

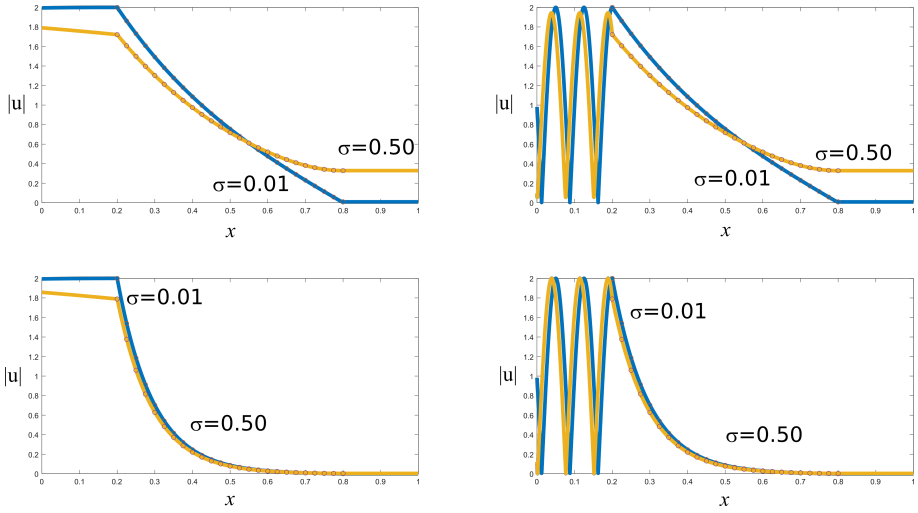

Figure 5. Wave amplitude vs. position in the domain with the inclusion spanning the region from 0.2 to 0.8. Top row: $\gamma = 0.25$, bottom row: $\gamma = 1.0$.

More importantly, Fig. 5 shows the corresponding amplitude field. It is now seen that the proposed model offers an effective way of controlling the decay of the amplitude inside the inclusion by increasing the wavenumber parameter γ.

Conclusions

In the present paper a new contrast model for material parameters in fictitious domains has been proposed for use in steady-state dynamic problems. The model is based on the diffusion equation and effectively removes the presence of resonance in the fictitious domain and allows for a tunable reduction of the field amplitude within the domain.

References

[1] M. Berggren and F. Kasolis. Weak material approximation of holes with traction-free boundaries. *SIAM Journal on Numerical Analysis*, 50(4):1827–1848, 2012.

[2] N.L. Pedersen. Maximization of eigenvalues using topology optimization. *Structural and Multidisciplinary Optimization*, 20(1):2–11, 2000.

[3] F. Kasolis, E. Wadbro and M. Berggren. Analysis of fictitious domain approximations of hard scatterers. *SIAM Journal on Numerical Analysis*, 53(5):2347–2362, 2015.

Proceedings of the 32nd Nordic Seminar on Computational Mechanics
A.H. Niemi and H. Koivurova (Eds.)

Friday_v3_correct__.zip: How about version control?

Juha Jeronen[1]

(1)Global Boiler Works Oy, juha.jeronen@gbw.fi

Summary. In computational research in the engineering sciences, the established knowledge, methods and tools from computer science, information technology, and software engineering together present a huge untapped potential for productivity. We look at version control, which is a family of tools used by software industry professionals to automatically track code changes. This enables reliable archival and comparison of existing versions, as well as eliminates the human error of accidentally resuming work from an outdated base version. Modern tools facilitate teamwork even simultaneously on the same file. Finally, beside source code, the same tools can manage LaTeX sources for articles and books just as well.

Key words: computational research, tools, software engineering, best practices, version control, git

Introduction

Computational research in the engineering sciences can be roughly described as one part mechanics, one part mathematics, and one part software engineering. However, in academia, knowledge of effective and efficient tools and practices for software development is often in practice limited to departments or faculties of information technology or computer science. In the engineering sciences, software engineering is often performed in an ad-hoc manner, even though creating solvers for numerical simulations forms an integral part of the work.

Software development is a complex endeavor. Even though libraries provide much of the algorithmically complex low-level functionality of any real-world numerical solver (e.g. sparse linear equation system solvers, eigenvalue solvers), an element of engineering is always required for the custom code that combines the components into a useful application. Occasionally one also needs to engineer custom algorithms, and implement mathematical models (e.g. new material models) for which no software yet exists. To develop software effectively and efficiently, one stands to benefit from the established knowledge, methods and tools in computer science, information technology, and software engineering.

Theoretical and practical advances such as functional programming and automated testing increase program reliability, leading to less time spent finding bugs. Following established principles of code organization, patterns and idioms improves code structure, increasing maintainability and reusability.

However, as software engineering is a large topic, here we concentrate only on a specific family of tools that significantly enhances the trackability of code changes, and by extension, in a scientific context, the verifiability of already performed research, namely version control. Specifically, we focus on a popular distributed version control system (DVCS) called *git*.

The main benefits of version control include the reliable archival and identification of each existing version, as well as convenient comparison between any two existing versions. It also eliminates the human error of accidentally resuming work from an outdated base version. In the rare case where that nevertheless happens, it is possible to extract just the changes, and if the base versions are similar enough, to automatically re-apply the changes onto the correct base

version. Version control also facilitates collaboration, by making it convenient to review and merge changes from multiple sources, even if several people edit the same file simultaneously. In the merge step, human intervention is required only if the edits conflict with each other; otherwise the system can merge automatically.

Version control not only keeps source code versioning manageable, but it can help with managing versioning and collaboration also with other kinds of text documents, such as LaTeX sources for scientific papers and books. Some scientific editor software, such as the graphical LaTeX-based word processor *LyX*, actually employ *git* as a change-tracking engine.

Understanding version control

To understand and appreciate version control, we must first understand the spirit of software engineering. The aim is to produce correct software quickly. It is no surprise the prevailing opinion in the software engineering community is that an integral part of an effective strategy to achieve the aim is to automate as much of the process as reasonably possible.

For example, static code analyzers and static type checkers automatically check program source code, helping to eliminate certain classes of human error before the program is even run. Build systems automate the compilation process, helping to make it repeatable. Automated tests detect regressions, i.e. situations where changes to the code cause a previously discovered and already fixed issue to reappear. Packaging systems automate the installation process of the software for end users. Usually such installation packages are generated automatically. For a sampling of developments in software engineering automation, see [3].

In certain contexts, even programming itself can be automated. Code generation techniques shift the responsibility for writing repetitive, formulaic parts of a program to the computer. A classic example is GNU Bison, which automatically generates parsers for programming languages, based on a high-level formal grammar specification. In a sense, the Lisp community has taken this idea to its logical extreme. The Racket programming language, a modern Lisp in the Scheme family, is mostly built in itself [4], via *syntactic macros*: essentially, code that writes code. (This train of thought leads to a related recurring theme in software engineering, *abstraction*, but that is beyond the scope of this presentation; see e.g. [5].)

During its lifetime, software typically needs to be able to change, so that it can be extended to fulfill new requirements, as well as to allow fixing any issues discovered during use. This meta-requirement introduces the need to track code changes, and identify versions, reliably. The essential motivation behind version control is to automate this.

Following [1], version control systems (VCS) can be roughly divided into three generations, where the main historical trend is toward increased concurrency. First-generation systems had no networking support, and operated on one file at a time. Second-generation systems stored the version history on a centralized server, and were able to operate on multiple files. Third-generation systems work in a distributed manner and operate on changesets. During the past decade, the third-generation systems *git* and *mercurial* (*hg*) have both become widely used, and are currently the *de facto* standard tools for version control.

In a distributed version control system (DVCS), the full version history is stored locally on the user's computer. The local histories (*forks*) belonging to different users may evolve independently, and each may have multiple branches. Branches can be selectively synchronized between different forks. Often, in practice, a master fork is kept (in *git* usually called *origin* and stored on a network-accessible server), but this is not strictly required. In DVCS, the purpose of the master fork is just to help synchronization between users, and to have an official master in projects where that is desirable. Network access is required only during synchronization.

An important development from the last decade is the rise of a kind of social media for version control. Many open-source projects use a collaborative revision control site such as GitHub or BitBucket as their main source-code distribution channel. From a social perspective,

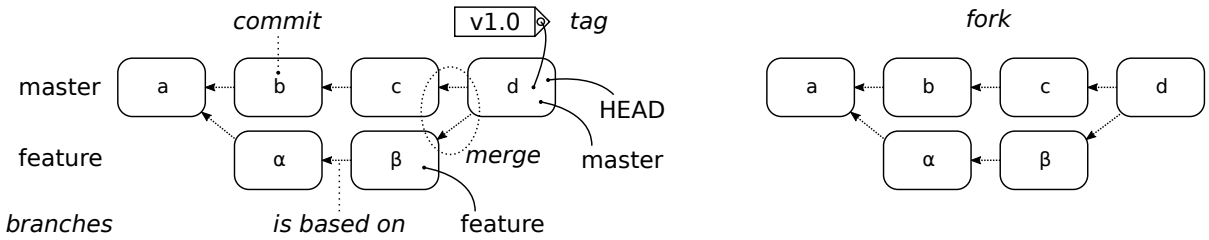

Figure 1. Some *git* concepts. In *git*, changesets are first-class. The transient labels *master* and *feature* in the middle are the actual branches; the content of a revision is constructed (roughly) by following the arrows. The label moves when a new commit is added. *HEAD* is the tip of the currently active branch.

this has a major impact, for two reasons. First, having a centralized service and a unified presentation format makes it much easier for prospective users to search for open-source software. Secondly, these sites host additional services beyond just third-generation version control. For example, GitHub provides a public online issue tracker for any project that wants one, as well as pull requests (PR), a collaboration feature where users may upload changes made to someone else's project and request for a merge. (Not to be confused with `git request-pull`, which is the original command-line feature without the added social functionality.) Transparency and repeatability of science stand to benefit from openly publishing any custom code that acts as a basis for scientific claims; collaborative revision control sites can thus be useful for science, too.

Core concepts of the git version control system

The version of the directory tree of the project that is currently being worked on forms the *working tree*. The version history is stored separately, so even if a file is deleted from the working tree, it remains (essentially forever) in the history. The working tree is separate from the *HEAD revision*, which is the latest version in the history (on the branch that is being worked on). Figure 1 illustrates some key concepts with the help of a simple example version history.

When we edit the files in our project as usual, the working tree changes. The history remains as-is. When we are done with a particular set of changes (a *changeset*), and wish to record it into the history, we first add our changes to the *staging area*. This is an intermediate storage location, separate from both the history and the working tree, used for preparing the next changeset.

The basic unit of recording a set of changes is the *commit*. It is also a verb; the act of recording a changeset into the history is called *committing*. The system automatically records information such as which lines of which files were changed, by whom, and when. This allows the VCS to construct, upon request, the full history of a file or a particular line in a file, showing who changed it and when. (In git, this feature is called `git blame`.)

It is possible to compare any two revisions (including the working tree and the revision currently in the staging area) to see what has changed. This is called *diffing*; the automatically generated comparison report is the *diff*. Diffing is particularly valuable for both collaboration and debugging. A diff can also act as a *patch*: a set of changes to be replayed later.

To facilitate later searching, when committing, we must enter a descriptive *commit message*. These messages are automatically saved into a searchable *commit log*. For first-time users of version control, the need to manually describe every changeset may appear foreign and intimidating. Why such bureaucracy?

The unfortunate fact is that commit messages cannot be automatically generated, since their whole purpose is to explain what a particular changeset means to a human. This is precisely where their advantage lies. Describing our commits gives us searchability and auditability, while using terms meaningful to us. Having to be explicit about the meaning helps bring clarity to the thought process, helping to isolate conceptually separate changes (for presentation

purposes, as well as being able to easily look at or pick just those changes later). And in any case, it is cheap. It is reasonable to commit no more often than when a changeset can be considered reasonably complete. Usually one short line is enough as the message, such as "add feature X", "resolve issue Y", "fix off-by-one error", "clean up the implementation of Z". Note the wording; it is customary to write the first line of the message in the imperative mood. This is short, to the point, and quick to read when browsing the log.

For organization purposes, or if concerned about losing work in progress, it is possible to *branch* off a given revision, and commit into the branch. The default branch is, by convention, usually named *master*. If a project is large enough to have separate stable and development branches, the latter is usually named *develop*. A project may have any number of branches. Typically additional branches are used for developing new features (one branch per feature).

Changes made in one branch can be *merged* into another branch, even if the files in the merge target branch have changed in between. This is what makes feature branches workable. Git is smart enough to figure out simple position changes (so line numbers in a patch do not have to be exact, as long as the context can be found). When not, the system reports the *merge conflict* to the user, showing both versions of each conflicting section, and asks the user to fix the conflict manually and then tell git to continue merging.

To clean up the commit log before merging a branch, it is possible to *amend* a commit to fix any typos in the message, or to *squash* several commits into one. The general convention is to not change any published commits, but any commits that are still local only can be reformatted this way before publishing them.

To communicate with a network-accessible server (or, in general, with another fork of the same project), one may *push* or *pull* changes. The other end is called the *remote*. Pulling updates the local fork using data from the remote (retrieving changes made by others), while pushing (assuming we have write access to the remote) updates the fork on the remote with the data in the local fork (publishing our changes).

The primary user interface of *git* is a set of command-line utilities. Graphical frontends exist, but many offer only basic features. However, Emacs has *Magit*, with excellent feature coverage and convenient single-keypress commands.

In conclusion, version control can offer trackability and auditability not only for software projects, but also for scientific authoring. *git* is a widely used third-generation, distributed version control system (DVCS), suitable for both single-user and collaborative use cases. In the presentation, we will look at some examples.

References

[1] E. Sink. *Version Control by Example*. Pyrenean Gold Press, 2011. 978-0983507901. https://ericsink.com/vcbe/index.html

[2] S. Chacon and B. Straub. *Pro Git*, 2nd edition. Apress, 2014. 978-1484200773. https://git-scm.com/book/en/v2

[3] European Research Consortium for Informatics and Mathematics. *ERCIM News*. Special issue on Automated Software Engineering. July 2004. https://www.ercim.eu/publication/Ercim_News/enw58/EN58.pdf

[4] M. Flatt, R. Culpepper, D. Darais and R. B. Findler. Macros that Work Together: Compile-time bindings, partial expansion, and definition contexts. *Journal of Functional Programming*, 22(2), 181–216, 2012. 10.1017/S0956796812000093

[5] H. Abelson, G. J. Sussman and J. Sussman. *Structure and Interpretation of Computer Programs*, 2nd edition. MIT press, 1984. 978-0262010771. https://mitpress.mit.edu/sites/default/files/sicp/index.html

Proceedings of the 32nd Nordic Seminar on Computational Mechanics
A.H. Niemi and H. Koivurova (Eds.)

On the integration of an evolution equation based high-cycle fatigue model

Juha Jeronen[1], Reijo Kouhia[2], Joonas Lahtinen[2] and Heikki Orelma[2]

(1)Global Boiler Works Oy, juha.jeronen@gbw.fi
(2)Tampere University, reijo.kouhia@tuni.fi, joonas.lahtinen1992@gmail.com, heikki.orelma@tuni.fi

Summary. Computation of the fatigue strength in high-cycle loading may require high computer power. In this paper, backward difference schemes and discontinuous Galerkin time-integration methods are compared in solving a continuum based high-cycle fatigue model.

Key words: high-cycle fatigue, evolution equations, endurance surface, time integration

Introduction

Ottosen, Stenström and Ristinmaa proposed in 2008 [7] a concept for a macroscopic high-cycle fatigue (HCF) model which treats all stress components in a unified manner and is suitable for arbitrary loading histories, thus liberating from the definition of an equivalent cycle, which is a severe drawback of many existing HCF models. Another benefit of the continuum based model is its natural extensibility to anisotropy, low-cycle fatigue, stochastic and stress gradient features [5, 3, 4, 8]. The basic ingredients of the continuum based HCF model are the endurance surface and the evolution equations for its movement and the fatigue damage. In [7] the endurance surface for isotropic fatigue is defined as

$$\beta = \frac{1}{\sigma_{-1}} \left(\overline{\sigma} + A \operatorname{tr}(\boldsymbol{\sigma}) - \sigma_{-1} \right) = 0, \tag{1}$$

where the effective von Mises type stress is

$$\overline{\sigma} = \sqrt{\frac{3}{2} \operatorname{tr}(\boldsymbol{s} - \boldsymbol{\alpha})^2}, \tag{2}$$

where $\boldsymbol{s} = \boldsymbol{\sigma} - \operatorname{tr}(\boldsymbol{\sigma}) I$ is the deviatoric stress tensor and I the identity tensor. σ_{-1} is the fatigue stress amplitude for a fully reversed loading and A describes the slope of the Haigh diagram. More complex forms of the endurance surface have been published, see [1, 2]. Movement of the endurance surface is described by the deviatoric tensor $\boldsymbol{\alpha}$, for which a Zieger type evoluion is chosen:

$$\dot{\boldsymbol{\alpha}} = \begin{cases} C(\boldsymbol{s} - \boldsymbol{\alpha}) \dot{\beta}, & \text{if } \beta, \dot{\beta} \geq 0, \\ 0, & \text{otherwise.} \end{cases} \tag{3}$$

The evolution equation for damage development is postulated as

$$\dot{D} = \begin{cases} g\left(\beta, D\right) \dot{\beta}, & \text{if } \beta, \dot{\beta} \geq 0, \\ 0, & \text{otherwise.} \end{cases} \tag{4}$$

Here, the original [7] damage function $g(\beta) = K \exp(L\beta)$ is used. The three additional material parameters C, K and L can be calibrated from the S-N curves.

Integration

As in the implicit integration of plastic constitutive models, the trial value of the rate of the endurance surface is determined assuming that $\dot{\boldsymbol{\alpha}} = \boldsymbol{0}$, which results in

$$\dot{\beta}_{\text{trial}} = \frac{1}{\sigma_{-1}} \left(\frac{3}{2} \frac{(\boldsymbol{s} - \boldsymbol{\alpha})}{\overline{\sigma}} + A\boldsymbol{I} \right) : \dot{\boldsymbol{\sigma}}, \tag{5}$$

where : denotes the double dot product $\boldsymbol{A} : \boldsymbol{B} = \text{tr}(\boldsymbol{A}\boldsymbol{B}^T)$. If $\beta_{\text{trial}} \geq 0$ and $\dot{\beta}_{\text{trial}} \geq 0$, then loading occurs, and taking the $\boldsymbol{\alpha}$-tensor evolution into account results in

$$\dot{\beta} = \frac{1}{\sigma_{-1} + C\overline{\sigma}} \left(\frac{3}{2} \frac{(\boldsymbol{s} - \boldsymbol{\alpha})}{\overline{\sigma}} + A\boldsymbol{I} \right) : \dot{\boldsymbol{\sigma}}. \tag{6}$$

In contrast to standard plasticity, the evolution does not occur if $\beta_{\text{trial}} \geq 0$ and $\dot{\beta}_{\text{trial}} < 0$.

Compared methods

Backward difference schemes

The backward difference formula method of order k (BDFk) applied to $\dot{\boldsymbol{\alpha}}$ can be written as

$$\dot{\boldsymbol{\alpha}}(t_n, \boldsymbol{\alpha}_n) \approx \sum_{j=0}^{k} c_j \boldsymbol{\alpha}_{n-j} =: f(t_n, \boldsymbol{\alpha}_n) \tag{7}$$

where the constants c_j arise from the derivatives of Lagrange interpolation polynomial basis functions ℓ_j at t_n, which can be expressed as

$$\ell_j(t) = \prod_{\substack{0 \leq i \leq k \\ i \neq j}} \frac{t - t_{n-i}}{t_{n-j} - t_{n-i}}, \tag{8}$$

$$c_j := \ell_j'(t_n). \tag{9}$$

Discontinuous Galerkin approach

Let us denote a generic evolution equations as

$$\dot{\boldsymbol{y}} = \boldsymbol{f}(\boldsymbol{y}), \tag{10}$$

where $\boldsymbol{y} = [\boldsymbol{\sigma}, \omega]^T$ and $\boldsymbol{f} = [\boldsymbol{f}_\sigma, f_\omega]^T$. The discontinuous Galerkin method of degree q can be stated as follows [6]. For a given time interval $I_n = (t_n, t_{n+1}]$, find $\boldsymbol{y}$ (polynomial of degree q) such that

$$\int_{I_n} (\dot{\boldsymbol{y}} - \boldsymbol{f}(\boldsymbol{y}))^T \hat{\boldsymbol{y}} \mathrm{d}t + [\![\boldsymbol{y}_n]\!]^T \hat{\boldsymbol{y}}_n^+ = 0. \tag{11}$$

For the test functions $\hat{\boldsymbol{y}}$, polynomials of degree q are used. The notations $\boldsymbol{y}_n^+$ and $\boldsymbol{y}_n^-$ are the limits $\boldsymbol{y}_n^\pm = \lim_{\epsilon \to 0} \boldsymbol{y}(t_n \pm |\epsilon|)$, $[\![\boldsymbol{y}_n]\!] = \boldsymbol{y}_n^+ - \boldsymbol{y}_n^-$. These notations are illustrated in Fig. 1.

Concluding remarks

A preliminary study for the assesment of the backward difference and discontinuous Galerkin time integration methods for an evolution equation based high-cycle fatigue model has been performed.

Acknowledgements

This research has been supported in part by Business Finland (former Tekes - the national Technology Agency of Finland), project ISA (Intelligent Steel Applications) Dnro 7204/31/2018.

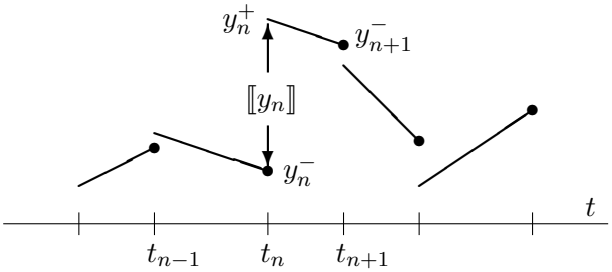

Figure 1. Discontinuous Galerkin method, dG(1); notation.

References

[1] R. Brighenti, A. Carpinteri, and S. Vantadori. Fatigue life assessment under a complex multiaxial load history: an approach based on damage mechanics. *Fatigue & Fracture of Engineering Materials & Structures*, 35(2):141–153, 2012. doi:10.1111/j.1460-2695.2011.01600x.

[2] R. Brighenti, A. Carpinteri, and N. Corbari. Damage mechanics and Paris regime in fatigue life assessment of metals. *International Journal of Pressure Vessels and Piping*, 104:57 – 68, 2013. ISSN 0308-0161. doi:http://dx.doi.org/10.1016/j.ijpvp.2013.01.005.

[3] T. Frondelius, S. Holopainen, R. Kouhia, N.S. Ottosen, M. Ristinmaa, and J. Vaara. A continuum based macroscopic unified low-and high cycle fatigue model. EDP Sciences, 2019. To be published in ICMFF12 Proceedings, 8 pages.

[4] T. Frondelius, T. Kaarakka, R. Kouhia, J. Mäkinen, H. Orelma, and J. Vaara. Stochastic continuum approach to high-cycle fatigue: modelling stress history as stochastic process. Manuscript 21 pages, 2019.

[5] S. Holopainen, R. Kouhia, and T. Saksala. Continuum approach for modeling transversely isotropic high-cycle fatigue. *European Journal of Mechanics A/Solids*, 60:183–195, 2016. doi:10.1016/j.euromechsol.2016.06.007.

[6] P. Hansbo K. Eriksson, D. Estep and C. Johnsson. *Computational Differential Equations*. Studentlitteratur, 1996.

[7] N.S. Ottosen, R. Stenström, and M. Ristinmaa. Continuum approach to high-cycle fatigue modeling. *International Journal of Fatigue*, 30(6):996–1006, June 2008. doi:10.1016/j.ijfatigue.2007.08.009.

[8] N.S. Ottosen, M. Ristinmaa, and R. Kouhia. Continuum approach to high-cycle fatigue modeling - consideration to stress gradients. *International Journal of Fatigue*, 116:128–139, 2018. doi:10.1016/j.ijfatigue.2018.05.024.

Proceedings of the 32nd Nordic Seminar on Computational Mechanics
A.H. Niemi and H. Koivurova (Eds.)

Cost-optimized rise of tied-arch bridges

Esko Järvenpää[1] and Antti H. Niemi[2]

[1] WSP Finland Oy, esko.jarvenpaa@wsp.com
[2] Structures and Construction Technology Research Unit, University of Oulu, antti.niemi@oulu.fi

Summary. We optimize the rise of a tied-arch bridge based on minimization of the total costs for the whole bridge structure. The optimal height of the arch is found by using the force length method and integral calculations over the tied-arch structure. Load-bearing material quantities are determined for the arch rib, the tie structure and the hanger cables. The cost increase depending on the height of the arch has been taken into account. The optimal rise *l/h* is shown to be dependent on the span length of the arch.

Key words: bridge engineering, structural optimization, tied-arch bridge

Introduction

The maximum span length of arch bridge has reached 552 m and longer spans are designed. The modern construction material is steel, often used as composite structure with concrete.

The arch itself is the major player in the structure. Generally used *l/h*-relation of arches has been in the range of 4 to 7, as in Ref. [1]. Actually, many research papers refer to traditionally used rises of arches being as optimal values.

The shapes of arches follow often geometric well-known shapes like circle, catenary, parabola and ellipse. Combinations of these shapes are used, too. In the bridges one should forget old tradition and use only momentless shapes for permanent loads, as in Ref. [2].

Parabolic arch is used in this study. The accuracy is acceptable for preliminary studies, but for the final design it is not recommended because of the bending moment as in Ref [3]. In reality the distribution of vertical loads carried by the arch is never uniform, which is needed for momentless parabola.

Optimal Rises of Tied-Arch Bridges

Optimal rise for minimum material quantity for constant stress

The minimum of the axial force length of the momentless structure gives also the minimum material quantity of the structure. In the force length method, the axial forces of the form-found momentless structure are multiplied by the lengths of the structure members, as in Ref [3]. The

material quantities of each structure component can be calculated dividing the force length by the stress used and multiplying this by the material density.

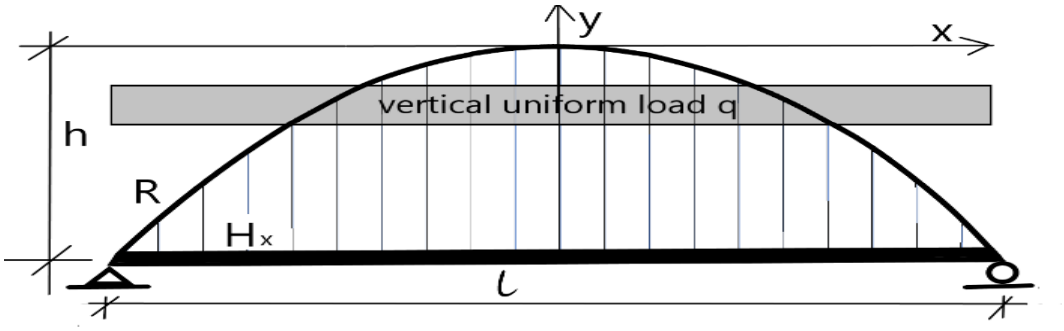

Figure 1. Parabolic tied arch.

The sum of force lengths of the parabolic tied-arch is

$$f_{a+t+h} = 2\int_0^{l/2} \frac{2ql^2}{8h}\left(1+\frac{64h^2}{l^4}x^2\right)\,dx + \frac{ql^2}{8h}\int_0^{l} dx + 2q\int_0^{l/2}\left(h-\frac{4hx^2}{l^2}\right)dx$$
$$= ql\left(\frac{l^2}{8h}+\frac{2h}{3}\right) + ql\left(\frac{l^2}{8h}\right) + ql\left(\frac{2h}{3}\right) \qquad (1)$$

The minimum of the force length function, when $q = 1$ and $l = 1$, is found from the equation

$$\frac{df_{a+t+h}}{dh} = -\frac{1}{8h^2}+\frac{2}{3}-\frac{1}{8h^2}+\frac{2}{3} = 0 \qquad (2)$$

The optimum rise of parabolic arch for the minimum load bearing material in tied-arch bridge is

$$h = \frac{l\sqrt{3}}{4} \quad \text{and then } l/h = 2{,}309 \qquad (3)$$

as in Ref. [4].

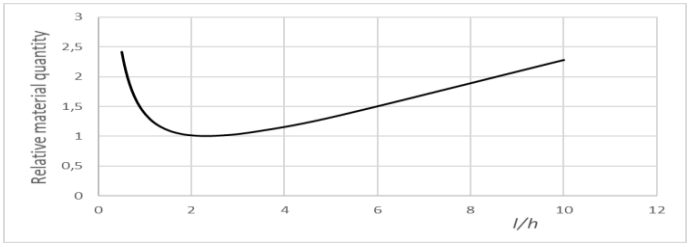

Figure 2. Relative load bearing material quantity in tied-arch structure, the minimum at l/h = 2,309 when equal stresses are used.

Optimal cost-effective rise using fixed unit prices

The cost-optimized height h is found from the condition

$$\frac{dC_{a+t+h}}{dh} = qlC_a\left(-\frac{l^2}{8h^2}+\frac{2}{3}\right)+qlC_t\left(-\frac{l^2}{8h^2}\right)+qlC_h\left(\frac{2}{3}\right) = 0. \qquad (4)$$

and the optimal height $h_{optimum}$ of the tied-arch becomes

$$h_{optimum}=l\sqrt{3(C_a+C_t))/(16(C_a+C_h)} \quad (5)$$

where
l is the span length of the arch,
C_a is the unit cost of arch rib divided by the assumed stress level,
C_t is the unit cost of the tie divided by the assumed stress level
C_h *is* the unit cost of the hangers.

The relative cost as function of the rise *l/h* is shown in Fig. 3.

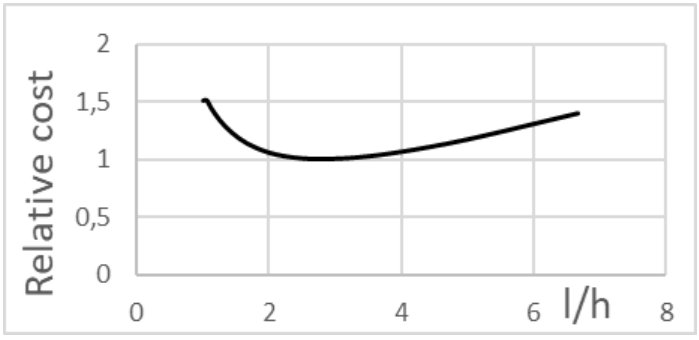

Figure 3. Relative costs of the tied-arch structure in relation to *l/h* using the stresses and fixed unit prices as given in the example below, minimum at *l/h* = 2,795.

Optimal cost-effective rise in relation to the height of arch

We suppose that the unit price in steel structures at a bridge site from the ground level price, to the height *H* [m], increases by *e* [€/kg]. We assume also that the price increases in the second power of the height *h*. The relative cost function of the steel of the arch is then

$$C_a = C_a + \frac{ey^2}{\sigma_c H^2} \quad (6)$$

and

$$y = \frac{4h}{l^2}x^2. \quad (7)$$

Denoting $e/\sigma_c H^2 = k$, we get the total cost function of tied-arch bridge as

$$C_{a+t+h}=\frac{2l^2}{8h}\int_0^{l/2}(1+\frac{64h^2}{l^4}x^2)(C_a+k\frac{4h}{l^2}x^2)dx$$

$$+2C_t\int_0^{l/2}\frac{l^2}{8h}dx+2C_h\int_0^{l/2}(h-\frac{4h}{l^2}x^2)dx. \quad (8)$$

Setting $\frac{dC_{a+t+h}}{dh} = 0$, we get a quartic equation for the optimal height *h*

$$5760ph^4+(4480C_t+4480C_t+168l^2p)h^2-840l^2(C_a+C_h)=0 \quad (9)$$

Example

Calculate the cost-optimized heights of the tied-arch bridge when the unit price of steel at bridge site, on ground level, is 8 €/kg and at the level of 100 m 15 €/kg. The price increases

quadratically (Figure 4). The unit price used for ties and hangers are 20 €/kg and 30 €/kg, respectively. The stresses used for permanent loads are: arch 150 MPa, tie 700 MPa and hangers 450 MPa.

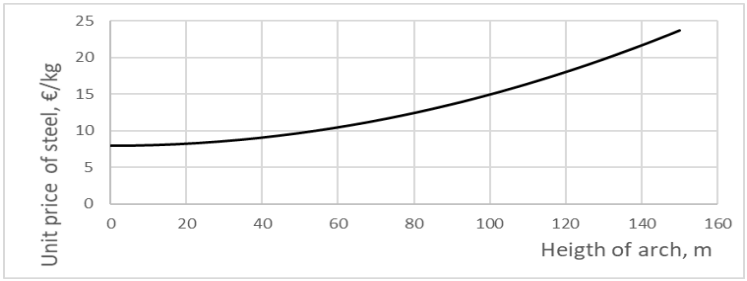

Figure 4. Unit price of steel in relation to the height.

As an example, when the span length is 500 m, the *l/h*-value for minimum costs is 4,0. Figure 5 shows the optimum *l/h*-values in relation to the span length calculated using parabolic arch.

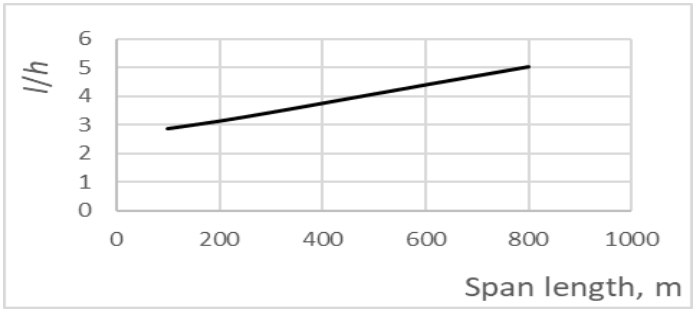

Figure 5. Cost-optimum *l/h* in relation to span length when the price of steel in the arch depends on the arch height (in the example case).

The optimal rise relation of tied arches, with vertical hangers, depends on the span length. The calculations for cost minimum rise relation for tied arch bridges from spans to 150 m to 500 results *l/h*-relations from 3,0 to 4,0 respectively. The optimal heights are higher than traditionally used.

Acknowledgements

This research has been supported by Oulun rakennustekniikan säätiö. The support is gratefully acknowledged.

References

[1] Chen,S., Nakamura,S., Chen,B.,Wu,Q., Nishikawa,T., (2013). Comparison between steel arch bridges in China and Japan, Journal of JSCE, Vol. 1, 214-227.

[2] Lewis,W.,(2016).Mathematical model of a moment-less arch. Proceedings of the Royal Society A, doi: 10.1098/rspa.2016.0019.

[3] Järvenpää, E., Niemi, A. H., Tervaoja, J.,(2019). Shape of arch–is it important? Structures & Architecture – Gruz (ed). Taylor & Francis Group, London, ISBN978-1-138-03599-7.

[4] Tyas,A., Pichugin, A.V.,Gilbert,M.,(2010). Optimum structure to carry a uniform load between pinned supports: exact analytical solution, Proceedings of the Royal Society, published 20 October. DOI: 10.1098/rspa.2010.0376.

Proceedings of the 32nd Nordic Seminar on Computational Mechanics
A.H. Niemi and H. Koivurova (Eds.)

Micropolar plate model for lattice core sandwich panels

Anssi Karttunen[1], Praneeth Nampally[2], JN Reddy[2], Jani Romanoff[1]

(1)Aalto University, Department of Mechanical Engineering, Aalto, FI-00076, Finland, anssi.karttunen@aalto.fi, jani.romanoff@aalto.fi
(2)Texas A&M University, Department of Mechanical Engineering, College Station, TX 77843-3123, USA, praneeth.nampally@tamu.edu, jnreddy@tamu.edu

Summary. A 2-D micropolar equivalent single-layer (ESL), first-order shear deformation (FSDT) plate model for 3-D lattice core sandwich panels is developed.

Key words: Constitutive modeling, micropolar plate, local bending, local twisting

Introduction

We develop a 2-D micropolar equivalent single-layer (ESL), first-order shear deformation (FSDT) plate model for 3-D lattice core sandwich panels. First, 3-D lattice core unit cells are modeled by classical beam and shell finite elements. A discrete-to-continuum transformation is applied to the microscale unit cells and their strain and kinetic energy densities are expressed in terms of the macroscale 2-D plate kinematics. The hyperelastic constitutive relations and the equations of motion (via Hamilton's principle) for the micropolar plate are derived by assuming energy equivalence between the 3-D unit cells and the 2-D plate. The Navier solution is developed for the 2-D micropolar ESL-FSDT plate model to study the bending, buckling, and free vibration of simply-supported lattice core sandwich panels. In a line load bending problem [1], a 2-D classical ESL-FSDT plate model yields displacement errors of 34–175% for face sheet thicknesses of 2–10 mm compared to a 3-D FE solution, whereas the 2-D micropolar model gives only small errors of 2.7–3.4% as it can emulate the 3-D deformations better through non-classical antisymmetric shear behavior and local bending and twisting.

Numerical example

Let us consider the buckling of web-core sandwich panels subjected to uniaxial and biaxial compression. We use the Navier solution for two-dimensional ESL-FSDT plate models based on micropolar and classical elasticity. In addition, a 3-D finite element model for web-core sandwich panels is used to provide accurate reference solutions against which the ESL-FSDT models can be evaluated.

Figure 1 presents the setup for the buckling problems and the critical buckling modes calculated by the 3-D FE model. Figures 2(a) and 2(b) show the lowest buckling loads up to $m = 11$ (m is the number of half-waves in $x-$direction) under uniaxial and biaxial compression, respectively. In both cases we can see that the 2-D micropolar ESL-FSDT plate results are in good agreement with the 3-D FE results, whereas the 2-D classical results are not. The classical model can predict well only the lowest mode ($m = 1, n = 1$) but note that it predicts the critical mode incorrectly in both cases, as the buckling loads decrease in an non-physical manner as the mode number increases.

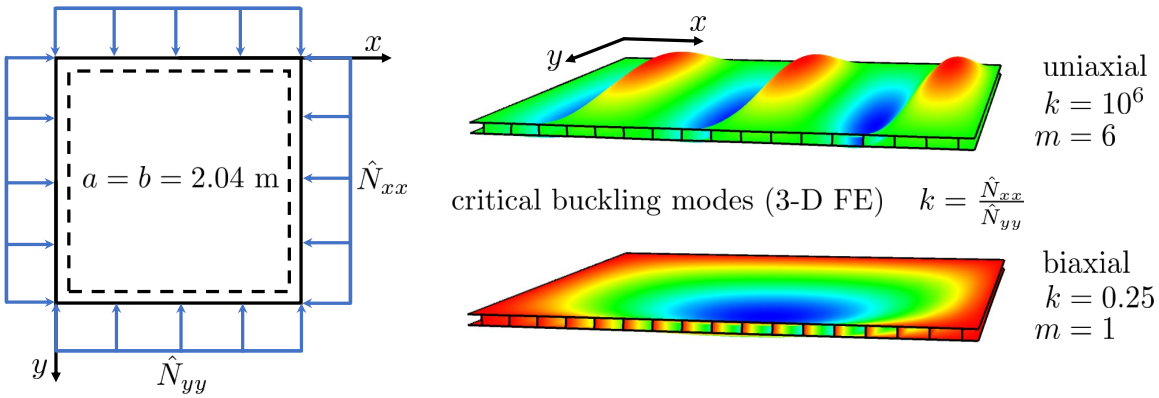

Figure 1. Setup for web-core plate buckling analysis and the critical buckling modes for uniaxial and biaxial compression.

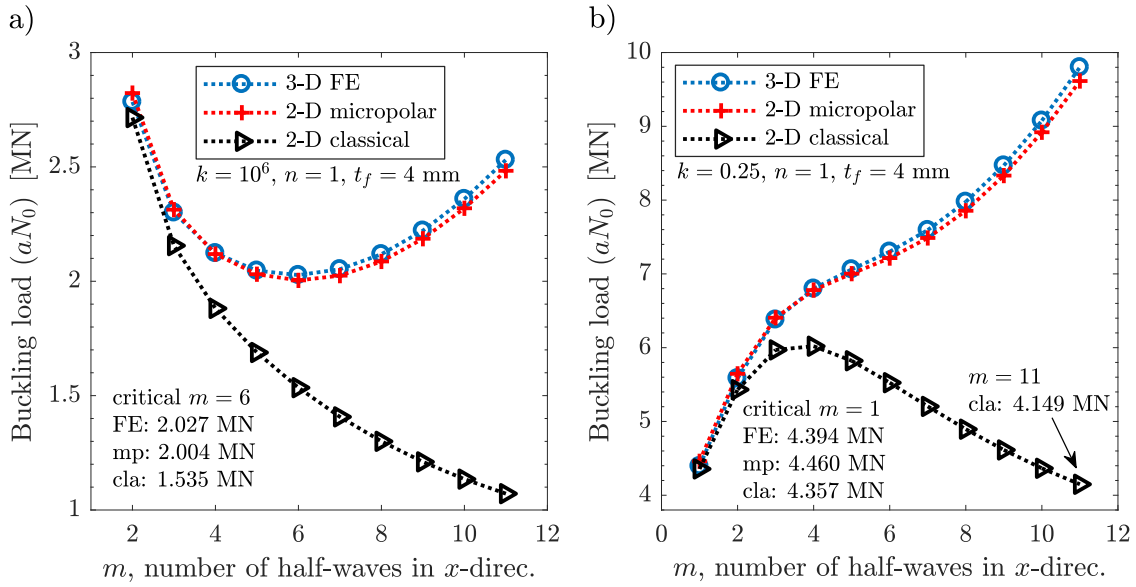

Figure 2. Buckling loads of a web-core sandwich panel under a) uniaxial and b) biaxial compression. The ESL-FSDT plate model based on classical elasticity gives erroneous results for the critical buckling mode and load, whereas the 2-D micropolar model is in good agreement with the 3-D results in both cases.

References

[1] A. T. Karttunen, J. N. Reddy, and Jani Romanoff. Two-scale micropolar plate model for web-core sandwich panels. *International Journal of Solids and Structures*, 170:82-94, 2019.

Proceedings of the 32nd Nordic Seminar on Computational Mechanics
A.H. Niemi and H. Koivurova (Eds.)

Finite element modeling of Al6082 Plasma Electrolytic Oxidation coatings

Sergei Khakalo[1], Anssi Laukkanen[1], Tomi Suhonen[1], Kenneth Holmberg[1], Etienne Bousser[2], Aleksey Yerokhin[2], Philip J. Withers[2], and Allan Matthews[2]

[(1)]VTT Technical Research Centre of Finland, sergei.khakalo@vtt.fi, anssi.laukkanen@vtt.fi, tomi.suhonen@vtt.fi, kenneth.holmberg@vtt.fi
[(2)]The University of Manchester, United Kingdom, etienne.bousser@manchester.ac.uk, aleksey.yerokhin@manchester.ac.uk, p.j.withers@manchester.ac.uk, allan.matthews@manchester.ac.uk

Summary. For oxide coatings, prepared by applying plasma electrolytic oxidation (PEO) to aluminium alloy Al6082, this conference contribution presents the finite element (FE) microstructural modeling of the PEO coatings. By utilizing the coating phase maps, obtained by electron back-scattered diffraction (EBSD) technique, the corresponding images have been converted into FE models with a detailed microstructure representation. By utilizing experimental data such as loading-unloading curves obtained upon micro-indentation using a Berkovich tip on the coatings cross-sections and surfaces, the material models representing the coating constituent phases have been calibrated.

Key words: micro-indentation, hardness, finite element modeling, PEO coatings, mechanical performance

Introduction

Weight is one of key factors influencing vehicle energy consumption and emissions. Hence, there is a growing effort to replace conventional steels and cast irons with light metals and alloys, e.g., aluminum and magnesium. Although these metals have good strength-to-weight characteristics, they suffer from poor corrosion and wear properties. Coating a surface with a thin layer changes the surface material properties and is an important tool for controlling friction, corrosion and wear. PEO is a relatively novel surface modification technique to create ceramic coatings on the surface of metals, such as aluminium, and their alloys (Refs. [1, 2]).

The present contribution focuses on the FE microstructural modeling of Al6082 PEO coatings of three different thicknesses, namely, 15 µm, 20 µm and 30 µm, which are labeled, respectively, as PEO-15µm, PEO-20µm and PEO-30µm coatings. By performing FE simulations of the micro-indentation tests using conical and spherical tips, the influence of the aluminium oxide phases on the coating mechanical performance has been computationally investigated. The local stress distributions on microstructural level have been studied in details. The FE modelling has been

carried out using VTT Propertune™ which is a computational modelling-based material design methodology providing a portfolio of software packages combined with commercial modelling tools such as Abaqus (Refs. [3,4]).

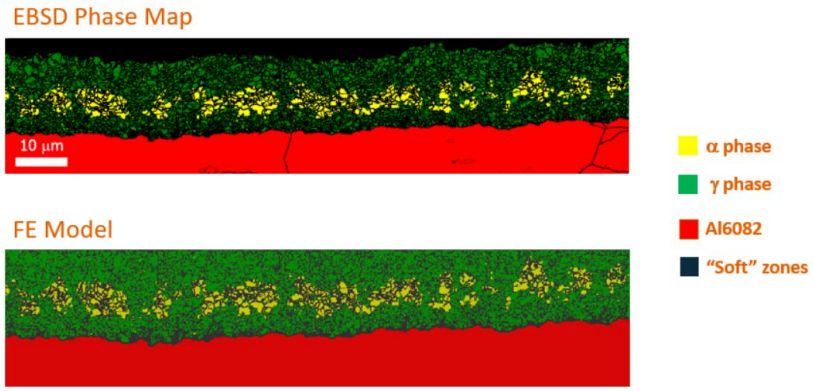

Figure 1. EBSD phase map of PEO-20µm coating (top) and corresponding FE model (bottom).

FE model generation and calibration

By utilizing OOF2 program (Ref. [5]) the EBSD phase map images have been converted into pixel-based FE models (see figure 1). For the PEO-15µm FE model (see figure 2), numerical simulations have been performed in axially symmetric problem setting by utilizing an elastic conic tip made of diamond with 70.3° half-angle. The coating has width 48.55 µm and thickness 11.2 µm under the indenter. The computational domain has been extended such that the total area is of 248.5 µm × 576.25 µm size.

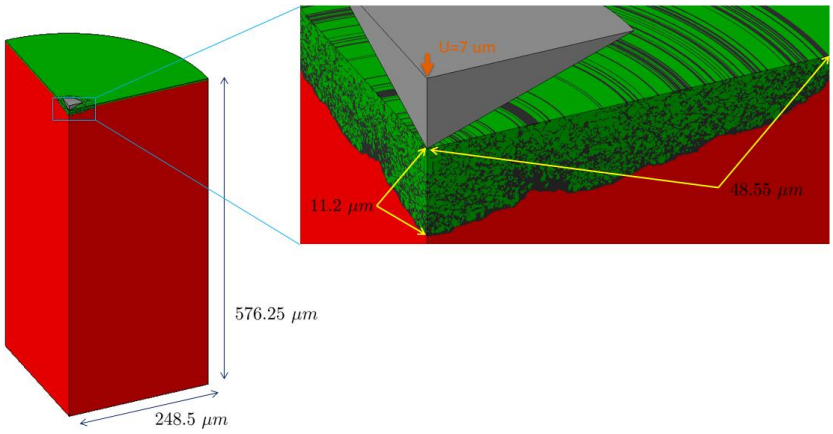

Figure 2. FE model of PEO-15µm coating indentation with a conic tip in an axisymmetric problem setting.

The green colour corresponds to γ-Al_2O_3 phase, the indenter material is depicted in grey, Al6082 substrate has red colour. The material models are chosen to be isotropic perfectly plastic with Young's modulus E, Poisson's ratio ν and yield stress σ_Y. The material phases are perfectly connected, i.e., displacements are continuous at the material interface. For determining the elastic modulus and the Poisson's ratio of the phases, the following expression is used (Ref. [6])

$$\frac{1}{E_r} = \frac{1-\nu^2}{E} + \frac{1-\nu_i^2}{E_i} \tag{1}$$

which links the measured data for the reduced modulus E_r with the elastic constants of the sample (E and ν) and the indenter (E_i and ν_i). The yield stress values have been calibrated by accomplishing a series of numerical simulations on indentation with a conic tip. The material parameter values are collected in table 1.

Table 1. Material parameter values used in simulations.

	E, [GPa]	ν	σ_Y, [GPa]
Indenter	1140	0.07	-
Al6082	71	0.33	0.28
γ-Al_2O_3	210.9	0.21	5.8

The dark colour in figure 2 represents areas being the secondary phases, grain boundaries, zones with porosity and microcracks which are treated as soft material and considered to be isotropic perfectly plastic as well. For the soft material model validation, the experimental data on hardness versus penetration depth obtained by the PEO-15µm coating surface micro-indentation (with Berkovich tip) have been utilized. Experimental data are presented as the blue dots in figure 3. Final thickness of the polished coating specimen used in the experimental study is 9 µm. The soft material has the same Poisson's ratio as the aluminium oxide. The Young's modulus and yield stress are calibrated by fitting the FE simulation results with the experimental data. Figure 3 shows and compares the simulation results for two sets of the soft material moduli values.

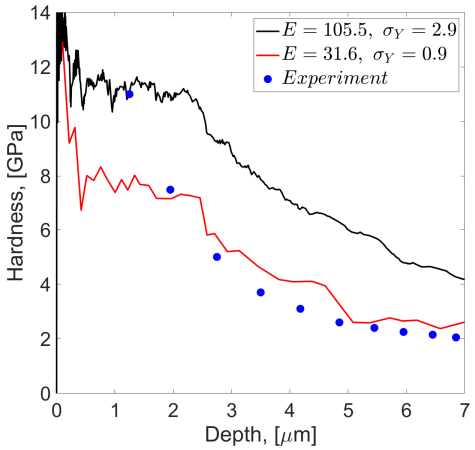

Figure 3. FE simulation results of PEO-15µm coating indentation. Values for Young's modulus E and yield stress σ_Y of soft material are given in GPa.

References

[1] A.L. Yerokhin, X. Nie, A. Leyland, A. Matthews, S.J. Dowey, Plasma electrolysis for surface engineering, *Surface and Coatings Technology*, 122:73–93, 1999.

[2] A.L.Yerokhin, V.V. Lyubimov, R.V. Ashitkov, Phase formation in ceramic coatings during plasma electrolytic oxidation of aluminium alloys, *Ceramics International*, 24:1–6, 1998.
[3] K. Holmberg, A. Laukkanen, E. Turunen, T. Laitinen, Wear resistance optimisation of composite coatings by computational microstructural modelling, *Surface and Coatings Technology*, 247:1–13, 2014.
[4] C.T. Wang, T.J. Hakala, A. Laukkanen, H. Ronkainen, K. Holmberg, N. Gao, R.J.K. Wood, T.G. Langdon, An investigation into the effect of substrate on the load-bearing capacity of thin hard coatings, *Journal of Materials Science*, 51:4390–4398, 2016.
[5] A.C.E. Reid, R.C. Lua, R.E. Garcia, V.R. Coffman, S.A. Langer, Modelling microstructures with OOF2, *International Journal of Materials and Product Technology*, 35:361–373, 2009.
[6] W.C. Oliver, G.M. Pharr, An improved technique for determining hardness and elastic modulus using load and displacement sensing indentation experiments, *Journal of Materials Research*, 7:1564–1583, 1992.

Proceedings of the 32nd Nordic Seminar on Computational Mechanics
A.H. Niemi and H. Koivurova (Eds.)

Goal Oriented Adaptive Isogeometric Methods applied to Structural Mechanics

Trond Kvamsdal*[1,2], Mukesh Kumar[3], Arne M. Kvarving[2], and Knut M. Okstad[2]

[(1)]Department of Mathematical Sciences, Norwegian University of Science and Technology, Trondheim, Norway. Trond.Kvamsdal@ntnu.no
[(2)]Department of Applied Mathematics and Cybernetics, SINTEF Digital, Norway. Trond.Kvamsdal@sintef.no, Arne.M.Kvarving@sintef.no, Knut.M.Okstad@sintef.no
[(3)]Department of Mathematics, College of Charleston, Charleston, SC, USA. kumarm@cofc.edu

Summary. Goal oriented recovery of sectional forces and stresses in structural mechanics

Key words: Isogeometric analysis, Goal oriented adaptivity, sectional forces, stresses

Introduction

The new paradigm of Isogeometric analysis, which was introduced by Thomas J. R. Hughes et al. [1], demonstrates that much is to be gained with respect to efficiency, quality and accuracy in analysis by replacing traditional Finite Elements by volumetric B-splines or NURBS elements. However, B-splines and NURBS are not flexible as they lack the possibilities of local refinement. However, the LR B-splines proposed by [2] facilitate adaptive mesh refinement [3].

To do *Goal Oriented Adaptivity* (GOA) i.e., adapt the finite element mesh for an identified *Quantity of Interest (QI)* (e.g., stress at a point or stress resultants at a cross section) we need a reliable *a posteriori error estimator* to drive the adaptive refinement procedure. Kumar, Kvamsdal and Johannessen [4] developed Continuous Global L_2 (CGL2) and Superconvergent Patch Recovery (SPR) error estimation methods applicable for LR B-splines, whereas in [5] we constructed an error estimator based on a Serendipity pairing of approximation spaces. We achieved very good results for all approaches (i.e., effectivity indices closed to 1) when applied to classical benchmark problems.

We will herein present results obtained for GOA for recovery of stresses and sectional forces in structural mechanics. The error estimates are based on use of CGL2.

References

[1] T. J. R. Hughes, J. A. Cottrell and Y. Bazilevs: Isogeometric analysis: CAD, finite elements, NURBS, exact geometry and mesh refinement, *Computer Methods in Applied Mechanics and Engineering*, 194:4135-4195, 2005.

[2] T. Dokken, T. Lyche and K. F. Pettersen: Polynomial Splines over Locally Refined Box-Partitions. *Computer Aided Geometric Design*, 30:331-356, 2013

[3] K. A. Johannessen, T. Kvamsdal, and T. Dokken. Isogeometric analysis using LR B-splines. *Computer Methods in Applied Mechanics and Engineering*, 269:471–514, 2014.

[4] Kumar, M., Kvamsdal, T. and Johannessen, K. A. Superconvergent patch recovery and a posteriori error estimation technique in adaptive isogeometric analysis. *Computer Methods in Applied Mechanics and Engineering*, 316:1086-1156, 2017.

[5] M. Kumar, T. Kvamsdal, and K.A. Johannessen: Simple a posteriori error estimators in adaptive isogeometric analysis. *Computer and Mathematics with Applications*, 70: 1555-1582, 2015.

Proceedings of the 32nd Nordic Seminar on Computational Mechanics
A.H. Niemi and H. Koivurova (Eds.)

Least Squares Stabilized Nitsche in CutIGA

Mats G. Larson[1] and Karl Larsson [2]

(1) Mathematics, Umeå University, mats.larson@umu.se
(2) Mathematics, Umeå University, karl.larsson@umu.se

Summary. We present a recently developed least squares stabilized symmetric Nitsche method for enforcement of Dirichlet boundary conditions for elliptic problems of second order in cut isogeometric analysis (CutIGA). We consider C^1 splines and stabilize the standard Nitsche method by adding an element wise least squares terms in the vicinity of the Dirichlet boundary and an additional term on the boundary which involves the tangential gradient. This approach enables us to prove coercivity, without invoking standard inverse estimates, and optimal order a priori error estimates.

Key words: isogeometric analysis, cut elements, cutfem, stabilization, least squares

Introduction

Cut finite element methods [2] allow the boundary of the computational domain to cut through the mesh in an arbitrary way leading to so called cut elements in the vicinity of the boundary. Since cut elements are not shape regular standard inverse inequalities used in the analysis of Nitsche's method for weak enforcement of Dirichlet boundary conditions does not hold and therefore the method must be stabilized in some way to guarantee coercivity. Standard approaches such as face based stabilization [2] or agglomeration [1, 6] leads to fill in in the stiffness matrix, which is avoided in the new method since the stabilization is element based.

In this note we review a recent version of Nitsche's method for cut isogeometric analysis proposed in [5] that enables us to prove coercivity without using inverse inequalities. The new formulation requires C^1 spline spaces and involves an additional least squares control of the Laplacian on elements close to the boundary and a tangential gradient control along the boundary. The additional terms provide better discrete representations of the function spaces used in analysis of the continuous elliptic problem and are therefore less sensitive to the underlying element geometry. In fact, we show coercivity for the new method in $V = H^2(\Omega)$, in contrast to standard Nitsche where coercivity is established for the finite element space V_h.

The Model Problem and Method

Let Ω be a domain in $\mathbb{R}^d$ with smooth boundary $\partial\Omega$ and consider the problem: find $u : \Omega \to \mathbb{R}$ such that

$$-\Delta u = f \quad \text{in } \Omega, \qquad u = g \quad \text{on } \partial\Omega \tag{1}$$

For sufficiently regular data there exists a unique solution to this problem and we assume that the solution satisfies the regularity estimate

$$\|u\|_{H^s(\Omega)} \lesssim \|f\|_{H^{s-2}(\Omega)} + \|g\|_{H^{s-1/2}(\partial\Omega)} \tag{2}$$

for some $s \geq 2$. Here and below $a \lesssim b$ means that there is a positive constant C such that $a \leq Cb$.

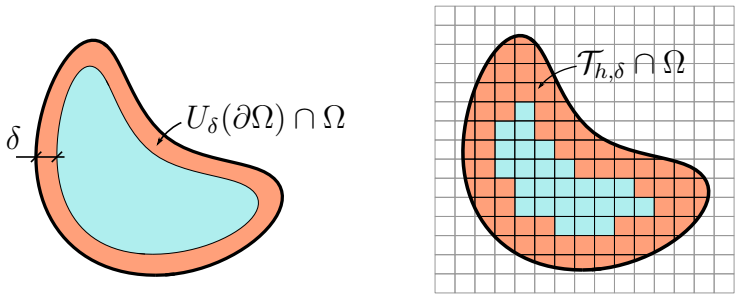

Figure 1. The subdomains $U_\delta(\partial\Omega)$ and $\mathcal{T}_{h,\delta} \cap \Omega$.

Let $\mathcal{T}_{h,0}$ be a partition of $\mathbb{R}^d$ into cubes with size h. Let $V_{h,0}$ be the space of C^1 splines of order $p \geq 2$ on $\mathcal{T}_{h,0}$, with standard basis $\mathcal{B}_{h,0}$. Let the active spline space be defined by

$$V_h = \operatorname{span}(\mathcal{B}_h), \qquad \mathcal{B}_h = \{\varphi \in \mathcal{B}_{h,0} \,|\, \operatorname{supp}(\varphi) \cap \Omega \neq \emptyset\} \tag{3}$$

The finite element method then takes the form: find $u_h \in V_h$ such that

$$A_h(u_h, v) = L_h(v) \qquad v \in V_h \tag{4}$$

The forms are defined as follows:

$$A_h(v, w) = a_h(v, w) - (n \cdot \nabla v, w)_{\partial\Omega} - (v, n \cdot \nabla w)_{\partial\Omega} + \beta b_h(v, w) \tag{5}$$
$$a_h(v, w) = (\nabla v, \nabla w)_\Omega + \tau\delta^2(\Delta v, \Delta w)_{\mathcal{T}_{h,\delta}\cap\Omega} \tag{6}$$
$$b_h(v, w) = (2 + \tau^{-1})\delta^{-1}(v, w)_{\partial\Omega} + 2\delta(\nabla_T v, \nabla_T w)_{\partial\Omega} \tag{7}$$
$$L_h(v) = (f, v)_\Omega - \tau\delta^2(f, \Delta v)_{\mathcal{T}_{h,\delta}\cap\Omega} - (g, n \cdot \nabla v)_{\partial\Omega} + \beta b_h(g, v) \tag{8}$$

and we employed the following notation:

- β is the penalty parameter which can take a moderate value, for instance $5 \leq \beta$, and $\tau > 0$ is a parameter which enables us to trade weight between the least squares bulk term and the standard Nitsche term.
- ∇_T is the tangential gradient at $\partial\Omega$ defined by $\nabla_T = P\nabla$, where $P = I - n \otimes n$ is the projection of vectors in $\mathbb{R}^d$ onto the tangent plane of the boundary $\partial\Omega$.
- In (6) and (8) we used the form

$$(v, w)_{\mathcal{T}_{h,\delta}\cap\Omega} = \sum_{T\in\mathcal{T}_{h,\delta}} (v, w)_{T\cap\Omega} \tag{9}$$

  where $\mathcal{T}_{h,\delta} \subset \mathcal{T}_h$ is defined by

$$\mathcal{T}_{h,\delta} = \mathcal{T}_h(U_\delta(\partial\Omega)) = \{T \in \mathcal{T}_h : T \cap U_\delta(\partial\Omega) \neq \emptyset\} \tag{10}$$

  and $U_\delta(\partial\Omega) = \{x \in \Omega : \operatorname{dist}(x, \partial\Omega) < \delta\}$ with $\delta \sim h$. In practice, if $\delta = h$ is used, $\mathcal{T}_{h,\delta}$ may be taken as the set of all elements that intersect the Dirichlet boundary $\partial\Omega$ and their neighbors, i.e. $\mathcal{T}_{h,\delta} = \mathcal{N}_h(\mathcal{T}_h(\partial\Omega))$, see Figure 1.

Discussion. The new terms, $\delta^2(\Delta v, \Delta w)_{\mathcal{T}_{h,\delta}\cap\Omega}$ and $\delta(\nabla_T v, \nabla_T w)_{\partial\Omega}$ with $\delta \sim h$, provide additional control on the elements in the vicinity of the boundary and along the boundary. The additional control along the boundary may be interpreted as weak enforcement of Dirichlet boundary conditions in $H^{1/2}(\partial\Omega)$, the trace space of $H^1(\Omega)$, and we note that

$$h^{-1}\|v\|^2_{\partial\Omega} + h\|\nabla_T v\|^2_{\partial\Omega} \tag{11}$$

is a discrete version of $\|v\|^2_{H^{1/2}(\partial\Omega)}$, which is more precise compared to the standard Nitsche method due to the presence of the second term. In the case when we do not have any cut elements we may employ an inverse inequality to conclude that

$$h^{-1}\|v\|^2_{\partial\Omega} + h\|\nabla_T v\|^2_{\partial\Omega} \lesssim h^{-1}\|v\|^2_{\partial\Omega} \tag{12}$$

and we recover the standard Nitsche penalty term. This is however not possible in the cut case where the additional term plays a key role. Furthermore, for $w \in H^1(\Omega)$ we have the standard estimate

$$|(n\cdot\nabla v, w)_{\partial\Omega}| \leq (\|\nabla v\|^2_\Omega + \|\Delta v\|^2_\Omega)^{1/2}\|w\|_{H^1(\Omega)} \tag{13}$$

and thus for the left hand side to be well posed we need control of $\|\Delta v\|_\Omega$ in addition to $\|\nabla v\|_\Omega$. We note that $\delta^2(\Delta v, \Delta w)_{\mathcal{T}_{h,\delta}\cap\Omega}$ provides such control close to the boundary, which turns out to be enough. Finally, if we do not have cut elements an inverse inequality gives

$$\delta^2\|\Delta v\|^2_\Omega \lesssim \|\nabla v\|^2_\Omega \tag{14}$$

since $\delta \sim h$ and thus in that case $\delta^2\|\Delta v\|^2_\Omega$ is dominated by $\|\nabla v\|^2_\Omega$, which is already present in the standard variational form.

Summary of Theoretical Results

We summarize the main results in the analysis of the stabilized finite element method. Define the norms

$$|||v|||^2_h = \|v\|^2_{a_h} + \|v\|^2_{b_h} \tag{15}$$

$$\|v\|^2_{a_h} = a_h(v,v) = \|\nabla v\|^2_\Omega + \tau\delta^2\|\Delta v\|^2_{\mathcal{T}_{h,\delta}\cap\Omega} \tag{16}$$

$$\|v\|^2_{b_h} = b_h(v,v) = (2+\tau^{-1})\delta^{-1}\|v\|^2_{\partial\Omega} + 2\delta\|\nabla_T v\|^2_{\partial\Omega} \tag{17}$$

- **Galerkin Orthogonality.** It holds

$$A_h(u-u_h, v) = 0 \qquad \forall v \in V_h \tag{18}$$

  This identity follows directly from the consistency of the standard Nitsche method and the fact that we have only added consistent least squares terms.

- **Weak Trace Form Inequality.** The following estimate holds

$$|(n\cdot\nabla v, w)_{\partial\Omega}| \lesssim \|v\|_{a_h}\|w\|_{b_h} \qquad v, w \in V \tag{19}$$

  where $V = H^2(\Omega)$.

- **Coercivity**. For $\beta > 0$ sufficiently large the form A_h is coercive

$$|||v|||^2_h \lesssim A_h(v,v) \qquad v \in V \tag{20}$$

  Note that we get coercivity on V not on V_h which is the case in the standard Nitsche method.

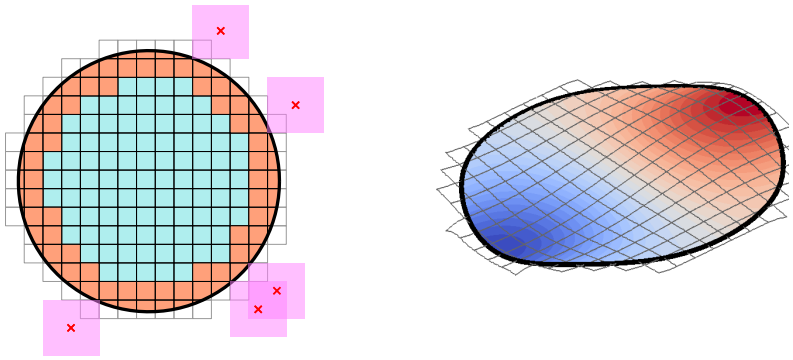

Figure 2. Numerical example. *Left:* Computational mesh with the subdomain $\mathcal{T}_{h,\delta} \cap \Omega$ and the support of C^1 splines selected for basis function removal indicated. *Right:* Numerical solution.

- **Continuity**. The form A_h is continuous

$$|A_h(v,w)| \lesssim |||v|||_h |||w|||_h \qquad v, w \in V \tag{21}$$

- **Error Estimates.** The following error estimates holds

$$|||u - u_h|||_h \lesssim h^p \|u\|_{H^{p+1}(\Omega)} \tag{22}$$

$$\|u - u_h\|_\Omega \lesssim h^{p+1} \|u\|_{H^{p+1}(\Omega)} \tag{23}$$

Conditioning of the Stiffness Matrix. Despite the fact that we have coercivity with respect to the energy norm $|||\cdot|||_h$ the stiffness matrix may be highly ill conditioned, possibly depending on the position of Ω in the background mesh $\mathcal{T}_{h,0}$. This can be understood by observing that $\min_{\varphi \in \mathcal{B}_h} |||\varphi|||_h$ may be arbitrarily small. To remedy this problem we may employ so called basis removal where we simply remove basis functions with very small energy norm without sacrificing accuracy, see [4] for details. If an iterative solver is used we first apply a preconditioner, see for instance [3], to the stiffness matrix.

Numerical Example

To illustrate the method we give a small numerical example in Figure 2 where we solve a non-homogeneous Dirichlet problem on a circular domain. For this example we use C^1 splines ($p = 2$) and parameter values $\delta = h$, $\beta = 5$ and $\tau = 0.1$.

References

[1] S. Badia, F. Verdugo, and A. F. Martín. The aggregated unfitted finite element method for elliptic problems. *Comput. Methods Appl. Mech. Engrg.*, 336:533–553, 2018.

[2] E. Burman, S. Claus, P. Hansbo, M. G. Larson, and A. Massing. CutFEM: discretizing geometry and partial differential equations. *Internat. J. Numer. Methods Engrg.*, 104(7):472–501, 2015.

[3] F. de Prenter, C. V. Verhoosel, G. J. van Zwieten, and E. H. van Brummelen. Condition number analysis and preconditioning of the finite cell method. *Comput. Methods Appl. Mech. Engrg.*, 316:297–327, 2017.

[4] D. Elfverson, M. G. Larson, and K. Larsson. CutIGA with basis function removal. *Adv. Model. Simul. Eng. Sci.*, 5(6):1–19, 2018.

[5] D. Elfverson, M. G. Larson, and K. Larsson. A new least squares stabilized Nitsche method for cut isogeometric analysis. *Comput. Methods Appl. Mech. Engrg.*, 349:1–16, 2019.

[6] A. Johansson and M. G. Larson. A high order discontinuous Galerkin Nitsche method for elliptic problems with fictitious boundary. *Numer. Math.*, 123(4):607–628, 2013.

Proceedings of the 32nd Nordic Seminar on Computational Mechanics
A.H. Niemi and H. Koivurova (Eds.)

Thurster Driveline Digital Twin – Bearing and Shaft Fatigue Life Prediction

Taneli Leppänen[1]

[(1)]Tampere University (EDR&Medeso), Taneli.leppanen@tuni.fi

Summary. Development of a digital twin for thruster driveline digital twin. Adaptation of ISO 16281 for bearing and DIN 743 for shaft fatigue analysis into a digital twin framework.

Key words: digital twin, fatigue, standards, ISO 16281, DIN 743, shafts, bearings

Introduction

International standards have for long been a cornerstone for fatigue life analysis in the design phase for machine elements, such as bearings and shafts. Fatigue life prediction is usually done based on the assumed operational profile of the machine and thus it has to be substantially conservative. This usually leads to over sized parts and shorter than needed maintenance intervals.

To more closely predict the fatigue life of machine elements we can embed sensors into our systems to monitor the actual operational conditions the machine and then perform the fatigue life analysis on our measured data. Since our data might not accurately represent the average conditions if e.g. it experiences some once in a lifetime loading in the early stages our model might be too conservative or if loading is only minimal, but we predict that some extreme loading will occur in the future, our prediction might be skewed. To account for the loadings we assume to happen, we generate the future loading profiles using Bayesian analysis.

This combination of live measurement data and physics-based analysis of a real asset is what is called the digital twin. In this master's thesis ISO 16281 standard for bearing fatigue life prediction and DIN 743 fatigue life prediction we adapted to a real time analysis of an asset based on measured loading profiles. As the aforementioned standards were developed for use in the design phase of the asset, provided some unique obstacles, but we were able to overcome these and adapt them into the digital twin environment.

Proceedings of the 32nd Nordic Seminar on Computational Mechanics
A.H. Niemi and H. Koivurova (Eds.)

Modeling friction and wear in dynamically loaded clamped metal contacts

A. Mäntylä[1], J. Hintikka[1], and T. Frondelius[1,2]

(1)Wärtsiä Finland Oy, antti.mantyla@wartsila.com
(1)Wärtsiä Finland Oy, jouko.hintikka@wartsila.com
(2)University of Oulu, tero.frondelius@oulu.fi

Summary. Methodology for damage modeling of cyclically loaded metal contacts is presented. Flexible multibody dynamics is used to simulate vibrations of large combustion engine powers system, and especially counterweights (CWs) bolted to the crankshaft. Vibration results match well with the measurement from the real engine. Non-linear finite element method is used to simulate contact behavior between the CW and crankshaft. Local hardening of the friction coefficient and material removal due to wear is considered by using contact subroutine in commercial finite element solver Abaqus. The methodology can be used to predict surface damage due to fretting and the effect of wear on contact behavior.

Key words: multibody dynamics, finite element method, contact, friction, fretting, wear

Introduction

Simulation of highly loaded clamped metal contacts has become utmost important in the development of medium speed combustion engines. In a large combustion engine, there are lots of heavily loaded contact interfaces and large moving sub-assemblies which reliability need to be ensured by simulation. Today, non-linear Finite Element Method (FEM) is used to simulate contacts, especially in industrial cases where geometries are complicated. Wärtsilä has a long history in structural FEM simulations starting at 1973 [1]. Also flexible multi-body simulation (MBS) methodology is commonly used in Wärtsilä to be able to capture complicated dynamics of engine components [2, 3]. Laboratory testing of large engines is expensive, and damage in critical contacts can lead to unexpected catastrophic failures. An example of connecting rod failure caused by fretting fatigue can be found from [4].

Fretting fatigue is a dangerous damage phenomenon in contacts caused by small-amplitude cyclic sliding. In fretting fatigue, localized cyclic surface stresses cause crack initiation even without remarkable macroscale stresses in the structure. Furthermore, fretting wear affects the contact pressure distribution and changes the contact behavior and may cause loosening of the contact. In fretting the coefficient of friction (COF) is varying a lot as a function of load cycles and loading, which sets numerical and theoretical challenges in the simulation of such cases. Some studies to consider variable friction [5] and non-uniform friction [6, 7] in the simulation of fretting experiments has been made. Effects of fretting wear have been studied by implementing Archard wear law [8, 9, 10]. However, applications of these kinds of models in component level simulations are very limited. One example without wear simulation can be found from [11].

This paper describes a contact model that considers local COF "hardening" and material removal due to wear in cyclically loaded clamped metal contacts. Model is implemented in commercial FEM solver Abaqus by using subroutine UINTER. The presented methodology is applied to a bolted contact interface between crankshaft and counterweight of a large, medium-

speed combustion engine to evaluate the risk of surface damage due to fretting and effect of wear on the functionality of the joint.

Methods

Power system dynamics of a large combustion engine is complicated due to several excitation sources. However, power system vibrations can be simulated accurately by using flexible multi-body simulation (MBS) even up to high frequencies. Such a model is shown in Fig.1 and similar MBS models are described in more detail in [2, 12]. MBS model was validated by acceleration measurements in a running engine by using the measurement device described in [13].

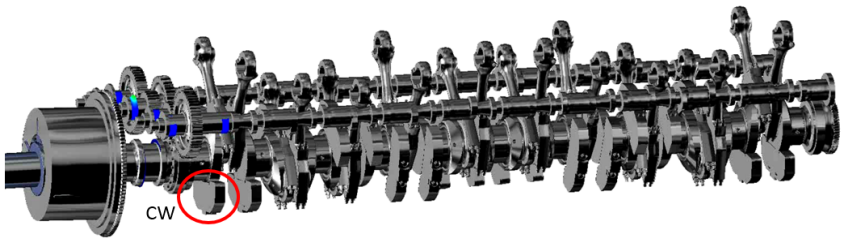

Figure 1. Flexible MBS model of large engine power system.

Contact stresses and displacements between the crankshaft and CW are solved by using the non-linear finite element model in Abaqus. The model includes one CW bolted to the piece of the crankshaft, and results from MBS are used as boundary conditions. Contact is modeled using the standard surface to surface discretization with the finite sliding formulation of Abaqus. However, the contact physics in normal and tangential directions are replaced by subroutine UINTER. Local COF evolution is described by using accumulated frictional energy dissipation. This approach is motivated by the COF measurements in [14], and it conveniently includes the effect of contact pressure and slip. Material removal due to wear is modeled by introducing a nodal gap according to Archard wear law. In fretting conditions, the hardening of COF is very fast, and max value of COF is usually obtained around some hundreds of cycles as can be seen from the results [15, 16]. Same experiments show that there is a stable value of COF below which contact stays in stick condition and surface damage does not occur. The maximum value of this stable limit is also used in the contact model. COF for analysis increment n is defined as

$$\mu_{n+1} = \begin{cases} \mu_n + k \cdot \Delta\gamma_{eq}^{sl} \cdot \tau_{eq} & \text{if} \quad \mu_{n+1} < \mu_{max} \\ \mu_{max} & \text{if} \quad \mu_{n+1} \geq \mu_{max}, \end{cases} \tag{1}$$

where k is a constant defining the speed of friction coefficient increase, $\Delta\gamma_{eq}^{sl}$ is equivalent "plastic" slip, τ_{eq} is equivalent shear traction and μ_{max} is maximum allowed value of the COF.

If the contact is sliding after the stabilized COF distribution is obtained, wear simulation is activated. This sequencing is done due to the fact that COF hardening is much faster than the effect of wear. Material removal depth due to wear is defined as

$$r_{n+1} = \begin{cases} r_n + w \cdot \Delta\gamma_{eq}^{sl} \cdot p & \text{if } p \geq p_{lim} \\ r_n & \text{if } p < p_{lim}, \end{cases} \tag{2}$$

where w is a constant, p is contact pressure and p_{lim} is the limit value below which the wear does not occur. In this case, low value of 1 MPa is used.

Results and discussion

MBS results show that crankshaft experiences low frequency (<100Hz) axial and torsional vibrations caused by the firing forces and higher frequency (>100 Hz) vibration coming from the gear trains and thrust bearing impacts. Comparison of simulated and measured acceleration spectrum in Fig.2 show that the MBS model can well capture CW vibration even up to 1kHz. Lowest CW natural frequencies are in the range of 200-1000Hz, and the most significant natural mode where CW wings are vibrating in opposite phase with each other is close to 400Hz.

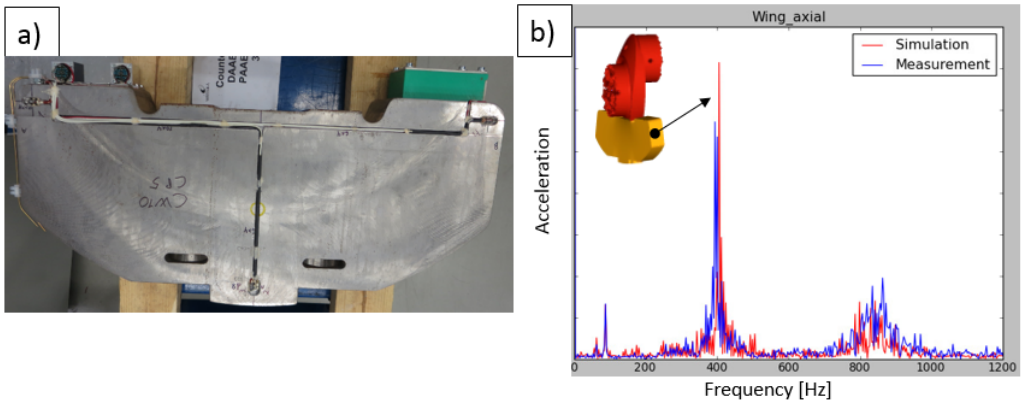

Figure 2. Simulated and measured CW acceleration spectra.

Non-linear contact simulation in Abaqus reveals that almost the whole contact areas are sliding with initial COF of 0.2. Stabilized COF distribution in Fig.3a shows areas where COF has not increased meaning that those areas have been all the time in stick, but elsewhere the COF has increased. Maximum allowed COF was 0.7 and some areas have reached this value meaning that surface damage would be expected on these areas based on the measurements in [15]. Some areas of the contact slide even with maximum COF of 0.7 and wear simulation results to about 0.1mm deep material removal as shown in Fig.3b. As wear only happens locally without causing loosening of the contact, it means that the contact shakes down to fully stuck condition. Future stress and fatigue analysis could be performed to investigate if the worn state is dangerous or not. The presented methodology can be applied to cyclically loaded clamped metal contacts to examine their functionality over the lifetime and also to predict if surface damage or wear occurs.

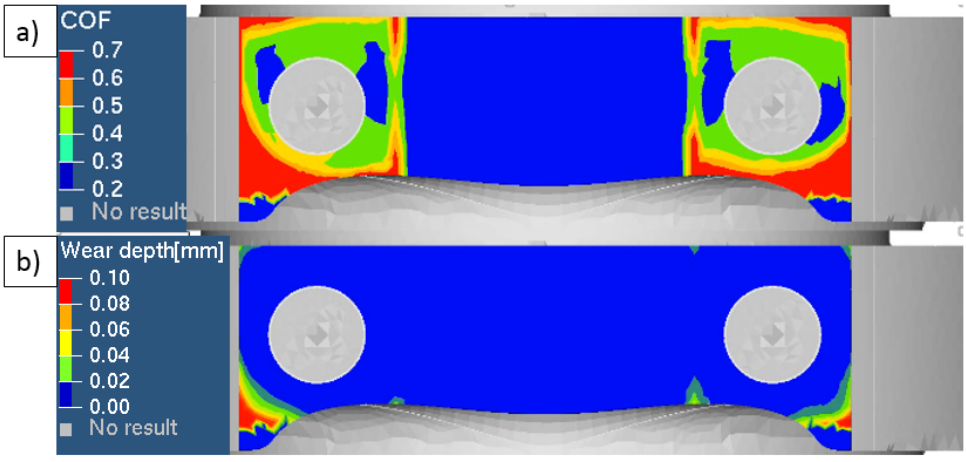

Figure 3. Simulated and measured CW acceleration spectra.

References

[1] Tero Frondelius, Hannu Tienhaara, and Mauri Haataja. History of structural analysis & dynamics of wärtsilä medium speed engines. *Rakenteiden Mekaniikka*, 51(2):1–31, 2018.

[2] Tero Frondelius, Pasi Halla-aho, and Antti Mäntylä. Crankshaft development with virtual engine modelling. In *CIMAC Congress Helsinki*, 2016.

[3] Jussi Göös, Anton Leppänen, Antti Mäntylä, and Tero Frondelius. Large bore connecting rod simulations. *Rakenteiden Mekaniikka*, 50(3):275–278, 2017.

[4] Roger Rabb, Pekka Hautal, and Arto Lehtovaara. Fretting fatigue in diesel engineering. In *CIMAC World Congress 2007*.

[5] Tongyan Yue and Magd Abdel Wahab. Finite element analysis of fretting wear under variable coefficient of friction and different contact regimes. *Tribology International*, 107(Supplement C):274 – 282, 2017.

[6] Sam Naboulsi and Ted Nicholas. Limitations of the coulomb friction assumption in fretting fatigue analysis. *International Journal of Solids and Structures*, 40(23):6497 – 6512, 2003.

[7] M Cheikh, S Quilici, and G Cailletaud. Presentation of ki-cof, a phenomenological model of variable friction in fretting contact. *Wear*, 2007.

[8] J. F. Archard. Contact and rubbing of flat surfaces. *Journal of Applied Physics*, 24(8):981–988, 1953.

[9] Toshio Hattori, Kouki Yamashita, and Yuusuke Yamashita. Simple estimation method of fretting fatigue limit considering wear process. *Tribology International*, 108(Supplement C):69 – 74, 2017. Proceedings of The 8th International Symposium on Fretting Fatigue.

[10] JJ Madge, SB Leen, IR McColl, and PH Shipway. Contact-evolution based prediction of fretting fatigue life: effect of slip amplitude. *Wear*, 262(9-10):1159–1170, 2007.

[11] Antti Mäntylä, Jussi Göös, Anton Leppänen, and Tero Frondelius. Large bore engine connecting rod fretting analysis. *Rakenteiden Mekaniikka*, 50(3):239–243, 2017.

[12] Teemu Kuivaniemi, Antti Mäntylä, Ilkka Väisänen, Antti Korpela, and Tero Frondelius. Dynamic gear wheel simulations using multi body dynamics. *Rakenteiden Mekaniikka*, 50(3):287–291, 2017.

[13] Pasi Halla-aho, Antti Mäntylä, Tero Frondelius, Tommi Helander, and Juha Hautala. Counterweight measurements device development. *Rakenteiden Mekaniikka*, 50(3):318–322, 2017.

[14] Jouko Hintikka, Arto Lehtovaara, and Antti Mäntylä. Fretting-induced friction and wear in large flat-on-flat contact with quenched and tempered steel. *Tribology International*, 92:191 – 202, 2015.

[15] Jouko Hintikka, Antti Mäntylä, Joona Vaara, Tero Frondelius, and Arto Lehtovaara. Stable and unstable friction in fretting contacts. *Tribology International*, 131:73 – 82, 2019.

[16] Jouko Hintikka, Arto Lehtovaara, Tero Frondelius, and Antti Mäntylä. Tangential traction instability in fretting contact below fully developed friction load. *Rakenteiden mekaniikka*, 50(3):175–178, 2017.

Acknowledgements

The authors would like to acknowledge the financial support of Business Finland in the form of a research project ISA Wärtsilä Dnro 7734/31/2018.

Proceedings of the 32nd Nordic Seminar on Computational Mechanics
A.H. Niemi and H. Koivurova (Eds.)

A numerical framework for rate-independent for Fleck and Willis crystal plasticity

Kim Lau Nielsen[1]

(1)Department of Mechanical Engineering, Section of Solid Mechanics, Technical University of Denmark, DK-2800 Kgs. Lyngby, Denmark

Summary. A vast amount of research continues to go into developing robust numerics to handle rate-independent crystal plasticity - either by making use of additional constitutive models or complex numerics. The present work attempts to circumvent such special measures by taking a new approach to develop a numerical solution procedure for a rate-independent crystal plasticity, relying on the Fleck and Willis gradient plasticity theory. The adopted constitutive model reduces to that of conventional plasticity in the limit of zero length parameter and, thus, constitutes a tool that covers both branches of plasticity.

Key words: Crystal plasticity, Rate-independent, Finite element modeling

Introduction

The issue with rate-independent crystal plasticity boils down to a uniqueness problem in determining which slip systems are active. In essence, plastic incompressibility requires five ($\alpha = 5$) linearly independent slip systems when adopting a Schmid-like relation of the plastic strain increment. This can be realized by written out: $\dot{\varepsilon}^p_{ij} = \sum_\alpha \mu^{(\alpha)}_{ij}\dot{\gamma}^{(\alpha)}$, with $\mu^{(\alpha)}_{ij}$ being the Schmid orientation tensor for the α'th slip system, and $\dot{\gamma}^{(\alpha)}$ the associated slip increment. The problem arises when one includes the 6'th slip system, being easily imaginable for real crystals (FCC crystals have 12 independent slip systems, BCC crystals have a many as 48). One thereby ends up with an over-determined system (the five plastic strain increment component is not uniquely described), whereby a particular solution is out of reach. Pierce et al. [1] demonstrated that this uniqueness problem can be circumvented by adopting a rate-sensitive model formulation where the increment of plastic strain is tied to the current stress state rather than the stress increments (as in the rate-independent case). This approach allows widening the parameter space, but it leaves a strain rate dependency in the model (although the model response can be pushed towards the rate-independent limit).

The present work attempts to follow a similar idea but here lets gradient effects regularized the problems at hand. The work takes offset in the Fleck and Willis theory where two equilibrium equations (or rather, one conventional equilibrium and one equilibrium for each slip system) is considered. These read: $\sigma_{ij,j} = 0$ (in absence of body forces) and $q^{(\alpha)} - \tau^{(\alpha)} - \xi^{(\alpha)}_i s^{(\alpha)}_i = 0$, where σ_{ij} is the Cauchy stress tensor, $\xi^{(\alpha)}$ is the higher order stress, $q^{(\alpha)}$ is the micro-stress, and $s^{(\alpha)}_i$ is the slip system direction. Based on the higher order equilibrium equation, Fleck and Willis put forward the Minimum Principle I which delivers the slip rate field to with a plastic multiplier with in a rate-independent framework (see e.g. Nielsen and Niordson [4]). In a crystal plasticity setup, the Minimum Principle I reads

$$H = \inf_{\dot{\gamma}^{(\alpha)*}} \int_V \Big(\tau_F[\gamma^{(\alpha)}_e]\dot{\gamma}^{(\alpha)*}_e + \xi^{E(\alpha)} s^{(\alpha)}_i \dot{\gamma}^{(\alpha)*}_{,i} - s_{ij}\mu^{(\alpha)}_{ij}\dot{\gamma}^{(\alpha)*} \Big) \mathrm{d}V - \int_S r^{(\alpha)}\dot{\gamma}^{(\alpha)*}\mathrm{d}S, \qquad (1)$$

where the flow stress on the α'th slip system is $\tau_F[\gamma_e^{(\alpha)}]$, the energetic higher order stress is $\xi^{E(\alpha)}$ (and $r^{(\alpha)}$ the related higher order tractions). It is worth to notice that the variation in the slip rate field is directly tied to the current stress state through Eq. (1), while only the magnitude of the field is determined in a subsequent step relying on the conventional equilibrium equation. It is the expectation that such dependency on the surrounding stress field for a specific material point (holding a number of slip systems) can facilitate a numerical implementation without further specialize algorithms, or additional constitutive models, to determine which slip systems are active. The proposed numerical procedure employs the finite element method and essentially extends the work in Nielsen and Niordson [4] (focusing on isotropic plasticity) to a corresponding crystal plasticity framework in line with Niordson and Kysar [3].

Results

The numerical procedure is demonstrated through Fig. 1, displaying the overall load-displacement curves when subjecting a HCP-like crystal to shear loading. The crystal is orientated such that the deformation takes place in the basal plane, while the slip systems are oriented at $\theta = [90, -30, 30]^\circ$ as indicated in the Fig 1. The new rate-independent framework is compared to its (readily implemented) visco-plastic counterpart for two distinct length scales and two levels of strain hardening. The prediction of the two models are very close when pushing the visco-plastic model towards the rate-independent limit. Moreover, it is seen that the new model easily copes with having one slip system (at 90°) active in the beginning, while continued strain hardening on that the first active slip system subsequently allows the two remaining slip systems to be activated.

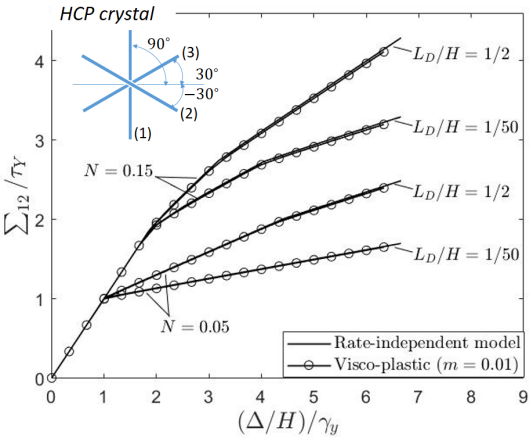

Figure 1. Load-displacement curve for monotonic shearing of a HCP-like single crystal.

Concluding remarks

A rate-independent crystal plasticity framework relying on the Fleck and Willis [2] plasticity theory has been implemented within a 1D finite element framework. Shear deformation of an oriented HCP crystal is considered and the activation of multiple slip system demonstrated.

Acknowledgements

The work is supported by the Danish Council for Independent Research, grant DFF-7017-00121.

References

[1] D. Pierce and R.J. Asaro and A. Needleman Material rate dependence and localized deformation in crystalline solids *Acta Metall.*, 1951–1976, 1983.

[2] N.A. Fleck and J.R. Willis A mathematical basis for strain-gradient plasticity theory. Part II: Tensorial plastic multiplier *J. Mech. Phys. Solids*, 1045–1057, 2009.

[3] C.F. Niordson and J.W. Kysar Computational strain gradient crystal plasticity *J. Mech. Phys. Solids*, 31–47, 2014.

[4] K.L. Nielsen and C.F. Niordson A numerical basis for strain-gradient plasticity theory: rate-independent and rate-dependent formulations *J. Mech. Phys. Solids*, 113-127, 2014.

Proceedings of the 32nd Nordic Seminar on Computational Mechanics
A.H. Niemi and H. Koivurova (Eds.)

Reliability of Finnish steel trusses under snow load in light of the design standard EN 1990

Antti H. Niemi

Structures and Construction Technology Research Unit
Faculty of Technology
University of Oulu, Finland
antti.niemi@oulu.fi

Summary. It is shown that some of the Finnish national choices concerning application of the EN 1990 structural design standard may lead to lower level of reliability than what is desired in the standard. Namely, the load combination rule that is currently being employed may lead to decreased level of reliability especially when variable loads constitute a major portion of the total load which is a typical situation for steel trusses located e.g. in the Finnish regions of North Ostrobothnia and Kainuu.

Key words: structural reliability, snow load, design principles of structures

Introduction

Let us assume a design situation where the behaviour of a critical structural component can be characterized by a group of random variables $\boldsymbol{X} = (X_1, X_2, \ldots, X_n)$, that represent e.g. loads, material properties or uncertainties related to the mathematical models. The limit state of the structure can then be characterized by a limit state function $g(\boldsymbol{X})$, which in the analysis of ultimate limit state can be assumed to be of the form

$$g(\boldsymbol{X}) = R(\boldsymbol{X}) - E(\boldsymbol{X}),$$

where $R(\boldsymbol{X})$ represents the resistance of the structural component and $E(\boldsymbol{X})$ represents the effect of an action to the component. Both quantities are assumed to be expressed in the same unit.

The safe, unsafe, and the ultimate limit state are then characterized by the conditions $g(\boldsymbol{X}) \geq 0$, $g(\boldsymbol{X}) < 0$, and, $g(\boldsymbol{X}) = 0$, respectively.

Let us consider a situation, where a structural component is loaded by a single variable load Q in addition to its self-weight G. The structural response is assumed to be linear with the same proportionality coefficient under both loads. If the uncertainties in the formulation and analysis of the mathematical model of the structure are denoted by the random variable θ_E, then the effect of the loads is given by

$$E = \theta_E(G + Q). \tag{1}$$

If θ_R is a similar random variable related to the uncertainties of the resistance model, then the limit state function becomes

$$g(\boldsymbol{X}) = \theta_R R - \theta_E(G + Q), \tag{2}$$

where the random variables are $\boldsymbol{X} = (G, Q, R, \theta_E, \theta_R)$. The failure probability p_f can then be written in terms of the joint probability density distribution $f_g(\boldsymbol{X})$ as

$$p_f = \int_{g(\boldsymbol{X}) \leq 0} f_g(\boldsymbol{X}) \, \mathrm{d}\boldsymbol{X}. \tag{3}$$

Determination of the joint probability density and computation of (3) constitute a major problem in structural reliability analysis. However, in the current situation, it can be assumed that the resistance and the load effect represent e.g. a single stress resultant such as normal force or bending moment that is used to determine the structural performance. Then the failure probability becomes

$$p_f = \int_{-\infty}^{\infty} f_E(z) \int_{-\infty}^{z} f_R(s)\,\mathrm{d}s\mathrm{d}z \tag{4}$$

Often, like in Annex C of EN 1990 [1], an alternative measure of reliability is defined by the reliability index β, which is related to the failure probability as

$$p_f = \Phi(-\beta), \tag{5}$$

where Φ is the cumulative distribution function of the standardised normal distribution.

Results for one variable load

In general, the design value of the action effect E_d for a single variable action is written as

$$E_d = \gamma_G G_k + \gamma_Q Q_k, \tag{6}$$

where G_k and Q_k are the characteristic values of the permanent and variable load, respectively, and γ_G and γ_Q are the corresponding partial factors. Similarly, the, design value of the resistance is

$$R_d = R_k/\gamma_M \tag{7}$$

where R_k is its characteristic value and γ_M denotes the partial factor for the material.

The National Building Code of Finland [3] defines the design load as the less favourable action from the two expressions

$$E_{d1} = 1.15G_k + 1.5Q_k \quad \& \quad E_{d2} = 1.35G_k \tag{8}$$

It is clear, that the level of reliability depends on the ratio of the characteristic load values defined as

$$\chi = Q_k/(G_k + Q_k). \tag{9}$$

Variation of the reliability index with χ for different choices of partial factors can be assesed by approximate computation of the failure probability (4). Following the approach of [2] and using there suggested probability distributions for generic actions, resistance, and uncertainties, the results shown in Fig. 1 can be obtained for a 50-year time period.

Concluding remarks

The results show that the target reliability of $\beta = 3.8$ set in the EN 1990 standard may not be reached by the choice (8) especially when χ is high (or very low). In a recent master's thesis work [4], it was shown that in a typical design situation of steel truss under snow load in Finland, the values of χ vary in the range 0.75-0.87, and the high end may be reached e.g. in the regions of North Ostrobothnia and Kainuu. The level of reliability could be increased by increasing the values of partial factors. It should be noted that similar conclusions have been drawn earlier in [5] by using slightly different arguments.

Finally, it should be noted that the reliability assessment depends heavily on the assumed probability distributions for different quantities and also on the approximative method used to evaluate the joint probability density (3). Therefore, the results of these preliminary studies should be approached with some caution. Anyway, it is clear that further investigations are necessary and a more detailed analysis is on the way [6, 7].

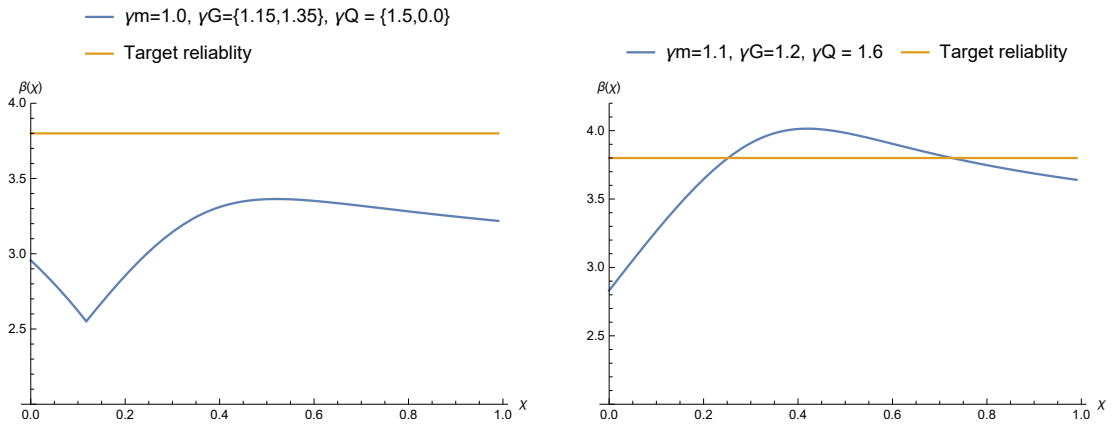

Figure 1. Variation of the reliabity index with χ.

Acknowledgements

This research has been supported by Oulun rakennustekniikan säätiö. The support is gratefully acknowledged.

References

[1] EN 1990:2002 Eurocode-Basis of Structural Design. European Committee for Standardisation, Brussels, 2002.

[2] H. Gulvanessian and M. Holicky (2005). *Eurocodes: using reliability analysis to combine action effects*. Proceedings of the Institution of Civil Engineers - Structures and Buildings.

[3] National Building Code of Finland. Strength and stability of structures. Basis of structural design for load-bearing structures. Ministry of Environment, Helsinki, 2016.

[4] Simo Impiö (2019). Tapaustutkimus lumen kuormittamien teräsrakenteiden luotettavuudesta. Diplomityö (In Finnish). University of Oulu, Faculty of Technology, Civil engineering. Oulu. 56 pp.

[5] Poutanen, T., Pursiainen, S., Mäkinen, J and Länsivaara, T. 2018. Combination of permanent and variable loads. Rakenteiden mekaniikka (Journal of Structural Mechanics), 51 (1), s. 1-9.

[6] Antti H. Niemi and Matti Kangaspuoskari. Lumikuormitettujen teräsristikoiden varmuus Suomessa standardin EN 1990 valossa. Osa I: suunnitteluperusteet (In Finnish, in preparation)

[7] Matti Kangaspuoskari and Antti H. Niemi. Lumikuormitettujen teräsristikoiden varmuus Suomessa standardin EN 1990 valossa. Osa II: kuormitustapaukset (In Finnish, in preparation)

Proceedings of the 32nd Nordic Seminar on Computational Mechanics
A.H. Niemi and H. Koivurova (Eds.)

Parametric modelling of cellular beam and plate structures by orthotropic strain gradient thermo-elasticity

Jarkko Niiranen[1], Sergei Khakalo[2], and Viacheslav Balobanov[2]

[(1)]Department of Civil Engineering, Aalto University, jarkko.niiranen@aalto.fi
[(2)]VTT Technical Research Centre of Finland, sergei.khakalo@vtt.fi, viacheslav.balobanov@vtt.fi

Summary. For three-dimensional cellular beam- and plate-like structures with a triangular microarchitecture, this conference contribution presents a family of two-scale beam and plate models relying on the anisotropic form of Mindlin's strain gradient elasticity theory of form II. A computational homogenization method is adopted for determining the constitutive parameters of the related classical and higher-order constitutive tensors. Isogeometric conforming Galerkin methods are applied for solving the beam and plate problems. Numerical examples illustrate the reliability and efficiency of the dimensionally reduced structural models and numerical methods – in capturing the bending size effects induced by the microarchitecture, in particular.

Key words: lattice microarchitecture, cellular structures, Euler–Bernoulli beam, Timoshenko beam, Kirchhoff plate, Reissner–Mindlin plate, size effects, strain gradient thermoelasticity, isogeometric analysis

Introduction

Cellular or lattice metamaterials, realized today even in nano- and micro-scales, have become an extremely promising class of lightweight, functional metamaterials. On one hand, the rapid development of additive manufacturing technologies for different parent materials across the scales has played an important role in this trend. On the other hand, the extreme fundamental properties of lattice architectures have increased the attractiveness of this class of metamaterials: high and adjustable stiffness-to-weight ratio, strength-to-weight ratio and surface-to-volume ratio have made different kinds of lattices apt for a variety of applications in machines, vehicles, buildings or bioproducts, e.g., as lightweight structures, dampers, absorbers, insulators, heat exchangers and filters.

Modeling the physics and mechanics of solids and structures with a lattice microarchitecture is neither trivial nor computationally cheap for several reasons mainly related to the complex geometries of the underlying microarchitecture (see the illustrations in Fig. 1).

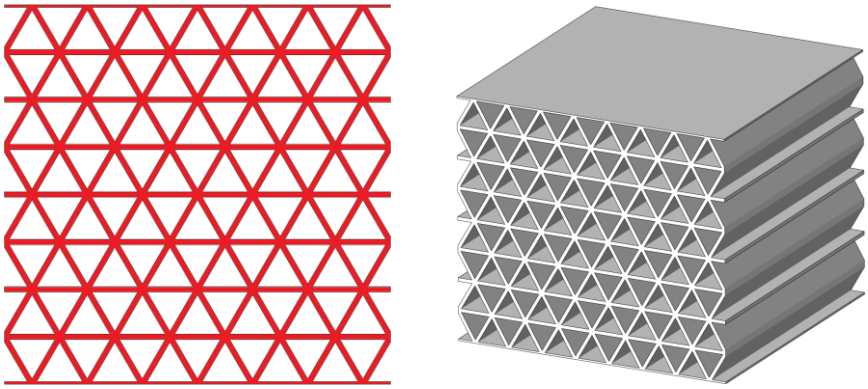

Figure 1. A triangular planar lattice (left) and its cellular spacial extrusion (right).

Structures, models and methods

The present contribution focuses on the theoretical and numerical physico-mathematical modeling of thin and thick beam- and plate-like structures composed of a cellular triangular microarchitecture metamaterial (see Fig. 2 and Fig. 3, left). The thermomechanical modelling of these microarchitectural structures is accomplished in the framework of orthotropic strain gradient thermo-elasticity (having origins in Ref. [1]) via the corresponding beam and plate models, Galerkin methods (see Refs. [2–10]) as well as computational homogenization of classical and non-classical types (see Refs. [5, 6, 9]).

In essence, it is shown that with generalized beam and plate models dimensionally reduced from a three-dimensional orthotropic Mindlin type strain gradient solid (formulated in Ref. [9]), the size-dependent mechanical bending of thin and thick beams and plates can be modelled in a theoretically novel and computationally efficient way (see Refs. [5, 6, 9]). A computational homogenization method determines the required set of non-classical material parameters via matching the global responses of full-field simulations with the corresponding ones of the chosen generalized beam or plate models for a representative family of simple test problems. The material parameters of the classical elasticity tensor, in turn, are determined by classical computational homogenization followed by a reduction to the constitutive counterparts of the beam and plate models. For the dimension reduction models, isogeometric conforming Galerkin methods are utilized for numerical solutions (Fig. 3, right), whereas in the computational validation full-field finite element analysis with standard two- or three-dimensional elements is used (Fig. 3, left).

A natural extension to the current results for beams and plates is to consider modelling analogous shell-like structures by generalized shell models, such as the Kirchhoff–Love model introduced in Ref. [10].

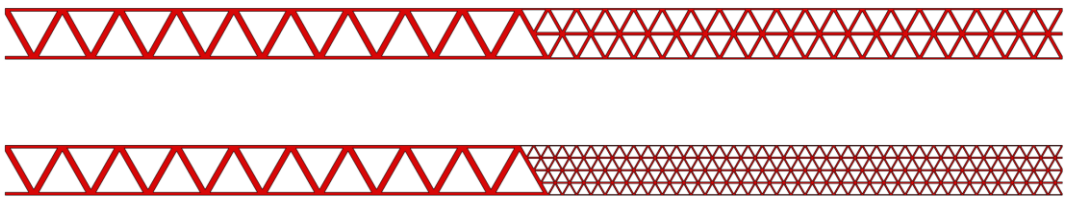

Figure 2. Beam-like planar structures with triangular lattice microarchitectures.

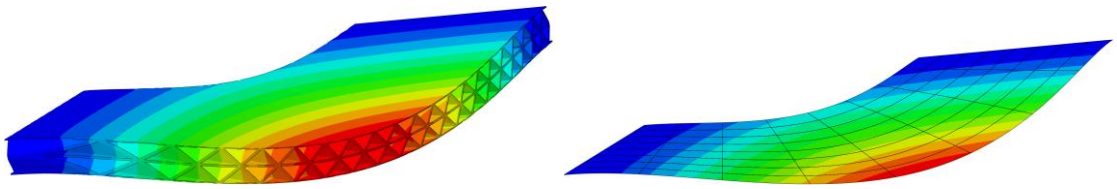

Figure 3. A plate-like cellular spacial structure (left, 3D FEM model) and its higher-order planar plate model (right, 2D IGA model) in bending.

References

[1] R. D. Mindlin, Micro-structure in linear elasticity, *Archive for Rational Mechanics and Analysis*, 16:51–78, 1964.

[2] J. Niiranen, V. Balobanov, J. Kiendl and S. Hosseini, Variational formulations, model comparisons and isogeometric analysis for Euler-Bernoulli micro- and nano-beam models of strain gradient elasticity, *Mathematics and Mechanics of Solids*, 24:312–335, 2019.

[3] V. Balobanov and J. Niiranen, Locking-free variational formulations and isogeometric analysis for the Timoshenko beam models of strain gradient and classical elasticity, *Computer Methods in Applied Mechanics and Engineering*, 339:137–159, 2018.

[4] S. T. Yaghoubi, V. Balobanov, S. M. Mousavi and J. Niiranen, Variational formulations and isogeometric analysis for the dynamics of anisotropic gradient-elastic Euler–Bernoulli and shear-deformable beams, *European Journal of Mechanics - A/Solids,* 69:113–123, 2018.

[5] S. Khakalo, V. Balobanov and J. Niiranen, Modelling size-dependent bending, buckling and vibrations of 2D triangular lattices by strain gradient elasticity models: applications to sandwich beams and auxetics, *International Journal of Engineering Science*, 127:33–52, 2018.

[6] S. Khakalo and J. Niiranen, Lattice structures as thermoelastic strain gradient metamaterials: Evidence from full-field simulations and applications to functionally step-wise-graded beams, *Composites Part B*, to appear, 2019.

[7] J. Niiranen and A. H. Niemi, Variational formulation and general boundary conditions for sixth-order boundary value problems of gradient-elastic Kirchhoff plates, *European Journal of Mechanics - A/Solids*, 61:164–179, 2017.

[8] J. Niiranen, J. Kiendl, A. H. Niemi and A. Reali, Isogeometric analysis for sixth-order boundary value problems of gradient-elastic Kirchhoff plates, *Computer Methods in Applied Mechanics and Engineering*, 316:328–348, 2017.

[9] S. Khakalo and J. Niiranen, Anisotropic strain gradient thermoelasticity for cellular structures: plate models, homogenization and isogeometric analysis, submitted, 2019.

[10] V. Balobanov, J. Kiendl, S. Khakalo and J. Niiranen, Kirchhoff–Love shells within strain gradient elasticity: weak and strong formulations and an H^3-conforming isogeometric implementation, *Computer Methods in Applied Mechanics and Engineering*, 344:837–857, 2019.

Proceedings of the 32nd Nordic Seminar on Computational Mechanics
A.H. Niemi and H. Koivurova (Eds.)

Achilles tendon modeling based on the absolute nodal coordinate formulation

Leonid Obrezkov[1], Ajay B. Harish[2] and Marko Matikainen[1]

(1)LUT University, Lappeenranta, Finland, Leonid.Obrezkov@lut.fi, Marko.Matikainen@lut.fi
(2)Leibniz Universität, Hannover, Germany, ajayharish.accts@gmail.com

Summary. In this work, we describe the soft biological tissue deformations for a rat Achilles tendon. The work has been done in the framework of the absolute nodal coordinate formulation (ANCF). Here we demonstrate the element based on this formulation for the modeling of soft tissues and further possible opportunities in multibody system dynamic applications through the objectivity test. For the modeling of biological tissue in the case of three-dimensional elasticity, we use the incompressible anisotropic Gasser-Ogden-Holzaphel (GOH) model. We also implement viscoelastic effects into our model with the generalized one-dimensional Maxwell model. The obtained results verified against the commercial finite element software ANSYS, moreover to check the description of the rat tendons we have taken used the obtained results from the practical experiments.

Key words: Biomechanics, Achilles tendon, Fibrous material, Incompressibility, Flexible multibody system dynamics

Introduction

The Achilles tendons are an important part of a biological organism. They are responsible for the transmission of mechanical forces produced by muscles to the bones. Although the attempts to understand the mechanism and functional role have been undertaken for a long period of time [1], they remain unclear [2, 3]. This fact is not a surprise, such as, it is an extremely complex system, the functioning of which depends on a huge number of factors, from each element of the living organism as age and physiological conditions, genetic factors, etc [4, 5]. In this case, the computational analysis even in the case of simplified models may give answers for the understanding and possible responses to the physical loading. One of the ways for the analysis of bodies subjected to large nonlinear geometrical and material deformations is the description with the absolute nodal coordinate formulation (ANCF). In this work, we will do our research based on the three-nodded element with quadratically interpolated position (displacement) field in longotudinal direction and linearily interpoalted in thickness directions [6]. Kinematics of this type of ANCF element is shown in Figure 1.

The peculiarity of the absolute nodal coordinate formulation is the usage of the components of the deformation gradient as rotational degrees of freedom. With the help of this element, we describe the model with several features related to the biological tissues, namely viscoelasticity, nonlinear elasticity, and anisotropy.

Model

In this work, the nearly incompressible material model is considered. In our case, at the continuum level we choose as the model of investigation the anisotropic Gasser-Ogden-Holzapfel (GOH) reinforced by one family fibres [8]. Then, the overall strain energy density function

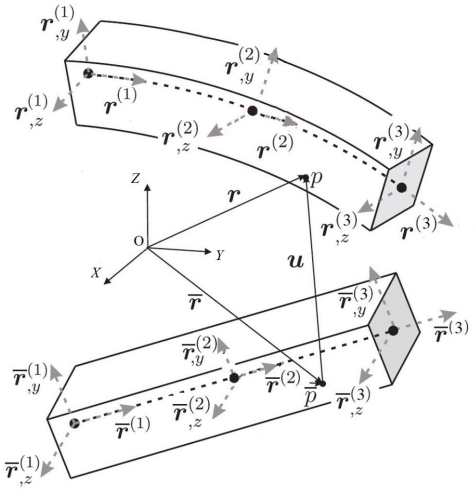

Figure 1. ANCF three-node deficient beam element with vector in current and referent configurations

is decomposed into volumetric and isochoric parts through decomposition of the deformation gradient

$$\mathbf{F} = J^{\frac{1}{3}}\overline{\mathbf{F}}, \tag{1}$$

where J is the determinant of the deformation gradient. The strain energy density has the following form

$$\Psi = \Psi_{iso}(\overline{\mathbf{C}},\ \overline{\mathbf{A}}) + \sum_{\alpha=1}^{m} \Upsilon_{\alpha}^{iso}(\overline{\mathbf{C}},\ \overline{\mathbf{A}},\ \Gamma_{\alpha}) + \Psi_{vol}(J), \tag{2}$$

Ψ_{vol} is volumetric part describes the hydrostatic pressure. Υ_{α}^{iso} are functions to characterize viscoelastic response (deceptive potential, responsible for the thermodynamic non–equilibrium state) [8]. From these expressions we derive the stress response, which has the following form

$$\mathbf{S} = 2\frac{\partial \Psi}{\partial \mathbf{C}} = \mathbf{S}_{vol} + \mathbf{S}_{iso} + \sum_{\alpha=1}^{m} \mathbf{Q}_{\alpha}, \tag{3}$$

$\mathbf{Q}_{\alpha}$ is non-equilibrium stresses in the sense of non-equilibrium thermodynamics, where

$$\mathbf{S}_{vol} = \frac{\partial \Psi_{vol}}{\partial J} J\mathbf{C}^{-1},\ \mathbf{S}_{iso} = 2\sum_{k} \frac{\partial \Psi_{iso}}{\partial \overline{I}_k}\frac{\partial \overline{I}_k}{\partial \mathbf{C}},\ \mathbf{Q}_{\alpha} = 2\frac{\partial \Upsilon_{\alpha}^{iso}}{\partial \mathbf{C}}. \tag{4}$$

The viscoelastic effects we describe with the generalized Maxwell model with the equation for $\mathbf{Q}_{\alpha}$ [8]

$$\mathbf{Q}_{\alpha} = \int_{0^+}^{T} \beta_{\alpha} \exp(-(T-t)/\tau_{\alpha}) \frac{d}{dt}\mathbf{S}_{iso}(t)\mathrm{d}t. \tag{5}$$

τ_{α} is relaxation time, β_{α} is a free-energy factor. Here, we also discuss the damage of tissue under deformation through the Mullins effect. It is described with discontinuous damage model [9].

$$\mathbf{S} = \mathbf{S}_{vol} + g(\Theta_s^m)\mathbf{S}_{iso} + \sum_{\alpha=1}^{m} \mathbf{Q}_{\alpha}, \tag{6}$$

where $g(\Theta_s^m)$ is a reduction factor.

$$\Theta_s^m = \max_{s\in[0,t]} \sqrt{\Psi_{iso}(s)}, g(x) = \beta_1 + (1-\beta_1)\frac{1-\exp(-x/\alpha)}{x/\alpha},\ \beta_1 \in [0,1],\ \alpha \in [0,\infty)$$

β_1 and α are regraded as given model parameters.

Result

The model with all named above features with in-house MATLAB code for the ANCF element was used to describe the simple uniaxial tension problem.

We have taken beam-like structures with circular cross-sections and applied them to describe the experiments with rat tendons. The first cycles were used for the optimisation routine and then with obtained parameters the model was extended up to the three cycles.

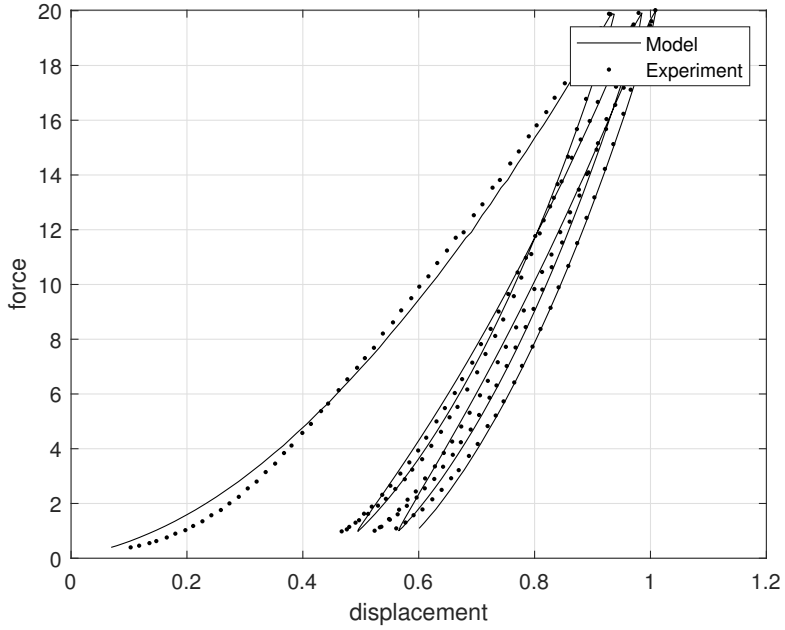

Figure 2. Load-displacement behavior of GOH beam

Conclusion

This work considers the behaviour of the ANCF elements in conjunction with the incompressible anisotropic model with viscoelastic and damage effects. The convergence of the system based on ANCF element was checked with varying different meshes and even in case one element it represents results well.

References

[1] J. D. Humphrey. Review paper: Continuum biomechanics of soft biological tissues. *Proceedings of the Royal Society A: Mathematical, Physical and Engineering Sciences*, 459:3–46, 2003.

[2] V. B. Shim, G. G. Handsfield, J. W. Fernandez, D. G. Lloyd, T. F. Besier. Combining in silico and in vitro experiments to characterize the role of fascicle twist in the Achilles tendon. *Scientific Reports*, 8:13856, 2018.

[3] M. Franchi, A. Trirè, M. Quaranta, E. Orsini, V. Ottani. Collagen structure of tendon relates to function. *The Scientific World Journal*, 7:404–420, 2007.

[4] T. A. Meister, E. Rexhaj, S. F. Rimoldi, U. Scherrer, C. Sartori. Fetal program-ming and vascular dysfunction. *Artery Research*, 21:69-77, 2018.

[5] B. Pierre, A. Stéphane, L. Susan, S. Michael. Mechanical identification of hyperelastic anisotropic properties of mouse carotid arteries. In: Proulx T. (eds), *Mechanics of Biological Systems and Materials, Volume 2. Conference Proceedings of the Society for Experimental Mechanics Series.*, New York, New York, 2011.

[6] K. Nachbagauer and A. S. Pechstein and H. Irschik and J. Gerstmayr A new locking-free formulation for planar, shear deformable, linear and quadratic beam finite elements based on the absolute nodal coordinate formulation. *Multibody System Dynamics*, 26: 245-263, 2011.

[7] G. Orzechowski, J. Frączeks. Nearly incompressible nonlinear material models in the large deformation analysis of beams using ANCF *Nonlinear Dynamics*, 82: 451-464, 2015.

[8] G. A. Holzapfel, T. C. Gasser. A viscoelastic model for fiber-reinforced composites at finite strains: Continuum basis, computational aspects and applications *Computer Methods in Applied Mechanics and Engineering*, 190: 4379-4403, 2001.

[9] L. A. Gracia, E. Peña, J. M. Royo, J. L. Pelegay, B. Calvo. A comparison between pseudo-elastic and damage models for modelling the Mullins effect in industrial rubber components *Mechanics Research Communications*, 36: 769-776, 2009.

Proceedings of the 32nd Nordic Seminar on Computational Mechanics
A.H. Niemi and H. Koivurova (Eds.)

On optimal design of lug joints

N. L. Pedersen

Dept. of Mechanical Engineering, Solid Mechanics
Technical University of Denmark
Nils Koppels Allé, Building 404, DK-2800 Kgs. Lyngby, Denmark
e-mail: nlp@mek.dtu.dk

Introduction

A lug or pinned connection is a simple assembly type that allows for quick assembly and disassembly. The connection have many practical applications both in mechanical and civil engineering cases. In the present work the loading on the assembly is assumed to be cyclic so that the design criteria for strength is fatigue, i.e. the maximum stress in the assembly. The usual design of lug joints is controlled by standards, e.g. ISO2338.

The stress state is 3 dimensional but still the normal design is constant through the thickness so focus is on the cross sectional design. The typical sectional design is circular and stress concentration factor charts can be found in the literature. The typical assumption used is that it is sufficient to use a 2D model, where a further assumption of either plane stress or plane strain is needed. In practical designs where the thickness is of the same order as the pin diameter we find that there is a significant variation in the stress in the axial direction. The same type of variation is also found in e.g. interference fits, see e.g. [1]. For simplification we will however here neglect the 3D effect on the stress concentration.

In the present work the aim is to minimize the stress concentration resulting in an increased strength of the connection. The finite element method (FEM) is used as the analysis tool, and for the successful application a number of aspects must be taken into account, and will be discussed in relation to the design. The different aspects includes,

- The definition of the stress concentration factor.
- Mesh refinement (in non-linear contact analysis).
- Head distance.
- Poisson's ratio.
- Plane stress or plane strain.
- Friction.
- Clearance.

The design optimization is performed using shape optimization. For the present optimization we have the special case that the shape to be designed is the contact zone. The selected shape parameterization used is the super elliptical one. Further information can be found in [2].

References

[1] N. L. Pedersen. On optimization of interference fit assembly. *Structural and multidisciplinary optimization*, 54(2): 349-359, 2016.

[2] N. L. Pedersen. Stress concentration and optimal design of pinned connections. *Journal of strain analysis for engineering design*, 54(2): 95–104, 2019.

Proceedings of the 32nd Nordic Seminar on Computational Mechanics
A.H. Niemi and H. Koivurova (Eds.)

FEM-DEM in Modeling Ice-structure Interaction Process

Janne Ranta, Arttu Polojärvi and Jukka Tuhkuri

Aalto University, Department of Mechanical Engineering, P.O. Box 14300, FI-00076 AALTO, Finland, e-mail: arttu.polojarvi@aalto.fi

Summary. This extended abstract briefly introduces our recent modeling work on ice loads on wide, inclined, Arctic marine structures, like drilling platforms or harbor structures. The work is based on hundreds of two-dimensional combined finite-discrete element method (FEM-DEM) simulations on ice-structure interaction process. In such processes, a floating sea ice cover, driven by winds and currents, goes through a failure process and breaks into a large number of ice blocks, which interact with each other and the structure. The ice load is the end result of this interaction process. We have used the simulation data i) to study the loading process and the related parameters, ii) to analyze the statistic of ice loads, and iii) to investigate the mechanisms that limit the ice load values on the structure.

Key words: Combined finite-discrete element method, ice loads, Arctic technology

Introduction

Arctic operations, such as marine transportation, offshore wind energy, and offshore drilling, require reliable prediction of sea ice loads applied on the structures. The ice loads arise from a complex and stochastic ice-structure interaction process. Simulations of ice-structure interaction process need to consider a complicated process including fragmentation of ice, formation and motion of ice blocks, and interactions between the blocks as well as between the blocks and the structure. Particle-based methods, such as discrete element and combined finite-discrete element method (DEM and FEM-DEM), allow detailed studies on complex ice loading scenarios and they are often used in ice engineering [1].

During the recent years, we have used 2D combined finite-discrete element method (2D FEM-DEM) simulations to study the mechanisms that limit peak ice loads on wide, inclined, offshore structures [2, 3, 4, 5]. Figure 1 illustrates our simulations, which have a floating and continuous ice sheet pushed against an inclined rigid structure. The initially intact ice sheet fails into a rubble pile of ice blocks, which interact with each other and the structure. Our studies have focused on parameter effects, statistics of ice loads, and on the mechanisms that limit the ice load values. This extended abstract briefly describes how we have used the simulations and summarizes some of the main results from our simulation-based studies.

Results

One interesting feature of 2D FEM-DEM simulations on ice-structure interaction processes is that they indicate that the loading process is sensitive to its initial conditions – the simulated ice-structure interaction processes themselves are deterministic. This sensitivity can be utilized to study the statistics of ice loads: we have used simulation sets containing tens of simulations, with each set including simulations with equal parameters, except slightly different initial conditions. Simulations within each set, differing by their initial conditions only, produced different ice loading processes and different maximum peak ice load values (Figure 2). The peak ice load data from hundreds of simulations has enabled us to study the statistics of peak ice loads.

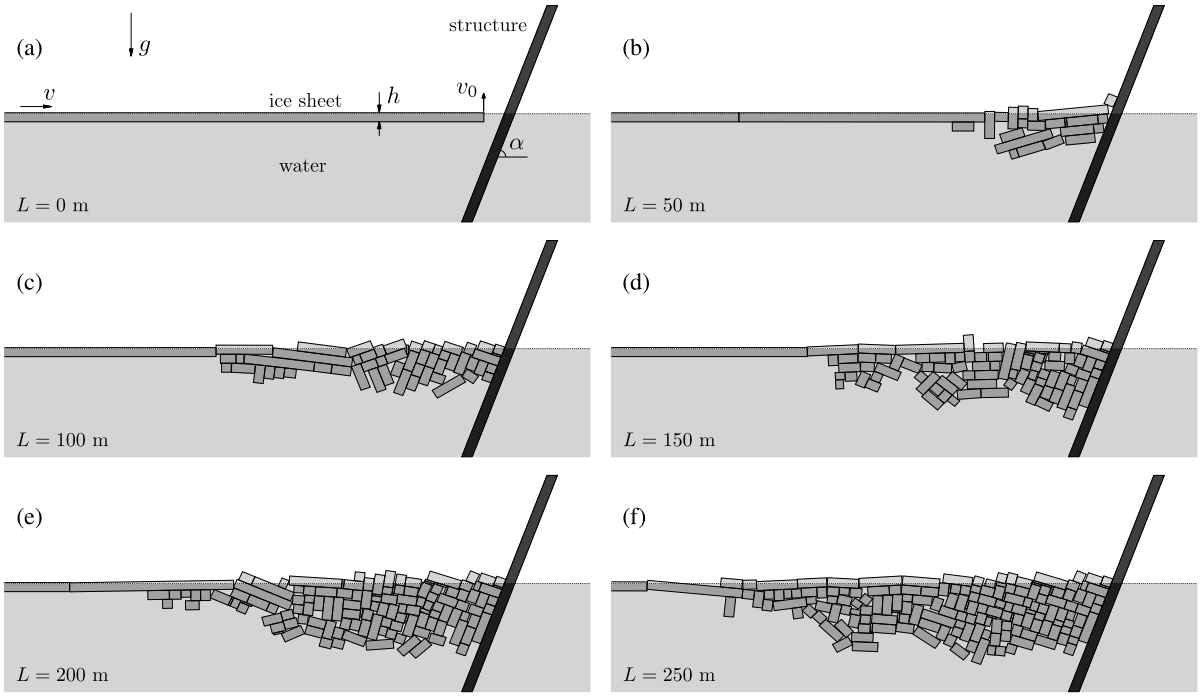

Figure 1. Snapshots of a 2D FEM-DEM-simulated ice-structure interaction process described by the length L of the ice pushed against an inclined structure. The ice sheet moves with velocity v and breaks into ice blocks in the vicinity of the structure. Broken ice forms an ice rubble pile in front of the structure. The first figure shows the initial vertical velocity perturbation v_0. Ice sheet thickness h was 1.25 m. Figure is from [2]

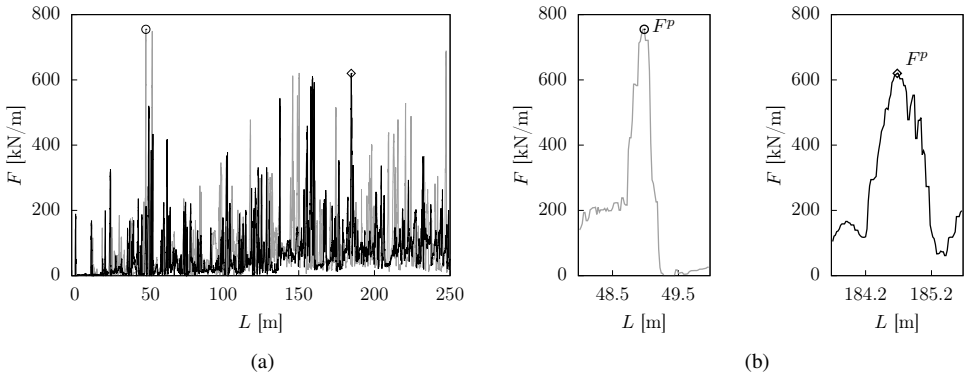

Figure 2. Two ice load F-records from two simulations with same parameterization but different initial conditions: (a) F plotted against length of pushed ice, L, and (b) close-ups of the maximum peak ice load, F^p, events. The value of F^p differs between the simulations. The ice thickness $h = 1.25$ m and the plastic limit $\sigma_p = 1$ MPa. Figure is from [5].

One central question that the studies on peak ice load statistics aim to answer is: What type of distributions do peak ice loads follow? Our work has shown that the peak load distributions in our simulations appear to be right-skewed and thus non-normal. Gumbel distribution appeared to describe the data well. Further we have shown, that the large scatter, which is typical for ice load data, is due to the ice-structure interaction process itself. Often it is believed that the scatter is due to sea ice being inhomogeneous. Due to the scatter, a large number of observations is needed when, for example, parameter effects are of interest: To reliably observe a 15 % difference in the mean peak load values due to a single parameter requires more than 80 observations in total. This is a very large number of observations to be attained experimentally.

The study on the parameter effects showed that the ice thickness has a very strong effect on peak ice load magnitudes. Further, the inclination angle of the structure also affects the loads, but the effect is less strong and decreases during the process. On the other hand, the effect of other parameters, such as ice-structure friction coefficient, is fairly weak. This encouraged us to search for simple peak ice load formulae, such as the one described below, whereas traditional models and design standards are formulated so that they require using fairly large number of parameters. In addition our simulations showed, that the relative importance of the parameters changes during the interaction process. This indicates that the stage of the interaction process should be taken into account in ice load models. Also this finding means, that the load models based on the experimental data with a small amount of ice pushed against a structure, may not account for the changes in the ice failure process and may, thus, lead to inaccurate ice load predictions.

In our studies on the mechanics of peak ice loads, we have shown that the peak ice load data is normalized with good accuracy by multiplying the load values with $1/\sqrt{h^3}$, where h is the ice thickness. This suggests that the peak ice load values are governed by buckling. We developed a buckling model, which quantifies the effect of the so-called force chains and the related peak ice load values in the interaction process with fair accuracy. Further, we have also extended the buckling model so that it accounts for a mixed-mode ice failure process, where the root cause of ice failure can be is either ice buckling or local edge crushing of ice. We also derived an algorithm, which is capable of producing large amounts of virtual ice load data that compares fairly well with full-scale observations.

Conclusions

Above we have introduced our numerical modeling work on ice loads on an inclined, wide, structure. The strength of numerical models is that they can be used to produce hundreds of interaction processes with full control over the model parameters. This control allows detailed studies on ice load statistics and the related mechanical phenomena. Such control is never available in full- or model-scale experiments. We believe that the understanding of ice load statistics allows conceiving simplified ice load models, which can be reliably used to study the ice loads on structures. This type of models have the potential of yielding insight for the analysis of complex ice-structure interaction processes.

References

[1] Tuhkuri, J., Polojärvi, A. A review of discrete element simulation of ice-structure interaction. *Philosophical Transactions of the Royal Society A: Mathematical, Physical and Engineering Sciences* (2018) 376 (2129), art. no. 20170335.

[2] Ranta, J., Polojärvi, A., Tuhkuri, J. The statistical analysis of peak ice loads in a simulated ice-structure interaction process. *Cold Regions Science and Technology* (2017) 133;46–55.

[3] Ranta, J., Polojärvi, A., and Tuhkuri, J. Ice loads on inclined marine structures - virtual experiments on ice failure process evolution. *Marine Structures* (2018) 57:72—86.

[4] Ranta, J., Polojärvi, A., Tuhkuri, J. Limit mechanisms for ice loads on inclined structures: Buckling. *Cold Regions Science and Technology* (2018) 147:34—44.

[5] Ranta, J., Polojärvi, A. Limit mechanisms for ice loads on inclined structures: Local crushing. *Marine Structures* (2019) 67, 102633.

Proceedings of the 32nd Nordic Seminar on Computational Mechanics
A.H. Niemi and H. Koivurova (Eds.)

Comparison 32CrMo12 QT steel fatigue testing with ultrasonic and servo-hydraulic testing machines

Taneli Rantakivi[1], Miikka Väntänen[1],Juha Kuoppala[1], Joona Vaara[2], Jari Larkiola[3], Tero Frondelius[2,3]

[(1)]Global Boiler Works Oy, Oulu taneli.rantakivi@gbw.fi
[(2)]Wärtsilä, Järvikatu 2-4, 65100 Vaasa, Finland
[(3)]Materials and Mechanical Engineering, Pentti Kaiteran katu 1, 90014 University of Oulu, Finland

Summary. This article presents the fatigue testing of 32CrMo12 QT steel in two kinds of fatigue testing machines. Results of the resonant fatigue testing machine and ultrasonic fatigue testing machine are compared.

Keywords: fatigue testing, QT steel, USF

Introduction

It is well-known that dynamically loaded components are vulnerable to fatigue failures. Fatigue testing is expensive and takes a lot of time with traditional testing methods. Ultrasonic fatigue testing machine uses piezoelectric transducers to generate ultrasonic testing frequencies. Global Boiler Works Oy conducts ultrasonic fatigue experiments with equipment developed by the Institute of Physics and Materials Science at University of Natural Resources and Life Sciences, Vienna (Physics BOKU Vienna). This equipment enables periodic testing, which is essential to combat the heating of specimens vibrating with a resonance close to 20 kHz [1].

Fatigue testing of 32CrMo12 steel

Quenched and tempered steels are often used in dynamically loaded machine components. In this paper, the tested material is 32CrMo12. It is a low alloy steel which has at least 2.8% Cr and 0.3% Mo. 32CrMo12 is typically used in the automotive industry and in general mechanical engineering components, such as crankshafts, which require high hardness and wear resistance. In this paper, the testing temperature is 80 °C and the stress ratio is R=0 for both testing machines.

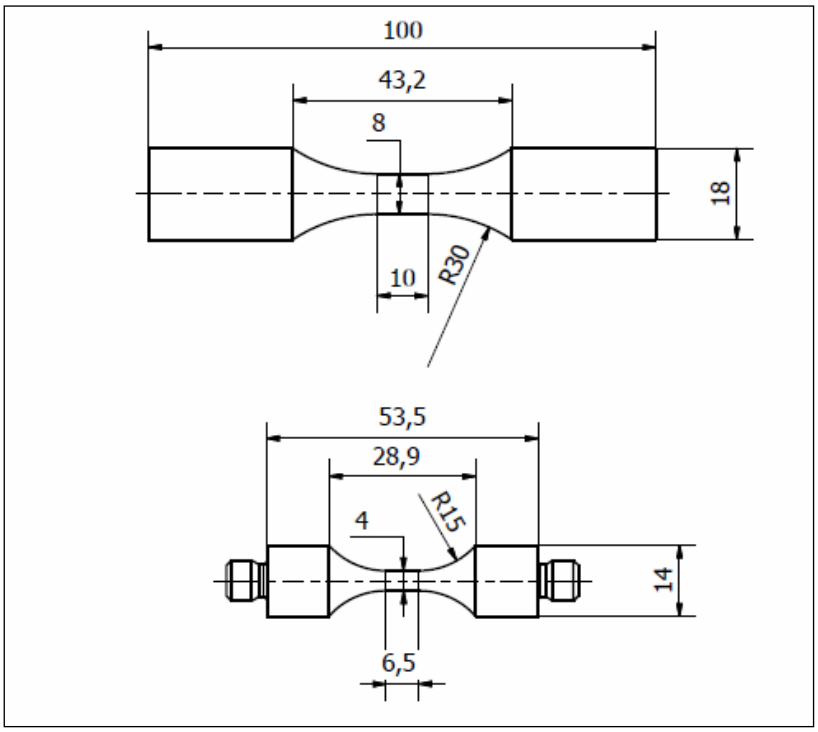

Figure 1. Fatigue test specimens' geometry. Above resonant fatigue testing specimen and below USF specimen.

Figure 1 shows the geometry of the samples used. Because of the different geometries, the risk volumes are different. The risk volumes of the specimens were 82mm^3 (USF) and 503mm^3 (resonant fatigue). Furya [2] noticed that if a USF specimen had smaller risk volume than specimen used with conventional fatigue testing, the results from ultrasonic testing will imply a higher fatigue limit than those from conventional fatigue testing. Lower fatigue limit is usually explained with the fact that a higher risk volume leads to a higher probability for the volume to include significantly large defects. Larger defects subsequently result in a lower fatigue strength. When using equal risk volumes, there is a good agreement between the ultrasonic and conventional fatigue test results [3].

If the specimens used are different sizes, the results can be compared using the size factor. The statistical size factor can be calculated with the weakest link approach according to equations (1)-(5) [4].

$$n = \frac{V_{eff}}{V_{ref}} \tag{1}$$

where V_{eff}=pulsator-specimen effective stress volume and V_{ref}=USF specimen effective stress volume

$$R = \sqrt[n]{0.5} \tag{2}$$

$$P = 1 - R \tag{3}$$

$$P = \frac{1}{\sqrt{2\pi}} \int_{-\infty}^{\lambda} e^{-\frac{x^2}{2}} dx \tag{4}$$

$$K_{size} = \frac{1}{1 + \lambda s_r} \tag{5}$$

Where K_{size}=statistical size factor, R=reliability of the single specimen, s_r = relative standard deviation of fatigue limit.

The used relative standard deviation value (s_r=0.1) based on the results of a separate Bayesian analysis of a normally distributed fatigue limit distribution after observing the USF data. Using formulas 1-5 the statistical size factor between the two specimens is calculated as K_{size}=1.09.

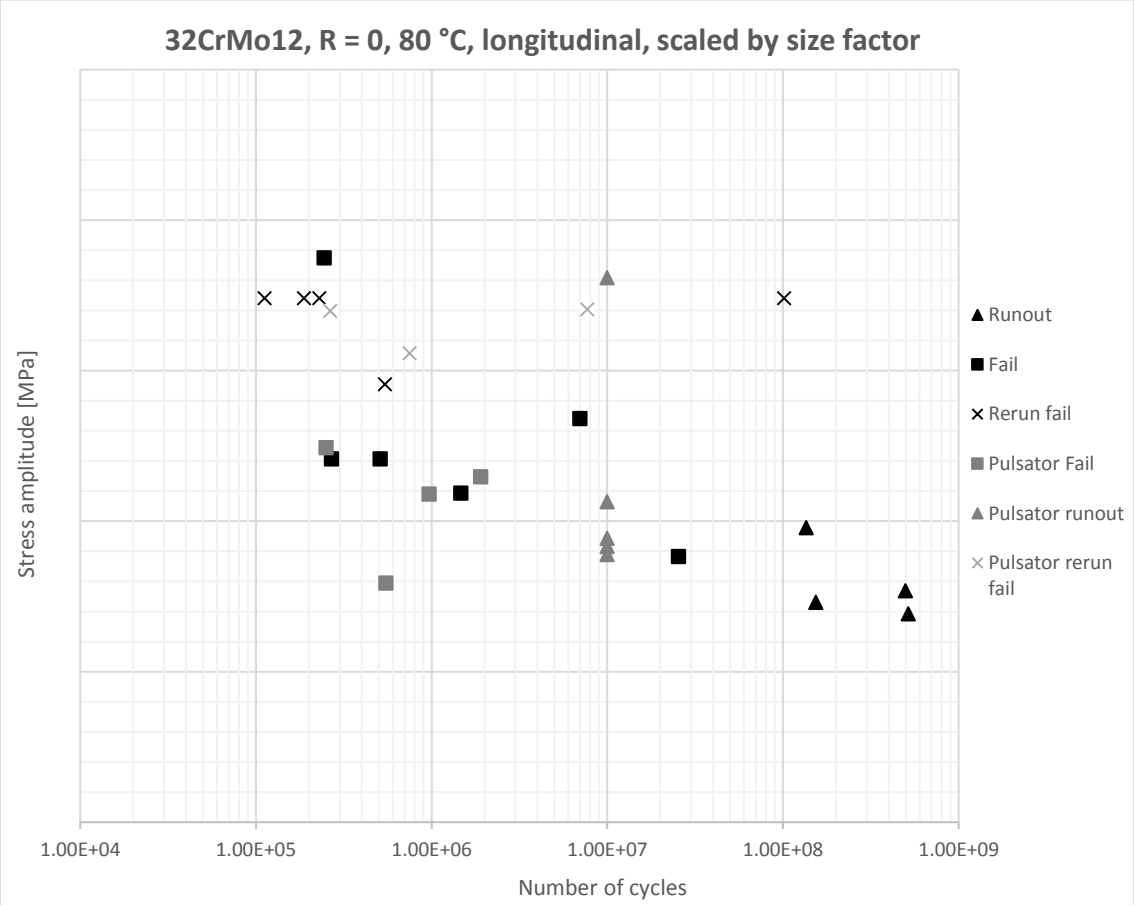

Figure 2. Fatigue testing results from longitudinal direction of grain flow.

Fatigue testing results presented in figure 2. With the presented simplified approach, the USF test amplitudes were directly scaled by the calculated size factor to account for the difference in risk volumes. Runout limit chosen for this series was 1e8 with the ultrasonic fatigue testing and 1e7 with the resonant fatigue testing machine. Runout specimens were retested at a higher

amplitude until they failed, denoted as “rerun fail” in figure 2. Based on the results shown in figure 2, the expected fatigue limit is approximately 245 MPa for the USF tests and 255 MPa for the resonant fatigue test series. It is important to note, here, that the estimated fatigue limit values correspond to a risk volume equal to that of a resonant fatigue test specimen. According to the results, the ultrasonic fatigue testing is a suitable method for studying the fatigue properties of a QT steel. A more precise comparison would be obtained by using samples with the same risk volume.

Conclusions

According to literature [5] and fatigue test results of 32CrMo12 steel, ultrasonic fatigue testing is a suitable method for studying the fatigue properties of QT steels. Ultrasonic fatigue testing is a fast and preferred testing method for very high cycle fatigue testing [6]. Conventional 100Hz fatigue testing takes about 11 days to reach 1e8 load cycles; the same amount of cycles is obtained in roughly 6 hours with the ultrasonic testing machine.

Acknowledgments

The authors would like to acknowledge the financial support of Business Finland in the form of research projects ISA Wärtsilä Dnro 7734/31/2018, and ISA GBW Dnro 7752/31/2018.

References

[1] H. Mayer. Recent developments in ultrasonic fatigue. Fatigue & Fracture of Engineering Materials & Structures, 39(1):3{29, 2015. ISSN 1574-6968. DOI: 10.1111/ffe.12365.

[2] Furuya, Y. (2008). Specimen size effects on gigacycle fatigue properties of high-strength steel under ultrasonic fatigue testing. Scripta Materialia - SCRIPTA MATER. 58. 1014-1017. 10.1016/j.scriptamat.2008.01.039.

[3] Furuya, Y., Hirukawa, H., & Takeuchi, E (2019) Gigacycle fatigue in high strength steels, Science and Technology of Advanced Materials, 20:1,643-656, DOI: 10.1080/14686996.2019.1610904

[4] Roger Rabb. Todennäköisyysteoriaan pohjautuva väsymisanalyysi. ISBN: 978-952-286-210-5. Books on demand. pages 308–309, 2013. ISSN ISBN: 978-952-286-210-5.

[5] Korhonen, J., Kuoppala, J., Väntänen, M., Vaara, J., Turunen, M., Kämäräinen, P., Laine, J., Silvonen, A. ja Frondelius, T. (2017) ”QT steel High Cycle Fatigue Testing with Ultrasonic”, Rakenteiden Mekaniikka, 50(3), ss. 304-308. DOI: 10.23998/rm.65059.

[6] Stanzl-Tschegg, S. (2014). Very high cycle fatigue measuring techniques. International Journal of Fatigue. 60. 2–17. DOI: 10.1016/j.ijfatigue.2012.11.016.

Proceedings of the 32nd Nordic Seminar on Computational Mechanics
A.H. Niemi and H. Koivurova (Eds.)

Waveguides that support trapped surface waves

K. M. Ruotsalainen

October 16, 2019

1 Introduction

1.1 The formulation of the problem

We consider the spectral Steklov problem

$$\begin{aligned} -\Delta u^\epsilon(x) &= 0,\ x \in \Omega^\epsilon, \\ \partial_\nu u^\epsilon(x) &= 0,\ x \in \partial\Omega^\epsilon \setminus \overline{\Gamma^\epsilon} \\ \partial_z u^\epsilon(x) &= \lambda^\epsilon u^\epsilon(x),\ x \in \Gamma^\epsilon, \end{aligned} \tag{1.1}$$

in a duct Ω^ϵ, see Fig.1.

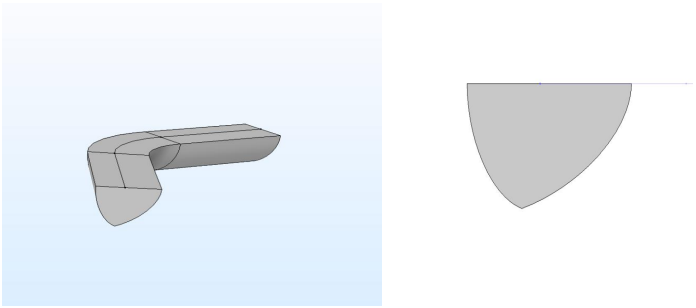

Figure 1: a) Curved channel, b) The cross-section

For the parameter $\epsilon = 0$ we have a straight cylinder $\Omega^0 = \mathbb{R} \times \Theta$ with a constant cross-section $\Theta \subset \mathbb{R}^2$ bounded by the line segment $\gamma = \{x' = (x_2, x_3) : x_3 = 0,\ |x_2| \le 1\}$ and a piecewise smooth curve connecting the points $(\pm 1, 0)$ inside the lower half plane $\mathbb{R}^2_- = \{x' :\ x_3 < 0\}$, see fig.2. Without loss of generality we assume that the length of γ is 2. Considering Ω^0 as the water domain, the free surface is denoted by $\Gamma = \mathbb{R} \times \gamma$ and by $\Sigma = \partial\Omega \setminus \overline{\Gamma}$ the union of walls and bottom.

The waveguide Ω^ϵ is obtained from Ω^0 by bending the channel in some local neighbourhood of the origin. Hence Υ^ϵ is a slightly deformed mid-line Υ^0 of Γ - the abscissa axis. The water domain Ω^ϵ is formed by sliding the cross-section Θ along the curve Υ^ϵ.

In the neighbourhood $\mathcal{U}$ of Υ^ϵ on the plane $\{x :\ x_3 = 0\}$, we introduce the local coordinate system (η, ς), where η is the oriented distance to Υ^ϵ and ς is

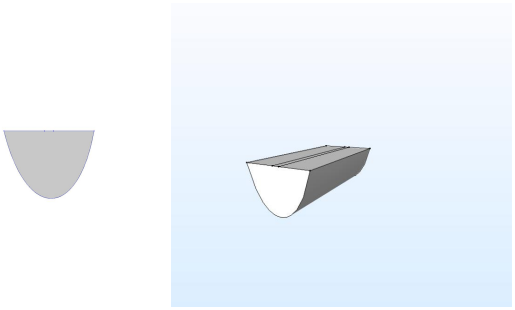

Figure 2: a) Free surface and the cross-section, b) a straight channel

the arc length on Υ^ϵ. We assume that the curvature $\kappa^\epsilon(\varsigma)$ of Υ^ϵ satisfies the conditions

$$\kappa^\epsilon(\varsigma) = \epsilon\kappa^0(\varsigma),\ \kappa^0(\varsigma) \in C^\infty(\mathbb{R}),\ \kappa^0(\varsigma) = 0 \text{ for } |\varsigma| > l > 0. \tag{1.2}$$

The curved channel with a constant cross-section Θ, Fig.1, is then

$$\Omega^\epsilon = \{x : \varsigma \in \mathbb{R},\ (\eta, z) \in \omega\}, \tag{1.3}$$

where $z = x_3$ is the vertical coordinate. According to (1.2), the channel (1.3) has cylindrical outlets to infinity $\Omega^\epsilon_\pm = \{x \in \Omega^\epsilon :\ \pm\varsigma > l\}$ and the curved middle part $\Omega^\epsilon_0 = \{x \in \Omega^\epsilon :\ |\varsigma| < l\}$, see Fig.1.

1.2 Spectra of the problem

It is well-known that the continuous spectrum σ^0_{co} of the problem is the closed real semi-axis $\overline{\mathbb{R}_+} = [0, +\infty)$ in the complex plane $\mathbb{C}$. The threshold values

$$0 = \Lambda_0 < \Lambda_1 \le \Lambda_2 \le \cdots \le \Lambda_j \le \cdots \to +\infty \tag{1.4}$$

divide σ^0_{co} into the intervals of constant multiplicity. In what follows we concern the first interval $(0, \Lambda_1)$. The entries of the sequence (1.4) are the eigenvalues of the model problem on the cross-section

$$\begin{aligned} -\Delta' U(x') &= 0,\ x' \in \omega, \\ \partial_\nu U(x') &= 0,\ x' \in \partial\omega \setminus \overline{\gamma}, \\ \partial_z U(x') &= \Lambda U(x'),\ x' \in \gamma, \end{aligned} \tag{1.5}$$

where Δ' is the Laplacian in the cross-section.

The spectrum of the problem in the straight channel is absolutely continuous but, for $\epsilon > 0$, the spectrum $\sigma^\epsilon = \overline{\mathbb{R}_+}$ of problem (1.1) may contain embedded eigenvalues forming the point spectrum σ^ϵ_p. The main goal: find a domain Θ and a curve Υ^ϵ, that is, the curvature κ^ϵ in (1.2), such that σ^ϵ_p includes at least one eigenvalue

$$\lambda^\epsilon = \Lambda_1 - \epsilon^2\mu^2. \tag{1.6}$$

1.3 Criteria for the trapped mode

In the sequel, we assume that the first positive eigenvalue in the sequence (1.4) is simple, that is

$$\Lambda_1 < \Lambda_2. \tag{1.7}$$

By the Max-Min principle, cf. [11, Ch. 22], the non-positive part of the M-spectrum of the problem

$$\begin{aligned} -\Delta' V(x') &= MV(x'),\ x' \in \omega, \\ \partial_\nu V(x') &= 0,\ x' \in \partial\omega \setminus \gamma, \\ \partial_z V(x') &= \Lambda_1 V(x'),\ x' \in \gamma, \end{aligned} \tag{1.8}$$

consists of two eigenvalues $M_0 < 0$ and $M_1 = 0$. The corresponding eigenfunctions are denoted by V_0 and V_1 normalized in the Lebesgue space $L^2(\omega)$:

$$\|V_0; L^2(\omega)\| = \|V_1; L^2(\omega)\| = 1.$$

Notice that $V_1 = U_1$.

The solution of perturbed problem with the parameter λ^ϵ in (1.6)

$$\begin{aligned} -\Delta' V^\epsilon(x') &= M^\epsilon V^\epsilon(x'),\ x' \in \omega, \\ \partial_\nu V^\epsilon(x') &= 0,\ x' \in \partial\omega \setminus \gamma, \\ \partial_z V^\epsilon(x') &= \lambda^\epsilon V^\epsilon(x'),\ x' \in \gamma, \end{aligned} \tag{1.9}$$

has the asymptotic expansion

$$\begin{aligned} M_q^\epsilon &= M_q + \epsilon^2 M_q^\sharp + \widetilde{M}_q^\epsilon, \\ V_q^\epsilon &= V_q + \epsilon^2 V_q^\sharp + \widetilde{V}_q^\epsilon. \end{aligned} \tag{1.10}$$

The correction terms in the asymptotic ansätze with $q = 0, 1$ are deduced from the problem

$$\begin{aligned} -\Delta' V_q^\sharp(x') - M_q V_q^\sharp(x') &= M_q^\sharp(x') V_q(x') =: F_q(x'),\ x' \in \omega, \\ \partial_\nu V_q^\sharp(x') &= 0,\ x' \in \partial\omega \setminus \gamma, \\ \partial_z V_q^\sharp(x') - \Lambda_1 V_q^\sharp(x') &= -\mu^2 V_q(x') =: G_q(x'),\ x' \in \gamma. \end{aligned} \tag{1.11}$$

Here the existence of $M^\sharp$ and $V^\sharp$ follows from the compatibility condition and

$$M_q^\sharp = \mu^2 \|V_q; L^2(\gamma)\|^2 > 0. \tag{1.12}$$

In the straight part of the channel there are two oscillatory and two exponential waves

$$w_{0\pm}^\epsilon(x) = a_0^\epsilon e^{\pm i m_0^\epsilon x_1} V_0^\epsilon(x'), \tag{1.13}$$

$$v_{1\pm}^\epsilon(x) = a_1^\epsilon e^{\pm m_1^\epsilon x_1} V_1^\epsilon(x'), \tag{1.14}$$

where

$$\begin{aligned} m_0^\epsilon &= \sqrt{-M_0^\epsilon} = m_0 + O(\epsilon^2), \qquad m_0 = \sqrt{-M_0} > 0, \\ m_1^\epsilon &= \sqrt{M_1^\epsilon} = \epsilon(m_1 + O(\epsilon^2)), \qquad m_1 = \mu \|U_1; L^2(\gamma)\| > 0. \end{aligned} \tag{1.15}$$

Furthermore, a_q^ϵ is a normalization factor:

$$a_q^\epsilon = (2m_q^\epsilon)^{-\frac{1}{2}} \|V_q^\epsilon; L^2(\omega)\|^{-1},\ q = 0, 1 \tag{1.16}$$

$$a_0^\epsilon = a_0^0 + O(\epsilon^2),\ a_0^0 = (2\sqrt{-M_0})^{-\frac{1}{2}}, \tag{1.17}$$

$$a_1^\epsilon = \epsilon^{-\frac{1}{2}} a_1^0 (1 + O(\epsilon^2)),\ a_1^0 = 2^{-\frac{1}{2}} \mu^{-1} \|V_q; L^2(\gamma)\|^{-1}. \tag{1.18}$$

Following [1], see also [7], we introduce the exponential wave packets

$$w_{1\pm}^\epsilon(x) = 2^{-\frac{1}{2}} (v_{1+}^\epsilon(x) \mp i v_{1-}^\epsilon(x)) \tag{1.19}$$

and by straightforward computation, we have

$$Q(w_{j\pm}^\epsilon, w_{k\pm}^\epsilon) = \pm i\delta_{j,k},\ Q(w_{j\pm}^\epsilon, w_{k\mp}^\epsilon) = 0,\ j, k = 0, 1, \tag{1.20}$$

where $\delta_{j,k}$ is the Kronecker symbol and $Q(\cdot, \cdot)$ is the symplectic (sesqui-linear and anti-Hermitian) form

$$Q(v, w) = \int_\omega \left(\overline{w(R, x')} \frac{\partial v}{\partial x_1}(R, x') - v(R, x') \overline{\frac{\partial w}{\partial x_1}(R, x')} \right) dx'.$$

It is known, see e.g. [1, 7, 9], that the orthogonality and normalization conditions (1.20) assure the existence of the following solutions to the problem $(\mathcal{P}^\epsilon)$:

$$\begin{aligned} Z_{0\pm}^\epsilon(x) &= \chi_\pm(\varsigma) w_{0\mp}^\epsilon(\varsigma, n, z) + \sum_{\theta=\pm} \chi_\theta(\varsigma) S_{\theta\pm}^\epsilon w_{0,\pm}^\epsilon(\varsigma, n, z) \\ &\quad + \chi_+(\varsigma) S_{1\pm}^\epsilon w_{1-}^\epsilon(\varsigma, n, z) + \chi_-(\varsigma) T_{1\pm}^\epsilon v_{1+}^\epsilon(\varsigma, n, z) + \widetilde{Z}_{0\pm}^\epsilon(x) \qquad (1.21) \\ Z_1^\epsilon(x) &= \chi_+(\varsigma) w_{1-}^\epsilon(\varsigma, n, z) + \sum_{\theta=\pm} \chi_\theta(\varsigma) S_{\theta 1}^\epsilon w_{0,\pm}^\epsilon(\varsigma, n, z) \\ &\quad + \chi_+(\varsigma) S_{11}^\epsilon w_{1+}^\epsilon(\varsigma, n, z) + \chi_-(\varsigma) T_{11}^\epsilon v_{1+}^\epsilon(\varsigma, n, z) + \widetilde{Z}_1^\epsilon(x). \qquad (1.22) \end{aligned}$$

Here, the remainders $\widetilde{Z}_{0\pm}^\epsilon(x)$ and $\widetilde{Z}_1^\epsilon(x)$ get the exponential decay $o(e^{-\delta|\varsigma|})$ while the exponents $\delta > 0$ are defined by the eigenvalues (1.7) and can be fixed independently on $\epsilon \in (0, \epsilon_0],\ \epsilon_0 > 0$.

The coefficients in (1.21) and (1.22) form a 3×3-matrix S^ϵ,

$$S^\epsilon = \begin{bmatrix} S_{\bullet\bullet}^\epsilon & S_{\bullet 1}^\epsilon \\ S_{1\bullet}^\epsilon & S_{11}^\epsilon \end{bmatrix},\ S_{\bullet\bullet}^\epsilon = \begin{bmatrix} S_{++}^\epsilon & S_{+-}^\epsilon \\ S_{-+}^\epsilon & S_{--}^\epsilon \end{bmatrix},\ S_{\bullet 1}^\epsilon = \begin{bmatrix} S_{+1}^\epsilon \\ S_{-1}^\epsilon, \end{bmatrix}$$

which is called *the augmented scattering matrix*, which is symmetric and unitary.

Theorem 1. *The condition*

$$S_{11}^\epsilon = -1 \tag{1.23}$$

is sufficient for the existence of trapped mode.

Assuming that the curvature is of the form

$$\kappa^0(\varsigma) = \kappa_0^0(\varsigma) + \tau_+ \kappa_+^0(\varsigma) + \tau_- \kappa_-^0(\varsigma) \tag{1.24}$$

$$\mu = \mu_0 + \tau_0 \tag{1.25}$$

of the quantities in (1.1) and (1.6). Using the asymptotic analysis the sufficient condition can be reduced to an abstract fixed point equation

$$\tau = T^\epsilon(\tau). \tag{1.26}$$

We shall make the following assumptions:
(A1): Let us introduce the quantities

$$J_1(\kappa^0) = \int_{-l}^{l} \kappa^0(\varsigma)\, d\varsigma, \quad K_1 = \int_\Theta U_1(n,z)\partial_n U_1(n,z)\, dndz\, K_0 = \int_\Theta V_0(n,z)\partial_n U_1(n,z)\, dndz. \tag{1.27}$$

The first assumption is that

$$K_0 \neq 0, K_1 \neq 0,\ K_1 J_1(\kappa^0) < 0. \tag{1.28}$$

(A2): The second condition is that Now we fix κ_0 and $\kappa^0_\pm$ such that

$$\mathrm{Re}\left((1+i)J_\pm(\kappa^0_0)\right) = 0, \tag{1.29}$$

$$\mathrm{Re}\left((1+i)J_\pm(\kappa^0_p)\right) = \delta_{\pm,k},\ k = \pm, \tag{1.30}$$

where the functionals $J_\pm$ are given by

$$J_\pm(\kappa^0) = a^0_0 \int_{-l}^{l} e^{\mp i m_0 \varsigma} \kappa^0(\varsigma) d\varsigma.$$

We will show that the operator T^ϵ is a contraction in the ball

$$\mathbf{B}_\rho = \{\tau = (\tau_0, \tau_+, \tau_-) \in \mathbb{R}^3 :\ |\tau| < \rho\}$$

for small positive ϵ and ρ. Thus the Banach fixed point theorem delivers a unique solution of (1.26) which additionally satisfies the estimate

$$|\tau| \leq c\epsilon. \tag{1.31}$$

In this way, we obtain the curved channel with a constant cross-section which has a trapped mode and the embedded eigenvalue

$$\lambda^\epsilon(\tau) = \Lambda_1 - \epsilon^2(\mu_0 + \tau_0)^2,$$

cf. (1.6) and (1.25).

References

[1] I.V. Kamotskii and S.A. Nazarov, An augmented scattering matrix and exponentially decreasing solutions of an elliptic problem in a cylindrical domain, Zap. Nauchn. Sem. St.-Petersburg Otdel. Mat. Inst. Steklov, Vol. 264 (2002), 66-82 (English transl.: Journal of Math. Sci., Vol. 111, No. 4 (2002), 3657-3666).

[2] T. Kato, *Perturbation theory for linear operators*, Die Grundlehren der Mathematischen Wissenschaften, Band 132, Springer-Verlag New York, Inc., New York, 1966

[3] N.I. Kuznetsov, V.G. Mazya and B.R. Vainberg, *Linear water waves*, Cambridge University Press, 2002.

[4] V.G. Mazya, S.A. Nazarov and B.A. Plamenevskii, *Asymptotic theory of elliptic boundary value problems in singularly perturbed domains*, Birkhäuser Verlag, Basel, 2000.

[5] S.A. Nazarov, A criterion for the existence of decaying solutions in the problem on a resonator with a cylindrical waveguide, Funkt. Anal. i Prilozhen, Vol. 40, No. 2 (2006), 20-32. (English transl.: Funct. Anal. Appl., Vol. 40, No. 2 (2006), 97-107).

[6] Nazarov S.A., Sufficient conditions for the existence of trapped modes in problems of the linear theory of surface waves, Zap. Nauchn. Sem. St.-Petersburg Otdel. Mat. Inst. Steklov, Vol. 369 (2009), 202-223.

[7] Nazarov S.A., Asymptotic expansions of eigenvalues in the continuous spectrum of a regularly perturbed quantum waveguide, Theoretical and mathematical physics. 2011. V. 167, N 2. P. 239–262 (English transl.: Theoretical and mathematical physics. 2011. V. 167, N. 2. P. 606–627).

[8] S.A. Nazarov, Trapped waves in a cranked waveguide with hard walls, Acoustic journal, Vol. 57 (2011), 746-754. (English transl.: Acoustical Physics,Vol. 57 (2011), 764-771).

[9] Nazarov S.A., Enforced stability of a simple eigenvalue in the continuous spectrum // Funkt. Anal. i Prilozhen. 2013. V. 47, N 3. P. 37–53 (English transl.: Funct. Anal. Appl. 2013. V. 475, N 3. P. 195–209).

[10] Nazarov S.A., Ruotsalainen K. M., Criteria for trapped modes in a cranked channel with fixed and freely floating bodies, Z. Angew. Math. Phys. 2014. V. 65, N 5. P. 977-1002.

[11] E. Zeidler, *Nonlinear functional analysis and its Applications, vol. II/A: Linear Monotone Operators*, Springer-Verlag New York, 1990

Proceedings of the 32nd Nordic Seminar on Computational Mechanics
A.H. Niemi and H. Koivurova (Eds.)

Numerical modelling of concrete fracture: a mesoscopic approach based on embedded discontinuity FEM

Timo Saksala

Tampere University, Civil Engineering, Finland, timo.saksala@tuni.fi

Summary. This article presents a numerical study on concrete failure under uniaxial compression. For this end, a fracture model based on the embedded discontinuity finite elements is employed. Concrete mesostructure, i.e. the aggregates and the cement matrix, is explicitly described by convex polygons. Numerical simulations (in 2D) demonstrate that the present approach can predict the salient features of concrete fracture modes even when the crack initiation is based solely on the first principal stress criterion.

Key words: mesoscopic model, concrete fracture, finite elements, embedded discontinuity

Introduction

Numerical modelling of concrete fracture processes is an important and challenging task in Civil Engineering. The classical approach based on homogenisation of the aggregates-in-cement matrix mesostructure is still the foremost method in analyses of concrete structures (especially large structures such as dams). However, the mesoscopic approach describing the aggregate-mortar structure explicitly is indispensable in the analyses of the effect of aggregate shape, size and mechanical properties on the overall behaviour of a specific concrete. Moreover, as aggregates introduce various fracture toughening mechanisms, such as crack stopping, redirection and branching [1], their explicit description is crucial.

This paper presents a numerical modelling approach where the concrete mesostructure is explicitly described and the concrete fracture is modelled based on the embedded discontinuity finite elements [2]. The original model presented by Saksala [3] is modified here by allowing cracks to initiate only in mode I, i.e. by the first principal stress (Rankine) criterion.

Concrete fracture model

Concrete fracture is described by the embedded discontinuity finite elements. In the present context this means that an ordinary constant strain triangle (CST) in enriched with special functions to model discontinuities [2, 3]. For a CST element with a strong discontinuity (crack) illustrated in Figure 1a, the displacement and strain fields are

$$\mathbf{u} = N_i \mathbf{u}_i^e + (H_{\Gamma_d} - \varphi)\boldsymbol{\alpha}_d, \quad \boldsymbol{\varepsilon} = \nabla N_i \otimes \mathbf{u}_i^e - \nabla\varphi \otimes \boldsymbol{\alpha}_d$$
$$\nabla\varphi = \arg\left(\max_{k=1,2} \frac{\left|\Sigma_{i=1}^{k} \nabla N_i \cdot \mathbf{n}\right|}{\left\|\Sigma_{i=1}^{k} \nabla N_i\right\|} \right) \tag{1}$$

where $\boldsymbol{\alpha}_d$ is the displacement jump vector, N_i and $\mathbf{u}_i^e$ are the standard interpolation function and displacement vector at node i (with summation on repeated i), and H_{Γ_d} is the Heaviside function at discontinuity Γ_d with normal $\mathbf{n}$. Finally, φ is a function that restricts the effect of the displacement jump within the corresponding finite element so that the essential boundary conditions remain unaffected. This function is chosen by criterion (1).

A bi-surface, plasticity inspired model for solving the displacement jump vector and the traction updates, as well as to control the softening behavior at the discontinuity. The components of this model are

$$\phi_{\mathrm{t}}(\mathbf{t}_{\Gamma_d}, \kappa, \dot{\kappa}) = \mathbf{n} \cdot \mathbf{t}_{\Gamma_d} - (\sigma_{\mathrm{t}} + q(\kappa, \dot{\kappa})), \quad \phi_{\mathrm{s}}(\mathbf{t}_{\Gamma_d}, \kappa, \dot{\kappa}) = |\, \mathbf{m} \cdot \mathbf{t}_{\Gamma_d}\, | - (\sigma_{\mathrm{s}} + \tfrac{\sigma_{\mathrm{s}}}{\sigma_{\mathrm{t}}} q(\kappa, \dot{\kappa}))$$
$$\dot{\boldsymbol{\alpha}}_d = \dot{\boldsymbol{\alpha}}_{\mathrm{I}} + \dot{\boldsymbol{\alpha}}_{\mathrm{II}} = \dot{\lambda}_{\mathrm{t}} \frac{\partial \phi_{\mathrm{t}}}{\partial \mathbf{t}_{\Gamma_d}} + \dot{\lambda}_{\mathrm{s}} \frac{\partial \phi_{\mathrm{s}}}{\partial \mathbf{t}_{\Gamma_d}}, \quad \dot{\mathbf{t}}_{\Gamma_d} = -\mathbf{E} : (\nabla\varphi \otimes \dot{\boldsymbol{\alpha}}_d) \cdot \mathbf{n}, \quad \dot{\kappa} = -\dot{\lambda}_{\mathrm{t}} \frac{\partial \phi_{\mathrm{t}}}{\partial q} - \dot{\lambda}_{\mathrm{s}} \frac{\partial \phi_{\mathrm{s}}}{\partial q} \tag{2}$$
$$q = h\kappa + s\dot{\kappa}, \quad h = -g\sigma_{\mathrm{t}} \exp(-g\kappa), \quad \dot{\lambda}_i \geq 0, \quad \phi_i \leq 0, \quad \dot{\lambda}_i \phi_i = 0, \quad i = \mathrm{t,s}$$

where ϕ_{t} and ϕ_{s} are the tension (mode I) and shear (mode II) loading functions, respectively, $\kappa, \dot{\kappa}$ are the internal variable and its rate, $\mathbf{m}$ is the crack tangent vector, σ_{t} and σ_{s} are elastic limits in tension and shear, respectively, $\boldsymbol{\alpha}_{\mathrm{I}}, \boldsymbol{\alpha}_{\mathrm{II}}$ are the mode I and II crack opening vectors, $\mathbf{E}$ is the elasticity tensor, $\dot{\lambda}_{\mathrm{t}}, \dot{\lambda}_{\mathrm{s}}$ are the mode I and II opening increments, respectively, h is the softening modulus, and s is the constant viscosity modulus. The softening slope parameter g is defined by the mode I fracture energy G_{Ic} by $g = \sigma_{\mathrm{t}}/G_{\mathrm{Ic}}$. It should be noted that that last equations in (2) are the consistency conditions. Viscosity is thus included in the spirit of the viscoplastic consistency approach.

A fracture occurs, i.e. a discontinuity is embedded in an element, upon violation of the Rankine criterion. However, once a crack is introduced, it can fail in both shear and tensile mode, as governed by model (2). The material point level behaviour is linear elastic up to fracture. However, as heterogeneity is naturally included in the model by the hard aggregates and the weak microcracks in the cement matrix, global nonlinear pre-peak behaviour can be captured, as will be shown in the numerical simulations.

The global equations of motion are solved with an explicit time integrator.

Concrete mesostructure

Concrete is described as a bi-phasic material with explicit aggregates in a mortar matrix. The aggregates are taken to be convex polygons. The resulting mortar-aggregate structure is meshed with the ordinary CST elements. Concrete contains inherent microcrack populations induced by hydration processes, for example. These cracks have, expectedly, a non-negligible influence on the concrete failure processes.

In the numerical concrete mesostructure in Figure 1b, the aggregates are represented by 50 polygons of different shapes and sizes. The blue lines (598 in total) represent the inherent microcrack population. The interface transition zone (ITZ) is here accounted for by lowering the strength to one half of the intact value of the elements surrounding the aggregates.

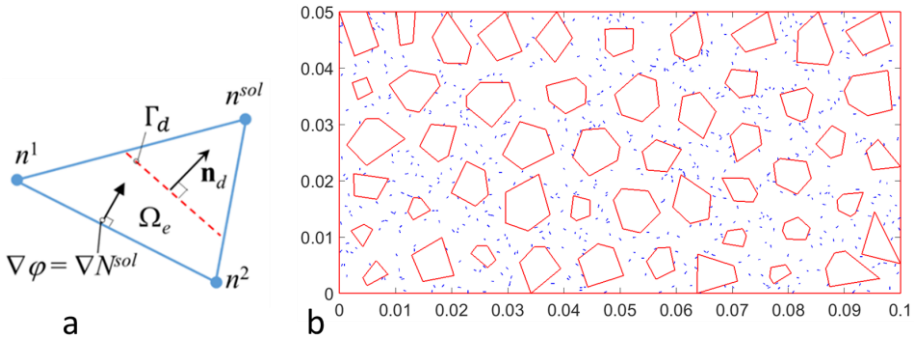

Figure 1. CST element with a discontinuity (a), and numerical concrete mesostructure (b).

The mortar is taken as the Portland cement while the aggregates are granitic rock Some of the key material properties are for mortar: E = 27.5 GPa; ν = 0.2; ρ = 2400 kg/m^3; σ_t = 3.5 MPa; σ_s = 7 MPa; G_{Ic} = 0.02 N/m and for aggregates: E = 60 GPa; ν = 0.17; ρ = 2400 kg/m^3; σ_t = 10 MPa; σ_s = 25 MPa; G_{Ic} = 0.04 N/m.

Numerical example

Uniaxial compression test is simulated as a numerical example. In addition to the original Rankine cracking criterion, where a crack is parallel to the first principal direction, a crack reorientation is tested: from among the element edge normals, the one that is most parallel to the first principal direction is selected. This scheme should result in a different kind of failure mode as, unlike in the Rankine criterion, the crack normal is not orthogonal to the loading direction. The simulation results are shown in Figure 2.

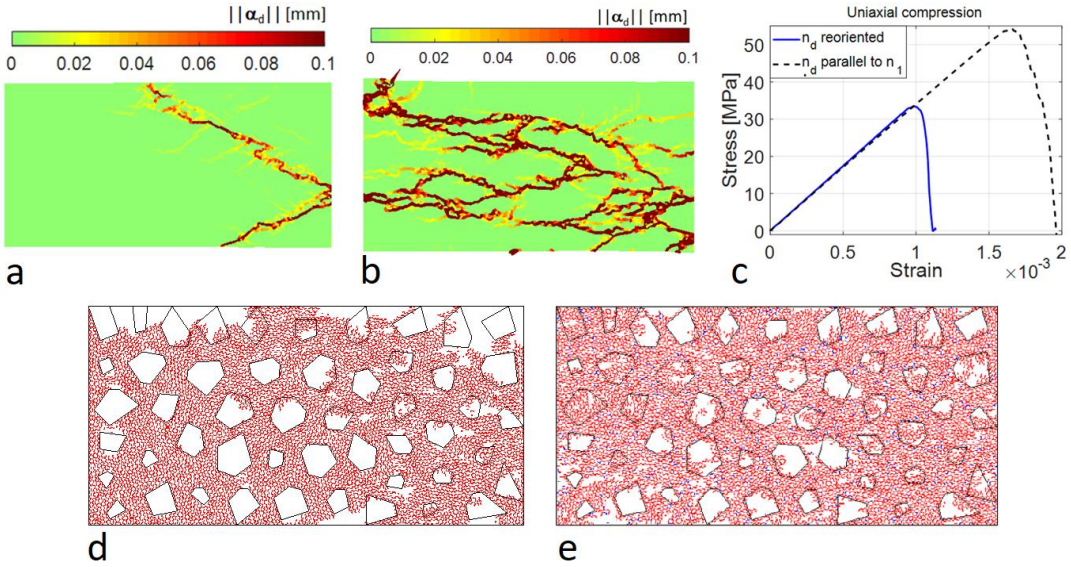

Figure 2. Uniaxial compression test: failure mode for crack reorientation (initial cracks and ITZ not included) (a) and for original orientation (initial cracks and ITZ included) (b), stress-strain responses (c), and crack distributions for crack reorientation (d) and for original orientation (e).

The failure modes (plotted as the magnitude of crack opening vectorss) shown in Figure 2a and b indeed attest different failure modes: the reorientation scheme results in a typical shear failure mode observed in the experiments [4] while the original Rankine criterion results in a multiple axial splitting mode, which is also observed in the experiments. The corresponding compressive strengths, as readable in Figure 2c, are 33 MPa and 54 MPa – typical values for normal and intermediate high strength concretes. Finally, Figure 2d and c show the final crack distributions. Cracks are almost everywhere in the numerical samples but the deformation (crack opening) localizes only in part of them to form macrocracks. Cracking occurs also in aggregates.

Conclusion

The concrete fracture modelling approach presented here show some predictive capabilities. Namely, by giving the mortar cement and the aggregates realistic material properties, low and high strength concrete behavior, including the peak stresses and the failure modes, in uniaxial compression can be replicated. Moreover, the simulation results with the first principal stress criterion corroborate the hypothesis that brittle materials failure in uniaxial compression is a violent multiple axial splitting mode.

Acknowledgements

This research was funded by Academy of Finland under grant number 298345.

References

[1] E.N. Landis, J.E. Bolander JE. Explicit representation of physical processes in concrete fracture. *Journal of Physics D: Applied Physics* 2009; 42:214002.

[2] A.E. Huespe, J. Oliver J. Crack Models with Embedded Discontinuities. In: G. Hofstetter, G. Meschke G (eds) Numerical Modeling of Concrete Cracking. pp 161-219, CISM, Udine 2011.

[3] T. Saksala. Numerical modelling of concrete fracture processes under dynamic loading: meso-mechanical approach based on embedded discontinuity finite elements. *Engineering Fracture Mechanics* 2018; 201: 282-297.

[4] J.G.M van Mier. *Fracture processes of concrete: assessment of material parameters for fracture models*, Boca Raton, CRC Press, 1996.

Proceedings of the 32nd Nordic Seminar on Computational Mechanics
A.H. Niemi and H. Koivurova (Eds.)

On periodic boundary conditions in Variationally Consistent Homogenisation of beams and plates

Adam Sciegaj[1,2], Peter Grassl[3], Fredrik Larsson[1], Karin Lundgren[2] and Kenneth Runesson[1]

(1) Department of Industrial and Materials Science, Chalmers University of Technology, Sweden, adam.sciegaj@chalmers.se, fredrik.larsson@chalmers.se, kenneth.runesson@chalmers.se
(2) Department of Architecture and Civil Engineering, Chalmers University of Technology, Sweden, karin.lundgren@chalmers.se
(3) School of Engineering, University of Glasgow, United Kingdom, peter.grassl@glasgow.ac.uk

Summary. A computationally efficient strategy to prescribe periodic boundary conditions on three-dimensional Representative Volume Elements (RVEs) is outlined. In particular, the cases of having an Euler-Bernoulli beam and a Kirchhoff-Love plate problem at the macroscale are considered within a computational homogenisation framework. Special solid elements for the boundary region of the periodic mesh have been developed, in which some of the degrees of freedom depend on those of their periodic counterparts, the macroscopic data and the size of the RVE.

Key words: periodicity, computational homogenisation, beam, plate, multiscale

Introduction

Computational Multiscale Modelling (CMM), specifically the FE^2 method, is suitable for analysis of large-scale reinforced concrete structures, such as e.g. bridges. Detailed results such as crack widths and crack patterns can be efficiently obtained for large structures, where conventional single-scale finite element analyses would be impractical. In the FE^2 method, the large-scale effective response is obtained from computational homogenisation of the response of Representative Volume Elements (RVEs), which are located at the integration points. The macroscopic fields are prescribed on the RVEs via suitable boundary conditions, and the response is homogenised (averaged) to produce a macroscopic quantity, cf. [1]. In order to increase computational efficiency of the model, the large-scale structure can often be modelled with plate/shell elements, while the detailed subscale response of the material is best described with three-dimensional RVE models. In this work, we outline the main formulation of the large-scale and subscale problems for macroscopic Euler-Bernoulli beams and Kirchhoff-Love plates. A computationally efficient way of prescribing the macroscopic fields via periodic boundary condition at the subscale, using special tetrahedral elements developed in this study, is presented.

Large-scale problem

The large-scale problem for an *Euler-Bernoulli beam*, which occupies region $[0, L]$ and is subjected to bending around the y-axis, can be expressed in the weak form as follows:

$$\int_0^L \bar{N} \frac{\partial \delta \bar{u}}{\partial x} \, \mathrm{d}x = [N_\mathrm{p} \delta \bar{u}]_0^L + \int_0^L b \delta \bar{u} \, \mathrm{d}x, \tag{1}$$

$$\int_0^L \bar{M} \frac{\partial^2 \delta \bar{w}}{\partial x^2} \, \mathrm{d}x = \left[M_\mathrm{p} \frac{\partial \delta \bar{w}}{\partial x} \right]_0^L - [V_\mathrm{p} \delta \bar{w}]_0^L - \int_0^L q \delta \bar{w} \, \mathrm{d}x, \tag{2}$$

for suitable test functions $\delta\bar{u}$ and $\delta\bar{w}$. Here, $\bar{u}$ and $\bar{w}$ are the macroscopic displacements in x- and z-directions, while b and q are the corresponding distributed loads. The forces N_{p}, V_{p}, and M_{p} are the prescribed normal forces, shear forces and bending moments, respectively. The effective normal force $\bar{N}$ and effective bending moment $\bar{M}$ are obtained from computational homogenisation upon solution of the pertinent RVE problem as

$$\bar{N} = \frac{1}{|L_\square|}\int_{\Omega_\square} \sigma_{xx}\ \mathrm{d}\Omega, \qquad\qquad \bar{M} = \frac{1}{|L_\square|}\int_{\Omega_\square} z\sigma_{xx}\ \mathrm{d}\Omega, \tag{3}$$

where σ_{xx} is the normal stress in x-direction, $L_\square$ is the length of the RVE in the x-direction, and $\Omega_\square$ is the volume of the representative volume element.

For a *Kirchhoff-Love plate* occupying region Ω with boundary $\partial\Omega = \Gamma$, the corresponding large-scale problem can be expressed in the weak form as follows:

$$\int_\Omega \bar{\boldsymbol{N}} : [\delta\bar{\boldsymbol{u}} \otimes \boldsymbol{\nabla}]\ \mathrm{d}\Omega = \int_\Gamma \boldsymbol{N}_{\mathrm{p}} \cdot \delta\bar{\boldsymbol{u}}\ \mathrm{d}\Gamma + \int_\Omega \boldsymbol{b}\cdot\delta\bar{\boldsymbol{u}}\ \mathrm{d}\Omega, \tag{4}$$

$$\int_\Omega \bar{\boldsymbol{M}} : \left[\delta\bar{w}\otimes \overset{*}{\boldsymbol{\nabla}}\right]\ \mathrm{d}\Omega = \int_\Gamma V_{\mathrm{i}}^K \delta\bar{w}\ \mathrm{d}\Gamma - \int_\Gamma M_{\mathrm{ii}}\frac{\partial\delta\bar{w}}{\partial i}\ \mathrm{d}\Gamma + \int_\Omega q\delta\bar{w}\ \mathrm{d}\Omega, \tag{5}$$

for suitable test functions $\delta\bar{\boldsymbol{u}}$ and $\delta\bar{\boldsymbol{w}}$. Here, $\boldsymbol{\nabla}$ and $\overset{*}{\boldsymbol{\nabla}}$ are the differential and curvature operators. The macroscopic fields $\bar{\boldsymbol{u}}^{\mathrm{T}} = [\bar{u}\ \bar{v}]$ and $\bar{w}$ are the in- and out-of-plane displacement fields, while $\boldsymbol{b}$ and q are the corresponding distributed loads. The forces $\boldsymbol{N}_{\mathrm{p}}$, V_{i}^K are the presribed boundary normal and Kirchhoff forces, while M_{ii} is the prescribed boundary bending moment. The effective membrane forces, $\bar{\boldsymbol{N}}$, and bending moments, $\bar{\boldsymbol{M}}$, can be obtained upon solving the RVE problem as

$$\bar{\boldsymbol{N}} = \frac{1}{|A_\square|}\int_{\Omega_\square} \hat{\boldsymbol{\sigma}}\ \mathrm{d}\Omega, \qquad\qquad \bar{\boldsymbol{M}} = \frac{1}{|A_\square|}\int_{\Omega_\square} z\hat{\boldsymbol{\sigma}}\ \mathrm{d}\Omega, \tag{6}$$

where $\hat{\boldsymbol{\sigma}}$ denotes the in-plane projection of the Cauchy stress and $A_\square$ is the area of the RVE in the xy-plane.

Subscale problem with periodic boundary conditions

The weak form of the three-dimensional boundary value problem on the RVE is defined in terms of finding the unknown displacement field $\boldsymbol{u}^{\mathrm{T}} = [u\ v\ w]$ from the momentum equilibrium relation

$$\int_{\Omega_\square} \boldsymbol{\sigma} : [\delta\boldsymbol{u}\otimes\boldsymbol{\nabla}]\ \mathrm{d}\Omega = \int_{\Gamma_\square} \hat{\boldsymbol{t}}\cdot\delta\boldsymbol{u}\ \mathrm{d}\Gamma, \tag{7}$$

with suitable boundary conditions and pertinent test functions $\delta\boldsymbol{u}$. In this relation, the RVE is defined within the region $\Omega_\square$ and is subjected to tractions $\hat{\boldsymbol{t}}$ on its boundary $\partial\Omega_\square = \Gamma_\square$. In this work, we consider periodic boundary conditions, which state that the fluctuation part of the total fields are equal at both boundaries of the RVE. To this end, we define the image (plus) side and the mirror (minus) side of the representative volume element. The difference in deformation at these two boundaries is simply governed by the (gradients of) macroscopic fields. For the *Euler-Bernoulli beam* we have the following relations linking the macro- and microfields:

$$u^+ - u^- = \left[\frac{\partial\bar{u}}{\partial x} - z\frac{\partial^2\bar{w}}{\partial x^2}\right]\left[x^+ - x^-\right], \tag{8}$$

$$w^+ - w^- = \frac{\partial\bar{w}}{\partial x}\left[x^+ - x^-\right], \tag{9}$$

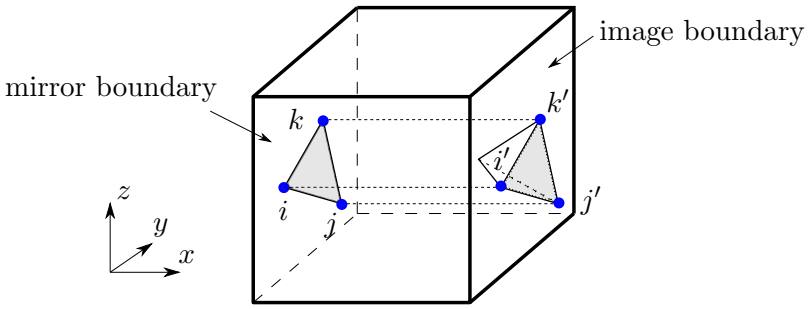

Figure 1. Boundary tetrahedral finite element in a cube RVE with periodicity in x-direction. Nodes i', j', and k' are replaced by their periodic counterparts i, j, k.

where x^+ and x^- are the x-coordinates of the image and mirror boundaries, respectively. For the *Kirchhoff-Love plate* at the macroscale the corresponding relations are:

$$u^+ - u^- = \left[\frac{\partial \bar{u}}{\partial x} - z\frac{\partial^2 \bar{w}}{\partial x^2}\right]\left[x^+ - x^-\right] + \left[\frac{\partial \bar{u}}{\partial y} - z\frac{\partial^2 \bar{w}}{\partial x \partial y}\right]\left[y^+ - y^-\right], \tag{10}$$

$$v^+ - v^- = \left[\frac{\partial \bar{v}}{\partial x} - z\frac{\partial^2 \bar{w}}{\partial x \partial y}\right]\left[x^+ - x^-\right] + \left[\frac{\partial \bar{v}}{\partial y} - z\frac{\partial^2 \bar{w}}{\partial y^2}\right]\left[y^+ - y^-\right], \tag{11}$$

$$w^+ - w^- = \frac{\partial \bar{w}}{\partial x}\left[x^+ - x^-\right] + \frac{\partial \bar{w}}{\partial y}\left[y^+ - y^-\right]. \tag{12}$$

The differences $x^+ - x^-$ and $y^+ - y^-$ represent the distances between the image and mirror boundaries normal to x and y directions. In the usual case of a cuboid RVE, these simply translate to the lengths in x- and y-direction, respectively.

Modified boundary tetrahedral finite element

In order to resolve relations (8)–(12) in the RVE model, a new element was developed and implemented in the open-source code OOFEM [4]. The element, inspired by similar periodic formulation from [2] and [3], is based on the classical tetrahedral element with linear shape functions and is intended to represent part of the image bounday of the RVE, cf. Figure 1.

The user defines the boundary element using only the corresponding nodes at the mirror boundary, the direction of periodicity and the size of the RVE. Additionally, one control node is defined for the model and is also used in the boundary element definition. The control node is intended to contain the macroscopic information about the effective fields within its degrees of freedom. Depending on the macroscopic problem (Euler-Bernoulli beam or Kirchhoff-Love plate), the control node has either 3 or 10 degrees of freedom - the partial derivatives in relations (8)–(12). Using these relations, it is possible to express the unknown degrees of freedom of any boundary element at the image boundary as function of the degrees of freedom of the corresponding nodes at mirror boundary and the macroscopic information from the control node, i.e.

$$\mathbf{u}' = \mathbf{T}\mathbf{u}, \tag{13}$$

where $\mathbf{u}'$ is the vector containing the displacement degrees of freedom at the image boundary, while $\mathbf{u}$ contains the displacement degrees of freedom of the corresponding nodes at the mirror boundary as well as the degrees of freedom of the control node. The matrix $\mathbf{T}$ is basically a unit matrix expanded by the corresponding entries from Equations (8)–(12). At any iteration step, after evaluating the element deformations $\mathbf{u}'$ according to Equation (13), the element stiffness matrix $\mathbf{K}'$ and internal force vector $\mathbf{f}'_{\text{int}}$ can be computed in the usual fashion. In order to transfer

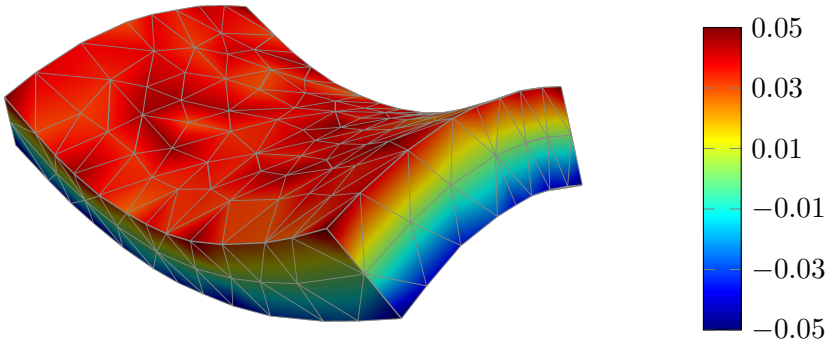

Figure 2. Contour plot of the strain ε_{yy} in a plate RVE subjected to macroscopic curvatures $\partial^2\bar{w}/\partial x^2 = 1$, $\partial^2\bar{w}/\partial y^2 = -1$

back to the mirror boundary and continue with the assembly, we use the following relations:

$$\mathbf{K} = \mathbf{T}^{\mathrm{T}}\mathbf{K}'\mathbf{T}, \qquad \mathbf{f}_{\mathrm{int}} = \mathbf{T}^{\mathrm{T}}\mathbf{f}'_{\mathrm{int}}. \tag{14}$$

Example response

In order to illustrate the method, a sample linear elastic RVE in shape of a cuboid with sizes $L_{\mathrm{x}} = 0.6$ m, $L_{\mathrm{y}} = 0.4$ m and $L_{\mathrm{z}} = 0.1$ m was considered. A periodic tetrahedral mesh was created following the method described in [2] and [3]. Subsequently, all elements with nodes at the image boundaries were replaced by the corresponding modified boundary tetrahedra. Macroscopic curvatures $\partial^2\bar{w}/\partial x^2 = 1$, $\partial^2\bar{w}/\partial y^2 = -1$ were imposed on the RVE by prescribing them as boundary conditions in the corresponding degrees of freedom of the control node. The deformed shape and a contour plot of the strain ε_{yy} can be seen in Figure 2. It is noteworthy that the obtained reaction forces in the control node are the effective forces (moments), that can be used directly in the FE^2 scheme.

Conclusions

We proposed new boundary tetrahedral elements, which make it possible to impose an arbitrary combination of macroscopic in-plane strains, slopes and curvatures as periodic boundary conditions on the RVE. This is a necessary step to apply the FE^2 procedure to large-scale structures modelled with beam and plate/shell elements.

References

[1] F. Larsson, K. Runesson and F. Su. Variationally consistent computational homogenization of transient heat flow. *International Journal for Numerical Methods in Engineering*, 81: 1659–1686, 2010.

[2] I. Athanasiadis, S. J. Wheeler and P. Grassl. Hydro-mechanical network modelling of particulate composites. *International Journal of Solids and Structures*, 130–131: 49–60, 2018.

[3] P. Grassl and M. Jirásek. Meso-scale approach to modelling the fracture process zone of concrete subjected to uniaxial tension. *International Journal of Solids and Structures*, 47: 957–968, 2010.

[4] B. Patzák. OOFEM - an object-oriented simulation tool for advanced modeling of materials and structures. *Acta Polytechnica*, 52(6):59–66, 2012

Proceedings of the 32nd Nordic Seminar on Computational
Mechanics A.H. Niemi and H. Koivurova (Eds.)

Numerical analysis of coupled nerve signal propagation

Kert Tamm[1], Tanel Peets[2], and Jüri Engelbrecht[3]

Department of Cypernetics, School of Science, Tallinn University of Technology
Akadeemia tee 21, 12618, Tallinn, Estonia
(1)kert@ioc.ee, (2)tpeets@ioc.ee, (3)je@ioc.ee

Summary. A coupled model describing the nerve pulse propagation in nerve axons is numerically studied and the characteristics of the emerging wave ensemble are described. The key phenomena observed are: (i) the velocity of the peak of the mechanical pulse is similar to the velocity of the action potential regardless of the sound velocity value in the lipid bi-layer, (ii) the velocity of the front and the shape of the mechanical wave depends on sound velocity in the lipid bi-layer, (iii) the shape of the mechanical wave can have an effect on the velocity and shape of the action potential.

Key words: nerve signal, pseudospectral method, ensemble of waves

Introduction and model equations

In this contribution, the effects associated with the nerve pulse propagation in nerve axons is investigated using mathematical modelling. The propagation process is composed of three connected phenomena: (i) the action potential (electrical signal), which is usually considered when nerve pulse propagation is modelled (see [1] and references therein), (ii) the mechanical wave propagating on the axon (nerve fibre) surface [2] and (iii) the pressure wave in the axoplasm inside the axon [3]. In this analysis, the thermodynamical effects are left aside. Possibilities for accounting for the thermodynamic effects within the present framework can be found in [4].

In a nutshell, our idea is simple. We take established single models describing all effects related to the nerve pulse propagation that should be considered, propose coupling terms between the processes that influence each other, and derive a coupled mathematical model describing an ensemble of waves related to the nerve pulse propagation [5].

For modelling the action potential (AP), the FitzHugh-Nagumo model (FHN) [6] in dimensionless form is used:

$$\begin{aligned} Z_T &= Z\left(Z - C_1 - Z^2 + C_1 Z\right) - I + DZ_{XX}, \\ I_T &= \varepsilon\left(ZC_2 - I\right), \end{aligned} \tag{1}$$

where Z is trans-membrane potential, I is the combined ion (recovery) current, D is a coefficient, $C_i = a_i + b_i$ where a_i are the 'electrical' activation coefficients, b_i are the 'mechanical' activation coefficients and X, T are the dimensionless spatial and time coordinates, respectively. Subscripts X, T here and further denote partial derivatives with respect to the indicated coordinate. The coefficients b_i could be taken as $b_1 = -g_1 U$ and $b_2 = -g_2 U$ where g_i are constants and U is from Eq. (2) – the feedback from the mechanical wave.

The mechanical wave (LW) in surrounding biomembrane is modelled by the improved Heimburg-Jackson (iHJ) model [7, 8]:

$$\begin{aligned} U_{TT} = {} & c^2 U_{XX} + NUU_{XX} + MU^2 U_{XX} + N\left(U_X\right)^2 + \\ & + 2MU\left(U_X\right)^2 - H_1 U_{XXXX} + H_2 U_{XXTT} + g_3 I_X, \end{aligned} \tag{2}$$

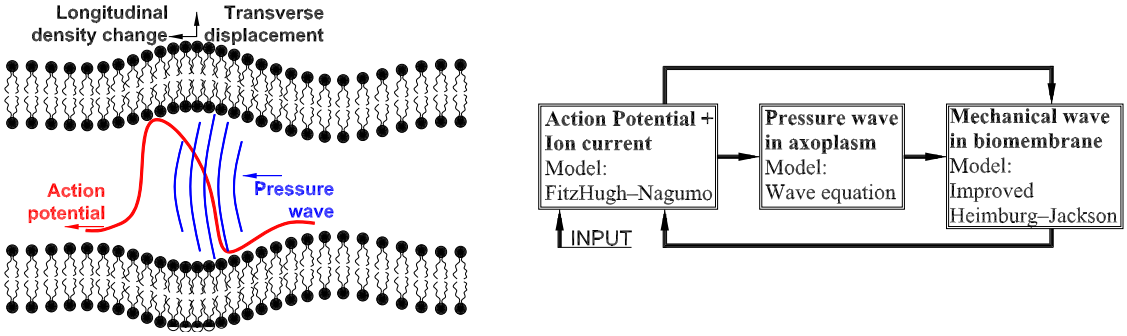

Figure 1. Illustrative scheme (right) for the wave ensemble and block diagram of the combined model for the nerve pulse propagation (left).

where $U = \Delta\rho$ is the dimensionless longitudinal density change in the lipid bi-layer, N, M are the nonlinear coefficients, H_1, H_2 are the dispersion coefficients, c is the velocity in the unperturbed state, g_3 is the coupling coefficient and I_X is the gradient of I from Eq. (1). It should be noted that while recovery current I is a positive pulse-type quantity, its gradient I_X is a bi-polar quantity which is important for the stability of the solution of the Eq. (2).

For the pressure wave (PW) is axoplasm, a classical wave equation with an added viscous term is used:

$$P_{TT} = c_f^2 P_{XX} - \mu P_T + F(Z, J, U), \tag{3}$$

where P is the dimensionless pressure, c_f is the sound velocity in axoplasm, μ is viscosity coefficient. Here $F(Z, J, U)$ is the coupling term accounting for the possible influence from the action potential (ion currents) and the mechanical wave in biomembrane. An illustrative scheme and a block diagram for the proposed model is shown in Fig. 1. In the present contribution a two component model containing the AP (Eq. (1)) and the LW (Eq. (2)) is used. Simulations including the PW can be found in [5].

Numerical scheme

A sech^2-type localized initial condition with an initial amplitude Z_o is applied to Eq. (1) and we make use of the periodic boundary conditions

$$Z(X, 0) = Z_o \,\mathrm{sech}^2\, B_o X;\; Z(X, T) = Z(X + 2Km\pi, T);\; m = 1, 2, \ldots, \tag{4}$$

where $K = 160$, i.e., the total length of the spatial period is 320π. For Eq. (2) we take initial excitation to be zero and make use of the periodic boundary conditions. The solution representing the mechanical wave described by Eq. (2) is generated over time as a result of coupling between the Eqs (1) and (2).

For numerical solving of the Eqs (1) and (2) we use the discrete Fourier transform (DFT) based pseudospectral method (PSM) [9]. Variable Z is represented in the Fourier space as

$$\widehat{Z}(k, T) = \mathrm{F}\left[Z\right] = \sum_{j=0}^{n-1} Z(j\Delta X, T) \exp\left(-\frac{2\pi \mathrm{i} jk}{n}\right), \tag{5}$$

where n is the number of space-grid points ($n = 2^{12}$ in the present paper), $\Delta X = 2\pi/n$ is the space step, $k = 0, \pm 1, \pm 2, \ldots, \pm(n/2 - 1), -n/2$; i is the imaginary unit, F denotes the DFT and F^{-1} denotes the inverse DFT. Basically, the idea of the PSM is to approximate space derivatives by making use of the DFT

$$\frac{\partial^m Z}{\partial X^m} = \mathrm{F}^{-1}\left[(\mathrm{i}k)^m \mathrm{F}(Z)\right], \tag{6}$$

reducing therefore the partial differential equation (PDE) to an ordinary differential equation (ODE) and then to use standard ODE solvers for integration with respect to time.

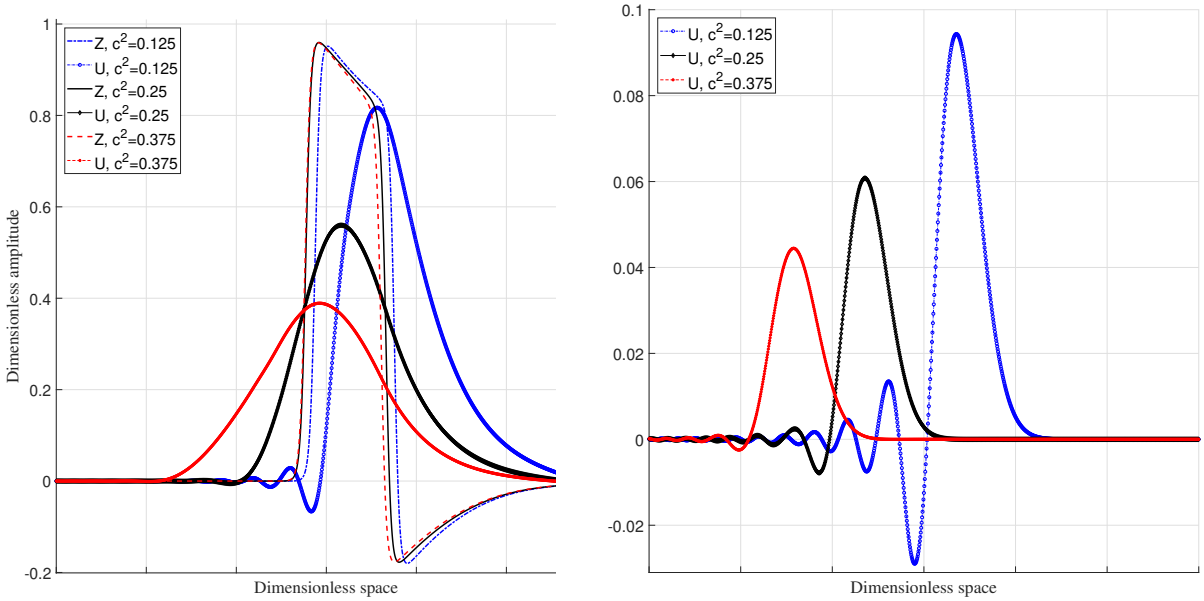

Figure 2. The left propagating solutions of Eqs (1) (variable Z) and (2) (variable U) . Parameters $D = 1$, $a_1 = 0.2$, $a_2 = 0.2$, $N = 0.05$, $M = 0.02$, $H_1 = 0.5$, $H_2 = 0.75$, $g_1 = 0.05$, $g_2 = 0.05$, $g_3 = 0.02$, $\varepsilon = 0.01$ (the left plot) and $\varepsilon = 0.05$ (the right plot).

Selected results

The solutions for the coupled model equations (1) and (2) at $T = 400$ are shown in Fig. 2. The initial 'spark' either leads to a formation of the propagating FHN action potential which then leads to formation of mechanical waves through coupling (Fig. 2 left) or if the initial value of the 'spark' is below the threshold for the FHN model (1) then it vanishes over a short time leading to a formation of only a small amplitude mechanical wave which proceeds to propagate without the FHN action potential (Fig. 2 right). Note the difference in the scales of the left and right panels in Fig. 2. Here only the waves propagating to the left are shown. The similar wave-profiles exist propagating to the right which are not shown.

In Fig. 2 (left) we compare action potentials Z and mechanical waves U at dimensionless time $T = 400$ provided the velocity of the low frequency sound is different for the lipid bi-layer. A number of essential characteristics for the coupled model system can be observed: (i) the velocity of the peak of the mechanical pulse is similar to the velocity of the action potential regardless of the sound velocity value in the lipid bi-layer within the considered parameter range, (ii) the velocity of the front and the shape of the mechanical wave depends on sound velocity in the lipid bi-layer for the Eq. (2), (iii) the shape of the mechanical wave can have an effect on the velocity and shape of the action potential (if $c^2 = 0.25$ for the mechanical wave then the corresponding action potential Z has propagated further compared with the case $c^2 = 0.125$).

In Fig. 2 (right) the wave-profiles of the mechanical wave at $T = 400$ when the initial excitation for the Eq. (1) is below the threshold at three different values for the c^2 is shown. It can be noted that while the front of the wave-profile propagates at the same velocities as in Fig. 2 (left), the peak of the packet travels faster than the corresponding wave-profile in Fig. 2 (left). While not shown here, it should be noted that the system can also support solitonic solutions. For example, in case of $c^2 = 0.755$ under the considered parameters (when $\varepsilon = 0.05$) a solution where the initial pulse is separated into a train of solitonic pulses emerges [10]. The cases shown here have an oscillatory structure.

The numerical results demonstrate a number of characteristics for the combined nerve pulse model which are qualitatively in line with the observations from the experiments. It must be stressed that presented profiles are for the longitudinal density change while in experiments

usually a transverse displacement is measured. However, the connection between longitudinal density change and transverse displacement can be established in a straightforward manner by drawing inspiration from theory of rods [8].

Finally, it must be mentioned that the results presented here represent a wave ensemble which is characteristic to a complex material. Complex materials are characterised by their internal structures and several fields may occur simultaneously. In case of simplified linear models, depending on initial or boundary conditions, several uncoupled waves may emerge, all propagating separately. In a complex case, these waves are coupled and the interaction of waves does not allow to consider them as single waves [11].

Acknowledgements

Draft of this contribution is published in arXiv:1906.01271 [physics.bio-ph]. This research was supported by the European Union through the European Regional Development Fund (Estonian Programme TK 124) and by the Estonian Research Council (projects IUT 33-24, PUT 434).

References

[1] C. Schwiening. A brief historical perspective: Hodgkin and Huxley. *Journal of Physiology*, 590(11):2571–2575, 2012.

[2] K. Iwasa, I. Tasaki and R. Gibbons. Swelling of nerve fibers associated with action potentials. *Science*, 210(4467):338–339, 1980.

[3] S. Terakawa. Potential-dependent variations of the intracellular pressure in the intracellularly perfused squid giant axon. *Journal of Physiology*, 369(1):229–248, 1985.

[4] K. Tamm, J. Engelbrecht and T. Peets. Temperature changes accompanying signal propagation in axons. *Journal of Non-Equilibrium Thermodynamics*, 44(3), 277–284, 2019.

[5] J. Engelbrecht, K. Tamm and T. Peets. Modeling of complex signals in nerve fibers. *Medical Hypotheses*, 120, 90–95, 2018.

[6] J. Nagumo, S. Arimoto and S. Yoshizawa. An active pulse transmission line simulating nerve axon. *Proceedings of the IRE*, 50(10): 2061–2070, 1962.

[7] T. Heimburg and A.D. Jackson. On soliton propagation in biomembranes and nerves. *Proceedings of the National Academy of Sciences of the USA*, 102(28), 9790–9795, 2005.

[8] J. Engelbrecht, K. Tamm and T. Peets. On mathematical modelling of solitary pulses in cylindrical biomembranes. *Biomechanics and Modeling in Mechanobiology*, 14:159–167, 2015.

[9] B. Fornberg. *A Practical Guide to Pseudospectral Methods*. Cambridge University Press, 1998.

[10] J. Engelbrecht, K. Tamm and T. Peets. On solutions of a Boussinesq-type equation with displacement-dependent nonlinearities: the case of biomembranes. *Philosophical Magazine*, 97(12): 967–987, 2017.

[11] J. Engelbrecht, A. Berezovski, T. Peets and K. Tamm. Wave ensembles in complex media. *Wave Motion*, submitted.

Proceedings of the 32nd Nordic Seminar on Computational Mechanics
A.H. Niemi and H. Koivurova (Eds.)

Nonlinear bending of microarchitectural thin beams within strain gradient elasticity

Loc V. Tran* and Jarkko Niiranen

Department of Civil Engineering, School of Engineering, Aalto University, Finland
* Corresponding author: loc.tran@aalto.fi

Abstract. This paper investigates the bending behaviour of beams by taking into account (1) material length scales according to Mindlin's strain gradient elasticity theory of form II, (2) small strains but moderate displacements based on the von Kármán strain assumptions. The principle of virtual work is used to derive the nonlinear governing equations in form of a sixth-order partial differential equation. Thereafter, a conforming Galerkin method based on an isogeometric approach is adopted to naturally fulfill the stringent C^2-continuity required by the beam model. Through numerical benchmarks, the accuracy and validity of the present theoretical formulations at linear and nonlinear regimes are confirmed.

Key words: beam, strain gradient elasticity, isogeometric analysis, geometrical nonlinearity

Introduction

Micro-beams are nowadays the key components in micro- and nano-electromechanical systems [1] such as micro sensors and actuators, atomic force microscopes, and so on. Therefore, they get an extreme attention from scientists and researchers as well. As observed through a number of experimental tests, the classical continuum mechanics without any intrinsic length scale parameters wrongly predicts and describes the static and dynamic behaviour of the small-size structures under various mechanical conditions, for example, in torsion of a copper wire [2], bending of an epoxy beam [3], and plastic hardening of a thin nickel beam [4]. This leads to the necessity of non-classical continuum theories which include material length scale parameters, in addition to the classical Lame's constants used in the conventional elasticity theory, in order to capture the size-dependencies. Another class of structures obeying the non-classical continuum theories is microarchitectural thin structures (of any scale) with the characteristic length scale of microstructures close to the dimensions of the structure itself, such as its thickness [5].

Strain gradient elasticity theory pioneered by Mindlin [6] is a well-known non-classical continuum theory which includes higher-order gradient terms of displacements (or strains) in the strain energy density. The Mindlin continuum theory can be simplified into some simple one-parameter continuum theories involving only one material length scale parameter, such as Aifantis's strain gradient theory [7] (ASGT), modified strain gradient theory (MSGT) [3], modified couple stress theory (MCST) [8] and simplified strain gradient theory (SSGT) [9]. Furthermore, from the point of view of structural mechanics and experiments, micro- or microarchitectural beams can exhibit large deformations in which the mid-plane stretching becomes dominant, resulting in a geometrical nonlinearity [10]. Within the nonlinear regime, analytical solution approaches work only in some simple cases of geometries, loadings and

boundary conditions. Therefore, numerical techniques must be developed for solving the complex partial differential equations governing the problem settings. Due to the salient features of isogeometric analysis, higher-order continuity achieved by using B-spline shape functions particularly, a conforming isogeometric C^{p-1}-continuous discretization (with order $p \geq 3$) is utilized to naturally fulfil the C^2-continuity requirement without any additional variables [11].

Objective

The main purpose of this paper is to further extend the study of strain-gradient-elastic thin beams [11] within the regime of nonlinear deformations:

First, we formulate a nonlinear strain-gradient-elastic beam model based on the general Mindlin's elasticity theory of form II. By appropriately choosing the length scale parameters, various simplified one-parameter formulations corresponding to the MSGT, ASGT, MCST and SSGT can be retrieved.

Second, we adopt isogeometric B-spline basis functions for implementing a conforming C^{p-1}-continuous method. Then by applying the Newton–Raphson method, the nonlinear beam bending problem is solved iteratively. Through numerical benchmarks, the accuracy and validity of the present theoretical formulations at linear and nonlinear regimes are confirmed.

Third, we demonstrate the advantage of applying the strain gradient elasticity theory for analyzing 2D triangular lattice structures. By using a one-dimensional reduction model for the corresponding microarchitectural beam structures, we significantly reduce the number of degrees of freedom resulting in essential savings in computational costs, while maintaining a valid level of accuracy, as compared to standard 2D finite element simulations.

References

[1] Y.-C. Hu, C. Chang, and S. Huang, Some design considerations on the electrostatically actuated microstructures. *Sensors and Actuators A: Physical*, 112(1):155–161, 2004.

[2] N. Fleck, et al., Strain gradient plasticity: theory and experiment. *Acta Metallurgica et materialia*, 42(2):475–487, 1994.

[3] D.C. Lam, et al., Experiments and theory in strain gradient elasticity. *Journal of the Mechanics and Physics of Solids*, 51(8):1477–1508, 2003.

[4] J.S. Stölken and A. Evans, A microbend test method for measuring the plasticity length scale. *Acta Materialia*, 46(14):5109–5115, 1998.

[5] S. Khakalo, V. Balobanov and J. Niiranen, Modelling size-dependent bending, buckling and vibrations of 2D triangular lattices by strain gradient elasticity models: Applications to sandwich beams and auxetics. *International Journal of Engineering Science*, 127:33–52, 2018.

[6] R.D. Mindlin, Micro-structure in linear elasticity. *Archive for Rational Mechanics and Analysis*, 16(1):51–78, 1964.

[7] E.C. Aifantis, On the role of gradients in the localization of deformation and fracture. *International Journal of Engineering Science*, 30(10):1279–1299, 1992.

[8] F. Yang, et al., Couple stress based strain gradient theory for elasticity. *International Journal of Solids and Structures*, 39(10):2731–2743, 2002.

[9] B. Altan and E. Aifantis, On some aspects in the special theory of gradient elasticity. *Journal of the Mechanical Behavior of Materials*, 8(3):231–282, 1997.

[10] S. Ramezani, A micro scale geometrically non-linear Timoshenko beam model based on strain gradient elasticity theory. *International Journal of Non-Linear Mechanics*, 47(8):863–873, 2012.

[11] J. Niiranen, et al., Variational formulations, model comparisons and numerical methods for Euler–Bernoulli micro- and nano-beam models. *Mathematics and Mechanics of Solids*, 24(1):312–335, 2019.

Proceedings of the 32nd Nordic Seminar on Computational Mechanics
A.H. Niemi and H. Koivurova (Eds.)

Continuum damage modelling of quasi-brittle materials by using the material point method

Quoc-Anh. Tran, Tuan H. A. Nguyen*, Jarkko Niiranen and Wojciech Sołowski

Department of Civil Engineering, Aalto University, Finland
(*) Corresponding author, email address: tuan.3.nguyen@aalto.fi

Summary. This works focuses on the modelling of damage of quasi-brittle materials in the framework of the Material Point Method (MPM). The adopted local damage formulation is enhanced with a localization limiter derived from the framework of fracture mechanics in terms of fracture energy. The model is therefore capable of simulating strain softening without suffering from mesh size dependency. The problems associated to highly distorted elements undergoing strain localization are effectively alleviated by using the Convected Particle Domain Interpolation Material Point Method combined with the generalized alpha scheme. Numerical tests are conducted for both quasi-static and dynamic loading conditions in order to demonstrate the features of the developed model.

Key words: continuum damage, localization limiter, fracture energy, MPM

Continuum damage model

Continuum damage models describe quasi-brittle fracture which exhibits strain softening and eventually leads to failure. In the so-called local continuum approaches, when reaching a certain level of an accumulated damage, strain softening results in the ill-posedness of the system of equations describing the deformation process. Consequently, numerical solutions suffer from mesh dependency and do not converge to physically meaningful solutions. In order to alleviate this problem, the non-local damage models, including integral [1] and differential types [2, 3], are introduced by incorporating an internal length scale parameter into the governing equations. However, both of the two approaches require additional variables, as the nonlocal strains must be calculated from their local counterparts, and therefore significantly increase the numerical effort. An alternative method is to integrate a length scale parameter, which plays the role of a localization limiter, directly into the softening law as proposed by Kurumatani *et al.* [4].

The material point method

The finite element method (FEM), while immensely popular in the industrial design and analysis software, cannot easily model extremely large deformations due to the problems of mesh distortion. When a mesh distorts, as in the case of strain localization inside damage zones, the

Jacobian matrices of the distorted elements become nearly singular, which exacerbates numerical errors. These errors accumulate through time steps and eventually lead to unphysical solutions. In this paper, the Material Point Method (MPM) [5] is introduced for tackling these situations without searching for neighbor particles like in other mesh-free methods. The MPM discretizes a continuum body with a finite set of material points in the original configuration and these points are tracked during the deformation process. Accordingly, a fixed Eulerian mesh is used to solve the balance equations of the problem. In this work, we adopt the Convected Particle Domain Interpolation [6] method, an advanced MPM version developed to enhance the numerical accuracy and stability. We also apply the generalized alpha scheme [7] in order to reduce the velocity oscillations of impact loadings. The proposed damage model and the MPM method are implemented in the Uintah software [8].

Fracture energy-based damage model in the framework of the MPM

This work presents MPM damage simulations of a quasi-brittle sample with the effect of the strain rate on the damage profiles taken into account. The damage formulation proposed in [4] is adopted. Herein, a history parameter of the strain intensity, which in turn drives a scalar damage parameter, is assigned to each material point. Through the loading process, the damage parameters are calculated and the state of the material is updated accordingly, which represents the damage propagation. The speed of material degradation is controlled by fracture energy in order to remedy the over-localization of damage during mesh refinements. A mesh convergence study is carried out under a quasi-static loading case by setting a low value for the loading rate. Then, the rate of loading is gradually increased and the corresponding structural responses and damage profiles are analyzed accordingly.

References

[1] C. Giry, F. Dufour and J. Mazars, "Stress-based nonlocal damage model", *International Journal of Solids and Structures,* vol. 48, pp. 3431-3443, 2011.

[2] R. H. J. Peerlings, R. de Borst, W. A. M. Brekelman and J. H. P. de Vree, "Grandient enhanced damage for quasi-brittle materials", *International Journal for Numerical Methods in Engineering,* vol. 39, pp. 937-953, 1996.

[3] T. H. A. Nguyen, T. Q. Bui and S. Hirose, "Smoothing gradient damage model with evolving anisotropic nonlocal interactions tailored to low-order finite elements", *Computer Methods in Applied Mechanics and Engineering,* vol. 328, pp. 498-541, 2018.

[4] M. Kurumatani, K. Terada, J. Kato, T. Kyoya and Kashiyama, "An isotropic damage model based on fracture mechanics of concrete", *Engineering Fracture Mechanics,* vol. 155, pp. 49-66, 2016.

[5] D. Sulsky, Z. Chen and H. L. Schreyer, "A particle method for history-dependent materials", *Computer Methods in Applied Mechanics and Engineering,* vol. 118, pp. 179-196, 1994.

[6] A. Sadeghirad, R. Brannon and J. Burghardt, "A convected particle domain interpolation technique to extend applicability of the material point method for problems involving massive deformations", *International Journal for Numerical Methods in Engineering,* vol. 86, pp. 1435-1456, 2011.

[7] Q. A. Tran and W. Solowski, "Temporal and null-space filter for the material point method," *International Journal for Numerial Methods in Engineering,* pp. 1-33, 2019.

[8] Unitah, "http://www.unitah.utah.edu," [Online].

Proceedings of the 32nd Nordic Seminar on Computational Mechanics
A.H. Niemi and H. Koivurova (Eds.)

Finite Element Simulation of the Performance of a Structural Electrolyte

Vinh Tu[1], Leif E. Asp[1], Natasha Shirshova[2], Fredrik Larsson[1], Kenneth Runesson[1], and Ralf Jänicke[1]

(1) Chalmers University of Technology, Division Material and Computational Mechanics, e-mail: vinh.tu@chalmers.se
(2) University of Durham, Research Group Future Energy Systems and Next Generation Materials and Microsystems

Summary. This contribution concerns the multi-scale and multi-physics finite element analysis of structural power composites, i.e. multifunctional composites with simultaneous load bearing and energy storing functionality. We are particularly interested in obtaining the effective macro-scale properties of the structural electrolyte by employing computational homogenization to capture the effects of micro-heterogeneities on the sub-scale. The sub-scale problem is defined by a statistical volume element that is numerically generated, and the effective properties are obtained by conducting virtual material testing on the synthetic microstructure.

Keywords: structural electrolyte, artificial microstructure, statistical volume element, computational homogenization, virtual material testing

Structural power composites

Carbon fibers are not only widely used as structural reinforcement materials; they are also attractive for use in electrode components due to their excellent intercalation properties. Combining and utilizing both of its functionalities, strength and ionic storage capacity, at once results in new multifunctional materials called structural power composites, such as the structural battery and structural supercapacitor that have simultaneous load bearing and energy storing functionality [1, 2].

If two different needs are addressed with a multifunctional material instead of two separate subsystems, then significant weight and volume savings can be achieved [2]. In short, this innovation enhances the system performance in various applications, and addresses the demand for more efficient and sustainable systems. However, due to the infancy of this technology, more studies need to be conducted.

In this contribution, we are particularly interested in the structural electrolyte, which is a crucial component for all structural power composites. The structural electrolyte's function is to be electrically insulating, but ionically conductive while being able to carry mechanical loads. The considered structural electrolyte consists of a highly porous solid polymer matrix, where the pores are interconnected and form a complex channel system that contains liquid electrolyte. Since both the solid phase and the pore space are continuous, the structural electrolyte forms a bicontinuous system. The aim of this contribution is to study the ionic conductivity and the stiffness of the structural electrolyte with finite element analysis.

Two-scale modeling by computational homogenization

In order to include the effects of micro-heterogeneities in the structural electrolyte microstructure, we employ computational homogenization [3] to separate the sub-scale and the macro-scale. Doing this allows us to compute the effective properties for the macro-scale via homogenization of the sub-scale problem. The sub-scale problem is defined by a Statistical Volume Element (SVE) that characterizes the material heterogeneity. The SVE is given by an artificial microstructure that is numerically generated in a fashion that enables us to use periodic boundary conditions. Different approaches to the artificial microstructure generation are used depending on the desired morphology of the structural electrolyte microstructure, see Figure 1.

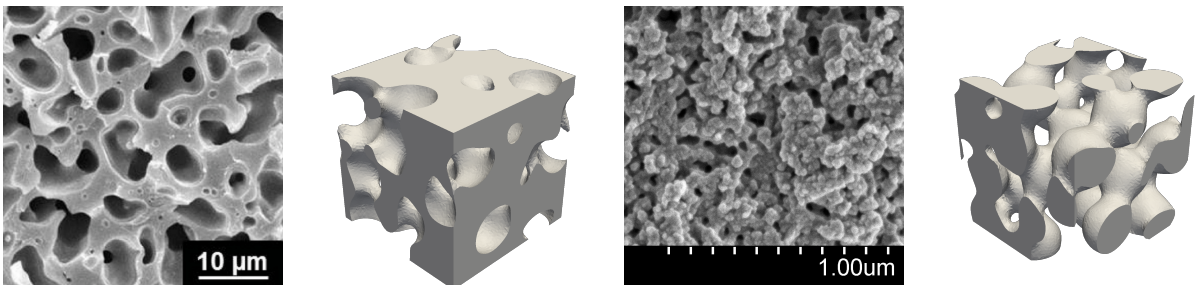

(a) (b) (c) (d)

Figure 1: SEM scans of the solid polymer matrix and corresponding artificial structures. (a) SEM scan 50MTM57/2.3M_1PC [4], and (b) its artificial counterpart. (c) SEM scan AB/0.65 [5][1], and (d) its artificial counterpart.

Since both the mechanical properties and the electrochemical conductivity are of interest, we solve the linear elasticity and linear diffusion problem on the sub-scale. Here, we assume that there is no mechanical resistance from the liquid electrolyte in the pore channels when the structural electrolyte is loaded mechanically, i.e. the structural electrolyte is considered to be a drained system. Furthermore, we assume that diffusion cannot take place in the solid polymer matrix, and that the diffusion problem is stationary and decoupled from the mechanical problem.

The strong form of the sub-scale linear elasticity and diffusion problem in the SVE domain $\Omega_\square$ is given as

$$-\boldsymbol{\sigma} \cdot \boldsymbol{\nabla} = \mathbf{0} \text{ in } \Omega_\square, \tag{1}$$

$$\boldsymbol{\sigma} = \mathbf{E} : \boldsymbol{\epsilon}, \tag{2}$$

$$\boldsymbol{\epsilon} \coloneqq (\boldsymbol{u} \otimes \boldsymbol{\nabla})^{\text{sym}}, \tag{3}$$

$$\boldsymbol{\nabla} \cdot \boldsymbol{j} = 0 \text{ in } \Omega_\square, \tag{4}$$

$$\boldsymbol{j} = -\boldsymbol{D} \cdot \boldsymbol{\nabla}\mu, \tag{5}$$

where $\boldsymbol{\sigma}$ is the sub-scale stress, $\boldsymbol{u}$ is the displacement field, $\boldsymbol{\epsilon}$ is the linear symmetric sub-scale strain and $\mathbf{E}$ is the sub-scale isotropic stiffness tensor for the linear elasticity problem. For the diffusion problem $\boldsymbol{j}$ is the sub-scale ion mass flux, μ is the sub-scale electro-chemical potential and $\boldsymbol{D}$ is the isotropic sub-scale conductivity tensor which is, in the simplest case of isotropy, defined as $\boldsymbol{D} = D\boldsymbol{I}$.

[1]Modified and reproduced with permission by Niklas Ihrner [5] under the license CC BY 3.0.

While formulating the corresponding weak forms is straightforward, the scale separation needs to be addressed properly. The prolongation rule employs an additive split of the displacement field and the electro-chemical potential field

$$\boldsymbol{u}(\boldsymbol{x}) = \boldsymbol{u}^{\mathrm{M}}(\boldsymbol{x}) + \boldsymbol{u}^{\mathrm{s}}(\boldsymbol{x}), \quad \boldsymbol{x} \in \Omega_{\square}, \tag{6}$$

$$\mu(\boldsymbol{x}) = \mu^{\mathrm{M}}(\boldsymbol{x}) + \mu^{\mathrm{s}}(\boldsymbol{x}), \quad \boldsymbol{x} \in \Omega_{\square}. \tag{7}$$

Here, $\boldsymbol{u}^{\mathrm{M}}(\boldsymbol{x})$ and $\mu^{\mathrm{M}}(\boldsymbol{x})$ are the smooth displacement and electro-chemical potential fields, while $\boldsymbol{u}^{\mathrm{s}}(\boldsymbol{x})$ and $\mu^{\mathrm{s}}(\boldsymbol{x})$ are the sub-scale displacement and electro-chemical potential fluctuation fields. The smooth fields are prescribed according to the assumption of first order homogenization as

$$\boldsymbol{u}^{\mathrm{M}}(\boldsymbol{x}) = \bar{\boldsymbol{\epsilon}} \cdot [\boldsymbol{x} - \bar{\boldsymbol{x}}], \quad \boldsymbol{x} \in \Omega_{\square}, \tag{8}$$

$$\mu^{\mathrm{M}}(\boldsymbol{x}) = \boldsymbol{\nabla}\bar{\mu} \cdot [\boldsymbol{x} - \bar{\boldsymbol{x}}], \quad \boldsymbol{x} \in \Omega_{\square}, \tag{9}$$

where the imposed macro-scale strain $\bar{\boldsymbol{\epsilon}}$ and electro-chemical potential gradient $\boldsymbol{\nabla}\bar{\mu}$ serve as the driving forces for respective problem. Rigid body motion on the macro-scale does not affect the mechanical response, and a constant macro-scale electro-chemical potential $\bar{\mu}$ is omitted since it does not change the diffusion process in the stationary case. The reference point $\bar{\boldsymbol{x}}$ is chosen arbitrarily, but a common choice is the SVE centre.

The next step is to specify the boundary conditions. The strongly periodic boundary conditions (SPBC) are mainly defined by the micro-periodicity assumption. Micro-periodicity assumes that the sub-scale fluctuation fields $\boldsymbol{u}^{\mathrm{s}}$ and μ^{s} are periodic on the boundary of the SVE. Before defining the micro-periodicity assumption formally, it is first necessary to introduce the boundary split $\Gamma_{\square} = \Gamma_{\square}^{+} \cup \Gamma_{\square}^{-}$, where $\Gamma_{\square}^{+}$ is the image boundary ("positive" side) and $\Gamma_{\square}^{-}$ is the mirror boundary ("negative" side). The consequence of introducing such a boundary split is that every point on a boundary gets a partner point on the opposite side. The next step is to introduce the periodic mapping operator $\varphi_{\mathrm{per}} : \Gamma_{\square}^{+} \mapsto \Gamma_{\square}^{-}$ such that $\boldsymbol{x}^{-} = \varphi_{\mathrm{per}}(\boldsymbol{x}^{+})$. Finally, the micro-periodicity of the displacement and ion concentration fluctuation field can be expressed as

$$\boldsymbol{u}^{\mathrm{s}}(\boldsymbol{x}) = \boldsymbol{u}^{\mathrm{s}}(\varphi_{\mathrm{per}}(\boldsymbol{x})), \quad \forall \boldsymbol{x} \in \Gamma_{\square}^{+}, \tag{10}$$

$$\mu^{\mathrm{s}}(\boldsymbol{x}) = \mu^{\mathrm{s}}(\varphi_{\mathrm{per}}(\boldsymbol{x})), \quad \forall \boldsymbol{x} \in \Gamma_{\square}^{+}. \tag{11}$$

Moreover, the symmetry condition of the sub-scale stress and ion mass flux are defined as

$$\boldsymbol{\sigma}(\boldsymbol{x}) \cdot \boldsymbol{n} = \boldsymbol{\sigma}(\varphi_{\mathrm{per}}(\boldsymbol{x})) \cdot \boldsymbol{n}, \quad \forall \boldsymbol{x} \in \Gamma_{\square}^{+}, \tag{12}$$

$$\boldsymbol{j}(\boldsymbol{x}) \cdot \boldsymbol{n} = \boldsymbol{j}(\varphi_{\mathrm{per}}(\boldsymbol{x})) \cdot \boldsymbol{n}, \quad \forall \boldsymbol{x} \in \Gamma_{\square}^{+}, \tag{13}$$

where $\boldsymbol{n}$ denotes the outward-pointing normal on $\Gamma_{\square}^{+}$. Hence, the surface fluxes $\boldsymbol{t} \coloneqq \boldsymbol{\sigma} \cdot \boldsymbol{n}$ and $j \coloneqq \boldsymbol{j} \cdot \boldsymbol{n}$ are anti-periodic.

Although the SPBC are defined here, they are implemented in a weak sense. Nevertheless, all of this gives a solvable sub-scale problem. Lastly, we introduce the homogenization of the sub-scale quantities which is defined by the SVE volume average operator

$$\langle \bullet \rangle_{\square} \coloneqq \frac{1}{|\Omega_{\square}|} \int_{\Omega_{\square}} \bullet \, \mathrm{d}\Omega, \tag{14}$$

which gives the macro-scale stress and ion mass flux in a post-processing step as

$$\bar{\boldsymbol{\sigma}} = \langle \boldsymbol{\sigma} \rangle_{\square}, \tag{15}$$

$$\bar{\boldsymbol{j}} = \langle \boldsymbol{j} \rangle_{\square}. \tag{16}$$

Since the linear elasticity problem is solved in a strain-controlled setting, and the macro-scale ion concentration gradient is prescribed in the linear diffusion problem, it becomes a trivial task to compute the corresponding effective properties based on the macro-scale constitutive equations.

Preliminary numerical results

The effective Young's modulus $\bar{E}$ (normalized) and the effective diffusion coefficient $\bar{D}$ (normalized) are computed for a wide range of porosities ϕ and structures, see Figure 2. Note that the different structures only exist in certain porosity ranges since each structural electrolyte must be a bicontinuous system.

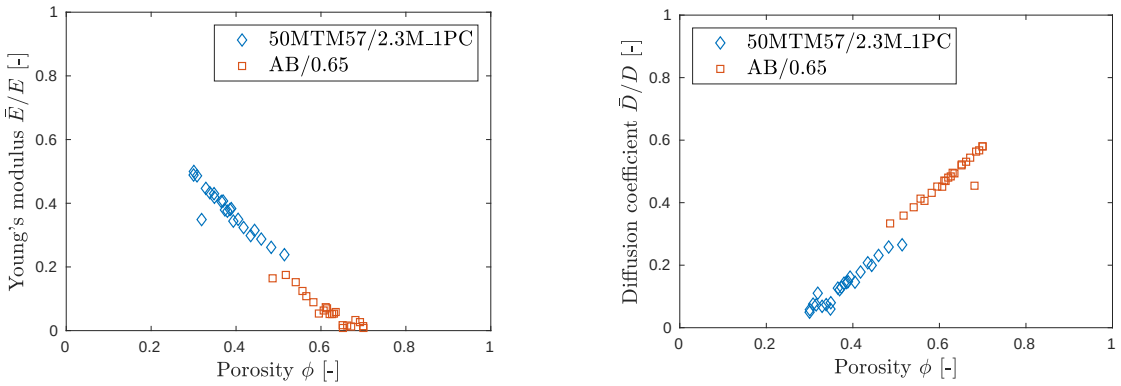

(a) (b)

Figure 2: Effective properties for different microstructures and their relevant ranges of porosity. (a) Effective Young's modulus (normalized). (b) Effective diffusion coefficient (normalized).

References

[1] J. F. Snyder, E. L. Wong, and C. W. Hubbard, "Evaluation of Commercially Available Carbon Fibers, Fabrics, and Papers for Potential Use in Multifunctional Energy Storage Applications", *Journal of The Electrochemical Society*, vol. 156, pp. A215-A224, 2009.

[2] L. E. Asp and E. Greenhalgh, "Structural Power Composites" in *Composites Science and Technology*, vol. 101, pp. 41-61, 2014.

[3] F. Larsson, K. Runesson, S. Saroukhani and R. Vafadari, "Computational homogenization based on a weak format of micro-periodicity for RVE-problems", *Computer Methods in Applied Mechanics and Engineering*, vol. 200, pp. 11-26, 2011.

[4] Shirshova et al., "Composition as a Means To Control Morphology and Properties of Epoxy Based Dual-Phase Structural Electrolytes", *The Journal of Physical Chemistry C*, vol. 118, pp. 28377-28387, 2014.

[5] N. Ihrner, W. Johannisson, F. Sieland, D. Zenkert and M. Johansson, "Structural Lithium Ion Battery Electrolytes via Reaction Induced Phase-Separation", *Journal of Materials Chemistry A*, vol. 5, pp. 25652-25659, 2017.

Proceedings of the 32nd Nordic Seminar on Computational Mechanics
A.H. Niemi and H. Koivurova (Eds.)

Mathematical modelling of sustainable bioresidual concrete

Tero Tuovinen[1], Teemu Leppänen[1] Joni Parkkonen[2], Jussi Virkajärvi[2], and Leena Turunen[3]

(1)University of Jyväskylä, Faculty of Inf. Technology, {tero.tuovinen, teemu.e.leppanen}@jyu.fi
(2)University of Jyväskylä, Department of Physics, {joni.parkkonen, jussi.virkajarvi}@jyu.fi
(3)Jyväskylä University of Applied Sciences, School of Technology, leena.turunen@jamk.fi

Summary. In the production of cement, which is the main component of concrete production, the process generates about 5% of the global carbon dioxide emissions. In addition, bioproduct and pulp mills produce significant quantities of soda ash and bio-ash, which is still largely unused. In this paper we will introduce our study related to improving the environmental friendliness of concrete used in construction by utilizing pulp mill waste while its long-term durability and strength and porosity properties meet the goals set for construction. The project 'sustainable bioresidual concrete' is on-going and only preliminary numerical results with measurements are presented here.

Key words: Concrete, Mathematical modelling, Sustainability, Carbon dioxide, Finite element method

Introduction

The aim of the project is to improve the environmental friendliness of concrete used in construction by using pulp mill waste while its long-term durability and strength and porosity properties meet the goals set for construction. In the project we will produce test pieces of concrete mixed in various ways, including cement, water, sand, ash and green liquor dregs (GLD). Concrete samples and their required strength and porosity properties are measured in both the JAMK's (Jyväskylä University of Applied Sciences) Concrete Technology Laboratory and by utilizing X-ray microtomography device of the Department of Physics at the University of Jyväskylä. In addition, samples and material and behavioral models are built on JYU's (University of Jyväskylä) Faculty of Information Technology to help optimize processes and sustainability.

One of the most important raw materials in construction is still concrete. While other forms of construction, such as wood and steel construction, are gaining in popularity, the application of these types of construction is much smaller than that of concrete construction. However, concrete as a building material is problematic; the production of one of its key components, cement, is environmentally harmful; it is estimated that 5% of the world's anthropogenic carbon dioxide emissions come from cement production. To prevent this, additives are used in the concrete, such as coal ash (= fly ash) and paper sludge as a waste-based source of calcite in cement [1].

The bio-ash and soda ash produced by the forest industry are not suitable for direct use as a concrete component. This has posed challenges for the recovery of forest industry waste in the construction industry. The project will result in a resource efficient way of utilizing the waste described above as a raw material and / or mixer for concrete. Studies show that fly ash improves many of the properties of concrete and reduces the amount of cement needed. Preliminary studies have also shown that the use of bio-ash and soda ash can improve the properties of concrete with respect to some criterias. The challenge so far has been considered due to variations in the composition of these waste fractions.

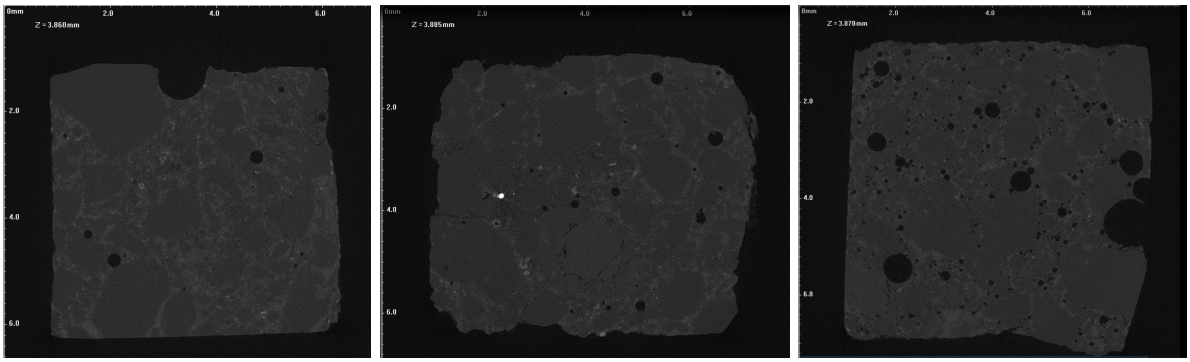

Figure 1. Cross sections from the concrete samples including 0% (left), 5% (center) and 10% (right) bio-ash.

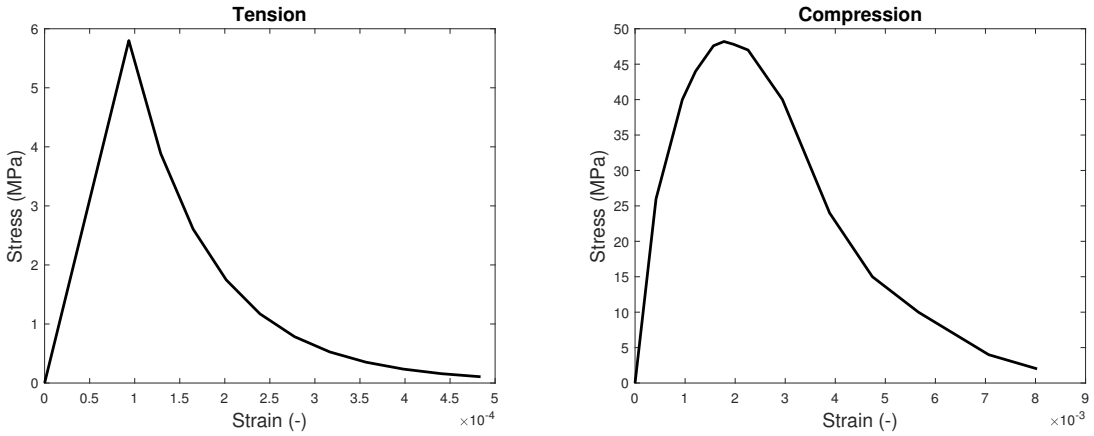

Figure 2. Material model for tension (left) and compression (right).

Concrete strength problems have been encountered especially in various infrastructures. One cause of the strength problems is the porosity of the concrete, which has caused, in particular, a decrease in compressive strength. Compressive strength is the most important strength property of concrete. However, the relationship between the porosity of concrete and its compressive strength is complex and has been extensively studied. However, at present, there are reliable mathematical models which can be used to predict the relationship between the porosity of a concrete and its strength; the main factor in the modeling is the pore size, and in particular the pore size distribution, which can be used to determine its effect on concrete strength.

Mathematical modelling of the case

X-ray tomography is used to reveal the structure of the samples having different amount of bio-ash, see Fig. 1. The size of the measured samples is roughly 5 mm×5 mm×5 mm. The pore size distributions are defined and used as a base structure of various sized simulation samples. Material model (Fig. 2) used in the simulations is based on typical behavior of concrete [2]. An example of simulated behavior under z-directional compressional stress is presented in Fig. 3. The developed model will be validated with respect to the data obtained and separate compression and/or endurance measurements. Once the model and the numerics involved in solving it are at a reliable level, multi-objective optimization can be initiated for a variety of material contents and uses.

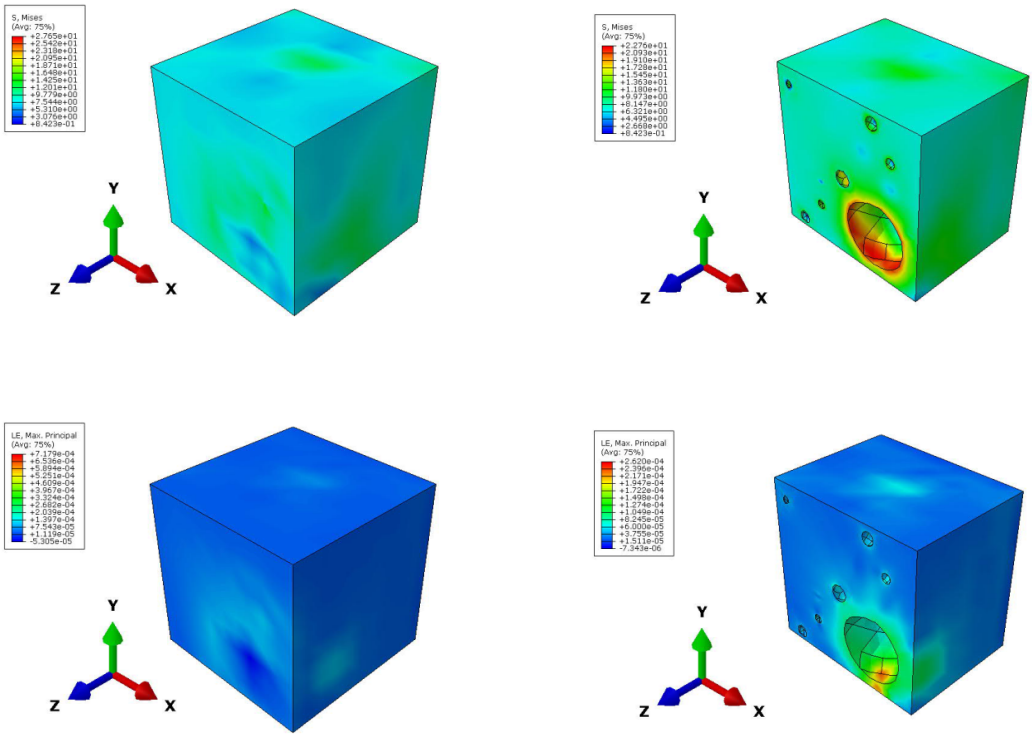

Figure 3. Simulated von Mises stress (top row) and maximum principal strain (bottom row) during the concrete damage under z-directional compressional stress. Size of the simulated sample is 0.5 mm×0.5 mm×0.5 mm.

Conclusions

In this paper, we have introduced the process model we use in mathematical modeling of biodesidual concrete and in strength and durability analyzes. Our aim is to produce more environmentally friendly concrete for the construction industry and to eliminate problematic soda ash from the paper and board industry.

Acknowledgements

This research is supported by Regional Council of Central Finland and European Regional Development Fund (ERDF) - Sustainable Bioresidual Concrete. Simulations are performed by commercial software ABAQUS which is licensed to CSC (the Finnish IT center for science).

References

[1] E. Adesanya, K. Ohenoja, T. Luukkonen, P. Kinnunen, M. Illikainen *One-part geopolymer cement from slag and pretreated paper sludge* Journal of Cleaner Production 185 (2018) 168-175.

[2] C.G. Koh, M.Q. Teng, T.H. Wee *A Plastic-Damage Model for Lightweight Concrete and Normal Weight Concrete* International Journal of Concrete Structures and Materials 2 (2008) 123-136.

Proceedings of the 32nd Nordic Seminar on Computational Mechanics
A.H. Niemi and H. Koivurova (Eds.)

Comparison of selected sequential design of experiment strategies for fatigue testing

Joona Vaara[1], Miikka Väntänen[2], Jukka Kemppainen[3] and Tero Frondelius[1,4]

(1)Wärtsilä, Järvikatu 2-4, 65100 Vaasa, Finland, joona.vaara@wartsila.com
(2)Global Boiler Works Oy, Lumijoentie 8, 90400 Oulu, Finland
(3)Applied and Computational Mathematics, Pentti Kaiteran katu 1, 90014 University of Oulu, Finland
(4)Materials and Mechanical Engineering, Pentti Kaiteran katu 1, 90014 University of Oulu, Finland

Summary. Selected sequential designs of experiment strategies were compared using simulated data. Namely, Staircase (up-and-down), D-optimal, objective and subjective predictive strategies were studied using Monte Carlo simulation. Subjective criteria are optimal for their objective, but might not give robust characterization of the general distribution. Staircase method was found to work surprisingly well, given a well chosen step size. The D-optimal and objective predictive strategies were found the most robust.

Key words: Sequential design of experiments, Fatigue testing

Introduction

Fatigue is still largely experimental science and thus robust, accurate and fast fatigue test machines and methods are needed to make fatigue testing more informative and cheaper. Recently, increased focus has been on improving the data analysis - extracting more information out of the same data set by means of statistical analysis and by including more relevant metadata as explanatory variables [1]. The latter approach requires development of more sophisticated models for the analysis. Another classical, and much studied, option to improve the information value of experiments is the design of experiments (DoE) [2]. In the field of fatigue, barring a few exceptions [3, 4], staircase method (also known as the up-and-down method) has cemented its popularity [5]. The design of experiment strategy was invented by Dixon and Mood in 1948 [6] with particular interest in finding the median value of the underlying distribution in binary response tests. Its popularity has been increased by its simplicity; little training is needed for the laboratory staff to perform tests using this strategy.

In non-linear models, the use of sequential design over batch design based on prior is superior. This is straight-forward to understand as the DoE based on prior information does not utilize the information from the test results and is thus unable to adapt to the changed situation. Wald [7] was a pioneer in developing sequential analysis. Adopting Bayesian approach is natural in the DoE problems as, from mathematical point of view, no design can be made without prior information. Another benefit of the Bayesian approach is the usefulness of the information retained in the full posterior in DoE problems. Predictions can be made from the posterior distribution and different loss/utility functions, indicating the purpose of the experiments, can be calculated from it to design the experiments [2]. Lindley introduced the measure of information provided by an experiment [8]. The D-optimality also has roots in the information theory - maximizing

the expected gain of Shannon information [9, 10, 11]. Predictive accuracy improvement can be formulated as utility function to drive the tests as well [2]. Other, and computationally more expensive DoE methods [12] rely on statistical decision making theory and Dynamic Programming [13].

In this paper, Staircase method, D-optimal, objective and subjective predictive design of experiment strategies were compared for testing the fatigue strength of pre-defined number of cycles.

Model

Consider the fatigue strength to be a random variable Z that follows Normal distribution

$$Z \sim \mathcal{N}(\mu, \sigma^2), \tag{1}$$

where μ is the location parameter and σ is the scale parameter. Testing at stress amplitude $x \in \mathcal{D}$ then yields a binary response $Y \in \mathcal{Y}$: the specimen either fails or survives. We can thus say, that the response is generated from a Bernoulli distribution with failure probability $p(x)$ that depends on the stress amplitude.

$$Y \sim \mathrm{Ber}(p(x)) \tag{2}$$

The probability of failure is equivalent to the probability of fatigue strength being lower than the applied stress amplitude

$$P(\text{fail}) = P(Z < x) \tag{3}$$

From this, it follows that

$$Y \sim \mathrm{Ber}(P(Z < x)) \tag{4}$$

As we adopt Bayesian framework, the likelihood is

$$f(y \mid \theta) = \begin{cases} P(Z < x), & y = 1 \text{ (fail)}, \\ 1 - P(Z < x), & y = 0 \text{ (survive)}, \end{cases} \tag{5}$$

where $\theta \in \Theta$ represents the parameter vector $[\mu, \sigma]$. We set the prior distributions for these parameters. If the observations were direct samples of fatigue limit, we could have used the conjugate prior of Normal-inverse-Gamma distribution for Normal distributed variable. As that is not the case, we choose the prior mean value to follow Normal distribution

$$\mu \sim \mathcal{N}(\mu_\mu, \sigma_\mu^2) \tag{6}$$

and the prior standard deviation to follow log-Normal distribution

$$\ln \sigma \sim \mathcal{N}(\mu_\sigma, \sigma_\sigma^2). \tag{7}$$

The updating of posterior is performed using Bayesian inference

$$f(\theta \mid y) = \frac{f(y \mid \theta) f(\theta)}{f(y)}, \tag{8}$$

where $f(\theta)$ is the prior distribution and $f(y) = \int f(y \mid \theta) f(\theta) d\theta$ is the evidence.

Staircase method

In the staircase method, initial test level x_0 is assigned, preferably close to the prior mean value. In addition, the step size d is determined before the tests. Dixon and Mood suggested that the step size should be between 0.5 to 2.0 times the true standard deviation of the fatigue strength [6]. In the algorithm, tests are initiated from the initial test level and if failure is observed, next test level is decreased by the step size; and after observation of survive, the next test level is increased by the step size.

$$x_{i+1} = \begin{cases} x_i - d, & y_i = 1 \text{ (fail)} \\ x_i + d, & y_i = 0 \text{ (survive)} \end{cases} \tag{9}$$

The stationary distributions have been analyzed in [14] and the test points are typically symmetrically distributed on both sides of the median value. The algorithm is designed to find the median value, but is not optimal for testing the standard deviation. Another problem with this method is that, combined with the Maximum Likelihood -method and relatively small sample sizes (20-30) typical for fatigue testing, it is quite common to get degenerate fatigue limit distributions. This occurs when the fatigue test has both responses (fail and survive) only at one test level, and above that every time the specimen have failed and below survived. The probability of getting such sample is naturally increased with too high step size. This stiffness of the algorithm and inability of changing the step size based on the observations is the cost for the simplicity of the algorithm.

D-optimal

Lindley states, that sometimes the purpose of the experiment can be to gain information of the world [8]. The D-optimality criterion can be derived both from Fisher's information matrix as well as from information theory [2]. The information theoretic approach maximizes the expected Kullback-Leibler divergence between the posterior and prior distributions

$$x_{i+1} = \arg\max_{x \in \mathcal{D}} \mathbb{E}_y \left[\int \log \left(\frac{f(\theta \mid y, x)}{f(\theta)} \right) f(\theta \mid y, x) d\theta \right] \tag{10}$$

Kullback-Leibler divergence is the expected gain in differential Shannon information [9, 10].

Predictive criteria

Sometimes the purpose of the experiment is to make predictions. This could be seen as the typical scenario for fatigue testing.

Objective

In objective testing we are interested of improving the prediction capabilities of the fatigue strength, without any specific load level in mind. One way to achieve this is to maximize the expected Kullback-Leibler divergence between the posterior and prior predictive distributions. Posterior predictive distribution can be calculated from

$$f(x \mid y) = \int f(x \mid \theta) f(\theta \mid y) d\theta \tag{11}$$

And prior predictive is

$$f(x) = \int f(x \mid \theta) f(\theta) d\theta \tag{12}$$

Finally, the next test level can be computed from

$$x_{i+1} = \arg\max_{x \in \mathcal{D}} \mathbb{E}_y \left[\int \log \left(\frac{f(z \mid y, x)}{f(z)} \right) f(z \mid y, x) dz \right]. \tag{13}$$

Subjective

In subjective testing the prediction accuracy of e.g. component specific load levels or predefined failure quantiles (required reliability) are of interest. Typically the expected variance is minimized. For the case of specific load level spectrum $w(x)$ with $\int w(x)dx = 1$ and interest in failure probability we get

$$x_{i+1} = \arg\min_{x \in \mathcal{D}} \mathbb{E}_y \left[\int w(z) \mathrm{Var}_\theta \left(F(z \mid \theta) \right) dz \right]. \tag{14}$$

For prediction accuracy of certain quantile $\hat{p}$ again the expected variance is minimized

$$x_{i+1} = \arg\min_{x \in \mathcal{D}} \mathbb{E}_y \left[\mathrm{Var}_\theta \left(F^{-1}(\hat{p} \mid \theta) \right) \right], \tag{15}$$

where $F^{-1}(\cdot \mid \theta)$ is the quantile function.

Methods

A simulation distribution for fatigue strength with parameters $(\mu, \sigma) = (200, 20)$ were arbitrarily chosen. The specimen-wise fatigue strengths were sampled for 50 specimen. This way each DoE algorithm operated on the same underlying data. A total of 500 repeats of Monte Carlo simulation were performed for each DoE algorithm. The DoE algorithms chosen for comparison were

- Staircase test with $(x_0, d) = (200, 20)$ (perfect guess)
- D-optimal criterion (Kullback-Leibler)
- Predictive Kullback-Leibler
- Predictive quantile (1/1000 failure probability)
- Predictive level (load $\sim \mathcal{N}(100, 10)$)
- Staircase test with $(x_0, d) = (200, 10)$
- Staircase test with $(x_0, d) = (200, 40)$

The prior hyperparameters were arbitrarily chosen to be $(\mu_\mu, \sigma_\mu) = (200, 50)$ and $(\mu_\sigma, \sigma_\sigma) = (3, 0.4)$ representing a generous amount of uncertainty. The credibility regions for prior cdfs are shown in Figure 1.

Following metrics were followed:

- Prediction distribution Kullback-Leibler divergence to the real simulation distribution
- Predictive distribution standard deviation
- Failure probability at stress corresponding to the true failure probability 1/1000
- Standard deviation of the failure probability prediction
- 1/1000 failure probability quantile mean
- 1/1000 failure probability quantile standard deviation

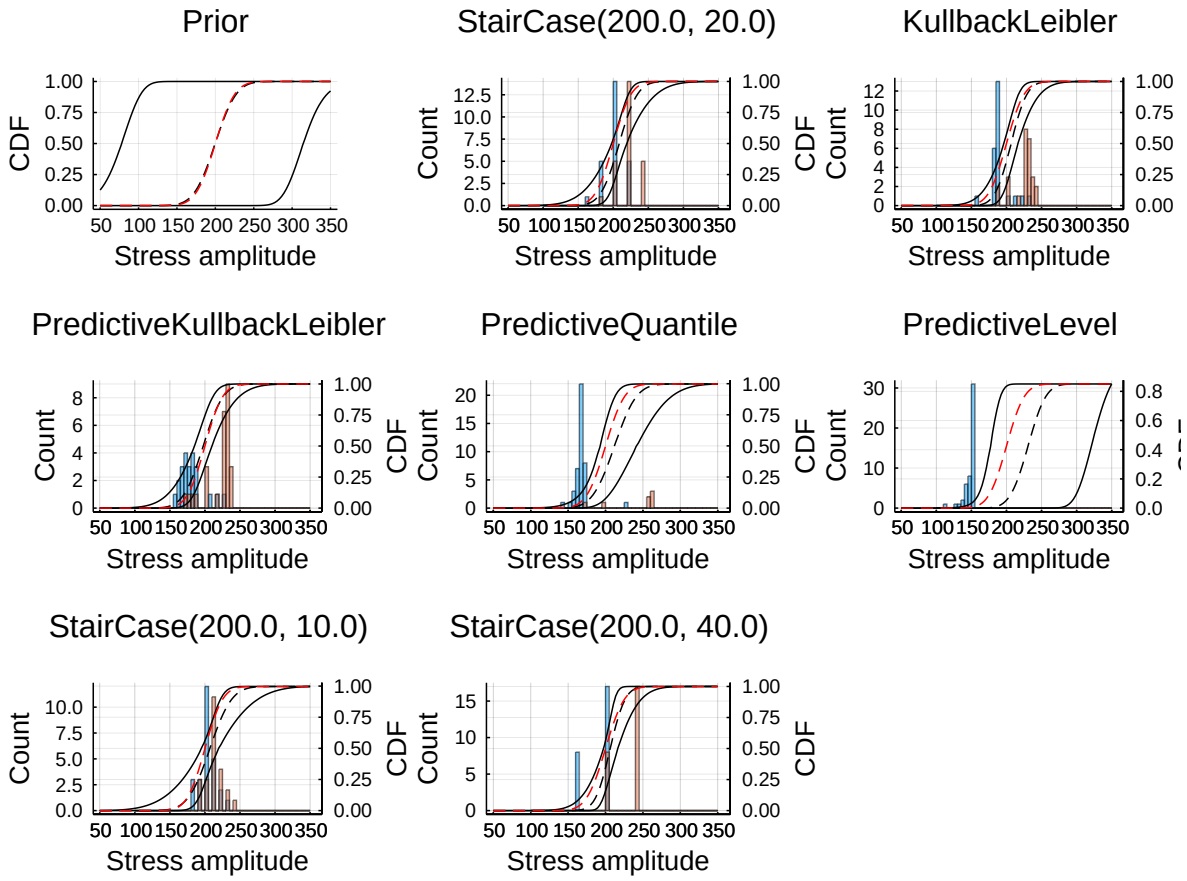

Figure 1. Overview of DoE algorithms allocation of 50 test points. Failed tests are shown with light brown and survived with light blue. The quantiles for CDFs are 1%, 50% (dashed) and 99% in black lines. The underlying simulation distribution CDF is plotted with red dashed line.

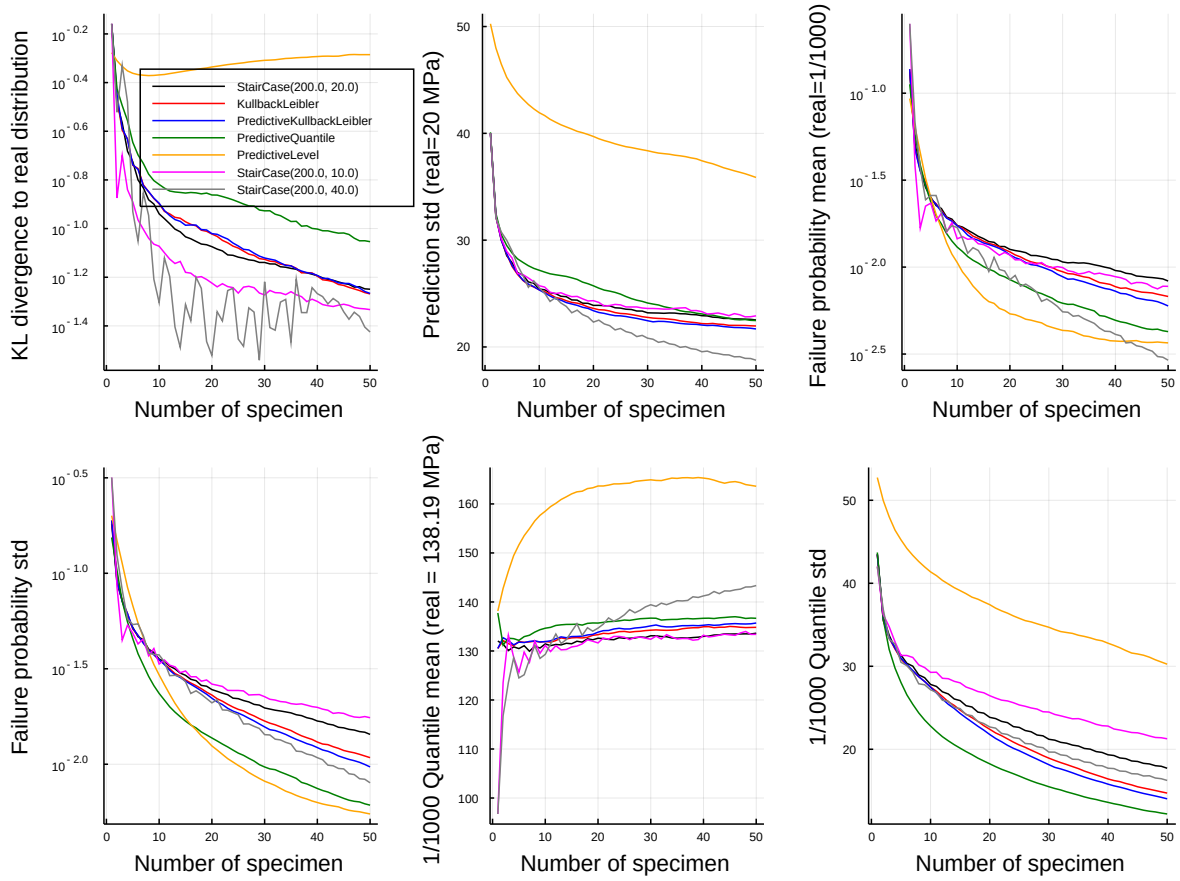

Figure 2. Results of the Monte Carlo simulation (500 repeats), the mean values of the pre-determined metrics for each DoE algorithm.

Results

An example of how the DoE algorithms allocate 50 test points is shown in Figure 1. It can be seen that the staircase test allocates test points symmetrically on both sides of median value, whereas both Kullback-Leibler based methods allocate resources on testing approximately 20% and 80% quantiles. Predictive quantile has the goal to minimize the 1/1000 failure probability quantile and thus it is natural for it to focus on testing the low quantiles, although the algorithm also tested some occasional high quantiles. The predictive level has the objective to minimize the prediction variance at stress amplitudes around 90-110 MPa, and is thus very focused on testing the very low quantiles, for which all the specimen have survived.

The results from the 500 repeats can be seen in Figure 2. The Kullback-Leibler divergence based control algorithms are stable performers; the development is steady but they are not the best in anything particular. The robustness of these algorithms can be seen as their strength. The predictive quantile is slightly worse in the objective metrics, but beats most algorithms in the low failure probability prediction and robustness of development for the low quantile estimates. The predictive level only shines in the low failure probability prediction, but performs sub-optimally for everything else. The Staircase methods with different step sizes have some interesting characteristics: the optimal step size ($d = \sigma$) is on par with the KL-based methods in the objective metrics, but performs worse in the prediction of the low failure probabilities. The low quantile prediction variance decreases with increase of step size. Similar trend is seen for the fatigue strength standard deviation. Two of the methods produced a non-conservative mean 1/1000 quantile: the highest step size Staircase method and the predictive level algorithm. The KL-based methods have, on average, lower 1/1000 quantile variance compared to the Staircase

method based tests indicating a better quantification of the standard deviation parameter.

Conclusions

Several sequential test planning strategies were presented and compared. If one has specific use for the fatigue test data in mind, the subjective utilities could be compelling. On the other hand, if one is interested in the general characteristics of fatigue strength, the Kullback-Leibler based methods seem robust also to low quantile estimates, that are typically of interest in fatigue dimensioning. The inability of Staircase method to adapt the step size based on the observations is seen as a clear disadvantage. Hybrid utilities, such as combination of quantile prediction and Kullback-Leibler divergence, and DoE based on dynamic programming could be worth studying for fatigue testing in the future.

References

[1] SP Zhu, Stefano Foletti, and Stefano Beretta. Probabilistic framework for multiaxial lcf assessment under material variability. *International Journal of Fatigue*, 103:371–385, 2017.

[2] Kathryn Chaloner and Isabella Verdinelli. Bayesian experimental design: A review. *Statistical Science*, pages 273–304, 1995.

[3] Miikka Väntänen, Joona Vaara, Jukka Aho, Jukka Kemppainen, and Tero Frondelius. Bayesian sequential experimental design for fatigue tests. *Rakenteiden Mekaniikka*, 50(3):201–205, 2017.

[4] Kenneth J Ryan. Estimating expected information gains for experimental designs with application to the random fatigue-limit model. *Journal of Computational and Graphical Statistics*, 12(3):585–603, 2003.

[5] Robert Eugene Little. Manual on statistical planning and analysis for fatigue experiments. (588), 1975.

[6] Wilfrid Joseph Dixon and Am M Mood. A method for obtaining and analyzing sensitivity data. *Journal of the American Statistical Association*, 43(241):109–126, 1948.

[7] Abraham Wald. Sequential tests of statistical hypotheses. *The annals of mathematical statistics*, 16(2):117–186, 1945.

[8] Dennis V Lindley et al. On a measure of the information provided by an experiment. *The Annals of Mathematical Statistics*, 27(4):986–1005, 1956.

[9] Claude Elwood Shannon. A mathematical theory of communication. *Bell system technical journal*, 27(3):379–423, 1948.

[10] Solomon Kullback et al. An application of information theory to multivariate analysis. *The Annals of Mathematical Statistics*, 23(1):88–102, 1952.

[11] Solomon Kullback. *Information theory and statistics*. Courier Corporation, 1997.

[12] Xun Huan and Youssef M Marzouk. Sequential bayesian optimal experimental design via approximate dynamic programming. *arXiv preprint arXiv:1604.08320*, 2016.

[13] Richard Bellman. Dynamic programming. *Science*, 153(3731):34–37, 1966.

[14] Assaf P Oron. Stationary and convergence properties of 'up-and-down' methods. 2006.

Proceedings of the 32nd Nordic Seminar on Computational Mechanics
A.H. Niemi and H. Koivurova (Eds.)

Crankshaft impact modelling

Antti-Jussi Vuotikka[1], Marko Jokinen[1], Pasi Halla-aho[2], Jukka Aho, Antti Mäntylä[2] and Tero Frondelius[3]

(1) Global Boiler Works Oy, firstname.surname@gbw.fi
(2) Wärtsilä, firstname.surname@wartsila.com
(3) University of Oulu, firstname.surname@oulu.fi

Summary. The longitudinal impact wave is going to be produced to the Wärtsilä 16 vee 32 crankshaft by hammering, which simulates the real impact phenomenon in the running engine with 17 ms period. In this study, this kind of measurement setup is modeled by using commercial Abaqus explicit finite element program. The intensity of the crankshaft energy levels, acceleration, and strains are followed 25 ms period after impact. This study shows the locations, which are needed to monitor during measurements and clarify how the impact wave may affect the high cycle fatigue safety.

Key words: Impact, wave propagation, Explicit FEM, Wärtsilä

Introduction

There are not directly any longitudinal forces or excitation in the running engine. The firing forces causes bending of the shafts and thus create a remarkable longitudinal extension of the crankshaft. An axial thrust bearing located near the flywheel end of the crankshaft limits the longitudinal movement of the crankshaft in the large-bore medium-speed combustion engine. Longitudinal movement consequently causes periodical impacts to the crankshaft, because it hits against the engine block through the bearing. This means that there are fluctuating kinetic and internal energies [1] in the crankshaft causing traveling strain waves to the body. The impact periodic is 17 ms coming from running speed of the engine. This phenomenon is planned to measure from the Wärtsilä 16 vee 32 crankshaft. [2, 3, 4]

Global Boiler Works Oy produces pneumatic linear impact hammers. The hammer is used to create impact energy which is needed in the measurements. The impact speed of the piston can be adjusted by using reference bar [5, 6] so that the corresponding energy level can be created as in the real phenomenon in the running engine. The hammer hits single direct impact to the flywheel end of the crankshaft near the axial thrust bearing.

Finite element method is used to study the measurement setup. There are analytical models for impacts and wave propagation phenomena, but the usage of these methods is limited into simple structures [7, 8]. Explicit FEM models accurately physical behavior of impact and wave propagation in complex shape structures, if method limitations are not ignored during the analysis. [9, 10, 11]

The analysis model consists part of the hammer, the mounting equipment, and complete crankshaft, see figure 1). The Hammer body is connected to anvil by using sliding contact. It is assumed that the hammer body does not affect the measurements, and it is ignored. The hammer components, which are included in the model, are the piston and the piston spring. The anvil and fastening ring are needed to mount the hammer into the crankshaft. Mounting components are included in the calculation model but without bolts. The crankshaft body is divided into

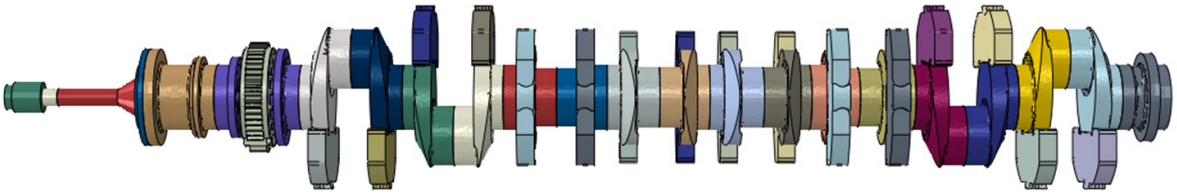

Figure 1. The different colors represent different sections in the analyzed calculation model. This is used to study energy distribution in the structure.

separate parts: head and end sections, gearwheel and crankpins. Every counterweight is a separate component.

Results

The energy levels are followed in the different parts of the analyzed structure. If we follow energy distribution between different parts of the model through the analysis time, we can find the most likely the locations where occurs the highest strain intensities and thus highest stresses without following single strain waves during the analysis.

The total impact energy goes through the head section of the crankshaft creating highest strain energies into it. Traveling energy wave excites the first shafts and counterweights. The traveling wave reflects countless times from every discontinuity surfaces. Impact energy reaches the end section of the crankshaft within 2.5 ms of the impact.

One hypothesis was that the impact energy is trapped into the head section of the crankshaft due to large discontinuous surface of the first shaft. This could not be seen from the results. Still, the highest peak energies are in the first two crankpins and their counterweights through the analyzed time. The highest strain intensities are probably found from the fillets of these crankpin shafts. According to results, the mean intensity of the strain is $\pm 5\,\mu$strain, which is possible to measure from the pin surface by using strain gauges. The peak amplitude strains are close to $20\,\mu$strain in the same locations.

The strain gauge measurement is not so optimal for the counterweights. Most of the energy stays in the kinetic form in the counterweights due to their shape and location in the crankshaft. According to this result, accelerometers are recommended to use vibration measurements of the counterweights, especially the first and the third counterweight.

Conclusion

The impact causes measurable strain waves. The analysis results showed that the most exciting results could be found from the head and the first two crankpins. These locations are recommended to be instrumented carefully. The periodical loading and the high intensity of the strain can affect to fatigue durability of the component.

There are several sources of damping in the engine, but the effect of damping was estimated to be small in this case. Thus, damping effects were ignored in this initial analysis. Forthcoming measurements show the effect of damping in the real structure, which helps to evaluate better the reliability of the results of the finite element analysis.

Acknowledgements

The authors would like to acknowledge the financial support of Business Finland in the form of a research projects ISA Wärtsilä Dnro 7734/31/2018, and ISA GBW Dnro 7752/31/2018.

References

[1] Herbert Kolsky. *Stress waves in solids*, volume 1098. Courier Corporation, 1963.

[2] Ilkka Väisänen, Antti Mäntylä, Antti Korpela, Teemu Kuivaniemi, and Tero Frondelius. Medium speed engine crankshaft analysis. *Rakenteiden Mekaniikka*, 50(3):341–344, 2017. open access. URL: `https://doi.org/10.23998/rm.64916`.

[3] Tero Frondelius, Pasi Halla-aho, and Antti Mäntylä. Crankshaft development with virtual engine modelling. In *CIMAC Congress Helsinki*, 2016.

[4] Rune Nordrik and Haavard Solbakken. Vibration characteristics of a v20 medium speed gas engine. simulation and measurement. In *CIMAC, CIMAC World Congress on Combustion Engine, 26th, Bergen, NO, 2010-06-14 - 2010-06-17*, 2010.

[5] M. Jokinen, A.-J. Vuotikka, and S.-G. Sjölind. Suorassa pyörötangossa etenevän jännitysaallon kokeellinen mittaus. *In: Mäkinen, R. et al.(toim.). Proceedings ot the 10th Finnish Mechanics Days, X Suomen Mekaniikkapäivät, Jyväskylä, 3.–4.12. 2009*, 2009.

[6] A.-J. Vuotikka, M. Jokinen, and S.-G. Sjölind. Suorassa pyörötangossa etenevän jännitysaallon analysointi FEM:llä. *In: Mäkinen, R. et al.(toim.). Proceedings ot the 10th Finnish Mechanics Days, X Suomen Mekaniikkapäivät, Jyväskylä, 3.–4.12. 2009*, 2009.

[7] Dan Stoianovici and Yildirim Hurmuzlu. A critical study of the applicability of rigid-body collision theory. *TRANSACTIONS-AMERICAN SOCIETY OF MECHANICAL ENGINEERS JOURNAL OF APPLIED MECHANICS*, 63:307–316, 1996.

[8] A Żak and M Krawczuk. Assessment of flexural beam behaviour theories used for dynamics and wave propagation problems. *Journal of Sound and Vibration*, 331(26):5715–5731, 2012.

[9] D Cerniglia, A Pantano, and N Montinaro. 3d simulations and experiments of guided wave propagation in adhesively bonded multi-layered structures. *NDT & E International*, 43(6):527–535, 2010.

[10] Friedrich Moser, Laurence J Jacobs, and Jianmin Qu. Modeling elastic wave propagation in waveguides with the finite element method. *Ndt & E International*, 32(4):225–234, 1999.

[11] Emmanuel Le Clezio, Mihai Valentin Predoi, Michel Castaings, Bernard Hosten, and Martine Rousseau. Numerical predictions and experiments on the free-plate edge mode. *Ultrasonics*, 41(1):25–40, 2003.

Proceedings of the 32nd Nordic Seminar on Computational Mechanics
A.H. Niemi and H. Koivurova (Eds.)

Fatigue Testing - Informativity of the Experimental Data

Miikka Väntänen[1], Joona Vaara[2], Jukka Kemppainen[3] and Tero Frondelius[2,4]

(1)Global Boiler Works Oy, Lumijoentie 8, 90400 Oulu, Finland, miikka.vantanen@gbw.fi
(2)Wärtsilä, Järvikatu 2-4, 65100 Vaasa, Finland
(3)Applied and Computational Mathematics, Pentti Kaiteran katu 1, 90014 University of Oulu, Finland
(4)Materials and Mechanical Engineering, Pentti Kaiteran katu 1, 90014 University of Oulu, Finland

Summary. Information content of fatigue test data is discussed in this paper. Two popular approaches to quantifying the informativity of experimental data are described. A small numerical example is presented to show the process of quantifying the information gains when inferring the fatigue limit from binary data.

Key words: information content, fatigue test, Kullback-Leibler divergence

Introduction

Quantifying the informativity of any experimental data has been under research and studies for decades. The increased interest is easy to understand and can be explained by two problems of interest: the inference and the decision problem [1]. For either problem, the idea is to maximise the benefits of the tests - be it maximising the overall information gained or to help with reaching a specific decision. Understanding the potential information value helps in both the experimental design as well as analysing the already observed experimental data.

In fatigue testing, inferring the fatigue limit/strength of a material subject to a pre-defined test runout limit is a common task. Usually, fatigue limit is defined as the threshold stress amplitude that the material withstands for an infinite number of cycles without a failure. As such, it is impossible to verify experimentally. This leads to the concept of censored data. A failure observation is considered censored data in terms of fatigue limit. It is safe to assume that within the limits of measuring accuracy, the fatigue limit of the tested specimen is lower than the failure-inducing load level. Similarly, a runout observation can be considered as censored data with respect to fatigue life. It can be stated that the specimen did not fail within the number of loading cycles tested, but could fail if the test was continued. The indirectness of fatigue test data limits the amount of information gained. Brooks [2] studied the information loss with different types of censored data. This paper presents some of the main concepts on the informativity of experimental data. A practical example is shown for analysing the expected information gain with respect to censored data.

Test Information Quantity

In 1948, Shannon [3] provided the groundwork in information theory, especially for the field of communication engineering. Based on Shannon's initial ideas on (discrete) entropy, Lindley [1] extended the concept to assess the information content of a continuous distribution. Lindley describes the initial prior information of the parameters interest as

$$g_0 = \int p(\theta) \log p(\theta)\, d\theta, \tag{1}$$

where $p(\cdot)$ denotes a probability distribution and θ represents the parameter vector. This definition is equal to the additive inverse of differential entropy, which was presented by Shannon in his own attempt to expand his discrete entropy to continuous distributions [4].

Similarly, in terms of observed y, the updated information one has about the parameters can be defined by [1]

$$g_1(y) = \int p(\theta \mid y) \log p(\theta \mid y)\, d\theta. \tag{2}$$

The average amount of information provided by the observation y is simply defined by the expected difference of the two states

$$g(p(\theta)) = \mathbb{E}_y (g_1(y) - g_0). \tag{3}$$

In addition to Lindley, Kullback and Leibler among others further expanded Shannon's ideas to statistical theory (see e.g., [5]. The Kullback-Leibler divergence [6] is a measure commonly used to analyse the difference between two distributions. The measure is not limited to either discrete or continuous distributions. Within the Bayesian framework, it is considered as a measure of the information gained when moving from prior to posterior distribution.

The Kullback-Leibler (later abbreviated as KL) divergence can be calculated for continuous distributions as [7]

$$D_{\mathrm{KL}}(p \mid\mid q) = \int_{-\infty}^{\infty} p(\theta \mid y) \ln \left(\frac{p(\theta \mid y)}{q(\theta)} \right) d\theta, \tag{4}$$

where the usual notation of the Bayesian approach is used; $p(\theta \mid y)$ denotes the posterior probability density having observed data y and $q(\theta)$ is the prior probability density. Maximising the KL divergence leads to a Bayesian experimental D-optimal test design [8].

Fatigue limit example

The following example focuses on the analysis of a normally distributed fatigue limit in the Bayesian framework. The data is assumed binary, i.e., the data likelihood is defined by

$$\mathcal{L}(y, c|\theta) = \begin{cases} F(y|\theta) \mid c = 0 \\ \bar{F}(y|\theta) \mid c = 1 \end{cases}, \tag{5}$$

where y represents the testing load level, $F(\cdot)$ denotes a cumulative distribution function, $\bar{F}(\cdot)$ is the complementary cumulative distribution function and c is the respective binary censoring factor. Here, c value of 0 stands for a failure observation and 1 stands for a runout observation.

Given that the fatigue limit is assumed normally distributed, the prior parameter probability space can be defined by two parameters; the distribution mean value parameter μ and the deviation parameter σ. For the numerical example, let the parameters follow normal distributions

$$\mu \sim \mathcal{N}(500, 20) \tag{6}$$

and

$$\sigma \sim \mathcal{N}(100, 30), \tag{7}$$

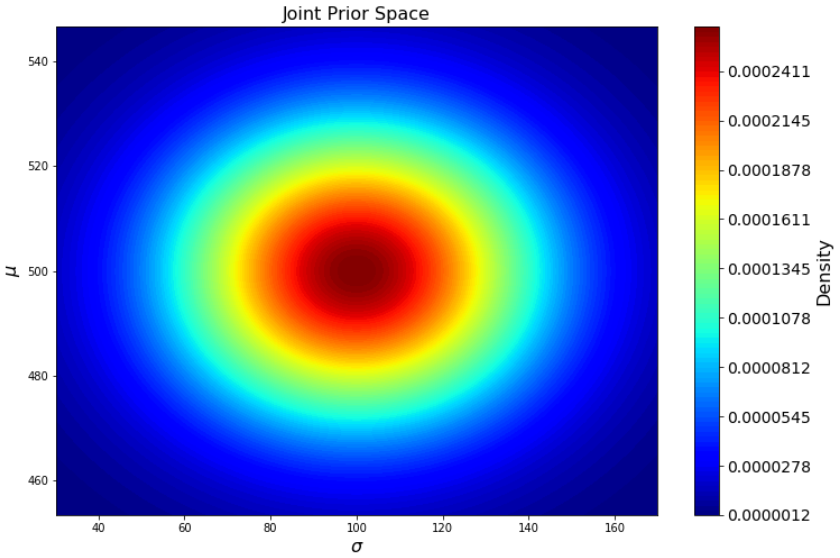

Figure 1. Prior probability space.

where $\mathcal{N}(loc, scale)$ denotes a normal density function with mean *loc* and standard deviation *scale*. Figure 1 shows the contour plot of the joint prior space described by the parameter distributions.

The prior predictive fatigue limit distribution for an untested specimen is defined by

$$f(\sigma_l) = \int f(\sigma_l \mid \theta) f(\theta) d\theta, \tag{8}$$

where σ_l stands for the fatigue limit random variable, and $f(\cdot)$ for a probability density function. The posterior distribution after observing data (y, c) can be defined using the data likelihood (5)

$$f(\theta \mid y, c) = \mathcal{L}(y, c \mid \theta) f(\theta) \tag{9}$$

Similarly, after observing fatigue data (y, c), the posterior predictive distribution for the fatigue limit of an untested specimen is described by

$$f(\sigma_l | y, c) = \int f(\sigma_l \mid \theta) f(\theta | y, c) d\theta. \tag{10}$$

For predicting the fatigue limit distribution of the tested specimen, the specimen specific posterior predictive density is defined as

$$f(\sigma_l) = \int f(\sigma_l \mid \theta, \alpha(y, c), \beta(y, c)) f(\theta \mid y) d\theta, \tag{11}$$

where the parameters α and β represent the censoring bounds defined by the binary data. Figure 2 shows the predictive distributions for all the cases mentioned above. The posterior predictive distributions are plotted after observing data $y = 550$, $c = 1$. The figure shows how the runout observation with relatively high loading shifts the common predictive distribution to higher load values. Additionally, when analysing the fatigue limit of the tested specimen, the observed runout limit truncates the specimen-specific posterior predictive distribution.

Figure 3 shows three different approaches to quantifying the *expected information gain* from a single specimen test using the KL divergence. The approaches are based on different goals.

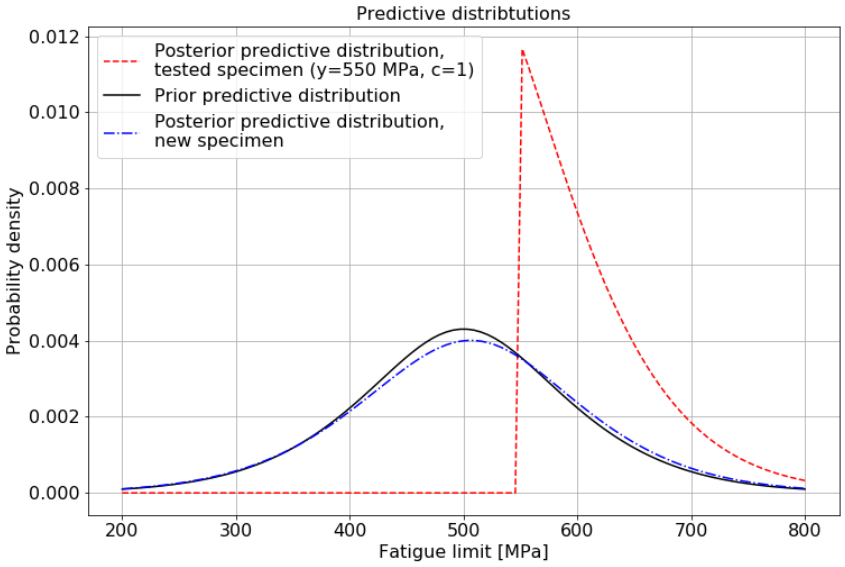

Figure 2. Prior and posterior predictive distributions.

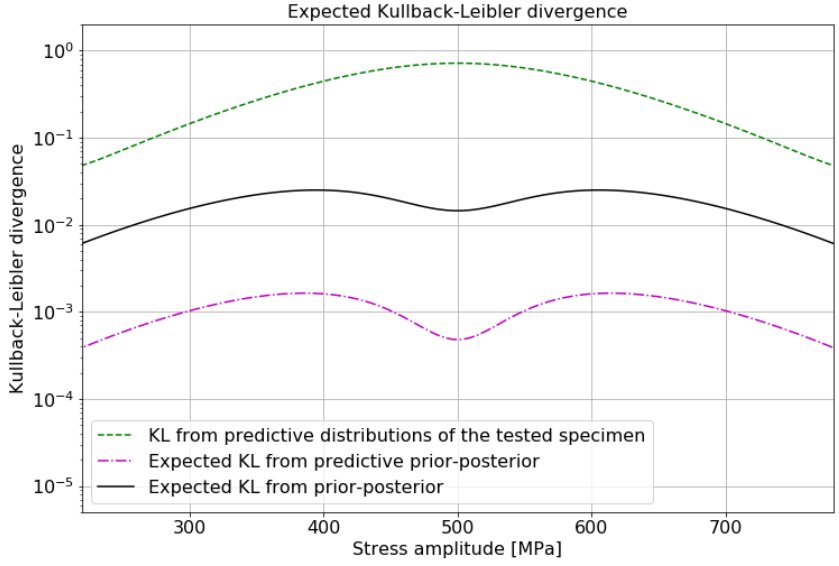

Figure 3. Different approaches with Kullback-Leibler divergence.

The expected divergence distribution obtained from prior to posterior (solid black line) is analogous to the distribution that is maximised for a Bayesian D-optimal design. Similarly used for different test designs [8] is the expected KL divergence (dashed purple curve) from predictive prior distribution to predictive posterior distribution. Lastly, the top-most green line represents an approach quantifying the expected information gain on the predictive fatigue limit distribution of the *tested specimen*. The estimation is equal to the expected KL divergence between the prior predictive and the (truncated) specimen-specific distribution.

The results show that there is a significant difference between the expected information gain from a test with the different approaches. It is especially interesting to note that a test provides

more information about the predictive specimen-wise distribution compared with the common distributions. Additionally, the optimal testing point is located in the mean value of the prior predictive distribution, unlike with the KL measures from common distributions.

References

[1] Dennis V Lindley et al. On a measure of the information provided by an experiment. *The Annals of Mathematical Statistics*, 27(4):986–1005, 1956.

[2] RJ Brooks. On the loss of information through censoring. *Biometrika*, 69(1):137–144, 1982.

[3] Claude Elwood Shannon. A mathematical theory of communication. *Bell system technical journal*, 27(3):379–423, 1948.

[4] Thomas M Cover and Joy A Thomas. *Elements of information theory*. John Wiley & Sons, 2012.

[5] Solomon Kullback et al. An application of information theory to multivariate analysis. *The Annals of Mathematical Statistics*, 23(1):88–102, 1952.

[6] Solomon Kullback. *Information theory and statistics*. Courier Corporation, 1997.

[7] Christopher M Bishop. *Pattern recognition and machine learning*. springer, 2006.

[8] Kathryn Chaloner and Isabella Verdinelli. Bayesian experimental design: A review. *Statistical Science*, pages 273–304, 1995.

Proceedings of the 32nd Nordic Seminar on Computational Mechanics
A.H. Niemi and H. Koivurova (Eds.)

Multiscale design optimization of structures with solid coating and periodic infill lattice

Eddie Wadbro[1] and Bin Niu[2]

(1)Department of Computing Science, Umeå University, SE-901 87 Umeå, Sweden, eddiew@cs.umu.se
(2)School of Mechanical Engineering, Dalian University of Technology, 116024, Dalian, People's Republic of China, niubin@dlut.edu.cn

Summary. We consider multiscale topology optimization of an infill structure. The structure is composed of an optimized layout configuration at the macroscale with uniform optimized microstructures as infill lattices coated by a thin skin. The design optimization of the infill lattice is performed simultaneously with the topology optimization of macroscale structure, which also includes the coating. Several numerical examples demonstrate the effectiveness of the proposed method optimization.

Key words: Topology optimization, mathematical morphology, coated structures, periodic infill

Introduction

In this work, we optimize a structure that has a solid coating and a periodic infill pattern, which consists of a periodic distribution of uniform optimized microstructures. Figure 1 schematically illustrates such a structure.

Henceforth, we refer to the overall layout of the structure as the macroscale design, while the microscale design denotes the infill pattern's arrangement. The coating at the macroscale is designed by using the mathematical morphology based nonlinear filters [8, 9, 3]. These morphology mimicking non-linear filters also distinguish the skin and the infill lattice parts of the design at the macroscale and realize length scale control on the topologies of the macrostructure as well as the microstructure. The design optimization of the lattice layout is performed simultaneously as the design of the macroscale structure. The two-scale topology optimization method PAMP [5, 6] designs the macro layout and micro topologies. In this work, the classic Solid Isotropic Material Penalization (SIMP) method [1, 7] designs the layout at the microstructure. The novel implementation of asymptotic homogenization (NIAH) [2] computes the effective properties of periodic microstructure.

Morphology

Mathematical morphology is a branch of image analysis, which uses a set B, typically referred to as the structuring element, to probe and gain information about another set $M \subset \mathbb{R}^d$. Heijmans' review [4] provides a good introduction to mathematical morphology. The standard morphological operators are defined for subsets of $\mathbb{R}^d$. Recently, Hägg and Wadbro [3] extended the definitions of the basic morphological operators for subsets of a bounded domain $\Omega \subset \mathbb{R}^d$, and it is these operators that we will use below.

Figure 3 illustrates important morphological to identify the coating the infill parts on the macroscale. More precisely, Figure 3 shows (i) the so-called structuring element B, (ii) the

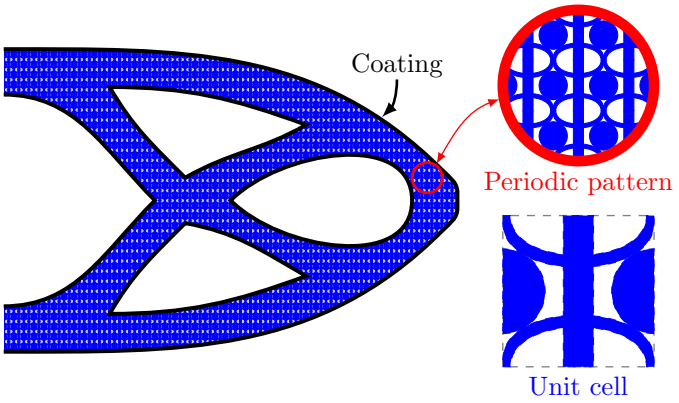

Figure 1. Schematic illustration of the macroscopic layout, the shell surfaces, and the microstructure of the infilled lattice

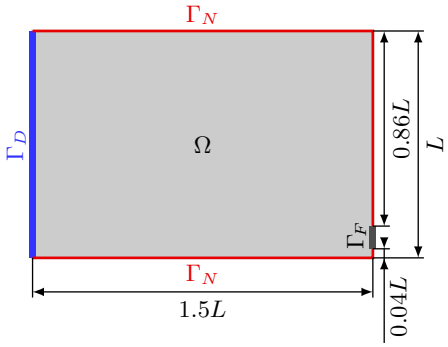

Figure 2. The macroscale computational domain

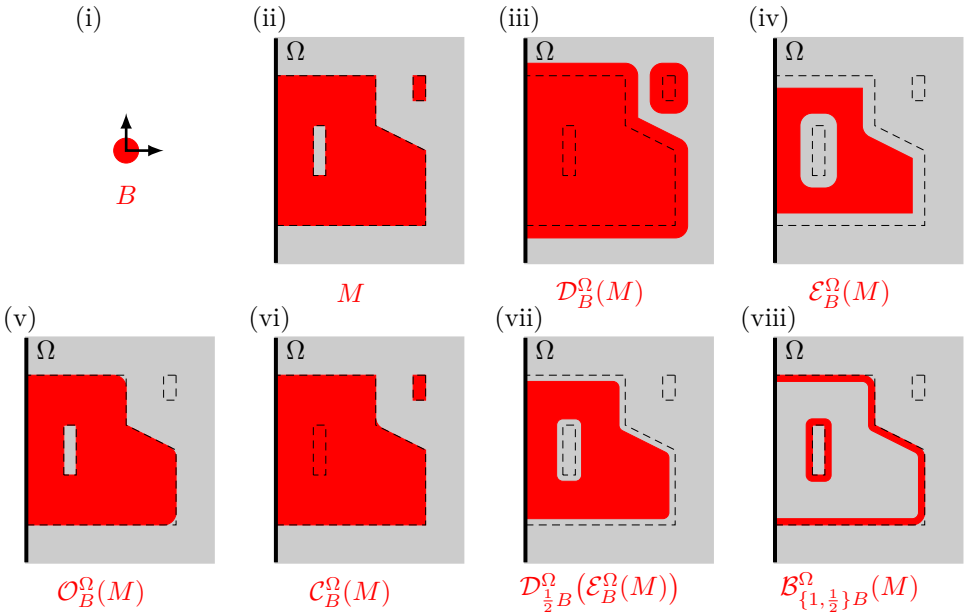

Figure 3. Illustration of morphological operations.

domain M, (iii) M dilated by B relative Ω, (iv) M eroded by B relative Ω, (v) M opened by B relative Ω, (vi) M closed by B relative Ω, (vii) the interior of the physical domain, and (viii) an identified boundary region for the physical domain. The operators involved are defined as

$$\begin{aligned} \mathcal{D}_{rB}^\Omega(M) &= \{m+b \mid m \in M,\, b \in rB\} \cap \Omega, & \mathcal{O}_{rB}^\Omega(M) &= \mathcal{D}_{rB}^\Omega\big(\mathcal{E}_{rB}^\Omega(M)\big), \\ \mathcal{E}_{rB}^\Omega(M) &= \{y \in \Omega \mid y + rB \subset (\mathbb{R}^d \setminus \Omega) \cup M\}, & \mathcal{C}_{rB}^\Omega(M) &= \mathcal{E}_{rB}^\Omega\big(\mathcal{D}_{rB}^\Omega(M)\big), \end{aligned} \tag{1}$$

where $r > 0$, $rB = \{x \in \mathbb{R}^N \mid r^{-1}x \in B\}$, and $y + rB = \{x \mid x - y \in rB\}$. We let r_c denote the width of the coating ($0 < r_c < r$), then the difference

$$\mathcal{B}_{\{r,r_c\}B}^\Omega(M) = \mathcal{D}_{rB}^\Omega\big(\mathcal{E}_{rB}^\Omega(M)\big) - \mathcal{D}_{\hat{r}B}^\Omega\big(\mathcal{E}_{rB}^\Omega(M)\big), \tag{2}$$

where $\hat{r} = r - r_c$, identifies a strip along the boundary of M.

Problem statement

Figure 1 illustrates the test case we consider, and Figure 2 illustrates the macroscale computational domain. The structure clamped at its left side Γ_D and subject to a vertical traction force

on boundary portion Γ_F, which occupies 10 % of the right side of the macroscale design domain Ω.

We discretize the microscale unit cell Y by $M = m_x \times m_y$ square elements and use an element-wise constant microscale design function α_h. By using this function, we define the microscale material indicator function η_h by using a morphology mimicking filtering procedure based on the harmonic mean [8, 9, 3]. Here, $\eta_h = 1$ where the base material is present and $\eta_h = 0$ in void regions. We discretize the macroscale design domain Ω by $N = n_x \times n_y$ square elements. We define our macroscale design function ρ_h to be an element-wise constant function and let $\boldsymbol{\rho} = [\rho_1, \rho_2, \ldots, \rho_N]^T$, where ρ_n is the value of ρ_h in Ω_n. To identify the infill and coating at the macroscale, we use combinations of morphology mimicking filters.

Here, we are interested in minimizing the compliance of the structure with a given minimal length scale as well as under a material budget on both the microscale and the microscale. We evaluate the material volume fraction on the microscale as

$$V(\boldsymbol{\alpha}) = \sum_{m=1}^{M} v_m^{\mathrm{MI}} \boldsymbol{\mathcal{C}}_{r_m}^{Y}(\boldsymbol{\alpha})_m, \tag{3}$$

where $v_m^{\mathrm{MI}} = |Y_m|/|Y|$ is the volume fraction of element m on the microscale and $\boldsymbol{\mathcal{C}}_{r_m}^{Y}$ approximates close operator relative to the microscale unit cell Y. On the macroscale, the relative cost of the coating material compared to the base material is w_{coat}. Thus, we evaluate the resource cost of the used material as

$$W(\boldsymbol{\rho}, \boldsymbol{\alpha}) = V(\boldsymbol{\alpha}) \sum_{n=1}^{N} v_n^{\mathrm{MA}} \boldsymbol{\mathcal{C}}_r^{\Omega}(\boldsymbol{\rho})_n + \big(w_{\mathrm{coat}} - V(\boldsymbol{\alpha})\big) \sum_{n=1}^{N} v_n^{\mathrm{MA}} \boldsymbol{\mathcal{B}}_{\{r,r_c\}}^{\Omega}(\boldsymbol{\rho})_n^2. \tag{4}$$

where $v_n^{\mathrm{MA}} = |\Omega_n|/|\Omega|$ is the volume fraction of the nth element on the macroscale, and $\boldsymbol{\mathcal{C}}_r^{\Omega}$ and $\boldsymbol{\mathcal{B}}_{\{r,r_c\}}^{\Omega}$ approximate the close and boundary indicator operators on the macroscale. The resulting optimization problem is

$$\begin{aligned} \min_{(\boldsymbol{\rho},\boldsymbol{\alpha}) \in \mathbb{R}^N \times \mathbb{R}^M} \quad & J(\boldsymbol{\rho}, \boldsymbol{\alpha}) \\ \text{subject to} \quad & W(\boldsymbol{\rho}, \boldsymbol{\alpha}) \leq W^*, \quad 0 \leq \rho_n \leq 1, \quad n = 1, 2, \ldots, N \\ & V^{\mathrm{MI}}(\boldsymbol{\alpha}) \leq V^*, \quad 0 \leq \alpha_m \leq 1, \quad m = 1, 2, \ldots, M \\ & \boldsymbol{K}^{\mathrm{MA}}(\boldsymbol{\rho}, \boldsymbol{\alpha}) \boldsymbol{u} = \boldsymbol{f}, \end{aligned}$$

where, $J(\boldsymbol{\rho}, \boldsymbol{\alpha}) = \boldsymbol{f}^T \boldsymbol{u}$ is the compliance, and $\boldsymbol{K}^{\mathrm{MA}}(\boldsymbol{\rho}, \boldsymbol{\alpha}) \boldsymbol{u} = \boldsymbol{f}$ is the governing equation, where $\boldsymbol{K}^{\mathrm{MA}}$ is the global stiffness matrix, $\boldsymbol{u}$ is the macroscale displacement vector, and $\boldsymbol{f}$ is the global load vector. The element stiffness matrix is

$$\boldsymbol{k}_e^{\mathrm{MA}}(\boldsymbol{\rho}, \boldsymbol{\alpha}) = E_{\min} \boldsymbol{k}_0 + \big(\boldsymbol{k}_e^{\mathrm{H}}(\boldsymbol{\alpha}) - E_{\min} \boldsymbol{k}_0\big)\, \mathcal{O}_{rB}^{\Omega}(\boldsymbol{\rho})_e^p + \big(E_{\mathrm{coat}} \boldsymbol{k}_0 - \boldsymbol{k}_e^{\mathrm{H}}(\boldsymbol{\alpha})\big) \left(\mathcal{B}_{\{r,r_c\}B}^{\Omega}(\boldsymbol{\rho})_e^2\right)^q,$$

where $\boldsymbol{k}_e^H(\boldsymbol{\alpha})$ is the homogenized element stiffness matrix corresponding to the current microstructure and $\boldsymbol{\mathcal{O}}_{rB}^{\Omega}$ approximates the close and boundary indicator operators on the macroscale.

Results

Figure 4 shows four results optimized using a discretization of 768×512 elements on the macroscale and 256×256 elements on the microscale. The results are obtained using $r = 10h^{\mathrm{MA}}$, $r_m = 6h^{\mathrm{MI}}$, and from left to right $r_c = \{8, 6, 4, \text{ and } 2\}h^{\mathrm{MA}}$, where h^{MA} and h^{MI} are the element sizes on the macroscale and microscale, respectively. The top row shows the macroscale designs, the middle row shows the coating, and the bottom row shows a 3-by-3 repetition of the microscale designs.

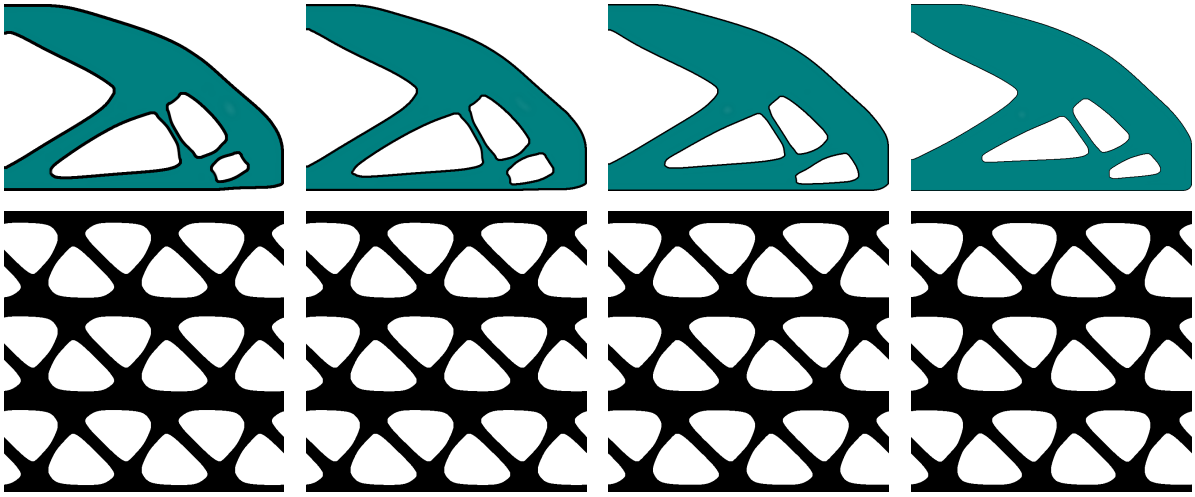

Figure 4. Results for four different coating radii. The top row shows the macroscale designs and the bottom row shows a 3-by-3 repetition of the microscale designs.

References

[1] M. P. Bendsøe. Optimal shape design as a material distribution problem. *Structural optimization*, 1(4):193–202, 1989.

[2] G. Cheng, Y.-W. Cai, and L. Xu. Novel implementation of homogenization method to predict effective properties of periodic materials. *Acta Mechanica Sinica*, 29(4):550–556, 2013.

[3] L. Hägg and E. Wadbro. On minimum length scale control in topology optimization. *Structural and Multidisciplinary Optimization*, 58(3):1015–1032, 2018.

[4] H. J. A. M. Heijmans. Mathematical morphology: A modern approach in image processing based on algebra and geometry. *SIAM Review*, 37(1):1–36, 1995.

[5] L. Liu, J. Yan, and G. Cheng. Optimum structure with homogeneous optimum truss-like material. *Computers & Structures*, 86(13–14):1417–1425, 2008.

[6] B. Niu, J. Yan, and G. Cheng. Optimum structure with homogeneous optimum cellular material for maximum fundamental frequency. *Structural and Multidisciplinary Optimization*, 39(2):115–132, 2009.

[7] G. I. N. Rozvany, M. Zhou, and T. Birker. Generalized shape optimization without homogenization. *Structural optimization*, 4(3–4):250–252, 1992.

[8] O. Sigmund. Morphology-based black and white filters for topology optimization. *Structural and Multidisciplinary Optimization*, 33(4–5):401–424, 2007.

[9] K. Svanberg and H. Svärd. Density filters for topology optimization based on the pythagorean means. *Structural and Multidisciplinary Optimization*, 48(5):859–875, 2013.

Author index